
2 **Consolidation and longevity of the CMS**
3 **Resistive Plate Chamber system in view of the**
4 **High-Luminosity LHC Upgrade**

5



Alexis Fagot

Thesis to obtain the degree of
Doctor of Philosophy in Physics
Academic year 2018-2019



⁷

⁸ Promotors: Dr. Michael Tytgat
Prof. Dr. Dirk Ryckbosch

⁹
¹⁰ Ghent University
¹¹ Faculty of Sciences
¹² Department of Physics and Astronomy
¹³ Proeftuinstraat 86, B-9000 Ghent, Belgium
¹⁴ Tel.: +32 9 264.65.28
¹⁵ Fax.: +32 9 264.66.97

¹⁶



Alexis Fagot

Thesis to obtain the degree of
Doctor of Philosophy in Physics
Academic year 2018-2019



17

Acknowledgements

18

19

XX/XX/2018

Alexis Fagot

Table of Contents

21	Acknowledgements	i
22	Nederlandse samenvatting	vii
23	English summary	ix
24	1 Introduction	1-1
25	2 Investigating the TeV scale	2-1
26	2.1 The Standard Model of Particle Physics	2-1
27	2.1.1 A history of particle physics	2-2
28	2.1.2 Construction and validation of the Standard Model	2-15
29	2.1.3 Investigating the TeV scale	2-16
30	2.2 The Large Hadron Collider & the Compact Muon Solenoid	2-20
31	2.2.1 LHC, the most powerful particle accelerator	2-21
32	2.2.2 CMS, a multipurpose experiment	2-25
33	2.2.2.1 The silicon tracker, core of CMS	2-27
34	2.2.2.2 The calorimeters, measurement of particle's energy	2-27
35	2.2.2.3 The muon system, corner stone of CMS	2-29
36	3 Muon Phase-II Upgrade	3-1
37	3.1 Motivations for HL-LHC and the upgrade of CMS	3-2
38	3.2 High Luminosity LHC and muon system requirements	3-3
39	3.3 Necessity for improved electronics	3-6
40	3.4 New detectors and increased acceptance	3-7
41	3.4.1 Gas electron multipliers	3-8
42	3.4.2 Improved forward resistive plate chambers	3-12
43	3.4.3 Installation schedule	3-14
44	3.5 Implications of the different upgrades on the Level-1 Trigger. Improvement of	
45	physics performance.	3-15
46	3.6 Ecofriendly gas studies	3-19
47	4 Physics of Resistive plate chambers	4-1
48	4.1 Principle	4-1
49	4.2 Rate capability and time resolution of Resistive Plate Chambers	4-3
50	4.2.1 Operation modes	4-3
51	4.2.2 Standard gas mixture for RPCs operated in collider experiments	4-5
52	4.2.3 Detector designs and performance	4-9
53	4.2.3.1 Double gap RPC	4-11
54	4.2.3.2 Multigap RPC (MRPC)	4-13
55	4.2.3.3 Charge distribution and performance limitations	4-16

56	4.3	Signal formation	4-18
57	4.3.1	Energy loss at intermediate energies	4-19
58	4.3.2	Primary ionization	4-23
59	4.3.3	Development and propagation of avalanches	4-27
60	4.3.4	Drift and diffusion of the electron cloud	4-31
61	4.3.5	Space charge effect & streamers	4-33
62	4.4	Effect of atmospherical conditions on the detector's performance	4-37
63	5	Longevity studies and Consolidation of the present CMS RPC subsystem	5-1
64	5.1	Testing detectors under extreme conditions	5-2
65	5.1.1	GIF	5-4
66	5.1.2	GIF++	5-5
67	5.2	Preliminary studies at GIF	5-7
68	5.2.1	RPC test setup	5-7
69	5.2.2	Geometrical acceptance of the setup layout to cosmic muons	5-9
70	5.2.2.1	Description of the simulation layout	5-10
71	5.2.2.2	Simulation procedure	5-11
72	5.2.2.3	Results and limitations	5-12
73	5.2.3	Photon flux at GIF	5-14
74	5.2.4	Results and discussions	5-17
75	5.3	Longevity tests at GIF++	5-20
76	5.3.1	Selection and characterization of CMS RPCs for longevity at GIF++	5-20
77	5.3.2	RPC test setup	5-22
78	5.3.3	GIF++ data flow	5-24
79	5.3.4	Measurements performed during beam periods	5-26
80	5.3.4.1	Efficiency scans	5-26
81	5.3.4.2	Rate scans	5-26
82	5.3.4.3	Offline analysis and Data Quality Monitoring	5-27
83	5.3.5	Measurements performed during irradiation periods	5-28
84	5.3.5.1	Longevity scans	5-29
85	5.3.5.2	Daily rate monitoring scans	5-30
86	5.3.5.3	Weekly noise monitoring scans	5-31
87	5.3.5.4	Weekly source scans	5-31
88	5.3.5.5	Weekly current scans	5-32
89	5.3.5.6	Resistivity measurements	5-32
90	5.3.6	Results and discussions	5-32
91	6	Improved RPC investigation and preliminary electronics studies	6-1
92	6.1	FEE candidate for the production of iRPCs	6-1
93	6.1.1	CMS RPCROC: the RPC upgrade baseline	6-2
94	6.1.2	INFN Front-End Electronics: a robust back-up solution	6-3
95	6.2	Preliminary tests at CERN	6-3
96	7	Conclusions and outlooks	7-1
97	7.1	Conclusions	7-1
98	7.2	Outlooks	7-1

A A data acquisition software for CAEN VME TDCs	A-1
A.1 GIF++ DAQ file tree	A-1
A.2 Usage of the DAQ	A-2
A.3 Description of the readout setup	A-3
A.4 Data read-out	A-3
A.4.1 V1190A TDCs	A-4
A.4.2 DataReader	A-7
A.4.3 Data quality flag	A-10
A.5 Communications	A-12
A.5.1 V1718 USB Bridge	A-13
A.5.2 Configuration file	A-14
A.5.3 WebDCS/DAQ intercommunication	A-17
A.5.4 Example of inter-process communication cycle	A-17
A.6 Software export	A-18
B Details on the offline analysis package	B-1
B.1 GIF++ Offline Analysis file tree	B-1
B.2 Usage of the Offline Analysis	B-2
B.2.1 Output of the offline tool	B-3
B.2.1.1 ROOT file	B-3
B.2.1.2 CSV files	B-5
B.3 Analysis inputs and information handling	B-6
B.3.1 Dimensions file and IniFile parser	B-7
B.3.2 TDC to RPC link file and Mapping	B-8
B.4 Description of GIF++ setup within the Offline Analysis tool	B-9
B.4.1 RPC objects	B-9
B.4.2 Trolley objects	B-10
B.4.3 Infrastructure object	B-10
B.5 Handeling of data	B-12
B.5.1 RPC hits	B-13
B.5.2 Clusters of hits	B-14
B.6 DAQ data Analysis	B-15
B.6.1 Determination of the run type	B-16
B.6.2 Beam time window calculation for efficiency runs	B-17
B.6.3 Data loop and histogram filling	B-18
B.6.4 Results calculation	B-21
B.6.4.1 Rate normalisation	B-21
B.6.4.2 Rate and activity	B-23
B.6.4.3 Correction of muon performance parameters	B-25
B.6.4.4 Strip masking tool	B-27
B.6.4.5 Output CSV files filling	B-29
B.7 Current information extraction	B-31

140

Nederlandse samenvatting –Dutch Summary–

141

English summary

List of Figures

143

144	2.1	Solar spectrum with spectral lines as it appeared visually to Fraunhofer.	2-2
145	2.2	Through the gold foil experiment Rutherford could show that most of the mass of atoms was contained in a positively charged nucleus and could then propose a more accurate atomic model than that of Thomson.	2-3
146			
147			
148	2.3	Figure 2.3a: The orbits in which the electron may travel according to the Bohr model of the hydrogen atom. An electron jumps between orbits and is accompanied by an emitted or absorbed amount of electromagnetic energy ($h\nu$). The orbits radius increases as n^2 . Figure 2.3b: Elliptical orbits with the same energy and quantized angular momentum $l = 0, 1, \dots, n - 1$ in the case $n = 5$. Figure 2.3c: Illustration of quantum mechanical orbital angular momentum. The cones and plane represent possible orientations of the angular momentum vector for $l = 2$ and $m = -2, -1, 0, 1, 2$	2-5
149			
150			
151			
152			
153			
154			
155	2.4	Figure 2.4a: The spectral lines of mercury vapor lamp anomalous Zeeman effect without magnetic field (A) and with magnetic field (B - transverse Zeeman effect & C - longitudinal Zeeman effect). Figure 2.4b: Stern-Gerlach experiment: Silver atoms travelling through an inhomogeneous magnetic field, and being deflected up or down depending on their spin.	2-6
156			
157			
158			
159			
160	2.5	Figure 2.5a: desintegration of a μ -meson in an emulsion. Figure 2.5b: track of a π -meson in an emulsion signed by Lattes, Powell, and Occhialini.	2-9
161			
162	2.6	Figure 2.6a: Meson octet. Figure 2.6b: Baryon octet. Figure 2.6c: Baryon decuplet.	2-10
163	2.7	Discovery of the J/Ψ by both SPEAR (SLAC [74]) in Figure 2.7a and AGS (BNL [75]) in Figure 2.7b. In Figure 2.7a, the cross section versus energy is showed for (a) multi hadron final states, (b) e^+e^- final states, and (c) $\mu^+\mu^-$, $\pi^+\pi^-$ and K^+K^- final states.	2-11
164			
165			
166	2.8	Figure 2.8a: the color field of QCD only allows for "white" baryons, particles composed of quarks, to exist. Examples are given for mesons, composed of a quark and its anti-quark, and hadrons, composed of 3 differently colored quarks or anti-quarks, but other exotic baryons have been predicted and observed, such as tetraquarks and pentaquarks. Figure 2.8b: a crossed analysis performed thanks to the data collected by various experiment at different energies have showed that the coupling constant evolves as predicted by the mechanism of asymptotic freedom [87].	2-12
167			
168			
169			
170			
171			
172			
173	2.9	Energy spectrum of beta particles emitted by a source of ^{210}Bi	2-13
174	2.10	As explained through Figure 2.10a, the Wu experiment consisted in measuring the prefered direction of emission of beta rays of a Cobalt source placed in a stable magnetic field aligned, in one case, and anti-aligned, in the other case, with the nuclear spin. The result of Figure 2.10b showed a violation of parity.	2-14
175			
176			
177			

178	2.11	The elementary particles of the Standard Model are shown along with their properties. Their interactions with the strong, weak and electromagnetic forces have been explicated using color squares. In the left column, the scalar higgs boson is depicted. The center is focused on the matter particles, the fermions, and the right column on the force carriers, the gauge bosons. The role of the Higgs boson in electroweak symmetry breaking is highlighted, and the corresponding way properties of the various particles differ in the (high-energy) symmetric phase (top) and the (low-energy) broken-symmetry phase (bottom) are shown.	2-16
186	2.12	Figure 2.12a: Total proton-proton cross-section as a function of the collisions center-of-mass energy \sqrt{s} [116] with cosmic-ray data from Akeno Observatory and Fly's Eye Collaboration. Figure 2.12b: Total proton-(anti)proton and interaction channel cross-sections in the TeV scale.	2-17
190	2.13	Rotation curve (points) of galaxy M33 compared with best fitting model (line). The short-dashed line represents the rotation profile that would be expected from the observation of the stellar disc alone [124].	2-18
193	2.14	Cosmic Microwave Background as measured by the space observatory Planck which mean temperature is $T_\gamma = (2.7255 \pm 0.0006)$ K with anisotropies of the order of a few μK	2-19
196	2.15	CERN accelerator complex.	2-21
197	2.16	Pictures of the different accelerators. From top to bottom: first the LINAC 2 and the Pb source of LINAC 3. Then the Booster and the LEIR. Finally, the PS, the SPS and the LHC.	2-23
200	2.17	Figure 2.17a: schematics of the LHC cryodipoles. 1: Superconducting Coils, 2: Beam pipe, 3: Heat exchanger Pipe, 4: Helium-II Vessel, 5: Superconducting Bus-bar, 6: Iron Yoke, 7: Non-Magnetic Collars, 8: Vacuum Vessel, 9: Radiation Screen, 10: Thermal Shield, 11: Auxiliary Bus-bar Tube, 12: Instrumentation Feed Throughs, 13: Protection Diode, 14: Quadrupole Bus-bars, 15: Spool Piece Bus-bars. Figure 2.17b: magnetic field and resulting motion force applied on the beam particles.	2-24
207	2.18	Figure 2.18a: picture of the LHC quadrupoles. Figure 2.18b: magnetic fields and resulting focussing force applied on the beam by 2 consecutive quadrupoles.	2-25
209	2.19	Picture of the CMS barrel. The red outer layer is the muon system hosted into the red iron return yokes. The calorimeters are the blue cylinder inside in magnet solenoid and the tracker is the inner yellow cylinder built around the beam pipe.	2-25
212	2.20	View of the CMS apparatus and of its different components.	2-26
213	2.21	Slice showing CMS sub-detectors and how particles interact with them.	2-27
214	2.22	CMS tracker.	2-27
215	2.23	Figure 2.23a: picture of the ECAL. Figure 2.23b: picture of the lead tungstate crystals composing the ECAL.	2-28
217	2.24	CMS hadron calorimeter barrel.	2-28
218	2.25	A quadrant of the muon system, showing DTs (yellow), RPCs (blue), and CSCs (green).	2-29
220	2.26	Figure 2.26a: Barrel wheel with its detector rings and return yokes. Figure 2.26b: CSC endcap disk with the 2 CSC stations. The outer station is made of 10 deg detectors while the inner station is made of 20 deg detectors. Figure 2.26c: RPC endcap disk. The inner station is not equipped and the inner CSC station can be seen.	2-30

224	2.27 Figure 2.27a: Cross section of a DT module showing the two superlayers measuring the ϕ coordinate, perpendicular to the cross section plane, and the superlayer measuring the η coordinate, placed in between the two others with honeycomb and parallel to the cross section plane. The DT detector is sandwiched in between 2 RPCs whose readout strips are perpendicular to the cross section plane, measuring the ϕ coordinate. Figure 2.27b: A DT cell is shown together with its electric field. The path of a muon through a superlayer is shown.	2-30
231	2.28 Figure 2.28a: cathode strips and anode wire layout of a CSC panel. Figure 2.28b avalanche development and charge collection by anode wires and induction on cathode strips inside of a CSC panel.	2-31
234	2.29 Muon track reconstruction through the 6 panels of a CMS CSC using the information of anode wire groups and cathode strip charge distribution combined with comparator bits to decide on which half strip the muon is more likely to have passed.	2-31
237	2.30 Double gap layout of CMS RPCs. Muons passing through the gas volumes will create electron-ions pairs by ionising the gas. this ionisation will immediately translate into a developing avalanche.	2-32
240	3.1 Slice of the CMS detector showing example of passage of SM particles and R-hadrons. On the one hand, lepton-like HSCPs will appear to behave like slow and heavy muons. On the other hand, R-hadrons are likely to convert into other kind of charged or neutral R-hadrons due to interactions inside the detector volume.	3-3
244	3.2 Detailed timeline projection of for LHC and HL-LHC operation until 2039 showing the evolution of the instantaneous and integrated luminosity as designed (Figure 3.2a) and in the ultimate case where the instantaneous luminosity is increased to $7.5 \times 10^{34} \text{ cm}^{-2}\text{s}^{-1}$ (Figure 3.2b) [160, 172].	3-4
248	3.3 Absorbed dose in the CMS cavern after an integrated luminosity of 3000 fb. Using the interaction point as reference, R is the transverse distance from the beamline and Z is the distance along the beamline.	3-5
251	3.4 A quadrant of the muon system, showing DTs (yellow), RPCs (blue), and CSCs (green). The locations of new forward muon detectors for Phase-II are contained within the dashed box and indicated in red for GEM stations (ME0, GE1/1, and GE2/1) and dark blue for improved RPC (iRPC) stations (RE3/1 and RE4/1).	3-5
255	3.5 Comparison of the simulated time residuals in between reconstructed and true muon times without (blue) and with (red) the upgraded RPC link system.	3-7
257	3.6 RMS of the multiple scattering displacement as a function of muon p_T for the proposed forward muon stations. All of the electromagnetic processes such as bremsstrahlung and magnetic field effect are included in the simulation.	3-8
261	3.7 Schematics of a GEM showing the cathode on top, the GEM foil separating the gas volume into the drift region, in between the cathode and foil, and the induction region, in between the GEM foil and the anode, and the anode on which a 2D readout is installed. A negative voltage is applied on the cathode while the anode is connected to the ground.	3-9
265	3.8 Left: Picture of a CMS GEM foil provided by a scanning electron microscope. Right: Representation of the electric field lines in a GEM hole and of the amplification that electrons and ions undergo in the hole's volume due to the very intense electric field.	3-9

268	3.9 Schematic representation of CMS triple GEMs. The gas volume is divided into 4 areas. The drift area is the region where the primary electrons are created before being amplified a first time while passing through the first GEM foil. Then the process of drift and amplification is repeated twice in following two transfer areas and GEM foils. Finally, the charges have been amplified enough to induce current in the read-out strips while in the last drift area. The dimensions, potentials and electric fields are provided.	3-10
275	3.10 Simulated efficiency and rate of the standalone Level-1 muon trigger using tracks reconstructed in CSCs and all GEM stations compared with Phase-I values in the case where only CSCs are used or CSCs+GE1/1. The zones of inefficiency of the CSC subsystem are compensated by the addition of GEMs during Phase-II and the trigger rates is kept from increasing due to the high luminosity.	3-10
280	3.11 Figure 3.11a: Simulated resolution of the muon direction measurement $\Delta\phi$ with Phase-II conditions. In the second endcap station, the resolution is compared in the case of CSCs (ME2/1) alone and CSCs+GEMs (GE2/1+ME2/1) while a similar resolution measurement is given in the case of the first station (GE1/1+ME1/1). Figure 3.11b: The addition of GEM detectors on stations 1 and 2 (ME0 is considered to contribute to station station 1) as redundant system to CSCs allows to improve the muon momentum improvement through a more accurate measurement of the local bending angles ϕ_1 and ϕ_2	3-11
288	3.12 Simulation of the impact of RPC hit inclusion onto the local trigger primitive efficiency in station 3 (left) and station 4 (right). The contribution of iRPC starts above $ \eta = 1.8$	3-12
291	3.13 Expected hit rate due to neutrons, photons, electrons and positrons at HL-HLC instantaneous luminosity of $5 \times 10^{34} \text{ cm}^{-2}\text{s}^{-1}$ in RE3/1 and RE4/1 chambers. The sensitivities of iRPCs used in the simulation for each particle are reported and differ from one endcap disk to another as the energies of the considered particles varies with the increasing distance from the interaction point.	3-13
296	3.14 Measured average charge per avalanche as a function of the effective electric field for different gas gap thickness in double gap RPCs using HPL electrodes.	3-14
298	3.15 Data flow of the Level-1 Trigger during Phase-II operations.	3-15
299	3.16 Efficiency of the L1 trigger in the endcap region after Phase-II upgrade in the case CSC/GEM/RPC hits are requested in at least 2 stations out of four (3.16a) and in all four stations (3.16b).	3-16
302	3.17 Resolution of the LCT ambiguous events thanks to the combination of CSC and iRPC readout data. Using CSCs only, 2 pairs of hits are possible.	3-17
304	3.18 The angular resolution on reconstructed muon tracks in the GEM overlap region $2.0 < \eta < 2.15$ is compared for Phase-II conditions in the case CSC are alone (Figure 3.18a) and in the case the GEMs' data, including ME0, is combined to which of CSCs (Figure 3.18b).	3-18
308	3.19 Comparison of L1 trigger performances for prompt muons with and without the addition of GEMs in the region $2.1 < \eta < 2.4$ at Phase-II conditions. GEMs would allow a reduction of the trigger accept rate by an order of magnitude (Figure 3.19a) while increasing the trigger efficiency (Figure 3.19b).	3-18

- 359 4.11 Distributions of the induced charge of fast signals on 2 mm (Figure 4.11a) and 8 mm
 360 (Figure 4.11b) RPCs exposed to a radiation rate of 100 Hz/cm². Average induced
 361 charge of fast signals as a function of the high voltage applied on 2 mm and 8 mm
 362 RPCs (Figure 4.11c). In the case of the 2 mm RPC, a saturation of the pre-amplifier
 363 was observed. The average of the distribution is underestimated and the median is
 364 showed together with the average to account for this bias [207]. 4-10
- 365 4.12 Time distributions of the leading, trailing, and average of both leading and trailing
 366 edges for 2 mm (top row) and 8 mm (bottom row) RPCs exposed to a 100 Hz/cm²
 367 radiation rate. The data was collected with RPCs operated at the voltage correspond-
 368 ing to the knee of the efficiency distribution, defined as the point where 95% of the
 369 maximum efficiency is obtained [207]. 4-11
- 370 4.13 Possible double-gap RPC layouts: a) "standard" 1D double-gap RPC, as used in
 371 CMS experiment, where the anodes are facing each other and a 1D read-out plane
 372 is sandwiched in between them, b) double read-out double-gap RPC as used in AT-
 373 LAS experiment, where the cathodes are facing each other and 2 read-out planes are
 374 used on the outer surfaces. This last layout can offer the possibility to use a 2D
 375 reconstruction by using orthogonal read-out planes. 4-12
- 376 4.14 Comparison of performance of CMS double and single gap RPCs using cosmic
 377 muons [203]. Figure 4.14a: Comparison of efficiency sigmoids. Figure 4.14b: Volt-
 378 age distribution at 95% of maximum efficiency. Figure 4.14c: $\Delta_{10\%}^{90\%}$ distribution. . . 4-12
- 379 4.15 Representation of different RPC layouts (wide gap on Figure (a), double gap on
 380 Figure (b) and multigap on Figure (c)), of the corresponding sensitive volume in
 381 gray, and of the associated avalanche size [193]. 4-13
- 382 4.16 Time distributions of the leading, trailing, and average of both leading and trailing
 383 edges for multigap RPCs consisting in two 4 mm (Figure 4.16a) and four 2 mm
 384 (Figure 4.16b) exposed to a 100 Hz/cm² radiation rate. The data was collected with
 385 RPCs operated at the voltage corresponding to the knee of the efficiency distribution,
 386 defined as the point where 95% of the maximum efficiency is obtained [193]. 4-14
- 387 4.17 Presentation of a study of a possible ALICE MRPC cell using 250 μm gas gaps,
 388 620 μm outer glass electrodes, and 550 μm inner floating electrodes (Figure 4.17a),
 389 and of its time resolution performance as a function of the applied high voltage for
 390 different radiation levels referred through different filter settings of the 740 GBq
¹³⁷Cs source the former CERN GIF facility [208]. 4-14
- 392 4.18 Particle identification applied to electrons in the STAR experiment. The identifica-
 393 tion is performed combining ToF and dE/dx measurements [213]. 4-15
- 394 4.19 Comparison of the detector performance of ALICE ToF MRPC [214] at fixed applied
 395 voltage (in blue) and at fixed effective voltage (in red). The effective voltage is kept
 396 fixed by increasing the applied voltage accordingly to the current drawn by the detector. 4-16
- 397 4.20 Ratio between total induced and drifting charge have been simulated for single gap,
 398 double-gap and multigap layouts [215]. The total induced charge for a double-gap
 399 RPC is a factor 2 higher than for a multigap. 4-17
- 400 4.21 Charge spectra have been simulated for single gap, double-gap and multigap lay-
 401 outs [215]. It appears that when single gap shows a decreasing spectrum, double and
 402 multigap layouts exhibit a spectrum whose peak is detached from the origin. The
 403 detachment gets stronger as the number of gaps increases. 4-17
- 404 4.22 The maximal theoretical efficiency is simulated for single gap, double-gap and multi-
 405 gap layouts [215] at a constant gap thickness of 2 mm and using an effective Townsend
 406 coefficient of 9 mm⁻¹. 4-18

407	4.23	Mass stopping power as a function of $\beta\gamma = p/Mc$ for positive muons in copper [115]. The total stopping power is indicated with solid line and local components with dashed lines. the vertical bands are used to indicate boundaries between different approximations used at different energy range.	4-18
408	4.24	Mean mass stopping power for liquid hydrogen, as used in bubble chambers, gaseous helium, carbon, aluminum, iron, tin, and lead without the inclusion of radiative effect at higher $\beta\gamma$ necessary for pions and muons in denser materials [115].	4-20
409	4.25	Mean excitation energies normalized to the atomic number as adopted by the ICRU [115, 219, 220].	4-21
410	4.26	Mean mass stopping power at minimum ionization as a function of the atomic number [115].	4-21
411	4.27	Example of straggling function $f(\Delta)$ of particles passing through 1.2 cm of Argon gas with a $\beta\gamma$ of 3.6 and represented with a solid line. The original Landau distribution is showed with a dashed line [221].	4-22
412	4.28	Evolution of straggling functions $f(\Delta)$ of particles passing through a volume of Argon gas with a $\beta\gamma$ of 3.6 with increasing thickness x [221].	4-22
413	4.29	Photo-absorption cross section as computed by HEED for nobles gases with different electric shell numbers [217].	4-24
414	4.30	Photo-absorption cross section as computed by HEED for typical RPC gas mixtures [217]. The RPC mixture with CO_2 corresponds to the mixture used by CALICE SDHCAL [225] while the other one was foreseen for the experimenter ATLAS [226] but has been changed since then.	4-25
415	4.31	Distributions of number of electrons (left) and energy loss (right) for a 5 GeV/c muon passing through 1.2 mm of Helium (Figure 4.31a), Argon (Figure 4.31b) or a typical RPC gas mixture (Figure 4.31c) [217].	4-26
416	4.32	Figure 4.32a: Mean cluster density for muons through different gas volumes [217]. Figure 4.32b: Distribution of the number of electrons per cluster for a 5 GeV/c muon traveling through a mixture of 96.7% $C_2H_2F_4$, 3% i- C_4H_{10} and 0.3% SF_6 [217, 226].	4-27
417	4.33	Townsend and attachment coefficient for a typical 96.7/3/0.3 mixture of $C_2H_2F_4$ /i- C_4H_{10} / SF_6 , at a temperature $T = 296.15$ K and a pressure $P = 1013$ hPa [217, 226].	4-28
418	4.34	Comparison of the distribution law of Furry and the Poisson law for $\bar{n} = 5$ [229].	4-28
419	4.35	Single-electron avalanche size distribution in a proportionnal counter filled with methylal at different E/p values. (a) 70, (b) 76.5, (c) 105, (d) 186.5, (e) 426V/cm torr [230].	4-29
420	4.36	Figure 4.36a: Comparison of avalanche size distributions for different values of Townsend and attachment coefficients. The effective Townsend coefficient is the same for both distributions. Figure 4.36b: Fluctuation in avalanche size for avalanche started by a single electron with $\alpha = 13 \text{ mm}^{-1}$ and $\eta = 3.5 \text{ mm}^{-1}$ [226].	4-31
421	4.37	Figure 4.37a: Electron mean drift velocity v_D in pure $C_2H_2F_4$ and typical RPC gas mixtures. Figure 4.37b: Transverse diffusion coefficient in pure $C_2H_2F_4$ and a typical RPC gas mixture. Figure 4.37c: Longitudinal diffusion coefficient in pure $C_2H_2F_4$ and a typical RPC gas mixture. All results are given with a pressure $P = 760$ Torr and a temperature $T = 296.15$ K [217].	4-32
422	4.38	Comparison of the free charge carriers in the gas after a time $t = 7.90$ ns in the case where no diffusion is taken into account to simulate the avalanche (Figure 4.38a) and in the case where the diffusion is implemented (Figure 4.38b) [217].	4-32
423	4.39	Schematic representation of an avalanche and of the electric field deformation it causes due to the local concentration of charge carriers [199].	4-34
424			
425			
426			
427			
428			
429			
430			
431			
432			
433			
434			
435			
436			
437			
438			
439			
440			
441			
442			
443			
444			
445			
446			
447			
448			
449			
450			
451			
452			
453			
454			
455			

456	4.40 Evolution of the charge induced by an avalanche started by a single electron in a 457 1.2 mm thick RPC with an applied electric field of 54 kV/cm in the case space 458 charge is not taken into account (Figure 4.40a) and in the case it is implemented into 459 the simulation (Figure 4.40b). The total induced charge is correlated to the size of 460 the avalanche [217].	4-35
461	4.41 Distributions of charge carriers within the gas volume of a 1.2 mm thick RPC and 462 the corresponding deformation of the electric field at different time steps with an 463 applied electric field of 55.5 kV/cm [217].	4-36
464	4.42 Representation of the weighting field in the volume of a RPC and the resulting in- 465 duced current in the strip placed at 1 V and its neighbour connected to the ground. 466 The induced current corresponds, as can be understood from Formula 4.22 [199].	4-37
467	4.43 Schematics of CMS RPC FEE logic.	4-38
468	4.44 Equivalence in between the charge of the induced signal in input of the CMS FEE 469 and the signal strength on the output of the pre-amplifier.	4-38
470	4.45 Description of the principle of a CFD. A comparison of threshold triggering (left) 471 and constant fraction triggering (right) is shown in Figure 4.45a. Constant frac- 472 tion triggering is obtained thanks to zero-crossing technique as explained in Fig- 473 ure 4.45b. The signal arriving at the input of the CFD is split into three components. 474 A first one is delayed and connected to the inverting input of a first comparator. A 475 second component is connected to the noninverting input of this first comparator. A 476 third component is connected to the noninverting input of another comparator along 477 with a threshold value connected to the inverting input. Finally, the output of both 478 comparators is fed through an AND gate.	4-39
479	4.46 Typical efficiency sigmoid of a CMS RPC detector. The black dots correspond to the 480 data, the blue line to the sigmoid fit and the opened cross to the knee and working 481 extracted from the fit line.	4-40
482	4.47 Effect of the temperature variation on the rate (Figure 4.47a) and the efficiency (Fig- 483 ure 4.47b) of a RPC [231].	4-41
484	4.48 Effect of the pressure variation on the rate (Figure 4.48a) and the efficiency (Fig- 485 ure 4.48b) of a RPC [232].	4-42
486	 5.1 Mean RPC Barrel (left column) and Endcap (right column) rate (top row) and current 487 (bottom row) as a function of the instantaneous luminosity as measured in 2017 p - p 488 collision data.	5-2
489	5.2 Figure 5.2a: The hit rate per region (Barrel, Endcap) is linearly extrapolated to 490 HL-LHC highest instantaneous luminosity ($5 \times 10^{34} \text{ cm}^{-2} \text{ s}^{-1}$) using the rate as 491 a function of instantaneous luminosity recorded by RPCs in 2017 showing a linear 492 dependence. Figure 5.2b: The integrated charge per region (Barrel, Endcap) is ex- 493 trapolated to HL-LHC integrated luminosity (3000 fb^{-1}) using the data accumulated 494 in 2016 in every HV channels.	5-3
495	5.3 CMS RPC mean integrated charge in the Barrel region (Figure 5.3a) and the Endcap 496 region (Figure 5.3b). The integrated charge per year is shown in blue. The red curve 497 shows the evolution of the accumulated integrated charge through time. The blank 498 period in 2013 and 2014 corresponds to LS1. The total integrated charge for the 499 entire operation period (Oct.2009 - Dec.2017) is estimated to be about 1.66 mC/cm^2 500 in the Barrel and 4.58 mC/cm^2 in the Endcap.	5-3

501	5.4	Layout of the test beam zone called X5c GIF at CERN. Photons from the radioactive source produce a sustained high rate of random hits over the whole area. The zone is surrounded by 8 m high and 80 cm thick concrete walls. Access is possible through three entry points. Two access doors for personnel and one large gate for material. A crane allows installation of heavy equipment in the area.	5-4
502	5.5	^{137}Cs decays by β^- emission to the ground state of ^{137}Ba (BR = 5.64%) and via the 662 keV isomeric level of ^{137}Ba (BR = 94.36%) whose half-life is 2.55min.	5-5
503	5.6	Floor plan of the GIF++ facility. When the facility downstream of the GIF++ takes electron beam, a beam pipe is installed along the beam line (z-axis). The irradiator can be displaced laterally (its center moves from $x = 0.65$ m to 2.15 m), to increase the distance to the beam pipe.	5-6
504	5.7	Simulated unattenuated current of photons in the xz plane (Figure 5.7a) and yz plane (Figure 5.7b) through the source at $x = 0.65$ m and $y = 0$ m [241]. With angular correction filters, the current of 662 keV photons is made uniform in xy planes.	5-6
505	5.8	Description of the RPC setup. Dimensions are given in mm. A tent containing RPCs is placed at 1720 mm from the source container. The source is situated in the center of the container. RE-4-2-BARC-161 chamber is 160 mm inside the tent. This way, the distance between the source and the chambers plan is 2060 mm. Figure 5.8a provides a side view of the setup in the xz plane while Figure 5.8b shows a top view in the yz plane.	5-7
506	5.9	RE-4-2-BARC-161 chamber is inside the tent as described in Figure 5.8. In the top right, the two scintillators used as trigger can be seen. This trigger system has an inclination of 10° relative to horizontal and is placed above half-partition B2 of the RPCs. PMT electronics are shielded thanks to lead blocks placed in order to protect them without stopping photons from going through the scintillators and the chamber.	5-8
507	5.10	Hit distributions over all 3 partitions of RE-4-2-BARC-161 chamber is showed. Top, middle and bottom figures respectively correspond to partitions A, B, and C. The profiles show that some events still occur in other half-partitions than B2, which corresponds to strips 49 to 64, in front of which the trigger is placed, contributing to the inefficiency of detection of cosmic muons. In the case of partitions A and C, the very low amount of data can be interpreted as noise. On the other hand, it is clear that a little portion of muons reach the half-partition B1, corresponding to strips 33 to 48.	5-8
508	5.11	Signals from the RPC strips are shaped by the FEE described on Figure 5.11a. Output LVDS signals are then read-out by a TDC module connected to a computer or converted into NIM and sent to scalers. Figure 5.11b describes how these converted signals are put in coincidence with the trigger.	5-9
509	5.12	Results are derived from data taken on half-partition B2 only. On the 18 th of June 2014, data has been taken on chamber RE-4-2-BARC-161 at CERN building 904 (Prevessin Site) with cosmic muons providing us a reference efficiency plateau of $(97.54 \pm 0.15)\%$ represented by a black curve. A similar measurement has been done at GIF on the 21 st of July with the same chamber giving a plateau of $(78.52 \pm 0.94)\%$ represented by a red curve.	5-10
510	5.13	Representation of the layout used for the simulations of the test setup. The RPC read-out plane is represented as a yellow trapezoid while the two scintillators as blue cuboids looking at the sky. The green plane corresponds to the muon generation plane within the simulation. Figure 5.8a shows a global view of the simulated setup. Figure 5.8b shows a zoomed view that allows to see the 2 scintillators as well as the full RPC plane.	5-11

550	5.14 Geometrical acceptance distribution as provided by the Monte Carlo simulation.	5-12
551	5.15 Correction of the efficiency without source. The efficiency after correction gets	
552	much closer to the Reference measurement performed before the study in GIF by	
553	reaching a plateau of $(93.52 \pm 2.64)\%$	5-13
554	5.16 Hit distributions over read-out partition B of RE-4-2-BARC-161 chamber to-	
555	gether with skew distribution fits corresponding to forward and backward coming	
556	muons.	5-14
557	5.17 Figure 5.17a shows the linear approximation fit performed on data extracted from	
558	table 5.2. Figure 5.17b shows a comparison of Formula 5.5 with the simulated flux	
559	using a and b given in figure 5.17a in formulae 5.3 and the reference value $D_0 =$	
560	50 cm and the associated flux for each absorption factor F_0^{ABS} from table 5.1	5-16
561	5.18 Efficiency (Figure 5.18a) and cluster size (Figure 5.18b) of chamber RE-4-2-BARC-161	
562	measured at GIF with Source OFF (red) and Source ON using different absorber set-	
563	tings: ABS 5 (green), ABS 2 (blue) and ABS 1 (yellow). The results are compared	
564	to the Reference values obtained with cosmics.	5-17
565	5.19 Rates in chamber RE-4-2-BARC-161 measured at GIF with Source OFF (red)	
566	and Source ON using different absorber settings: ABS 5 (green), ABS 2 (blue) and	
567	ABS 1 (yellow). On Figure 5.19b, the rates of Figure 5.19a were normalized to the	
568	measured efficiency and constant fits are performed on Source ON data showing the	
569	gamma rate in the chamber.	5-18
570	5.20 Evolution of the voltages at half maximum and at 95% of the maximum efficiency	
571	(Figure 5.20a), and of the maximum efficiency (Figure 5.20b) as a function of the	
572	rate in chamber RE-4-2-BARC-161. The data is extracted from the fits in Fig-	
573	ures 5.18a and 5.19b.	5-18
574	5.21 Presentation of a double-gap endcap RPC with its 3 RPC gaps. Due to the partitioni-	
575	ng of the read-out strips into 3 rolls, the TOP layer of gap is divided into 2 gaps:	
576	TOP NARROW (TN) and TOP WIDE (TW). The BOTTOM (B) only consists in 1	
577	gap.	5-19
578	5.22 Current density and charge deposition per gamma avalanche, defined as the current	
579	density normalized to the measured rate taken from Figure 5.19a as a function of	
580	the effective high voltage in chamber RE-4-2-BARC-161 measured at GIF with	
581	Source ON using different absorber settings: ABS 5 (green), ABS 2 (blue) and ABS	
582	1 (yellow).	5-20
583	5.23 Characterization of CMS RPC detectors foreseen to be used at GIF++ for longevity	
584	studies of the present system. Using cosmic muons, efficiency (Figure 5.23a) and	
585	cluster size (Figure 5.23b) were measured as well as noise rate (Figure 5.23c) and	
586	current density (Figure 5.23d). For each detector, the working voltage, defined as	
587	in Formula 4.25, was extracted from sigmoid fits performed in Figure 5.23a and the	
588	values of efficiency, cluster size, noise rate and current density at this voltage are	
589	reported using open crosses.	5-21
590	5.24 CMS RPC setup inside of GIF++ bunker during test beam (Figure 5.24a) and ageing	
591	periods (Figure 5.24b). The space in between the RPCs and the source is usually	
592	used by other detectors while the space in between T1 and the upstream wall is	
593	not filled. Due to the presence of the beam pipe, the trolley is moved away from the	
594	beam line during irradiation periods and placed further away from the source for less	
595	intense irradiation. The position of the trolley can vary due to the use of the space	
596	by other setups and is then not exact. In the contrary, the position of the chambers in	
597	the trolley is fixed and given in Figure 5.24c.	5-23

598	5.25	Visualtion of the main data flows in GIF++. The yellow flow lines corresponds to the DIP flow used for source, environmental and gas information. The red flow lines are for the CAEN flow through which the WebDCS communicates the voltages to be applied on the detectors using pressure and temperature informformation and retrieves the monitored voltages and currents. Finally, the blue flow lines corresponds to the DAQ flow through which the RPC data is collected from the TDCs by the computer.	5-24
599	5.26	DIP monitoring history accessed through GIF++ WebDCS interface.	5-25
600	5.27	Example of DQM page available on CMS RPC WebDCS in GIF++. Here is presented the rate measured in one of the tracking chabers, namely GT1_20_20-BKL_JUL16_4. The DQM page allows to click on each histogram to extend its view and to navigate through the histograms thanks to the left and right arrows.	5-27
601	5.28	Example of DQM ROOT Browser page available on CMS RPC WebDCS in GIF++. Here is presented the strip activity profile, defined as the rate profile normalized to the mean rate, in one of the tracking chabers, namely GT1_20_20-BKL_JUL16_4. Available ROOT files and histograms can be browsed thanks to the left panel showing the directory and files structures.	5-28
602	5.29	Longevity statistics of chamber RE2-2-NPD-BARC-9 in GIF++. For each month since July 2017, the integrated charge (in blue) as well as the time efficiency of irradiation (in gray) is reported.	5-28
603	5.30	Example of current monitoring (Figure 5.30a) and of corresponding integrated charge (Figure 5.30b) of chamber RE2-2-NPD-BARC-09. The decrease of current are related to a decrease of the voltage due to the daily rate scan procedure or to periods during which the source was turned OFF.	5-29
604	5.31	Example of rate (Figure 5.31a) and current (Figure 5.31b) monitoring of chamber RE2-2-NPD-BARC-09 with increasing integrated charge. The variations of rate and current are correlated and corresponds to change of source irradiation, gas flow, gas humidity, or environmental conditions.	5-30
605	5.32	Example of strip activity of chamber RE2-2-NPD-BARC-09 monitoring through time. The activity of a strip is defined as the rate of the individual channel normalized to the mean rate measured in the corresponding read-out partition.	5-31
606	5.33	Total integrated charge in the irradiated RPCs, RE2-2-NPD-BARC-9 and RE4-2-CERN-165, before starting August 2018 test beam period. The irradiation of the RE2 chamber started in June 2016 while the RE4 chamber couldn't be irradiated before November 2016.	5-33
607	6.1	PETIROC 2A block diagram.	6-2
608	6.2	The PETIROC time jitter as a function of the input signal amplitude, measured with and without internal clocks.	6-3
609	A.1	(A.1a) View of the front panel of a V1190A TDC module [242]. (A.1b) View of the front panel of a V1718 Bridge module [243]. (A.1c) View of the front panel of a 6U 6021 VME crate [257].	A-3
610	A.2	Module V1190A <i>Trigger Matching Mode</i> timing diagram [242].	A-4
611	A.3	Structure of the ROOT output file generated by the DAQ. The 5 branches (<code>EventNumber</code> , <code>number_of_hits</code> , <code>Quality_flag</code> , <code>TDC_channel</code> and <code>TDC_TimeStamp</code>) are visible on the left panel of the ROOT browser. On the right panel is visible the histogram corresponding to the variable <code>nHits</code> . In this specific example, there were approximately 50k events recorded to measure the gamma irradiation rate on the detectors. Each event is stored as a single entry in the <code>TTree</code>	A-10
612			
613			
614			
615			
616			
617			
618			
619			
620			
621			
622			
623			
624			
625			
626			
627			
628			
629			
630			
631			
632			
633			
634			
635			
636			
637			
638			
639			
640			
641			
642			
643			
644			
645			

646 A.4 The effect of the quality flag is explained by presenting the content of <code>TBranch</code> 647 <code>number_of_hits</code> of a data file without <code>Quality_flag</code> in Figure A.4a and the con- 648 tent of the same <code>TBranch</code> for data corresponding to a <code>Quality_flag</code> where all TDCs 649 were labelled as <code>GOOD</code> in Figure A.4b taken with similar conditions. It can be noted 650 that the number of entries in Figure A.4b is slightly lower than in Figure A.4a due 651 to the excluded events.	A-12
652 A.5 Using the same data as previously showed in Figure A.4, the effect of the quality 653 flag is explained by presenting the reconstructed hit multiplicity of a data file with- 654 out <code>Quality_flag</code> in Figure A.5a and the reconstructed content of the same RPC 655 partition for data corresponding to a <code>Quality_flag</code> where all TDCs were labelled as 656 <code>GOOD</code> in Figure A.5b taken with similar conditions. The artificial high content of bin 657 0 is completely suppressed.	A-12
658 A.6 WebDCS DAQ scan page. On this page, shifters need to choose the type of scan 659 (Rate, Efficiency or Noise Reference scan), the gamma source configuration at the 660 moment of data taking, the beam configuration, and the trigger mode. These in- 661 formation will be stored in the DAQ ROOT output. Are also given the minimal 662 measurement time and waiting time after ramping up of the detectors is over before 663 starting the data acquisition. Then, the list of HV points to scan and the number of 664 triggers for each run of the scan are given in the table underneath.	A-14
665 B.1 Example of expected hit time distributions in the cases of efficiency (Figure B.1a) 666 and noise/gamma rate per unit area (Figure B.1b) measurements as extracted from 667 the raw ROOT files. The unit along the x-axis corresponds to ns. The fact that 668 "the" muon peak is not well defined in Figure B.1a is due to the contribution of all 669 the RPCs being tested at the same time that don't necessarily have the same signal 670 arrival time. Each individual peak can have an offset with the ones of other detectors. 671 The inconsistancy in the first 100 ns of both time distributions is an artefact of the 672 TDCs and are systematically rejected during the analysis.	B-16
673 B.2 The effect of the quality flag is explained by presenting the reconstructed hit multi- 674 plicity of a data file without <code>Quality_flag</code> . The artificial high content of bin 0 is the 675 effect of corrupted data.	B-21
676 B.3 Display of the masking tool page on the webDCS. The window on the left allows the 677 shifter to edit <code>ChannelsMapping.csv</code> . To mask a channel, it only is needed to set the 678 3rd field corresponding to the strip to mask to 0. It is not necessary for older mapping 679 file formats to add a 1 for each strip that is not masked as the code is versatile and 680 the default behaviour is to consider missing mask fields as active strips. The effect 681 of the mask is directly visible for noisy channels as the corresponding bin turns red. 682 The global effect of masking strips will be an update of the rate value showed on the 683 histogram that will take into consideration the rejected channels.	B-28

List of Tables

684

685	3.1	Details of the greenhouse fluorinated gases used in CMS and of their GWP [171]. . .	3-19
686	4.1	Properties of the most used electrode materials for RPCs.	4-3
687	5.1	Total photon flux ($E\gamma \leq 662$ keV) with statistical error predicted considering a 688 ^{137}Cs activity of 740 GBq at different values of the distance D to the source along 689 the x-axis of irradiation field [239].	5-14
690	5.2	Correction factor c is computed thanks to Formula 5.4 taking as reference $D_0 =$ 691 50 cm and the associated flux F_0^{ABS} for each absorption factor available in table 5.1.	5-15
692	5.3	The data at D_0 in 1997 is taken from [239]. Using Formula 5.5, the flux at D , 693 including an error of 1 cm, can be estimated in 1997. Then, taking into account the 694 attenuation of the source activity, the flux at D can be estimated at the time of the 695 tests in GIF in 2014. Assuming a sensitivity of the RPC to $\gamma s = 2 \times 10^{-3}$, an 696 estimation of the hit rate per unit area is obtained.	5-16
697	5.4	Summary of the characterization measurement performed in Ghent on CMS RPC 698 detectors foreseen to be used at GIF++ for longevity studies of the present system. 699 For each detector, the working voltage, defined as in Formula 4.25, was extracted 700 from sigmoid fits performed in Figure 5.23a and the values of efficiency, cluster 701 size, noise rate and current density at this voltage are reported.	5-22
702	A.1	Inter-process communication cycles in between the webDCS and the DAQ through 703 file string signals.	A-18

List of Acronyms

List of Acronyms

706	AFL	Almost Full Level
707	ALCTs	anode local charged track boards
708	BARC	Bhabha Atomic Research Centre
709	BCS	Bardeen–Cooper–Schrieffer
710	BLT	Block Transfer
711	BMTF	Barrel Muon Track Finder
712	BNL	Brookhaven National Laboratory
713	BSM	Physics beyond the Standard Model
714	BR	Branching Ratio
715	CAEN	Costruzioni Apparecchiature Elettroniche Nucleari S.p.A.
716	CERN	European Organization for Nuclear Research
717	CFD	Constant Fraction Discriminator
718	CFEBs	cathode front-end boards
719	CKM	Cabibbo–Kobayashi–Maskawa
720	CMB	Cosmic Microwave Background
721	CMS	Compact Muon Solenoid
722	CSC	Cathode Strip Chamber
723	CuOF	copper-to-optical-fiber translators
724	DAQ	Data Acquisition
725	DCS	Detector Control Software
726	DQM	Data Quality Monitoring
727	DT	Drift Tube
728	ECAL	electromagnetic calorimeter
729	EMTF	Endcap Muon Track Finder
730	FCC	Future Circular Collider
731	FEB	Front-End Board
732	FEE	Front-End Electronics
733	FWHM	full-width-at-half-maximum
734	GEANT	GEometry ANd Tracking - a series of software toolkit platforms developed by CERN
735	GEB	GEM Electronics board
736	GEM	Gas Electron Multiplier
738	GIF	Gamma Irradiation Facility
739	GIF++	new Gamma Irradiation Facility
740	GWP	Global Warming Potential
741	HCAL	hadron calorimeter
742	HEP	High-Energy Physics
743	HL-LHC	High Luminosity LHC

744	HPL	High-pressure laminate
745	HSCPs	Heavy Stable Charged Particles
746	HV	High Voltage
747	ICRU	International Commission on Radiation Units & Measurements
748	iRPC	improved RPC
749	IRQ	Interrupt Request
750	ISR	Intersecting Storage Rings
751	LEIR	Low Energy Ion Ring
752	LEP	Large Electron-Positron
753	LHC	Large Hadron Collider
754	LS1	First Long Shutdown
755	LS2	Second Long Shutdown
756	LS3	Third Long Shutdown
757	LSP	lightest supersymmetric particle
758	LV	Low Voltage
759	LVDS	Low-Voltage Differential Signaling
760	MC	Monte Carlo
761	MCNP	Monte Carlo N-Particle
762	MiC1	first version of Minicrate electronics
763	mip's	minimum ionizing particles
764	MRPC	Multigap RPC
765	MSSM	Minimal Supersymmetric Standard Model
766	mSUGRA	minimal SUper GRAvity
767	NIM	Nuclear Instrumentation Module logic signals
768	OH	Optohybrid Board
769	OMTF	Overlap Muon Track Finder
770	PAI	Photo-Absorption Ionisation
771	PAIR	Photo-Absorption Ionisation with Relaxation
772	PMT	PhotoMultiplier Tube
773	PS	Proton Synchrotron
774	PU	pile-up
775	QCD	Quantum Chromodynamics
776	QED	Quantum Electrodynamics
777	RADMON	Radiation Monitoring
778	RMS	Root Mean Square
779	ROOT	a framework for data processing born at CERN
780	RPC	Resistive Plate Chamber
781	SC	Synchrocyclotron
782	SiPM	Silicon Photomultiplier
783	SLAC	Stanford Linear Accelerator Center
784	SM	Standard Model
785	SPS	Super Proton Synchrotron
786	SUSY	supersymmetry
787	TDC	Time-to-Digital Converter
788	TDR	Technical Design Report
789	ToF	Time-of-flight
790	TPG	trigger primitives
791	webDCS	Web Detector Control System
792	WIMPs	Weakly Interacting Massive Particles

⁷⁹³ YETS Year End Technical Stop



1

794

795

Introduction

796 Grasping an understanding of the world in which they are leaving in has always been part of hu-
797 mans lives. Beyond the metaphysical questioning of our origins and purpose, curiosity has brought
798 mankind to question its surroundings. Following the philosophy of ancient greeks and indians came
799 the development of sciences as the systematic experimentation aimed at testing hypothesis and re-
800 producing results obtained by fellow natural philosophers. With the industrial revolution and the
801 organisation of science, it became possible to go always further in the understanding of the universe
802 and of the matter in particular. Investigation on the constituant of matter proved to require more and
803 more powerful machines in order to break apart the bricks of the world into ever smaller pieces, study
804 their behaviour and extract new knowledge to help the development of humanity. So far, the largest
805 and most power machine that was built to study the particles composing matter and test the mod-
806 els thought by physicists to explain their behaviour is the Large Hadron Collider (LHC), a circular
807 particle accelerator used to collide protons and heavy ions. After only a few years of investigations
808 conducted thanks to the LHC, several discoveries, predicted by the existing models, have been made
809 and in the future, in order to boost the discovery potential on the LHC and be able to test hypothesis
810 lying beyond the already aknoledged models, the instantaneous luminosity, i.e. the rate of particle
811 interactions, will be slightly increased into a so called High Luminosity phase to boost its discovery
812 potential.

813 As the Large Hadron Collider will see its instantaneous luminosity be increased, the detectors
814 on the different experimental sites will have to suffer an increased background irradiation due to the
815 byproducts of the interaction of the beams with the infrastructure. This will cause for the detectors
816 a stress which implications need to be understood throughout the High Luminosity LHC (HL-LHC)
817 phase of operations. In the case of the Compact Muon Solenoid (CMS) experiment, it is important
818 to understand if the detectors that will be subjected to the higher levels of radiation will be able to
819 sustain higher detection rates while displaying the same performance they have so far been operated
820 at and if this level of performance of the detectors will stay stable for a period longer than 10 years.
821 More specifically, the detectors placed very close to the beam line will be the most subjected to the
822 change of luminosity. In CMS, the endcap detectors will then be particularly affected by the stronger

823 background radiation. The endcap detectors compose a part of the muon system of CMS and among
824 them, the Resistive Plate Chamber (RPC)s play a key role in providing the experiment a reliable
825 trigger on potentially interesting data.

826 CMS experiment main focus revolves around testing the Standard Model (SM) of particle physics
827 using a multipurpose detector design to detect the interaction products of the protons and ions col-
828 liding along the LHC. Looking at the successive evolution of the theoretical models that gave birth
829 to the SM, the need for very intense particle beams in high energy physics experiment becomes clear
830 in that the higher the center-of-mass energy for each interaction, the greater the probe on very small
831 cross-section processes predicted by the theory, justifying the successive increase in beam energy
832 and intensity at LHC.

833 The implications for LHC experiments and in particular for the CMS detector explain the need for
834 longevity and rate capability studies conducted on the Resistive Plate Chambers which are an impor-
835 tant part of its Muon System as it is needed to certify the quality of operation of the trigger detectors
836 throughout the lifetime of HL-LHC.

837 RPCs are gaseous detectors which physics principles are non trivial and are still being investigated.
838 Nevertheless, key processes driving the electron multiplication in the gas volume, rate capability and
839 ageing have been successfully identified and will define the parameters that will have to be taken into
840 consideration while producing the detectors extending the pseudo-rapidity coverage of RPCs toward
841 the beam line as well as the ones to be monitored during the on-going longevity and rate capability
842 certification campaign.

843 On the one hand, the present RPC sub-system consists in two different RPC productions. Indeed,
844 most of the RPC detectors were produced in view of the start of LHC activities in 2010. These
845 detectors were build in between 2007 and 2008 to equip the barrel and the 3 disks of each endcaps of
846 the CMS apparatus. But during the First Long Shutdown (LS1) of LHC in between end of 2012 and
847 2015, a fourth disk of endcap was added in order to reinforce the redundancy of the endcap trigger.
848 Hence, new RPC detectors using the same technology were built in between 2012 and 2013. These
849 two sets of detector productions only differ in the properties of the High-pressure laminate (HPL)
850 used for their electrodes that could lead to a different ageing rate. This is why spare detectors of
851 both production periods have been tested over the past years to certify their good operation through
852 HL-LHC.

853 On the other hand, producing detectors to equip a highly irradiated region such as the extension of
854 CMS RPC endcaps requires to substantially improve the ageing properties of the chosen technology
855 by reducing the charge deposition per ionizing particle. This can be achieve both by modifying the
856 design of the detector volume or by improving the signal to noise ratio of the Front-End Electron-
857 ics (FEE) used to process the charge collected by the read-out strips making them more sensitive to
858 weaker signals. Two improved RPC (iRPC) designs were selected and tested in order to extend of
859 CMS endcap coverage.

860 Thanks to the study presented in this document, preliminary conclusions will be brought on the pro-
861 duction of iRPCs and on the longevity of the present RPC system, providing with a better understand
862 of the future performance of the RPC sus-system within the CMS experiment.

2

863

864

Investigating the TeV scale

865 Throughout history, physics experiment became more and more powerful in order to investigate finer
866 details of nature to help understanding the building blocks of matter and the fundamental interactions
867 that bind them in the microscopic world. Nowadays, the Standard Model of particle physics is the
868 most accurate theory designed to explain the behaviour of particles and is able to make very precise
869 predictions that are constantly verified. Nevertheless, some hints of new physics are visible as bricks
870 are still missing to have a global description of the Universe.

871 To highlight the limits of the SM and test the different alternative theories, ever more powerful
872 machines are needed. It is in this context that the Large Hadron Collider has been thought and built
873 to accelerate and collide particles at energies exceeding anything that had been done before. Higher
874 collision energies and high pile-up imply the use of enormous detectors to measure the properties
875 of the interaction products. The Compact Muon Solenoid is a multipurpose experiment that have
876 been designed to study the proton-proton collisions of the LHC and give answers on various high
877 energy physics scenarios such as different supersymmetry (SUSY) extensions to the Standard Model
878 or Extra Dimensions models.

879

880 This Chapter will be the occasion to go through the history of the Standard Model of Particle
881 Physics to understand the research conducted today in High-Energy Physics (HEP) facilities. From
882 the discovery of the atom and of its inner structure to the development of the theories governing
883 the fundamental interactions, all the elements leading to the construction SM will be discussed.
884 Furthermore, highlight on the Physics beyond the Standard Model (BSM) will be given to replace
885 the document in the context of today's research. Finally, a full description of the LHC and of the
886 CMS detector will be provided.

887 2.1 The Standard Model of Particle Physics

888 In the early 21st century it is now widely accepted that matter is made of elementary blocks referred
889 to as *elementary particles*. The physics theory that classifies and describes the best the behaviour

and interaction of such elementary particles is the so-called Standard Model. The SM formalizes 3 of the 4 fundamental interactions (electromagnetic, weak and strong interactions). Its development happened since the 1960s thanks to a strong collaboration between theoretical and experimental physicists.

2.1.1 A history of particle physics

The idea that nature is composed of elementary bricks, called *atomism*, is not contemporary as it was already discussed by Indian or Greek philosophers during antiquity. In Greece, atomism has been rejected by *Aristotelianism* as the existence of *atoms* would imply the existence of a void that would violate the physical principles of Aristotle philosophy. Aristotelianism has been considered as a reference in the European area until the 15th century. With the *Rinascimento*, ancient text and history started to be more deeply studied. The re-discovery of Platon's philosophy would allow to open the door to alternative theories and give a new approach to natural sciences where experimentation would become central. A new era of knowledge was starting. By the beginning of the 17th century, atomism was re-discovered by philosophers. The very first attempt at estimating the number of *particles* in a volume would be provided by Magenous in 1646 by calculating that the number of *particles* in a stick of incense [1]. He would find a value of the order of 10^{18} simply by considering the time necessary to smell it everywhere in a large church after the stick was lit on. It is now known that this number only falls short by 1 order of magnitude.

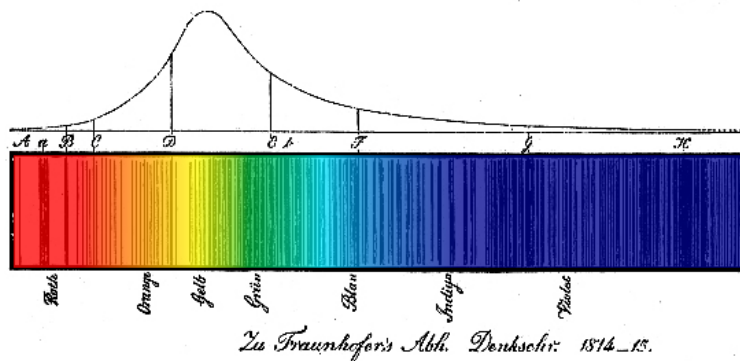


Figure 2.1: Solar spectrum with spectral lines as it appeared visually to Fraunhofer.

An alternative philosophy to atomism popularized by Descartes was *corpuscularianism*. Built on ever divisible corpuscles, contrary to atoms, its principles would be mainly used by alchemists like Newton who would later develop a corpuscular theory of light. Boyle would combine together ideas of both atomism or corpuscularianism leading to mechanical philosophy. The 18th century has seen the development of engineering providing philosophical thought experiments with repeatable demonstration and a new point of view to explain the composition of matter. Lavoisier would greatly contribute to chemistry and atomism by publishing in 1789 a list of 33 chemical elements corresponding to what are now called *atoms* [2]. In the early 19th century Dalton would summarize the knowledge on composition of matter [3]. In his atomic model, the atoms are ball-like constituents of the chemical elements. All atoms of a given element are identical, in size, mass, and other properties while the atoms of different element differ. He also considered that atoms cannot be divided into smaller particles, created nor destroyed and that they combine into chemical compounds.

920 The essence of chemical reaction would then be the combination, separation or rearrangement of
 921 atoms. Soon after, Fraunhofer would invent the spectrometer and discover the spectral lines in the
 922 sunlight spectrum, as shown in Figure 2.1 [4]. These would later be linked to the absorption by
 923 chemical elements present in the solar atmosphere by Kirchhoff and Bunsen. The rise of atomic
 924 physics, chemistry and mathematical formalism would unravel the different atomic elements and
 925 ultimately, the 20th century would see the very first sub-atomic particles.

926 **Discovery of the inner structure of the atom**

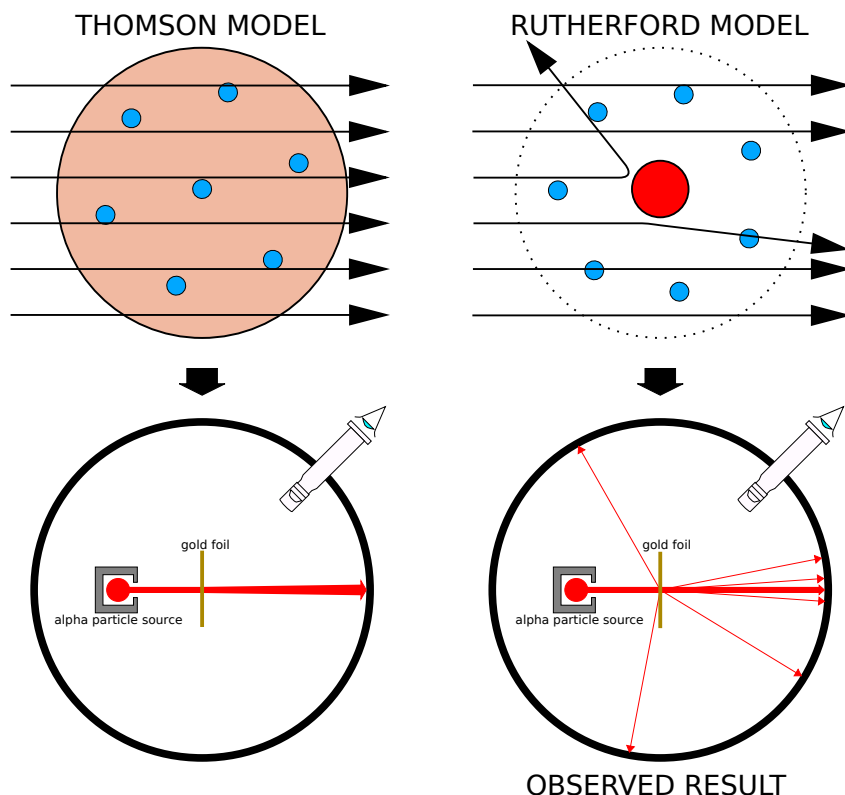


Figure 2.2: Through the gold foil experiment Rutherford could show that most of the mass of atoms was contained in a positively charged nucleus and could then propose a more accurate atomic model than that of Thomson.

927 The negatively charged *electron* would be the first to be discovered in 1897 by Thomson after 3
 928 decades of research on cathode rays [5]. He proved that the electrification observed in an electro-
 929 scope, as reported by Perrin [6], was due to the rays themselves. Hence, they had to be composed of
 930 electrically charged particles. In 1900, Becquerel would show the *beta rays* emitted by radium had
 931 the same charge over mass ratio as was measured by Thomson for cathode rays, pointing to electrons
 932 as a constituent of atoms [7]. This discovery lead to Thomson's plum pudding atomic model in
 933 which electrons are embed into a uniform positively charged atom [8]. In 1907, Rutherford and
 934 Royds showed that *alpha* particles were helium ions [9]. Indeed, once captured in a tube and sub-
 935 jected to an electric spark causing an electron avalanche, they could combine with two electrons to

936 form a ${}^4\text{He}$.

937 This discovery was directly followed by the constraint of the atom structure in between 1908
 938 and 1913 through the Geiger–Marsden gold foil experiments in which the deflection angle of alpha
 939 particles fired at a very thin gold foil was measured [10–13]. It highlighted that atoms were mainly
 940 empty with nearly all their mass contained into a tiny positively charged *nucleus*. With these two
 941 observations, Rutherford could formulate the Rutherford planetary model of the atom in 1911 [14],
 942 shown together with the Thomson plum pudding model in Figure 2.2. The link between atomic
 943 number and number of positive and negative charges contained into the atoms would fast be under-
 944 stood. Hence, the different kinds of element transmutations appeared to be purely nuclear processes
 945 making clear that the electromagnetic nature of chemical transformation could not possibly change
 946 nuclei. A new branch in physics appeared to exclusively study nuclei: *nuclear physics*. By studying
 947 alpha emission and the product of their interaction with nitrogen gas, Rutherford reported in 1919
 948 the very first nuclear reaction [15]. It lead to the discovery that the hydrogen nucleus was composed
 949 of a single positively charged particle that was later baptised *proton* [16]. This idea came from 1815
 950 Prout’s hypothesis proposing that all atoms are composed of “*protyle*” (i.e. hydrogen atoms) [17,
 951 18]. By using scintillation detectors, Rutherford could highlight typical hydrogen nuclei signature
 952 and understand that the impact of alpha particles with nitrogen would knock out an hydrogen nucleus
 953 and produce an oxygen 17, as explicated in Formula 2.1 and would then postulate that protons are
 954 building bricks of all elements.



955 With this assumption and the discovery of *isotopes* together with Aston, elements with identical
 956 atomic number but different masses, Rutherford would propose that all elements’ nuclei but hydro-
 957 gen’s are composed of both charged particles, protons, and of chargeless particles, which he called
 958 *neutrons* [16, 19]. These neutral particles would help maintaining nuclei as one, as charged protons
 959 were likely to electrostatically repulse each other. He then introduced the idea of a new force, a
 960 *nuclear* force. The first idea concerning neutrons was a bond state of protons and electrons as it was
 961 known that the beta decay, emitting electrons, was taking place in the nucleus. However, it was then
 962 shown that electrons being confined into the nucleus would hardly be possible due to Heisenberg’s
 963 uncertainty principle. Finally, in 1932, following the discovery of a new neutral radiation, Chadwick
 964 could discover the neutron as an uncharged particle with a mass similar to that of the proton which
 965 would solve the nucleus puzzle [20–24].

966 Development of the Quantum Electrodynamics

967 Historically, the development of the quantum theory revolved around the question of emission and
 968 absorption of discrete amount of energy through light. Einstein used the initial intuition of Planck
 969 about the black-body radiation to develop in 1905 a model to explain the photoelectric effect in
 970 which light was described by discrete *quanta* now called *photons* [25, 26]. For this model, Einstein
 971 introduced the concept of wave-particle duality as classical theory was not able to describe the phe-
 972 nomenon. With the new understanding of atoms and of their structure, classical theories also proved
 973 unable to explain atoms’ stability. Indeed, using classical mechanics, electrons orbiting around a
 974 nucleus should radiate an energy proportionnal to their angular momentum and hence, loose en-
 975 ergy through time and the spectrum of energy emission should then be continuous. However, it

976 was known since the 19th century and the discovery of spectral lines that the emission spectrum of
 977 material was discrete [4].

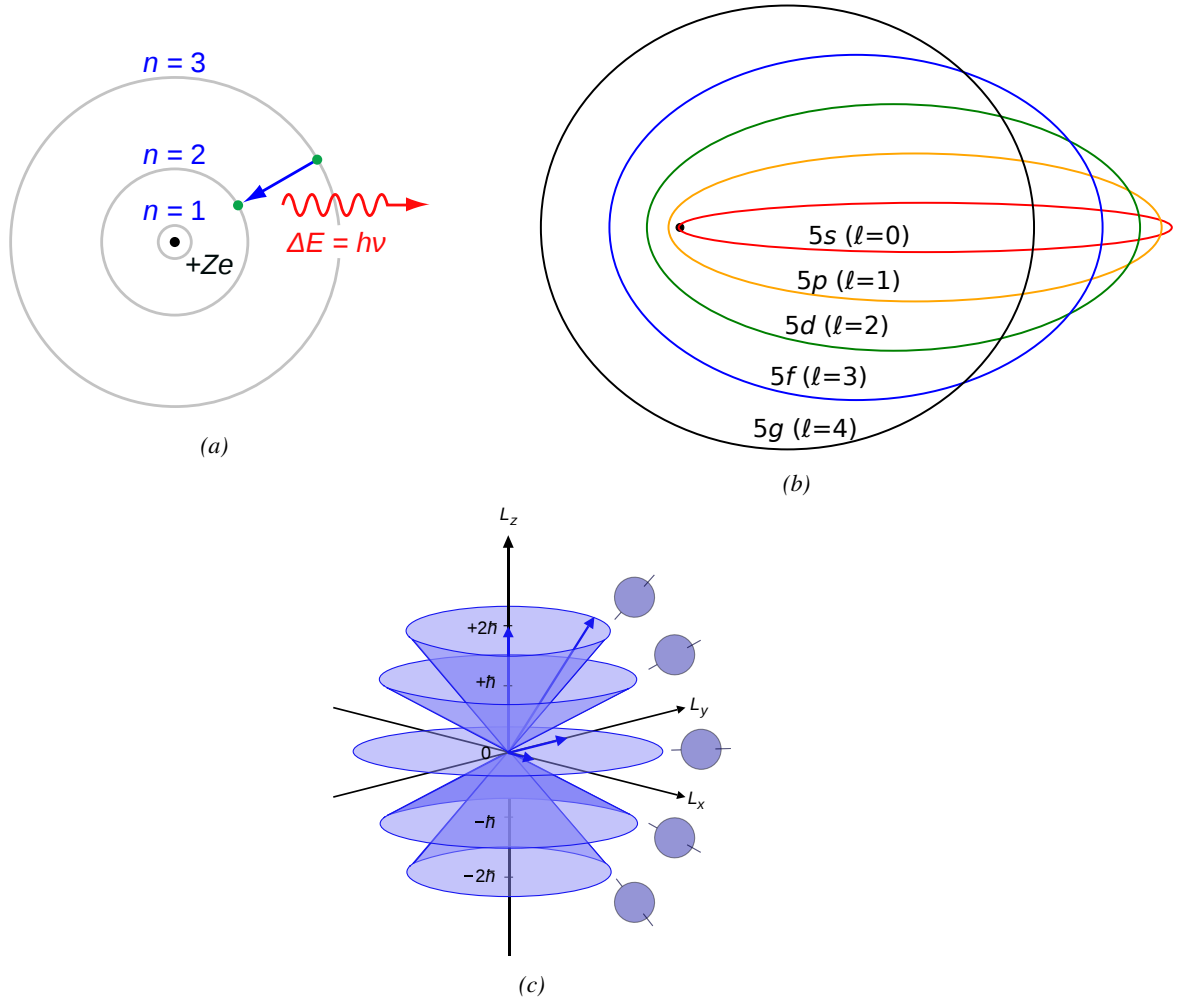


Figure 2.3: Figure 2.3a: The orbits in which the electron may travel according to the Bohr model of the hydrogen atom. An electron jumps between orbits and is accompanied by an emitted or absorbed amount of electromagnetic energy ($h\nu$). The orbits radius increases as n^2 . Figure 2.3b: Elliptical orbits with the same energy and quantized angular momentum $l = 0, 1, \dots, n - 1$ in the case $n = 5$. Figure 2.3c: Illustration of quantum mechanical orbital angular momentum. The cones and plane represent possible orientations of the angular momentum vector for $l = 2$ and $m = -2, -1, 0, 1, 2$.

978 In 1913 quantum physics would be introduced into the atomic model by Bohr to overcome the
 979 electron's energy loss due to orbiting radiation emission [27]. Using the correspondence principle
 980 stating that for large enough numbers the quantum calculations should give the same results than
 981 the classical theory, he proposed the very first quantum model of the hydrogen atom explaining
 982 the line spectrum by introducing the *principal quantum number* n describing the electron shell.
 983 The same year, Moseley would confirm Bohr's model through the Moseley's law [28]. Debye and
 984 then Sommerfeld would extend it by introducing the quantization of the angular momentum [29].

985 The quantization the z-component of the angular momentum would lead to the *second* and *third*
 986 *quantum numbers*, or *azimuthal* and *magnetic quantum number*, l and m . The second defines the
 987 orbital angular momentum of the electrons on their shells and hence, the shape of the orbital, while
 988 the third the available orbital on the subshell for each electron as shown in Figure 2.3.

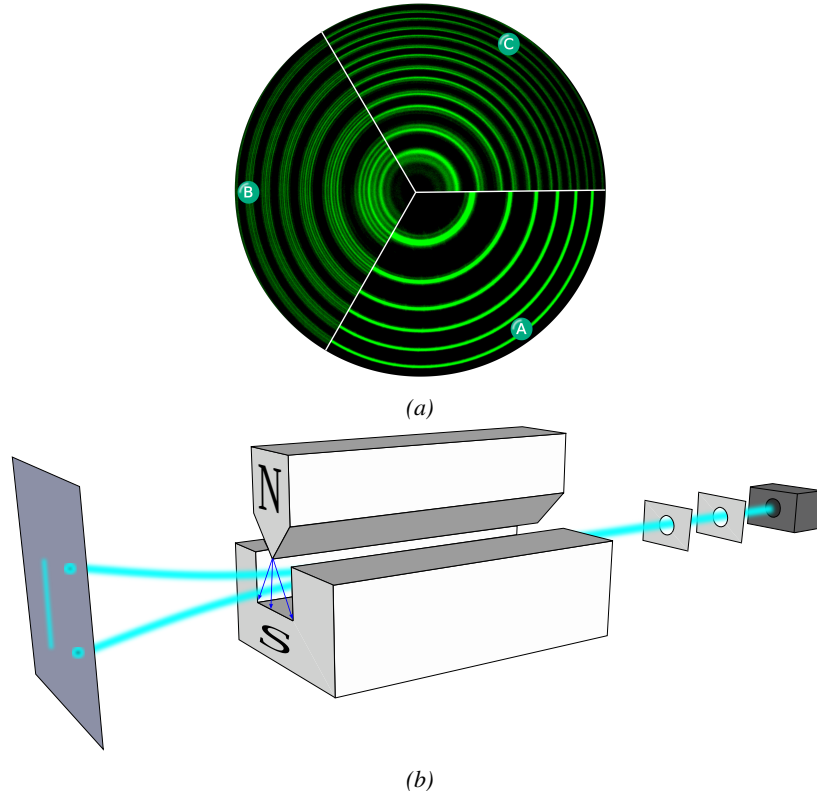


Figure 2.4: Figure 2.4a: The spectral lines of mercury vapor lamp anomalous Zeeman effect without magnetic field (A) and with magnetic field (B - transverse Zeeman effect & C - longitudinal Zeeman effect). Figure 2.4b: Stern–Gerlach experiment: Silver atoms travelling through an inhomogeneous magnetic field, and being deflected up or down depending on their spin.

989 Nevertheless, although the model was not only limited to spherical orbitals anymore, making
 990 the atom more realistic, the Zeeman effect couldn't be completely explained by just using n , l and
 991 m [30–33] nor could the result of the Stern-Gerlach experiment [34]. Both experiments are shown
 992 in Figure 2.4. A solution would be brought after Pauli in 1925 proposed together with his exclusion
 993 principle the idea of a new quantum degree of freedom in order to resolve the apparent problem [35,
 994 36]. This degree of freedom would be interpreted as an intrinsic angular momentum vector asso-
 995 ciated to the particle itself, not to the orbital [37], and associated to a new quantic number s , the
 996 *spin* projection quantum number explaining the lift of degeneracy to an even number of energy lev-
 997 els [38]. The new quantum number helped in theorizing the neutron as a neutral particle rather than
 998 a bond state of proton and electron confined in the nucleus itself.

999 The introduction of the *spin* happened one year after another attempt of improvement of the
 1000 theory was made by De Broglie in his Ph.D. thesis [39]. The original formulation of the quantum
 1001 theory only considered photons as energy quanta behaving as both *waves* and *particles*. De Broglie

1002 proposed that *all* matter are described by waves and that their momentum is proportional to the
 1003 oscillation of quantized electromagnetic field oscillators. This interpretation was able to reproduce
 1004 the previous version of the quantum energy levels by showing that the quantum condition involves
 1005 an integer multiple of 2π , as shown by Formula 2.2.

$$(2.2) \quad p = \hbar k \Leftrightarrow \int pdx = \hbar \int kdx = 2\pi\hbar n$$

1006 Although the intuition of De Broglie about the wave-particle duality of all matter was a step in
 1007 the right direction, his interpretation was semiclassical and it is in 1926 that the first fully quan-
 1008 tum mechanical wave-equation would be introduced by Schrödinger to describe electron-like parti-
 1009 cles, reproducing the previous semiclassical formulation without inconsistencies [40]. This complex
 1010 equation describes the evolution of the wave function Ψ of the quantum system, defined by its po-
 1011 sition vector \mathbf{r} and time t as an energy conservation law, in which the hamiltonian of the system \hat{H}
 1012 is explicit, by solving the Equation 2.3.

$$(2.3) \quad i\hbar \frac{\partial}{\partial t} |\Psi(\mathbf{r}, t)\rangle = \hat{H} |\Psi(\mathbf{r}, t)\rangle$$

1013 The spin would then be included into Schrödinger equation by Pauli to take into account the
 1014 interaction with an external magnetic field, as shown in Equation 2.4 in which the Hamiltonian
 1015 operator is a 2×2 matrix operator due to the Pauli matrices [38]. \mathbf{A} is the vector potential and ϕ is
 1016 the scalar electric potential.

$$(2.4) \quad i\hbar \frac{\partial}{\partial t} |\Psi\rangle = \left[\frac{1}{2m} (\sigma \cdot (\mathbf{p} - q\mathbf{A})^2 + q\phi) \right] |\Psi\rangle$$

1017 Later in 1927, Dirac would go further in his paper about emission and absorption of radiation
 1018 by proposing a second quantization not only of the physical process at play but also of the elec-
 1019 tromagnetic field [41]. His equation provided the ingredients to the first formulation of *Quantum*
 1020 *Electrodynamics (QED)* and the description of photon emission by electrons dropping into a lower
 1021 energy state in which the final number of particles is different than the initial one. Nevertheless,
 1022 in order to properly treat electromagnetism, the incorporation of the special relativity developed by
 1023 Einstein was necessary. Derived in 1928, the Dirac equation, shown as Equation 2.5, similarly to
 1024 Schrödinger equation, is a single-particle equation but it incorporates special relativity in addition to
 1025 quantum mechanics rules [42].

$$(2.5) \quad i\hbar\gamma^\mu \partial_\mu \psi - mc\psi = 0$$

1026 It features the 4×4 gamma matrices γ^μ built using 2×2 Pauli matrices and the unitary matrix, the
 1027 4-gradient ∂_μ , the rest mass m of any half integer spin massive particle described by the wave func-
 1028 tion $\psi(x, t)$, also called a Dirac spinor, and the speed of light c . In addition to perfectly reproduce
 1029 the results obtained with quantum mechanics so far, it also provided *negative-energy solutions* that
 1030 would later be interpreted as a new form of matter, *antimatter* [43, 44]. In the non-relativistic limit,
 1031 the Dirac equation gives a theoretical justification to the Pauli equation that was phenomenologically
 1032 constructed to account for the spin.

1033 The successes of the QED was soon followed with theoretical problems as computations of any
1034 physical process involving photons and charged particles were shown to be only reliable at the first
1035 order of the *perturbation theory* [45]. At higher order of the theory, divergent contributions were
1036 appearing giving nonsensical results. Only two effects were contributing to these infinities.

- 1037 • The self-energy of the electron (or positron), the energy that the particle has due to its own
1038 interaction with its environment.
- 1039 • The vacuum polarization, virtual electron–positron pairs produced by a background electro-
1040 magnetic field in the vacuum which is not an "empty" space. These virtual pairs affect the
1041 charge and current distributions generated by the original electromagnetic field.

1042 Solving this apparent problem was done by carefully defining the concepts of each observables,
1043 for example mass or charge, as these quantities are understood within the context of a non-interacting
1044 field equation. From the experimental point of view, they are abstractions as what is measured are
1045 "renormalized observables" shifted from their "bare" value by the interaction taking place in the
1046 measuring process. The infinities needed to be connected to corrections of mass and charge as those
1047 are fixed to finite values by experiment. This was the intuition of Bethe in 1947 who successfully
1048 computed the effect of such *renormalization* in the non-relativistic case [46]. Fully covariant formu-
1049 lations of QED including renormalization was achieved by 1949 by Tomonaga, Schwinger, Feynman
1050 and Dyson [47]. With the resolution of infinities, QED had mostly reached its final form, being still
1051 today the most accurate physical theory, and would serve as a model to build all other quantum field
1052 theories.

1053 **Development of the quark model and Quantum Chromodynamics**

1054 To explain the nuclear force that holds *nucleons* (protons and neutrons) together, Yukawa proposed
1055 in 1934 the existence of a force carrier called *meson* due to it's predicted mass in the range in between
1056 the electron and nucleon masses [48]. Discovered in 1936 by Anderson and Neddermeyer [49, 50],
1057 and confirmed using bubble chambers in 1937 by Street and Stevenson [51], a first meson candidate
1058 was observed in the decay products of cosmic rays. Assuming it had the same electric charge as
1059 electrons and protons, this particle was observed to have a curvature due to magnetic field that was
1060 sharper than protons but smoother than electrons resulting in a mass in between the two. But its
1061 properties were not compatible with Yukawa's theory, which was emphasized by the discovery of a
1062 new candidate in 1947, again in cosmic ray products using photographic emulsions [52–54]. The
1063 detection of the mu-meson and of the pi-meson in emulsions are showed in Figure 2.5.

1064 This new candidate, although it had a similar mass than the already believed *meson*, would rather
1065 decay into it. For distinction, the first candidate would then be renamed "*mu meson*" when the second
1066 would be the "*pi meson*". The *mu meson* was behaving like a heavy electron and didn't participate in
1067 the strong interaction whereas the pion was believed to be the carrier of the nuclear interaction. This
1068 lead to classify the *mu* in a new category of particles that shared similar properties called *leptons*
1069 under the name of *muon* together with the electron. The *pi meson* was finally found to be a triplet of
1070 particles: a positively charged, a negatively charged, and a neutral particle. The neutral *pi meson* has
1071 been more difficult to identify as it wouldn't leave tracks on emulsions nor on bubble chambers and
1072 needed to be studied via it's decay products. It was ultimately identified in University of California's
1073 cyclotron in 1950 through the observation of its decay into 2 photons [55].

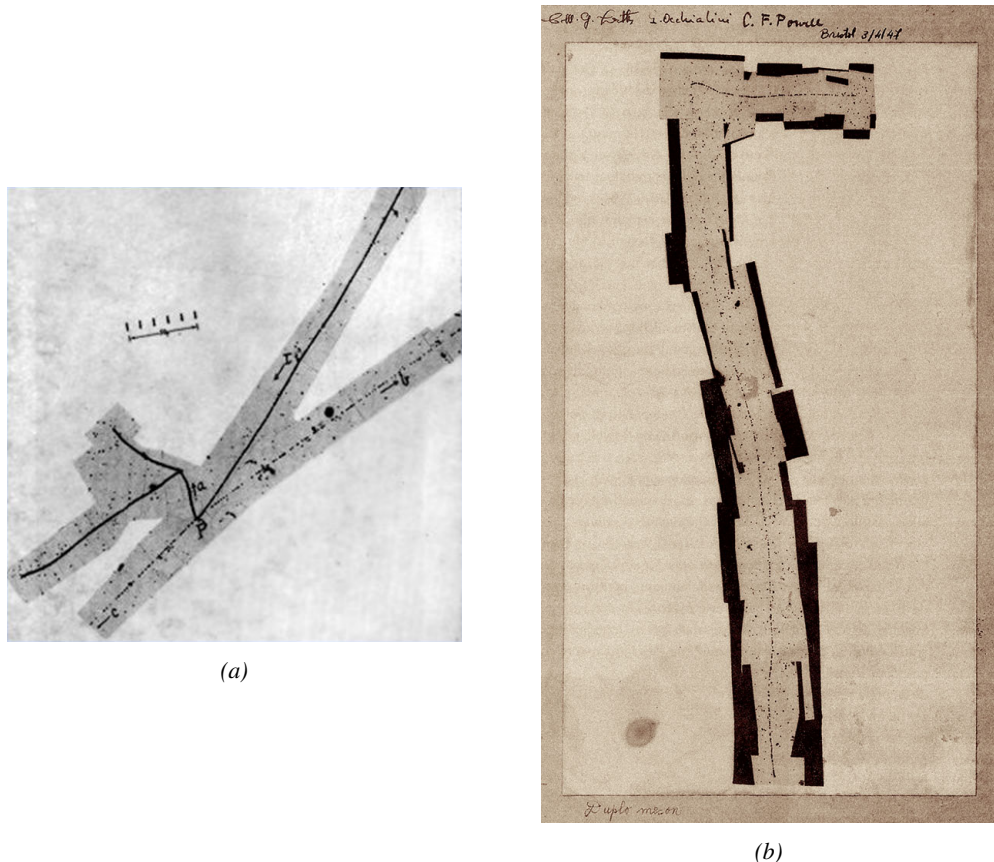


Figure 2.5: Figure 2.5a: desintegration of a μ -meson in an emulsion. Figure 2.5b: track of a π -meson in an emulsion signed by Lattes, Powell, and Occhialini.

Also discovered in 1947 but in cloud chamber photographs, the K meson has also been an important step towards the establishment of the Standard Model [56]. A triplet of particle, 2 charged and a neutral, with a mass roughly half that of a proton, were reported. These particles were baptised K meson in contrast to the "light" π and μ "L-mesons". The particularity of the K were their very slow decays with a typical lifetime of the order of 10^{-10} s much longer than the 10^{-23} s of π -proton reactions. The concept of *strangeness*, a new quantum number was then introduced thanks to an idea of Pais as an attempt to explain this phenomenon as *strange* particles appeared as a pair production of a strange and anti-strange particle [57].

With the development of synchrotrons, the particle *zoo* would grow to several dozens during the 1950s as higher energies were reachable through acceleration. In 1961, a first classification system, called *Eightfold Way*, was proposed by Gell-Mann [58]. It found its roots in the Gell-Mann–Nishijima formula, which relates the electric charge Q , the third component of the isospin I_3 , the *baryon* number B and the strangeness S , as explicated in Formula 2.6 [59–61].

$$(2.6) \quad Q = I_3 + \frac{1}{2}(B + S)$$

The isospin was a quantum number introduced in 1932 to explain symmetries of the newly

discovered neutron using representation theory of $SU(2)$ [62]. The baryon number, was introduced by Nishijima as a quantum number for baryons, i.e. particles of the same family as nucleons [59]. The mesons were classified in an octet and baryons of spin $\pm \frac{1}{2}$ and $\pm \frac{3}{2}$ were respectively classified into an octet and a decuplet, as shown in Figure 2.6. To complete the baryon decuplet, Gell-Mann predicted the existence of baryon Ω^- which would later be discovered in 1964 [63].

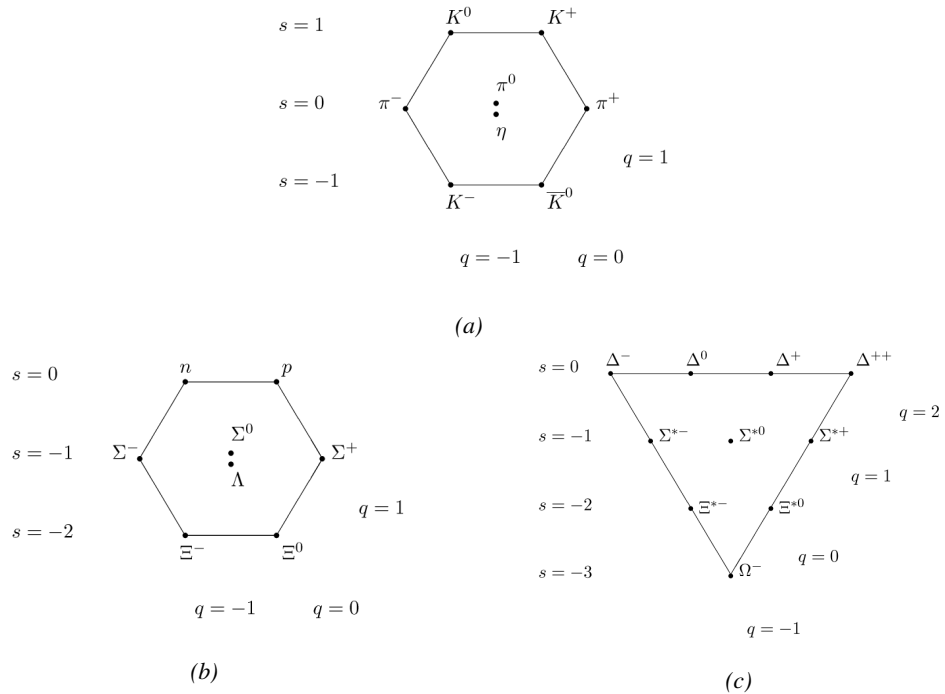


Figure 2.6: Figure 2.6a: Meson octet. Figure 2.6b: Baryon octet. Figure 2.6c: Baryon decuplet.

Gell-Mann, and independently Zweig, would then propose a full theoretical model in which *hadrons* (strongly interacting particles, i.e. mesons and baryons) were not elementary particles anymore [64–66]. They would rather be composed of 3 flavors of particles called *quarks* and their anti-particles. The 3 flavors were called *up*, *down* and *strange*. *Up* and *down* would be used to explain the nucleons and non-strange mesons, while *strange* would come into the composition of hadrons showing strangeness. *Up* and *down* flavors would be discovered in 1968 thanks to the deep inelastic scattering experiments conducted at the Stanford Linear Accelerator Center (SLAC) [67, 68], and *strange* could only be indirectly validated even though it provided a robust explanation to *kaon* (K) and *pion* (π).

However, in the decade following the Gell-Mann-Zweig quark model proposition, several improvement to the model were brought. First by Glashow and Bjorken the same year that predicted the existence of a fourth quark flavor, the *charm*, that would equalize the then known number of quarks and leptons [69, 70]. Finally in 1973 by Kobayashi and Maskawa that would increase the number of quarks to 6 to explain the experimental observation of CP violation [71, 72]. These two quarks would be referred to as *top* and *bottom* for the first time in 1975 [73]. It's only after these additions to the quark model that finally the *charm* would be discovered in 1974 at both SLAC and Brookhaven National Laboratory (BNL) [74, 75]. A meson where the *charm* is bonded with an

1110 anti-charm, called J/ψ and presented in Figure 2.7, would help convince the physics community of
1111 the validity of the model. The *bottom* would be discovered soon after in 1977 in Fermilab [76] and
1112 indicated the existence of the *top* that would resist to discovery until Fermilab's experiments CDF
1113 and D \emptyset in 1995 due its very large mass and the energy needed to produce it [77, 78].

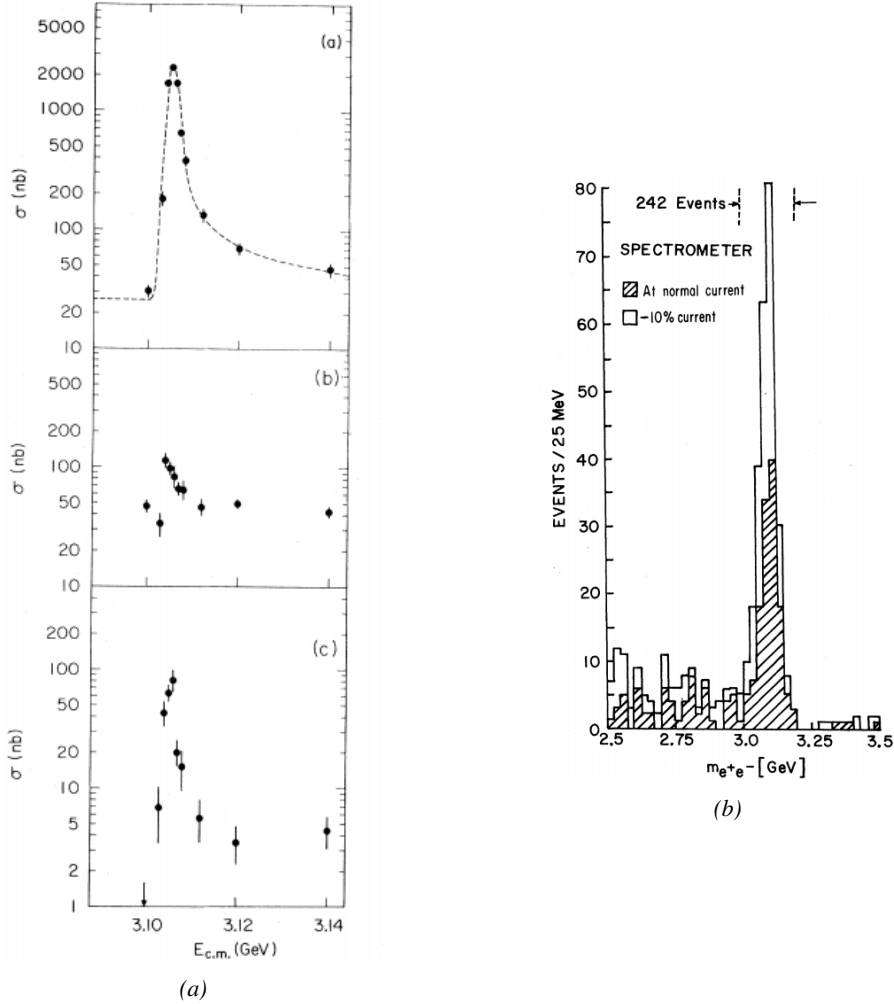


Figure 2.7: Discovery of the J/ψ by both SPEAR (SLAC [74]) in Figure 2.7a and AGS (BNL [75]) in Figure 2.7b. In Figure 2.7a, the cross section versus energy is showed for (a) multi hadron final states, (b) e^+e^- final states, and (c) $\mu^+\mu^-$, $\pi^+\pi^-$ and K^+K^- final states.

1114 As remarked by Struminsky, due to mesons such as Ω^- or Δ^{++} , the first SU(3) model already
1115 should have possessed an additional quantum number [79]. Indeed, these mesons are composed
1116 of 3 identical quarks, respectively 3 *strange* and *up* quarks, with parallel spins, which should be
1117 forbidden by the exclusion principle. Independently, Greenberg, and Han and Nambu proposed
1118 an additional SU(3) degree of freedom for the quarks [80, 81]. It would later be referred to as
1119 *color charge gauge*, that could interact through *gluons*, the gauge boson octet corresponding to this
1120 degree of freedom. The color field is presented in Figure 2.8a. Nevertheless, as observing free

quarks to prove their existence proved to be impossible, two visions of the quarks were argued. On one side, Gell-Mann proposed to see quarks as mathematical construct instead of real particles, as they are always confined, implying that quantum field theory would not describe entirely the strong interaction. He promoted the S-matrix approach to treat the strong interaction. Opposed to this vision, Feynman on the contrary argued that quarks are real particles, that he would call *partons*, that should be described as all other particles by a distribution of position and momentum [82]. The implications of quarks as point-like particles would be verified at SLAC and helped abandon the S-matrix to the benefit of QFT [83]. The concept of *color* would then be added to the quark model in 1973 by Fritzsch and Leutwyler together with Gell-Mann to propose a description of the strong interaction through the theory of Quantum Chromodynamics (QCD) [84]. The discovery the same year of asymptotic freedom within the QCD by Gross, Politzer and Wilczek, allowed for very precise predictions thanks to perturbation theory [85, 86]. The evolution of the gauge constant of QCD with respect to the energy as described by asymptotic freedom is showed in Figure 2.8b.

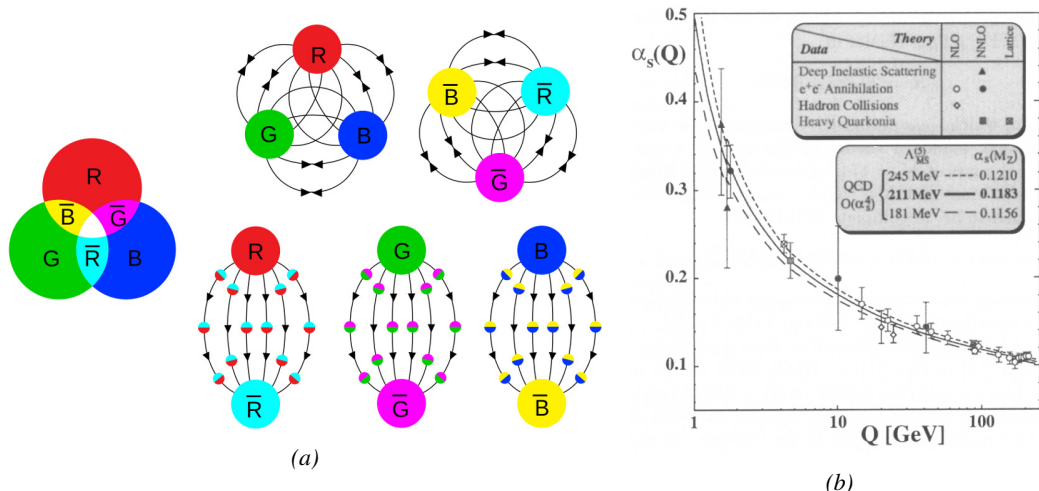


Figure 2.8: Figure 2.8a: the color field of QCD only allows for "white" baryons, particles composed of quarks, to exist. Examples are given for mesons, composed of a quark and its anti-quark, and hadrons, composed of 3 differently colored quarks or anti-quarks, but other exotic baryons have been predicted and observed, such as tetraquarks and pentaquarks. Figure 2.8b: a crossed analysis performed thanks to the data collected by various experiment at different energies have showed that the coupling constant evolves as predicted by the mechanism of asymptotic freedom [87].

1134 The Weak interaction, spontaneous symmetry breaking, the Higgs mechanism and the Elec- 1135 troweak unification

1136 The weak interaction is the process that causes radioactive decays. Thanks to the neutron discov-
1137 ery [23], Fermi could explain in 1934 beta radiation through the beta decay process in which the
1138 neutron decays into a proton by emitting an electron [88]. Though the missing energy observed dur-
1139 ing this process triggered a huge debate about the apparent non conservation of energy, momentum
1140 and spin of the process, Fermi, as Pauli before him [89], proposed that the missing energy was due to
1141 a neutral not yet discovered particle that would then be baptised *neutrino*. The impossibility to detect
1142 such a particle would leave some members of the scientific community sceptical, but hints of energy
1143 conservation and of the existence of the neutrino were provided by measuring the energy spectrum

¹¹⁴⁴ of electrons emitted through beta decay, as there was a strict limit on their energy, as showed in
¹¹⁴⁵ Figure 2.9.

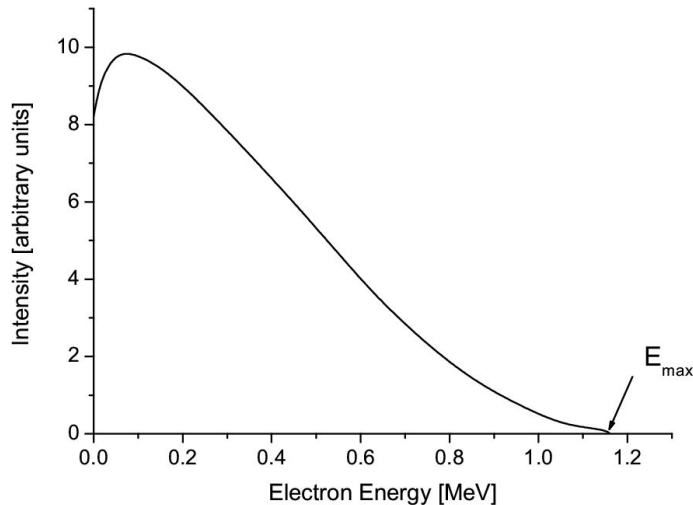


Figure 2.9: Energy spectrum of beta particles emitted by a source of ^{210}Bi .

¹¹⁴⁶ It's only 30 years later in 1953 that it would be discovered by the team of Cowan and Reines
¹¹⁴⁷ using the principle of inverse beta decay described through Formula 2.7 [90].

$$(2.7) \quad \bar{\nu} + p \rightarrow n + e^+$$

¹¹⁴⁸ The experiment consisted in placing water tanks sandwiched in between liquid scintillators near
¹¹⁴⁹ a nuclear reactor with an estimated neutrino flux of $5 \times 10^{13} \text{ cm}^{-2} \text{ s}^{-1}$. However, in order to explain
¹¹⁵⁰ the absence of some reactions in the experiment of Cowan and Reines, and constraint the beta decay
¹¹⁵¹ theory of Fermi and extend it to the case of the muon, Konopinski and Mahmoud proposed in 1953
¹¹⁵² that the muon decay would eject a particle similar to the neutrino [91]. They predicted the existence
¹¹⁵³ of a muon neutrino that would be different than the one involved in the beta decay, related to the
¹¹⁵⁴ electron. With this, the idea of *lepton number* would arise. The *muon neutrino* would successfully
¹¹⁵⁵ be detected in 1962 by Lederman, Schwartz and Steinberger [92].

¹¹⁵⁶
¹¹⁵⁷ The theory could not be valid though as the probability of interaction, called *cross-section*, would
¹¹⁵⁸ have been increasing without limitation with the square of the energy. Fermi had proposed a two
¹¹⁵⁹ vector current coupling but Lee and Yang noted that an axial current could appear and would violate
¹¹⁶⁰ parity [93]. Gamov and Teller had already tried to account for such parity violation by describ-
¹¹⁶¹ ing Fermi's interaction through allowed (parity-violating) and superallowed (parity-conserving) de-
¹¹⁶² cays [94]. The Wu experiment in 1956 would confirm the parity violation [95], as showed by Fig-
¹¹⁶³ ure 2.10. But the success of QED as a quantum field theory would spark the development of such a
¹¹⁶⁴ theory to describe the weak interaction.

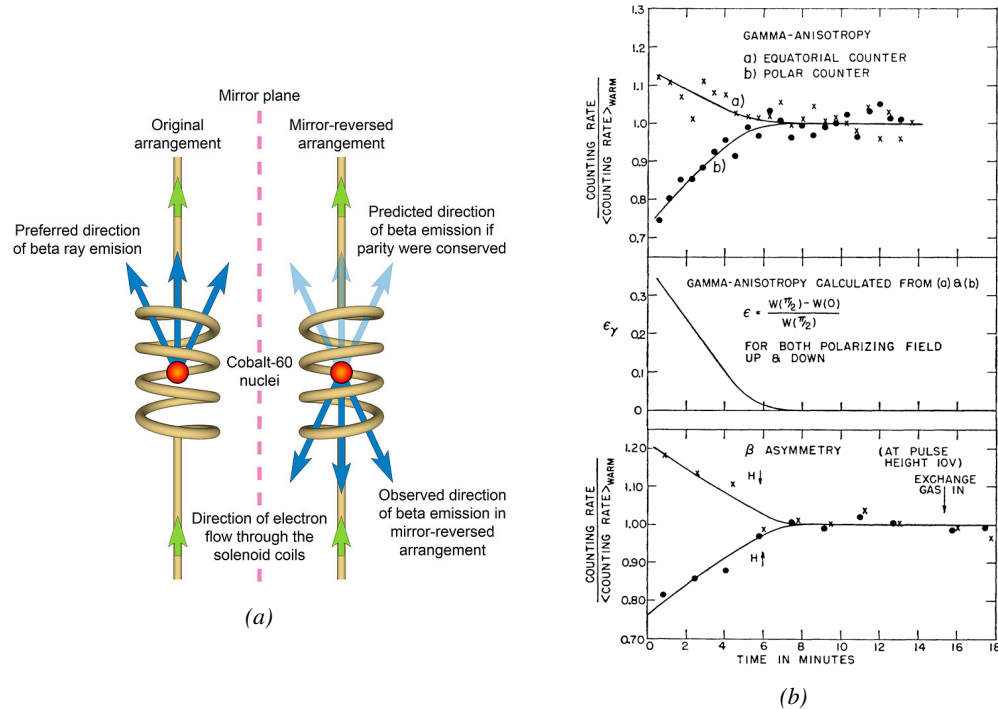


Figure 2.10: As explained through Figure 2.10a, the Wu experiment consisted in measuring the preferred direction of emission of beta rays of a Cobalt source placed in a stable magnetic field aligned, in one case, and anti-aligned, in the other case, with the nuclear spin. The result of Figure 2.10b showed a violation of parity.

As previously discussed, the great success of QED was built on an underlying symmetry, interpreted as a gauge invariance so that the effect of the force is the same in all space-time coordinates, and of the possibility to renormalize it in order to resolve infinities. In 1967 Weinberg found a way to unite both the electromagnetic and weak interaction into a gauge theory involving 4 gauge bosons, 3 of which were massive and carried out the weak interaction and a massless boson carrying the electromagnetic interaction [96]. Among the 3 massive bosons, 2 were charged and 1 was neutral, similarly to the previously theorized *pi meson* vector of the Yukawa model [48] and all have a mass much greater than nucleons and thus a very short life time implying a finite very short range contrary to the contact interaction originally proposed by Fermi.

Breakthrough in other fields of physics contributed in giving theoretical support and interpretation to the unified electroweak theory. The stepping stone would be the use of spontaneous symmetry breaking that was inspired to Nambu at the begining of the 1960s [97, 98] following the development of the Bardeen–Cooper–Schrieffer (BCS) superconductivity mechanism in 1957 [99]. Cooper had shown that BCS pairs, pairs of electrons bound together at low temperature, could have lower energy than the Fermi energy and were responsible for superconductivity. This lead to the discovery of Goldstone-Nambu bosons [100, 101] as a result of the spontaneous breaking of the chiral symmetry in a theory describing nucleons and mesons developped by Nambu and Jona-Lasinio in 1961, and now understood as a low-energy approximation of QCD. Simmilarly to the mechanism of energy gap appearance in superconductivity, the nucleon mass is suggested to be the result of a self-energy of a fermion field and is studied through a four-fermion interaction in which, as a consequence of the symmetry, bound states of nucleon-antinucleon pairs appear and can be regarded as virtual pions.

1186 Though the symmetry is maintained in the equations, the ground state is not preserved. Goldstone
 1187 showed that the bound states corresponds to spinless bosons with zero mass [101].

1188 Although the model in itself didn't revolutionize particle physics, spontaneous symmetry breaking
 1189 would be generalized to quantum field theories. As all fundamental interactions are described
 1190 using gauge theories based on underlying symmetries, processes such as the chiral symmetry breaking
 1191 would be introduced soon after the publication of Nambu and Jona-Lasinio. In 1962, Anderson,
 1192 following the idea of Schwinger who suggested that zero-mass vector bosons were not necessarily
 1193 required to describe the conservation of baryons, contrary to the bosons emerging from chiral
 1194 symmetry breaking [102], discussed the implications of spontaneous symmetry breaking in particles
 1195 physics [103]. A model was finally independently built in 1964 by Brout and Englert [104],
 1196 Higgs [105], and Guralnik, Hagen, and Kibble [106], who discovered that combining an additional
 1197 field into a gauge theory in order to break the symmetry, the resulting gauge bosons acquire a nonzero
 1198 mass. Moreover, Higgs stated that this implied the existence of at least one new massive, i.e. self-
 1199 interacting, scalar boson, that is now known as *Higgs boson*, corresponding to this additional field.
 1200 The Higgs mechanism today specifically refers to the process through which the gauge bosons of
 1201 the weak interaction acquire mass. In 1967, Weinberg could point to the Higgs mechanism to integrate
 1202 a Higgs field into a new version of the electroweak theory in which the spontaneous symmetry
 1203 breaking mechanism of the Higgs field would explicitly explain the masses of the weak interaction
 1204 gauge bosons and the zero-mass of photons [96].

1205 2.1.2 Construction and validation of the Standard Model

1206 The Standard Model of particle physics was built in the middle of the 1970s after the experimental
 1207 confirmation of the existence of quarks [107]. It is based on the assembly of the models previously
 1208 introduced and describing the fundamental interactions, except for gravitation, and their gauge
 1209 bosons as well as the way elementary "matter" particles interact with the fields associated with these
 1210 force carriers. In this sense, the development of QED and the unification of the electroweak interaction,
 1211 of the Yukawa interaction and of QCD, and of the Higg mechanism made it possible to explain
 1212 most of contemporary physics.

1213 In the SM, "matter" particles, are described by 12 fermion fields of spin $\frac{1}{2}$ obeying the Fermi-
 1214 Dirac statistics, i.e. subjected to the Pauli exclusion principle. To each fermion is associated its
 1215 corresponding antiparticle. The fermions are classified according to the way they interact and, thus,
 1216 according to the charges they carry. 6 of them are classified as quarks (u , d , c , s , t , and b) and
 1217 are subjected to all interactions and the 6 others as leptons (e^- , μ^- , τ^- , ν_e , ν_μ , and ν_τ). Leptons
 1218 are not subjected to the strong interaction and among them, the 3 neutrinos only interact weakly as
 1219 they are neutral particles, which explains why they are so difficult to detect. The gauge boson fields
 1220 are the gluons g for the strong interaction, the photon γ for the electromagnetic interaction and the
 1221 weak bosons W^+ , W^- , and Z^0 for the weak interaction. Finally, the Higgs field H^0 is responsible,
 1222 through the spontaneous symmetry breaking, of the mixing of the massless electroweak boson fields
 1223 W_1 , W_2 , W_3 , and B leading to the observable states γ , W^+ , W^- , and Z^0 that can gain mass while
 1224 interacting with the Higgs field. This picture of the SM is summarized through Figure 2.11 where
 1225 the antifermions are not shown.

1226 When the model was first finalized, the existence of the weak gauge bosons, of the charm, of the
 1227 third quark generation composed of top and bottom quarks to explain the observed CP violation was
 1228 not proven but the predictions were measured with good precision in the years following [74–78]. The
 1229 weak bosons W and Z would be discovered during the next decade in 1983 [108–111]. The

very last predicted elementary particle of the model that was not observed yet would prove to be very difficult to observe. The Higgs boson needed the start of the LHC to finally be observed in 2012 [112, 113]. A few years more of tests were necessary to measure its properties to confirm the observation of a scalar boson compatible with the predicted Higgs boson H^0 [114].

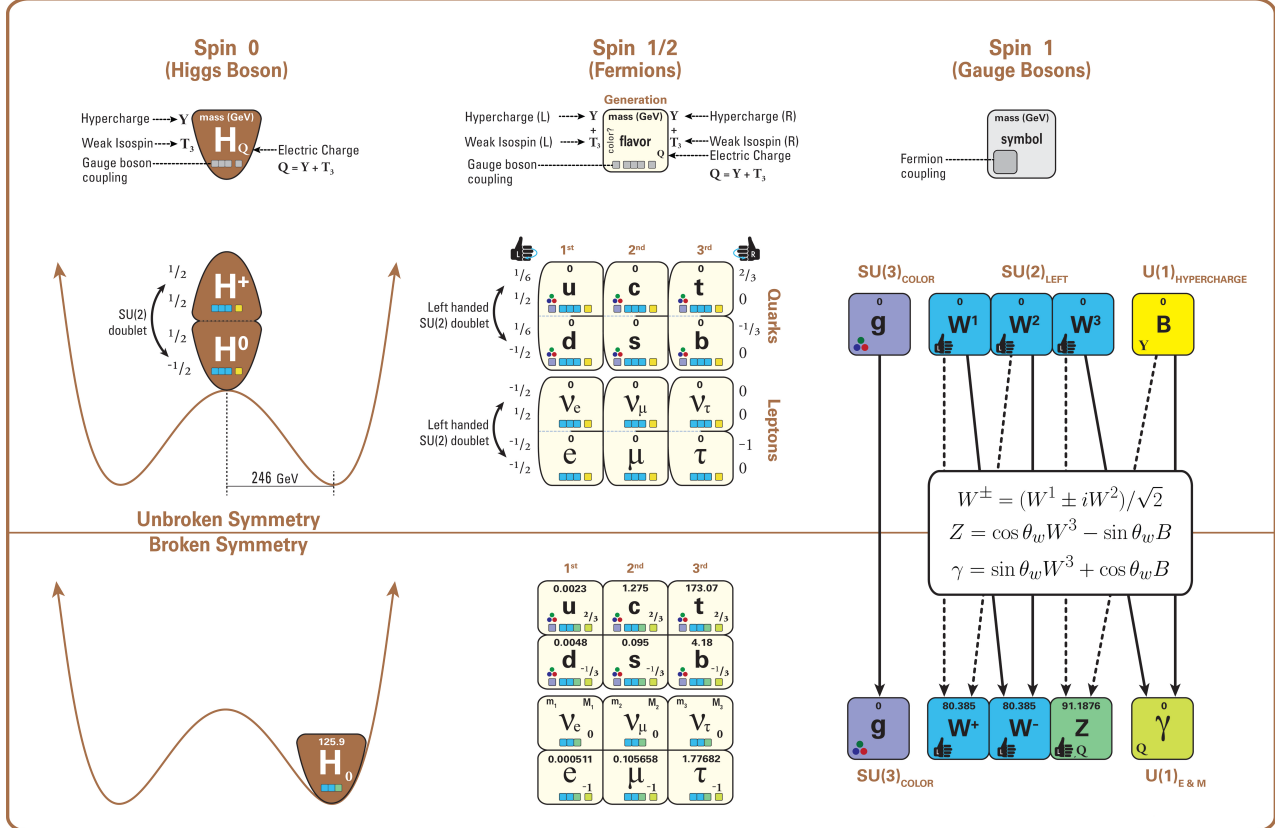


Figure 2.11: The elementary particles of the Standard Model are shown along with their properties. Their interactions with the strong, weak and electromagnetic forces have been explicated using color squares. In the left column, the scalar higgs boson is depicted. The center is focused on the matter particles, the fermions, and the right column on the force carriers, the gauge bosons. The role of the Higgs boson in electroweak symmetry breaking is highlighted, and the corresponding way properties of the various particles differ in the (high-energy) symmetric phase (top) and the (low-energy) broken-symmetry phase (bottom) are shown.

2.1.3 Investigating the TeV scale

In High-Energy Physics, the number of experimental events depends on the total interaction cross-section of the colliding particles and of the *instantaneous luminosity* [115]. The luminosity is a quantity providing an information on the interaction rate normalised to the interaction cross-section. The relationship between number of events N , cross-section and instantaneous luminosity \mathcal{L} is given in Formula 2.8.

$$(2.8) \quad \mathcal{L} = \frac{1}{\sigma} \frac{dN}{dt} \Leftrightarrow N = \sigma \int \mathcal{L} dt = \sigma \mathcal{L}_{int}$$

In the formula, the integral of the luminosity over time is referred to as the *integrated luminosity* \mathcal{L}_{int} . In fact, the instantaneous luminosity can be deduced from the beam parameters. New colliders now use bunched beams. The instantaneous luminosity then depends on the bunch crossing frequency f_{BX} , on the number of particles contained in each bunch n , and on the RMS transverse beam sizes in the horizontal, σ_x^* , and vertical directions, σ_y^* , at the level of the interaction point. The beam sizes can be assumed to be identical, leading to the relation of Formula 2.9.

$$(2.9) \quad \mathcal{L} = f_{BX} \frac{n^2}{\sigma^*}$$

This expression doesn't depend on time anymore and leads to a simple estimation of the integrated luminosity and hence, knowing the cross-section of each available physics channel, to the expected number of events in each channel. The total interaction cross section is the sum of all the different output channels allowed by the interaction process. In the case of highly relativistic protons, the proton-proton (pp) total cross-section increases with the center-of-mass energy of interactions, as can be seen from Figure 2.12.

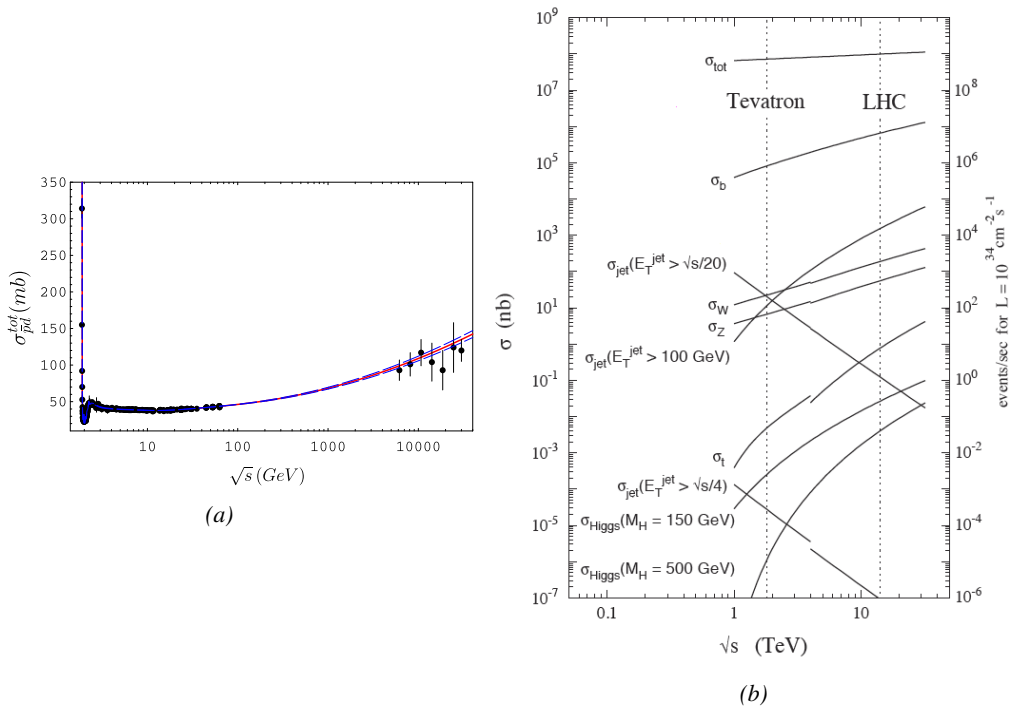


Figure 2.12: Figure 2.12a: Total proton-proton cross-section as a function of the collisions center-of-mass energy \sqrt{s} [116] with cosmic-ray data from Akeno Observatory and Fly's Eye Collaboration. Figure 2.12b: Total proton-(anti)proton and interaction channel cross-sections in the TeV scale.

Enhancing rare processes that allow to finely test the Standard Model is then achieved through an increase in both energy and luminosity. At the energy range that were scanned thanks to high-energy colliders, the SM is so far a well tested theory. Nevertheless, several hints of physics going beyond its scope have been observed. First of all, gravity is not explained through this model and

huge difficulties are encountered when trying to include it. The strength of gravitational interaction is expected to be negligible at the scale of elementary particles, nevertheless, adding gravitation in the perspective of developing a "*theory of everything*" leads to divergent integrals that could not be fixed through renormalization. Moreover, the SM considers neutrinos to be massless. But it was shown in the late 1960s by the Homestake experiment that the flux of solar neutrinos (i.e. ν_e) measured didn't match the predicted values [117]. The mechanism of neutrino oscillations as a solution to the discrepancy was proposed by Pontecorvo [118] and confirmed in the early 2000s by the Sudbury Neutrino Observatory [119]. This oscillation implies that neutrinos that can be observed are a superposition of massive neutrino states. The research on neutrino oscillation is already quite advanced with experiments looking at atmospheric, reactor or beam neutrinos in order to determine the elements of the mixing matrix (Pontecorvo–Maki–Nakagawa–Sakata matrix [120]) similar to the Cabibbo–Kobayashi–Maskawa (CKM) matrix describing the mixing of quarks [72]. Nevertheless, no answer to the origin of neutrino mass is yet provided.

Another intriguing fact is that the universe is dominated by matter. However, the SM predicted that matter and antimatter should have been created in equal amounts and no mechanism is able to explain this baryon asymmetry. The favoured model to explain this imbalance is the *baryogenesis* through electroweak symmetry breaking [121, 122]. Another possibility to explain the apparent asymmetry would be the existence of an electric dipole in any fundamental particle that would permit matter and antimatter particles to decay at different rates [123].

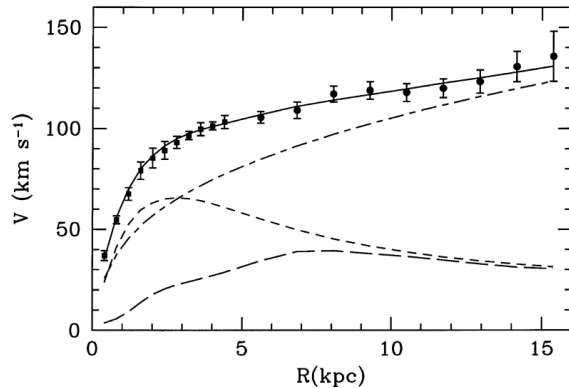


Figure 2.13: Rotation curve (points) of galaxy M33 compared with best fitting model (line). The short-dashed line represents the rotation profile that would be expected from the observation of the stellar disc alone [124].

The discrepancy of velocity dispersion of stars in galaxies with respect to the visible mass they contain is known since the end of the 19th century where Kelvin proposed that this problem could be solved if a great majority of the stars would be dark bodies, idea strongly criticized by Pointcaré [125]. Throughout the 20th century, physicists like Kapteyn [126] or Zwicky [127, 128], showed the first hints of a *dark matter* by studying star velocities and galactic clusters, followed by robust measurements of galaxy rotation curves by Babcock which suggested that the mass-to-luminosity ratio was different from what would be expected from watching the visible light [129]. Later in the 1970s, Rubin and Ford from direct light observations [130] and Rogstad and Shostak from radio measurements [131] showed that the radial velocity of visible objects in galaxies was increasing with increasing distance to the center of the galaxy. An example of galaxy rotation curve is provided in Figure 2.13. Finally observation of lensing effect by galaxy clusters, temperature

1286 distribution of hot gas in galaxies and clusters, and the anisotropies in the Cosmic Microwave Back-
 1287 ground (CMB), showed in Figure 2.14, kept on pointing to a *dark matter* [132]. From all the data
 1288 accumulated, the visible matter would only account to no more than 5% of the total content on the
 1289 visible universe [133]. Alternative theories have tried to investigate modified versions of the General
 1290 Relativity as this theory is only well tested at the scale of the solar system but is not sufficiently
 1291 tested on wider ranges or even theories in which gravitation is not a fundamental force but rather an
 1292 emergent one [134, 135]. But so far, such theories have difficulties to reproduce all the experimental
 1293 observations as easily as through dark matter.

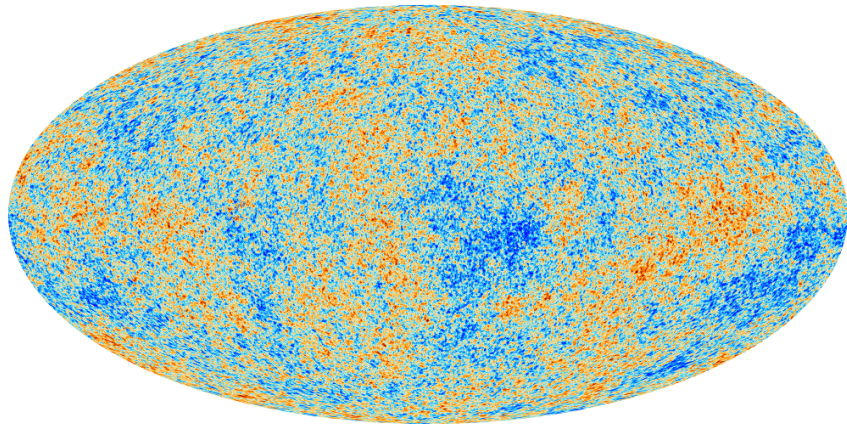


Figure 2.14: Cosmic Microwave Background as measured by the space observatory Planck which mean temperature is $T_\gamma = (2.7255 \pm 0.0006)\text{K}$ with anisotropies of the order of a few μK .

1294 A possible theory to offer dark matter candidates would be *supersymmetry* (SUSY) which pro-
 1295 poses a relationship in between bosons and fermions in the frame of the Minimal Supersymmetric
 1296 Standard Model (MSSM). In this model, each elementary particle, through a spontaneous space-
 1297 time symmetry breaking mechanism would have a *super partner* from the other family of particles,
 1298 pairing bosons and fermions together. The model was first introduced as a way to solve the *Hierar-*
 1299 *chy Problem* [136]. The discrepancy between the strength of the weak force and gravity translates
 1300 into a light Higgs boson compared to the *Planck Mass*. In the SM, the Higgs mass is left to be a
 1301 measured parameter rather than a calculated one even though the model requires a mass in between
 1302 100 and 1000 GeV/c^2 to stay unitary. Nevertheless, quantum corrections to the Higgs mass coming
 1303 from its interactions with virtual particles should make the scalar boson much heavier than what
 1304 measured [137]. Through the MSSM, the stability of fermion masses would provide stability to the
 1305 Higgs boson mass via the introduction of a fermionic super partner.

1306 On top of providing a solution to the Hierarchy Problem, the model comes with heavy dark
 1307 matter candidates in the TeV scale [138]. Indeed, in the case *R-parity* is not violated, the lightest
 1308 supersymmetric particle (LSP) cannot decay and could then explain the dark matter. The LSP in
 1309 the model is neutral and can only interact through the weak and gravitational interactions. Typical
 1310 candidates are the *neutralino*, the *sneutrino* or the *gravitino*.

1311 Finally, extensions to the MSSM, and in particular minimal SUper GRAvity (mSUGRA), include
 1312 general relativity as mediator of the symmetry breaking. mSUGRA gives access to the hidden sector
 1313 in which the MSSM only interacts gravitationally and suppresses the infites arising from attempts to
 1314 include gravity into the SM thanks to possible renormalization [139].

1315

In the case SUSY fails to be detected, alternative models exist to provide solutions to the Hierarchy Problem. The most investigated models are extra dimensions (Arkani-Hamed Dimopoulos Dvali [140, 141], Kaluza–Klein [142, 143] or Randall-Sundrum models [144, 145]) that usually also include gravitation.

Alternative models also exist for the production of dark matter candidates. Models with a hidden valley that would unravel the existence of a new group of light particles,

1322

All these different aspects of physics beyond the Standard Model of particle physics and the Standard Model itself can be tested through the use of very energetic and intense hadron and ion colliders. Powerful hadron colliders such as Tevatron and LHC are suited for searching for strongly interacting particles. Signatures for the MSSM would come from the super partners of quarks and gluons that can decay into a LSP that could then be identified as missing energy as it escapes the detectors undetected. But even in the case MSSM predictions are not to be seen, the other models treating dark matter also propose Weakly Interacting Massive Particles (WIMPs) that could be observed in similar ways than LSPs [**ASKEW2014**].

The LHC at CERN is a perfect tool to seek answers to these open questions.

1332 2.2 The Large Hadron Collider & the Compact Muon Solenoid

1333 Throughout its history, CERN has played a leading role in high energy particle physics. Large regional facilities such as CERN were thought after the second world war in an attempt to increase 1334 international scientific collaboration and allows scientists to share the forever increasing costs of 1335 experiment facilities required due to the need for increasing the energy in the center of mass to 1336 deeper probe matter. The construction of the first accelerators at the end of the 50s, the Synchro- 1337 cyclotron (SC) and the Proton Synchrotron (PS), was directly followed by the first observation of 1338 antinuclei in 1965 [146]. Strong from the experience of the Intersecting Storage Rings (ISR), the 1339 very first proton-proton collider that showed hints that protons are not elementary particles, the Super 1340 Proton Synchrotron (SPS) was built in the 70s to investigate the structure of protons, the preference 1341 for matter over antimatter, the state of matter in the early universe or exotic particles, and lead to the 1342 discovery in 1983 of the W and Z bosons [108–111]. These newly discovered particles and the elec- 1343 troweak interaction would then be studied in details by the Large Electron-Positron (LEP) collider 1344 that will help to prove in 1989 that there only are three generations of elementary particles [147]. 1345 The LEP would then be dismantled in 2000 to allow for the LHC to be constructed in the existing 1346 tunnel.

1348 2.2.1 LHC, the most powerful particle accelerator

1349 The LHC has always been considered as an option to the future of CERN. At the moment of the 1350 construction of the LEP beneath the border between France and Switzerland, the tunnel was built in 1351 order to accomodate what would be a Large Hadron Collider with a dipole field of 10 T and a beam 1352 energy in between 8 and 9 TeV [148] directly followed in 1985 with the creation of a 'Working 1353 Group on the Scientific and Technological Future of CERN' to investigate such a collider [149]. 1354 The decision was finally taken almost 10 years later, in 1994, to construct the LHC in the LEP 1355 tunnel [150] and the approval of the 4 main experiments that would take place at the 4 interaction 1356 points would come in 1997 [151] and 1998 [152]:

- 1357 • ALICE [153] has been designed in the purpose of studying the confinement of quarks through
 1358 exploration of the quark-gluon plasma that is believed to have been a state of matter that
 1359 existed in the very first moment of the universe.
- 1360 • ATLAS [154] and CMS [155] are general purpose experiments that have been designed with
 1361 the goal of continuing the exploration of the Standard Model and investigate new physics.
- 1362 • LHCb [156] has been designed to investigate the preference of matter over antimatter in the
 1363 universe through the CP violation.

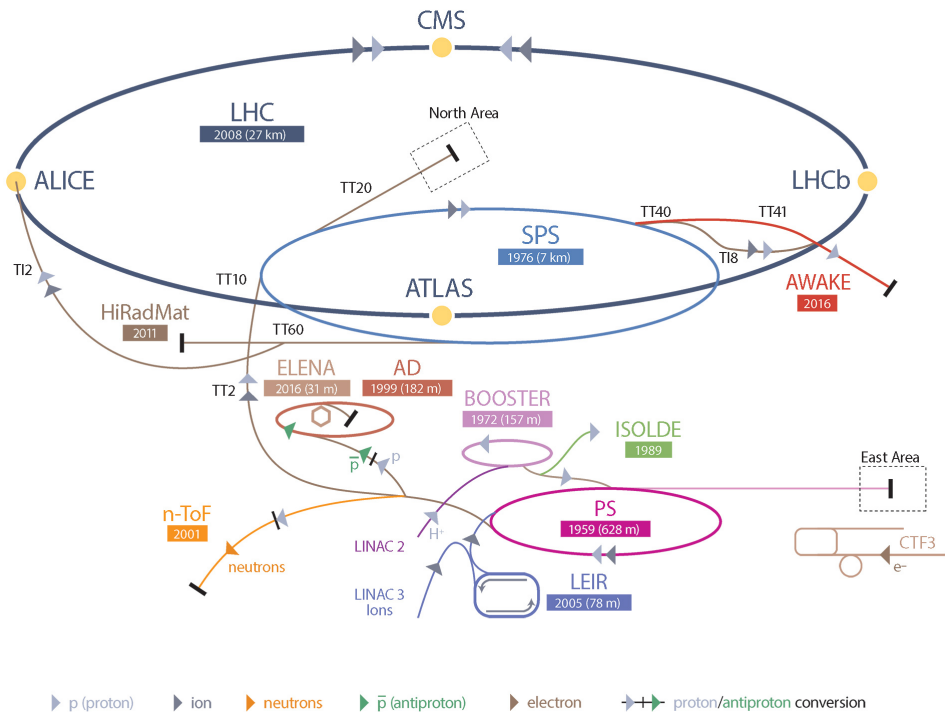


Figure 2.15: CERN accelerator complex.

1364 These large scale experiments, as well as the full CERN accelerator complex, are displayed on
 1365 Figure 2.15. The LHC is a 27 km long hadron collider and the most powerful accelerator used for
 1366 particle physics since 2008 [157]. The LHC was originally designed to collide protons at a center-
 1367 of-mass energy of 14 TeV and luminosity of $10^{34} \text{ cm}^{-2}\text{s}^{-1}$, as well as Pb ions at a center-of-mass
 1368 energy of 2.8 TeV/A with a peak luminosity of $10^{27} \text{ cm}^{-2}\text{s}^{-1}$. Run 1 of LHC, when the center-
 1369 of-mass energy only was half of the nominal LHC energy, was enough for both CMS and ATLAS
 1370 to discover the Higgs boson [114] and for LHCb to discover pentaquarks [158] and confirm the
 1371 existance of tetraquarks [159]. Nevertheless, after the Third Long Shutdown (LS3) (2024-2026),
 1372 the accelerator will be in the so called High Luminosity LHC configuration [160], increasing its
 1373 instantaneous luminosity to $10^{35} \text{ cm}^{-2}\text{s}^{-1}$ for pp collisions and to $4.5 \times 10^{27} \text{ cm}^{-2}\text{s}^{-1}$, boosting the
 1374 discovery potential of the LHC. The HL-LHC phase should last at least another 10 years depending
 1375 on the breakthrough this machine would lead to. Already a new accelerating device, the FCC, as
 1376 been proposed to prepare the future of high energy physics after the LHC.

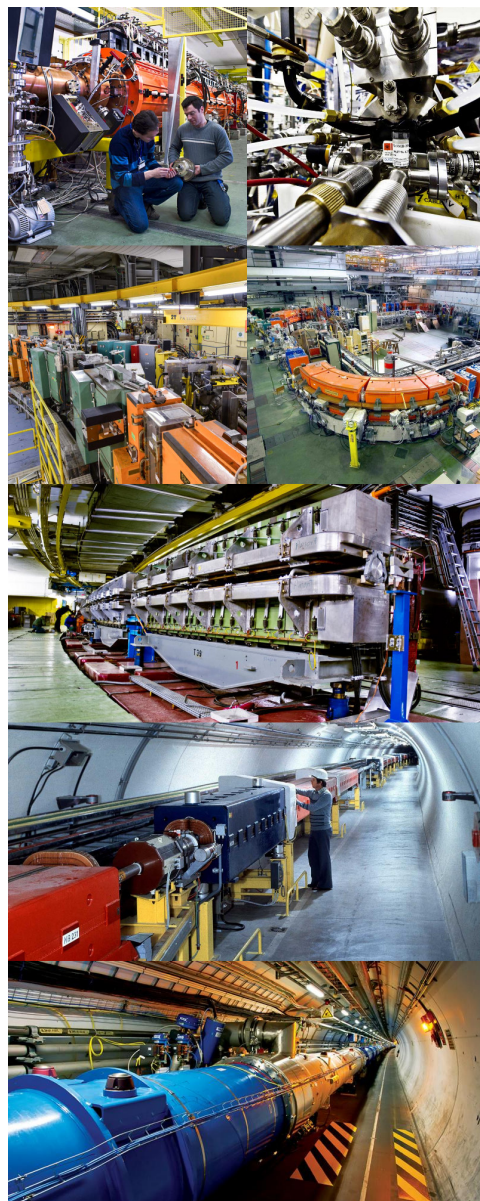


Figure 2.16: Pictures of the different accelerators. From top to bottom: first the LINAC 2 and the Pb source of LINAC 3. Then the Booster and the LEIR. Finally, the PS, the SPS and the LHC.

1377 The LHC is the last of a long series of accelerating devices. Before being accelerated by the
 1378 LHC, the particles need to pass through different acceleration stages. All these acceleration stages
 1379 are visible on Figure 2.15 and pictures of the accelerators are shown in Figure 2.16.

1380
 1381 The story of accelerated protons at CERN starts with a bottle of hydrogen gas injected into the
 1382 source chamber of the linear particle accelerator *LINAC 2 2* in which a strong electric field strips the
 1383 electron off the hydrogen molecules only to keep their nuclei, the protons. The cylindrical conductors,
 1384 alternatively positively or negatively charged by radiofrequency cavities, accelerate protons by

1385 pushing them from behind and pulling them from the front and ultimately give them an energy of
 1386 50 MeV, increasing their mass by 5% in the process.

1387 When exiting the LINAC 2, the protons are divided into 4 bunches and injected into the 4 superimposed synchrotron rings of the *Booster* where they are then accelerated to reach an energy of
 1388 1.4 GeV before being injected into the *PS*. Before the Booster was operational in 1972, the protons were directly injected into the *PS* from the LINAC 2 but the low injection energy limited the
 1390 amount of protons that could be accelerated at once by the *PS*. With the Booster, the *PS* accepts
 1391 approximately 100 times more particles.
 1392

1393 The 4 proton bunches are thus sent as one to the *PS* where their energy eventually reaches
 1394 26 GeV. Since the 70s, the main goal of this 628 m circumference synchrotron has been to supply
 1395 other machines with accelerated particles. Nowadays, not only the *PS* accelerates protons, it also
 1396 accelerates heavy ions from the *Low Energy Ion Ring (LEIR)*. Indeed, the LHC experiments are not
 1397 only designed to study *pp*-collisions but also *Pb*-collisions. Lead is first injected into the dedicated
 1398 linear collider *LINAC 3*, that accelerate the ions using the same principle than LINAC 2. Electrons
 1399 are stripped off the lead ions all along the acceleration process and eventually, only bare nuclei are
 1400 injected in the *LEIR* whose goal is to transform the long ion pulses received into short dense bunches
 1401 for LHC. Ions injected and stored in the *PS* were accelerated by the *LEIR* from 4.2 MeV to 72 MeV.

1402 Directly following the *PS*, is finally the last acceleration stage before the LHC, the 7 km long
 1403 *SPS*. The *SPS* accelerates the protons to 450 GeV and inject proton in both LHC accelerator rings
 1404 that will increase their energy up to 7 TeV. When the LHC runs with heavy lead ions for ALICE
 1405 and LHCb, ions are injected and accelerated to reach the energy of 2.8 TeV/A.

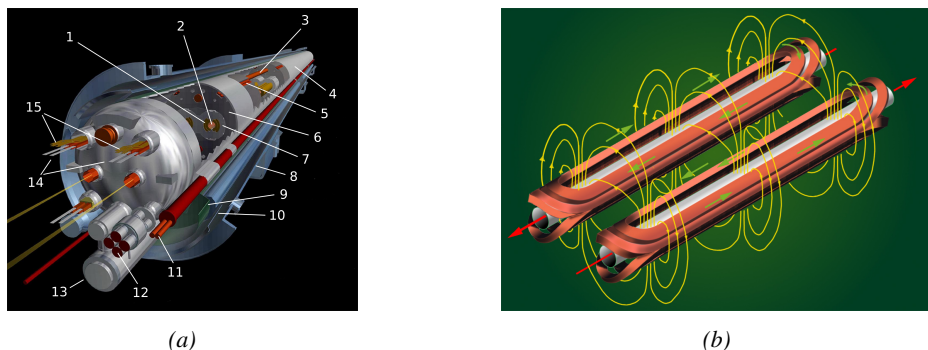


Figure 2.17: Figure 2.17a: schematics of the LHC cryodipoles. 1: Superconducting Coils, 2: Beam pipe, 3: Heat exchanger Pipe, 4: Helium-II Vessel, 5: Superconducting Bus-bar, 6: Iron Yoke, 7: Non-Magnetic Collars, 8: Vacuum Vessel, 9: Radiation Screen, 10: Thermal Shield, 11: Auxiliary Bus-bar Tube, 12: Instrumentation Feed Throughs, 13: Protection Diode, 14: Quadrupole Bus-bars, 15: Spool Piece Bus-bars. Figure 2.17b: magnetic field and resulting motion force applied on the beam particles.

1406 The LHC beams are not continuous and are rather organised in bunches of particles. When in *pp*-
 1407 collision mode, the beams are composed of 2808 bunches of 1.15×10^{11} protons separated by 25 ns.
 1408 When in *Pb* collision mode, the 592 *Pb* bunches are on the contrary composed of 2.2×10^8 ions
 1409 separated by 100 ns. The two parallel proton beams of the LHC are contained in a single twin-
 1410 bore magnet due to the space restriction in the LEP tunnel. Indeed, building 2 completely separate
 1411 accelerator rings next to each other was impossible. The dipoles of the 1232 twin-bore magnets are
 1412 shown in Figure 2.17 alongside the magnetic field generated along the dipole section to accelerate the
 1413 particles. The dipoles generate a nominal field of 8.33 T, needed to give protons and lead nucleons

¹⁴¹⁴ their nominal energy. Some 392 quadrupoles, presented in Figure 2.18, are also used to focus to the
¹⁴¹⁵ beams, as well as other multipoles to correct smaller imperfections.

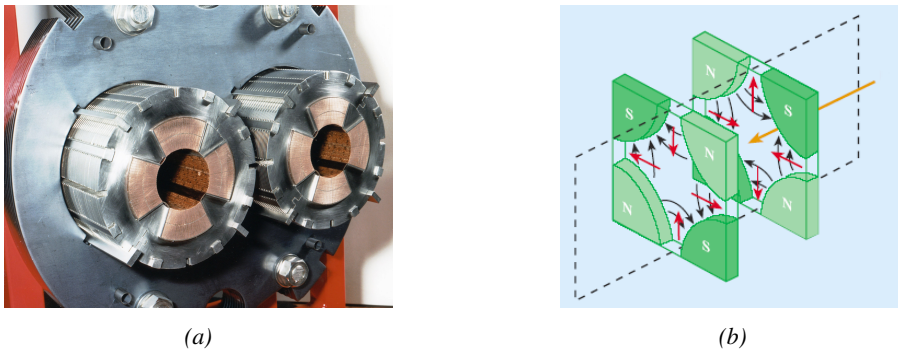


Figure 2.18: Figure 2.18a: picture of the LHC quadrupoles. Figure 2.18b: magnetic fields and resulting focussing force applied on the beam by 2 consecutive quadrupoles.

¹⁴¹⁶ 2.2.2 CMS, a multipurpose experiment

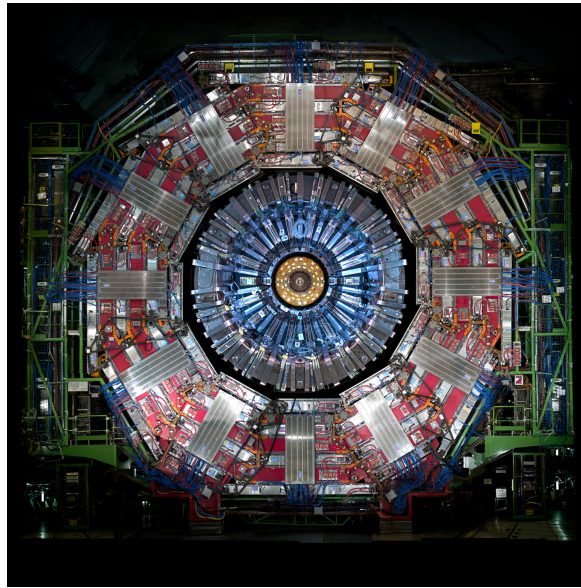


Figure 2.19: Picture of the CMS barrel. The red outer layer is the muon system hosted into the red iron return yokes. The calorimeters are the blue cylinder inside in magnet solenoid and the tracker is the inner yellow cylinder built around the beam pipe.

¹⁴¹⁷ Among the four main LHC experiments is the Compact Muon Solenoid used as a multipurpose
¹⁴¹⁸ tool to investigate the SM and physics beyond its scope. Proposed through a letter of intention
¹⁴¹⁹ in 1992 [155], and as its name suggests, this very compact detector's uses the muons as a clear tag
¹⁴²⁰ of most of SM and new physics interesting channels. In the original 1997 Technical Design Re-
¹⁴²¹ port (TDR) [161], the very first sentences were stating that "*Muons are an unmistakable signature*

of most of the physics LHC is designed to explore. The ability to trigger on and reconstruct muons at the highest luminosities is central to the concept of CMS, the Compact Muon Solenoid.” CMS participated in the discovery of the Higgs boson and the measurement of its properties and couplings together with ATLAS and is also actively involved in the search for SUSY and heavy ion collisions. Other exotic physics are also being investigated using the data collected by CMS.

The CMS apparatus in itself is the heaviest detector ever built starring a SI15m diameter and a 29 m length for a total weight of 14 kT. A thick 4 T solenoid magnet located at the beam interaction point hosts trackers and calorimeters. Extending in all directions around the magnet, heavy iron return yokes are installed to extend the magnetic field and support a muon system. The apparatus consists of a barrel, referring to the magnet and the detectors contained in it and the part of the muon system built directly in the cylinder around the magnet, and of 2 endcaps in the forward and backward region of the detector that closes the apparatus and complete the detection coverage along the beam line. A front view on the barrel is provided in Figure 2.19 while a detailed view of the apparatus is given in Figure 2.20.

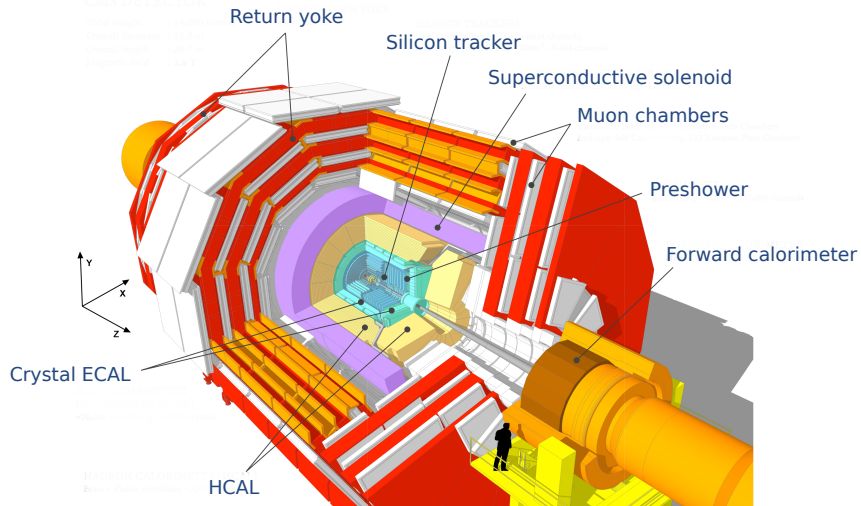


Figure 2.20: View of the CMS apparatus and of its different components.

In order to efficiently detect all long leaving particles and measure their properties with good precision, the CMS detector uses an onion like layout around of the interaction point in order to maximize the covered solid angle. As detailed in Figure 2.21, in the innermost region of the detector, closest to the interaction point, the silicon tracker records the trajectory of charged particles. Around it, the electromagnetic calorimeter (ECAL) stops and measure the energy deposition of electrons and photons. In the next layer, the hadron calorimeter (HCAL), hadrons are stopped are their energy measured. These layers are contained inside of the magnet of CMS, the superconducting solenoid. Outside of the magnet are the muon chambers embedded into iron return yokes used to control the magnetic field and gives muons, the only particles traveling completely through the whole detector, a double bending helping in reconstructing their energy and trajectory. Note that photons and neutral hadrons are differentiated from electrons and charged hadrons in the calorimeters by the fact that don’t interact with the silicon tracker and that they are not influenced by the magnetic field.

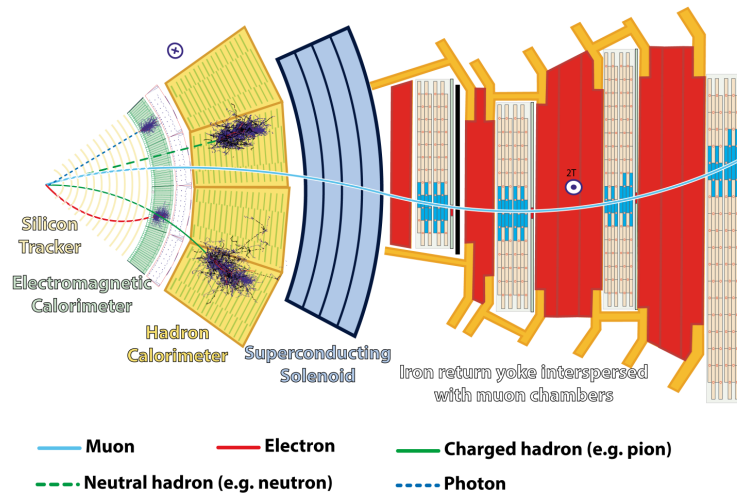


Figure 2.21: Slice showing CMS sub-detectors and how particles interact with them.

2.2.2.1 The silicon tracker, core of CMS

The silicon tracker visible on Figure 2.22 is divided into 2 different sub-systems: the *pixel detector* at the very core and the *microstrip detector* around it. This system is composed of 75 million individual readout channels with up to 6000 channels per squared centimeter for the pixels making it the world's biggest silicon detector. This density allows for measurements of the particle tracks with a precision of the order of $10\ \mu\text{m}$. This is necessary to reconstruct all the different interaction vertices with precision and have a precise measure of the curvature of the charged particles traveling through the magnetic field to estimate their charge and momentum.

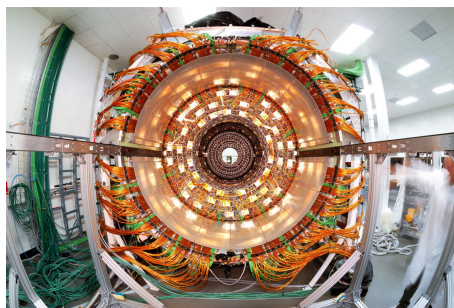


Figure 2.22: CMS tracker.

2.2.2.2 The calorimeters, measurement of particle's energy

The ECAL directly surrounding the tracker is composed of crystals of lead tungstate, PbWO_4 , a very dense but optically transparent material used to stop high energy electrons and photons. These crystal blocks basically are extremely dense scintillators which scintillate in fast, short light bursts proportionally to the energy deposition. The light is yielded rapidly and contained at 80% in the corresponding 25 ns lasting bunch crossing. Each crystal is isolated from the other by the carbon fiber matrix they are embedded in. It is composed of a barrel containing more than 60,000 crystals

and of closing endcaps containing another 15,000 crystals. In front of the ECAL endcap is installed a preshower detector made out of two layers of lead and silicon strip detectors to increase the spatial resolution close to the beam line for pion-photon and single-double photon discrimination purposes. Figure 2.23 shows the calorimeter inside of the magnet and the crystals.

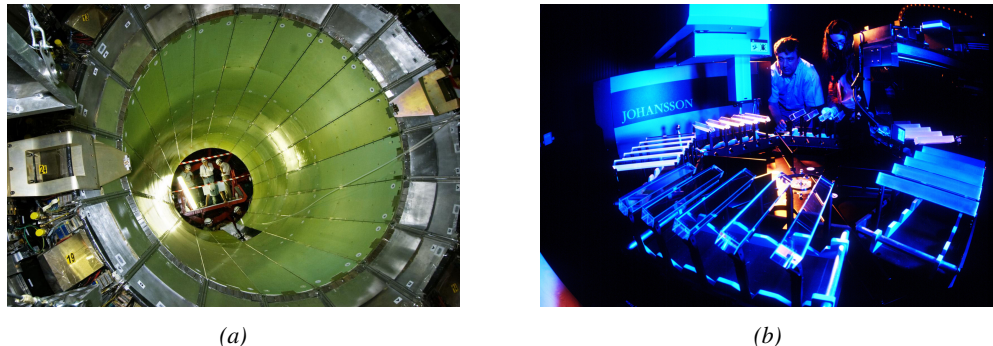


Figure 2.23: Figure 2.23a: picture of the ECAL. Figure 2.23b: picture of the lead tungstate crystals composing the ECAL.

The next layer is the HCAL measuring the hadrons momentum and providing indirect hints of non interacting neutral particles, such as neutrinos, as missing transverse momentum. Several layers of brass or steel are interleaved with plastic scintillators readout by photodiodes using wavelength-shifting fibers. The HCAL is also composed of a barrel, shown in Figure 2.24 and of endcaps. It also features forward calorimeters on both sides of CMS in the region very close to the beam line at high pseudorapidity ($3.0 < |\eta| < 5.0$). The role of these forward calorimeters, made using steel and quartz fibers, is to measure very energetic hadrons.



Figure 2.24: CMS hadron calorimeter barrel.

Finally, in the outer region of the apparatus, a muon system is used to trigger on potentially interesting event by identifying muons. Indeed, the muon system is a very important part of the CMS trigger infrastructure designed to efficiently select data from the enormous data flow received by the detectors as the LHC delivers collisions at a rate of 40 MHz with a pile-ip of 20 to 30 collisions per bunch crossing during Phase-I and up to 200 during Phase-II, representing billions of interactions per second among which a large quantity are low energy collisions that are not likely to produce new reactions, and which is physically impossible for nowadays technologies to cope with. Working at a maximum rate of 100 kHz, the trigger system is able to select the 100,000 more interesting events

1482 by looking at the energy distribution of the interaction products and clear signatures like muons
 1483 reconstructed by the muon system. the vast majority of these events will not finally be stored after
 1484 physics tests are applied.

1485 2.2.2.3 The muon system, corner stone of CMS

1486 The challenge for the muon system is to provide a robust and fast measurement of muons. Three
 1487 different subsystems, and soon 4 after LS2, compose the muon system as shown in Figure 2.25 in
 1488 which a quadrant of the CMS detector focused on muon system. Drift Tube (DT) are found in the
 1489 barrel region covering the low pseudorapidity region where particles transverse momentum is lower
 1490 and Cathode Strip Chamber (CSC) are found in the endcap region covering higher pseudorapidity
 1491 region closer to beam line where particles have a stronger momentum. The redundancy of the system
 1492 is insured by Resistive Plate Chambers in both the barrel and endcap region. Nevertheless, the region
 1493 closest to the beam line ($|\eta| > 1.8$) was not equipped with RPCs. This lack of redundancy in the high
 1494 pseudo rapidity region will be solved during LS2, the following Year End Technical Stop (YETS) in
 1495 2021 and 2022, and LS3 where the necessary services, detectors and Link System, that collects the
 1496 data and synchronizes them, will be installed.

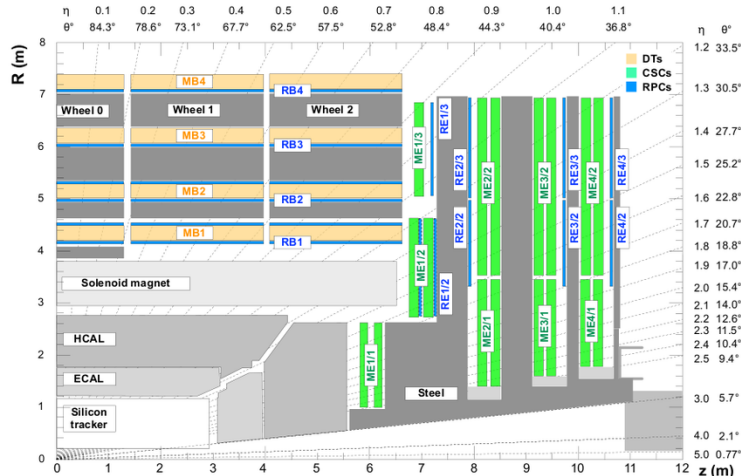


Figure 2.25: A quadrant of the muon system, showing DTs (yellow), RPCs (blue), and CSCs (green).

1497 The barrel region is divided into 5 *wheels* made out of 4 *rings* of detectors with iron return yokes
 1498 in between them whereas the endcaps are made out of 4 disks, each divided into pseudorapidity
 1499 stations, 2 for CSCs (except for the first disk where 3 stations are equipped) and 3 for RPCs, although
 1500 only 2 RPCs stations are equipped at present. The wheels and disks are shown in Figure 2.26. So
 1501 far, each subsystem was dedicated to a particular task. DTs, in the barrel, and CSCs, in the endcaps,
 1502 are used mainly for their spatial resolution. Indeed, DTs' resolution is of the order of 100 μm along
 1503 both the $(r - \phi)$ and $(r - z)$ components while the resolution of CSCs is similar but varies in a range
 1504 from 50 μm to 140 μm depending on the distance to the beamline. On the other hand, RPCs are used
 1505 for their time resolution as they can deliver an information on the muon tracks within 1.5 ns.

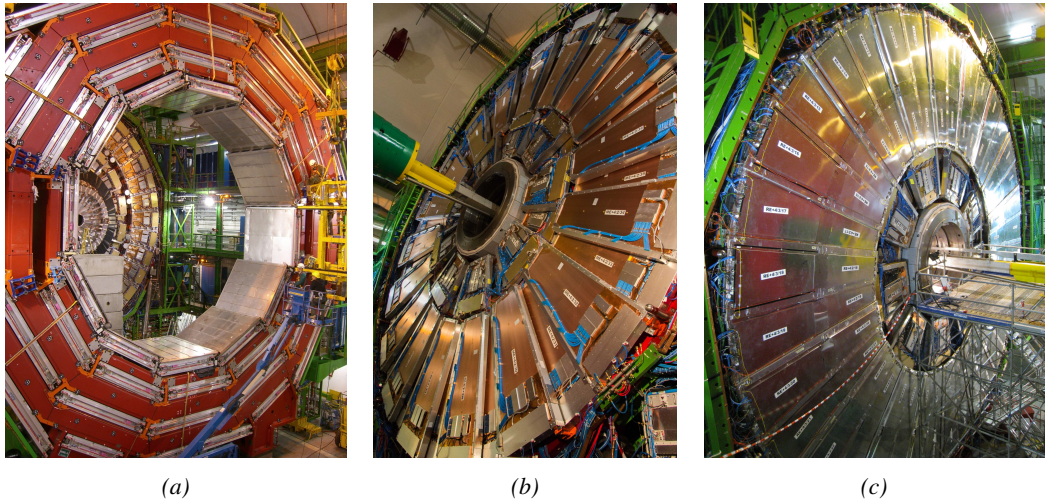


Figure 2.26: Figure 2.26a: Barrel wheel with its detector rings and return yokes. Figure 2.26b: CSC endcap disk with the 2 CSC stations. The outer station is made of 10 deg detectors while the inner station is made of 20 deg detectors. Figure 2.26c: RPC endcap disk. The inner station is not equipped and the inner CSC station can be seen.

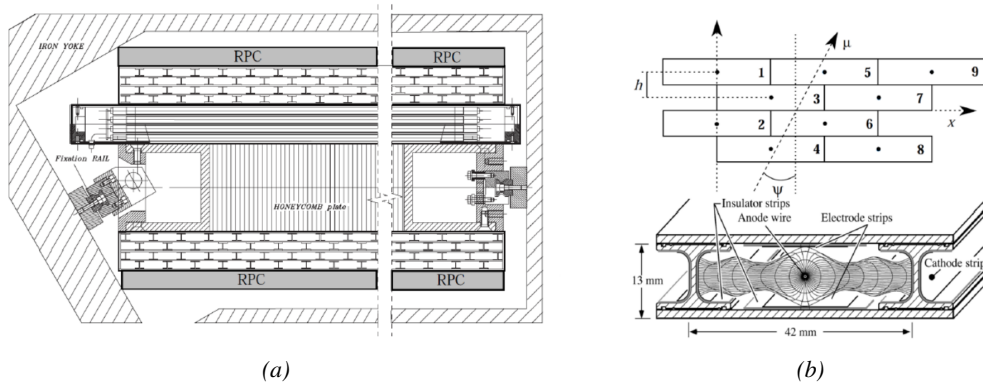


Figure 2.27: Figure 2.27a: Cross section of a DT module showing the two superlayers measuring the ϕ coordinate, perpendicular to the cross section plane, and the superlayer measuring the η coordinate, placed in between the two others with honeycomb and parallel to the cross section plane. The DT detector is sandwiched in between 2 RPCs whose readout strips are perpendicular to the cross section plane, measuring the ϕ coordinate. Figure 2.27b: A DT cell is shown together with its electric field. The path of a muon through a superlayer is shown.

The 250 CMS DTs, found in the barrel covering the pseudorapidity region $0 < |\eta| < 1.2$ and whose structure is shown in Figure 2.27, are composed of 3 superlayers of DT cells. Two of these superlayers are dedicated to measuring the ϕ coordinate of the muons and while the last one measures the η (or z) coordinate. Each superlayer consists on 4 layers of 60 to 70 DT cells arranged in quincunx to allow for a precise reconstruction of the muon path through the DT layers. Each DT cell is a rectangular aluminium gas volume with a central anode wire. Cathode strips are placed on the narrow surface of the cells and electrode strips are placed on the wide surface to help shaping

1513 the electric field to ensure a consistent drift velocity of electrons in the drift volume. These detectors
 1514 are operated using a 85/15 mixture of Ar and CO_2 .

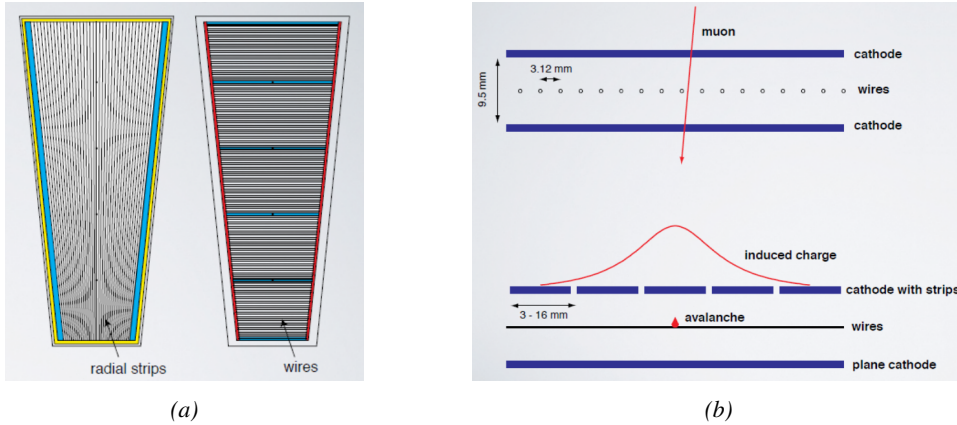


Figure 2.28: Figure 2.28a: cathode strips and anode wire layout of a CSC panel. Figure 2.28b avalanche development and charge collection by anode wires and induction on cathode strips inside of a CSC panel.

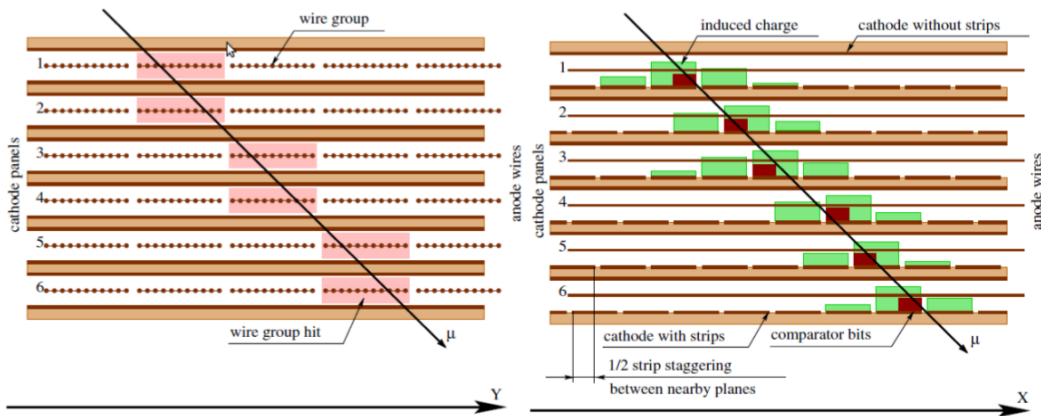


Figure 2.29: Muon track reconstruction through the 6 panels of a CMS CSC using the information of anode wire groups and cathode strip charge distribution combined with comparator bits to decide on which half strip the muon is more likely to have passed.

1515 The 540 CMS CSCs, found in the endcaps covering the pseudorapidity region $0.9 < |\eta| < 2.5$
 1516 and described through Figures 2.28 and 2.29, are composed of 6 panels of CSC, each panel consisting
 1517 in a wide gas volume of 9.5 mm (7 mm in the case of ME1/1 station) containing anode wires and
 1518 whose surfaces are cathodes. The top cathode is a wide copper plane of the size of the gas volume.
 1519 The bottom cathode is divided into thin trapezoidal copper strips radially arranged to measure the
 1520 azimuthal coordinate ϕ with a pitch ranging from 8 to 16 mm. The $0.50 \mu m$ anode wires are placed
 1521 perpendicularly to the strips to measure radial coordinate r and are grouped by 10 to 15 with a wire
 1522 to wire space of 3.2 mm. In the specific case of ME1/1 placed against the HCAL endcap, the $0.30 \mu m$
 1523 anode wires have a wire to wire distance of 2.5 mm and are not disposed perpendicularly to the strips
 1524 but slightly tilted by an angle of 29 deg to compensate for the lorentz force due to the very strong

1525 local magnetic field of 4 T. These detectors are operated with a 40/50/10 mixture of Ar, CO₂ and
 1526 CF₄. Combining the information of the multiple CSC panels, the detectors achieve a very precise
 1527 measurement of the muon track.

1528 Despite their excellent spatial resolution, the wire chambers (DTs and CSCs) are limited in terms
 1529 of time resolution by the fact that the charge needs to drift towards the anode wire and be collected
 1530 before having the confirmation that a particle was detected as the drift volume is not used to develop
 1531 avalanches. Indeed, the stronger electric field close to the anode wire triggers the avalanche and the
 1532 gain of the detector. Due to the drift, the time resolution is thus limited at best to approximately 2 to
 1533 3 ns. In addition, even though the intrinsic time resolution of the tracking chambers is rather good
 1534 compared to the 25 ns in between successive collisions, the processing time of the trigger system
 1535 doesn't allow for very fast triggering as it provides a time precision of only 12.5 ns. Thus, detectors
 1536 fully dedicated to timing measurement have been installed as a redundant system. These detectors
 1537 are RPCs, also gaseous detectors but that use current induction instead of charge collection allowing
 1538 for a time resolution of the order of 1.5 ns only. Theoretically, depending on the design used, RPCs
 1539 could reach a time resolution of the order of 10 ps but in the context of LHC where bunch crossing
 1540 happen every 25 ns, a time resolution of 1.5 ns is sufficient to accurately assign the right bunch
 1541 crossing to each detected muon.

1542 The 1056 RPCs equipping the CMS muon system both in the barrel and endcap regions and
 1543 covering the pseudorapidity region $0 < |\eta| < 1.6$ are composed of two layers of RPC *gaps* as
 1544 described in Figure 2.30. Each gap consists in two resistive electrodes made out of 2 mm thick
 1545 Bakelite enclosing a 2 mm thick gas volume containing a 95.2/4.5/0.3 mixture of C₂H₂F₄, i –
 1546 C₄H₁₀ and SF₆. Due to this geometry, the electric field inside of a gap is homogeneous and linear
 1547 at every point in the gas translating into a uniform development of avalanches in the gas volume as
 1548 soon as a passing muon ionises the gas. The two gaps sandwich a readout copper strip plane. A
 1549 negative voltage is applied on the outer electrodes, used as cathodes, and the inner electrodes, the
 1550 anodes, are simply connected to the ground as well as the readout panel that picks up the current
 1551 induced by the accumulated charge of the growing avalanches in one or both of the gas gaps. This
 1552 OR system allows for a lower gain (i.e. a lower electric field) on both gaps to reach the maximal
 1553 efficiency of such a detector.

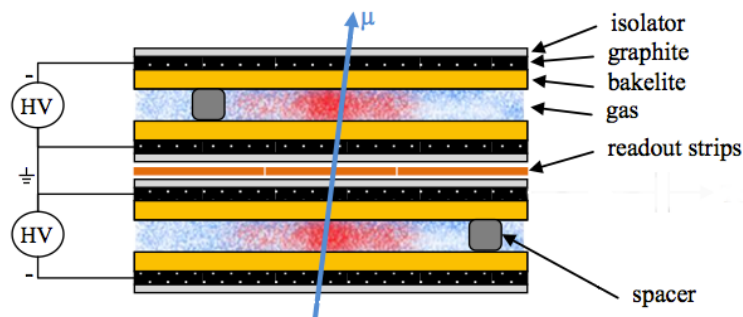


Figure 2.30: Double gap layout of CMS RPCs. Muons passing through the gas volumes will create electron-ion pairs by ionising the gas. this ionisation will immediately translate into a developing avalanche.

3

1554

1555

Muon Phase-II Upgrade

1556 The very first proton beam successfully circulated in the LHC in September 2008 directly followed
1557 by an incident leading to mechanical damage that would delay the LHC program for a year until
1558 November 2009, the very first collisions at a center-of-mass energy of 7 TeV taking place in March
1559 2010. The energy of the beam would be increased after a First Long Shutdown (LS1) starting
1560 early 2013 after less than 3 years of data taking. During the 2 years of shutdown, the upgrade of
1561 the accelerator allowed for several maintainances along the beam pipes, repair and consolidation
1562 of magnet connection and high-current splices. But not only the LHC was upgraded. Indeed, the
1563 experiments at the 4 collision points also took the advantage of this time to upgrade their system
1564 in prevision of the next LHC run (Run-II) until 2018 and the Second Long Shutdown (LS2) as
1565 the luminosity and energy of the beam would be continuously increasing. By the end of Run-
1566 II, the luminosity will have reached twice its nominal value when the center-of-mass energy has
1567 already got close to its nominal value by reaching an historical 13 TeV for the first time in 2017.
1568 The luminosity delivered by the collider will in the future be even further increased to improve its
1569 discovery potential giving no choice to experiments such as CMS to upgrade their technologies to
1570 cope with the increased radiation levels and detection rates.

1571 The next long shutdown will occur at the end of this year and will again be the occasion for sim-
1572 ilar maintenance and consolidation in prevision of Run-III and the future upgrade of LS3. Still, the
1573 main occupation of LS2 on LHC side will be the upgrade of LHC injectors. On the experiments side,
1574 LHCb and ALICE will, in a very tight schedule, implement major upgrades while ATLAS and CMS
1575 will wait until LS3 to upgrade their detectors in prevision of high luminosity *LHC-Phase-II*. ALICE
1576 main challenge is an upgrade of their apparatus to cope with the 50 kHz $Pb - Pb$ collisions. Simi-
1577 larly, LHCb will upgrade their frontend readout electronics to cope with the full 40 MHz collisions
1578 delivered by LHC. ATLAS will perform standard maintenance and CMS will focus on the urgent up-
1579 grade of the pixel detector and on the installation of new muon detectors in order to take profit of LS2
1580 time to mitigate the upgrade of detectors foreseen during LS3. Run-III will start in 2021 with the LHC
1581 at its nominal center-of-mass energy and will bring LHC-Phase-I to an end at the end of 2023. By
1582 then the luminosity will only increase to reach 2.5 times the nominal luminosity but during these 3

1583 years of run, the LHC will deliver as much integrated luminosity as what what brought during the al-
 1584 most 7 years of both Run-I and II of data taking. Phase-I will end with an overall 300 fb^{-1} delivered.
 1585

1586 3.1 Motivations for HL-LHC and the upgrade of CMS

1587 The first data taking period that took place until the start of LS1 and during which the LHC was
 1588 only operated at a center-of-mass energy of 7 TeV was sufficient to claim the discovery of a new
 1589 $125 \text{ GeV}/c^2$ particle compatible with the Higgs boson by both CMS and ATLAS in July 2012 and
 1590 hence achieve a major milestone in the history of science towards the understanding of the funda-
 1591 mental nature of the universe. Nevertheless, the LHC machine holds the potential to go further and
 1592 help unravel hte remaining misteries the high energy physics community is facing.

1593 Over its full lifetime, the HL-LHC is expected to deliver an outstanding integrated luminosity
 1594 of 3000 fb^{-1} leading, in the case of Higgs studies to measuring the couplings of the boson to a
 1595 precision of 2 to 5% thanks to the estimated 15 millions of Higgs created every year providing a
 1596 more precise measurement of potential deviations from the theoretical predictions and hence test its
 1597 properties with respect to the SM Higgs neutral boson. SUSY and heavy gauge boson studies would
 1598 also see their mass range limits pushed away by at least 1 TeV and could lead to a new breakthrough.
 1599 SUSY is a particularly important topic as it could give an answer to why the Higgs boson can stay so
 1600 light while coupled to heavy particles by introducing the contributions of the super partners on top
 1601 of providing dark matter candidates. Finally, the increase of luminosity will give the possibility to
 1602 investigate "exotic" mode like for example the models introducing extra dimensions to explain the
 1603 hierarchy problem.

1604 Many of these Standard Model extensions yield Heavy Stable Charged Particles (HSCPs), heavy
 1605 long-lived particles displaying a high momentum but a velocity significantly lower than the speed of
 1606 light [162–165] and/or a charge that differs from the elementary charge $\pm e$ [165–169]. Depending
 1607 on the model considered, Heavy Stable Charged Particles could be lepton-like heavy particles or on
 1608 the contrary R-hadron, particles composed of a supersymmetric particle and at least one quark. Due
 1609 to lifetimes of the order of a few ns HSCPs would travel for long enough distances to cross through
 1610 entire typical collider detectors while appearing almost stable but because of their slow velocity,
 1611 they can be reconstructed in different bunch crossings it reconstructed at all. Indeed, the trigger
 1612 algorithms in use at CMS were not designed for such slow particles and assume most particles of
 1613 interest will have a velocity close to the speed of light [165, 170]. As HSCPs are long-lived par-
 1614 ticles, their identification will be possible thanks to the muon system. The tracks associated to the
 1615 HSCPs would then be requested to be reconstructed in both the silicon detectors, for precise dE/dx
 1616 measurement, and the muon system detectors. In this case, the muon system will be used to per-
 1617 form Time-of-flight (ToF) measurements to discriminate between near spead-of-light particles and
 1618 slower ones. The full reconstruction will then look for useful signatures such as the large transverse
 1619 momentum of the candidates, their large ionisation energy loss alongside the low velocity accu-
 1620 rately measured thanks to the muon system. The main background will consist of wrongly measured
 1621 muons which should have a lower transverse momentum, a near to speed-of-light velocity and a low
 1622 ionisation energy loss. An example of passage of HSCPs through a slice of the CMS detector is
 1623 showed in Figure 3.1.

1624 The ToF measurement to identify beyond the Standard Model particles will mostly rely on the
 1625 time information provided by the Drift Tubes, in the barrel region of the detector, and Cathode Strip

1626 Chambers, in the endcaps. From CMS point of view it will then become necessary to increase the
 1627 acceptance and redundancy of the endcaps toward higher pseudo-rapidity. Moreover, the increased
 1628 background will become problematic in many ways and will force for upgrades or many sub-systems
 1629 of CMS.

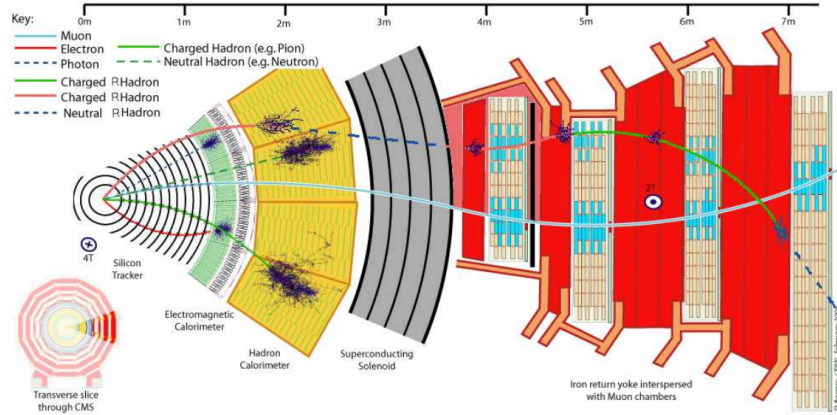


Figure 3.1: Slice of the CMS detector showing example of passage of SM particles and R-hadrons. On the one hand, lepton-like HSCPs will appear to behave like slow and heavy muons. On the other hand, R-hadrons are likely to convert into other kind of charged or neutral R-hadrons due to interactions inside the detector volume.

3.2 High Luminosity LHC and muon system requirements

1630 After approximately 15 years of operation, the LHC will undergo a new series of upgrade during
 1631 the LS3 in order to boost its discovery potential as showed in Figure 3.2. This moment onward is
 1632 what is referred to HL-LHC or Phase-II. The goal is to aim for a luminosity 5 to 7 times stronger
 1633 than the nominal one trying to reach even 10 times this value if possible. Increasing the luminosity
 1634 means that the beam size at the collision points needs to be reduced to boost the number of collisions
 1635 per bunch crossing. For this purpose, new focusing and bending magnets, and collimators will be
 1636 installed at the collision points as well as newly developed "crab cavities" that will tilt the particle
 1637 bunches just prior to the collisions by giving them transverse momentum and thus increasing their
 1638 meeting area. In addition, the full proton injection line will be upgraded.
 1639

1640 On the experiments side, the pile-up (PU) will be increased up to 150 to 200 interactions per
 1641 bunch crossing in ATLAS and CMS, making necessary a strong upgrade of the trigger system and
 1642 of the inner trackers and of the calorimeters. Both ATLAS and CMS will also need to upgrade
 1643 the muon trigger at the level of the endcaps mainly focusing on the coverage near the beam line in
 1644 order to increase the detection acceptance and event selection. Moreover, the increased luminosity
 1645 will also lead to an increased background rate and a faster ageing of the detectors. This PhD work
 1646 takes place into this very specific context of muon detector consolidation and certification for the
 1647 HL-LHC period in order to provide the CMS experiment with robust new detectors and confirm that
 1648 the present system will survive through the next 20 years of HL-LHC.

1649 The end of 2018 will mark the beginning of LS2 and the start of Phase-II upgrade activities.
 1650 From the HL-LHC period onwards, i.e. past LS3, the performance degradation due to integrated
 1651 radiation as well as the average number of inelastic collisions per bunch crossing, seen as pile-up
 1652 into the detectors' readout that far exceeds this of the original LHC plans, will rise substantially and

become a major challenge for all of the LHC experiments, like CMS, that were forced to address an upgrade program for Phase-II [171]. Dealing with the data from the muon detectors will force to upgrade the detectors and electronics towards the most recent technologies. Simultaneously, this will push new latency requirements onto the Level-1 trigger and the Data Acquisition (DAQ) that will only be fulfilled by upgrading the system with electronics having deeper buffering and faster processing. Simulations of the expected distribution of absorbed dose in the CMS detector under HL-LHC conditions show, in Figure 3.3, that detectors placed close to the beam line will have to withstand high irradiation, the radiation dose being of the order of a few tens of Gy.

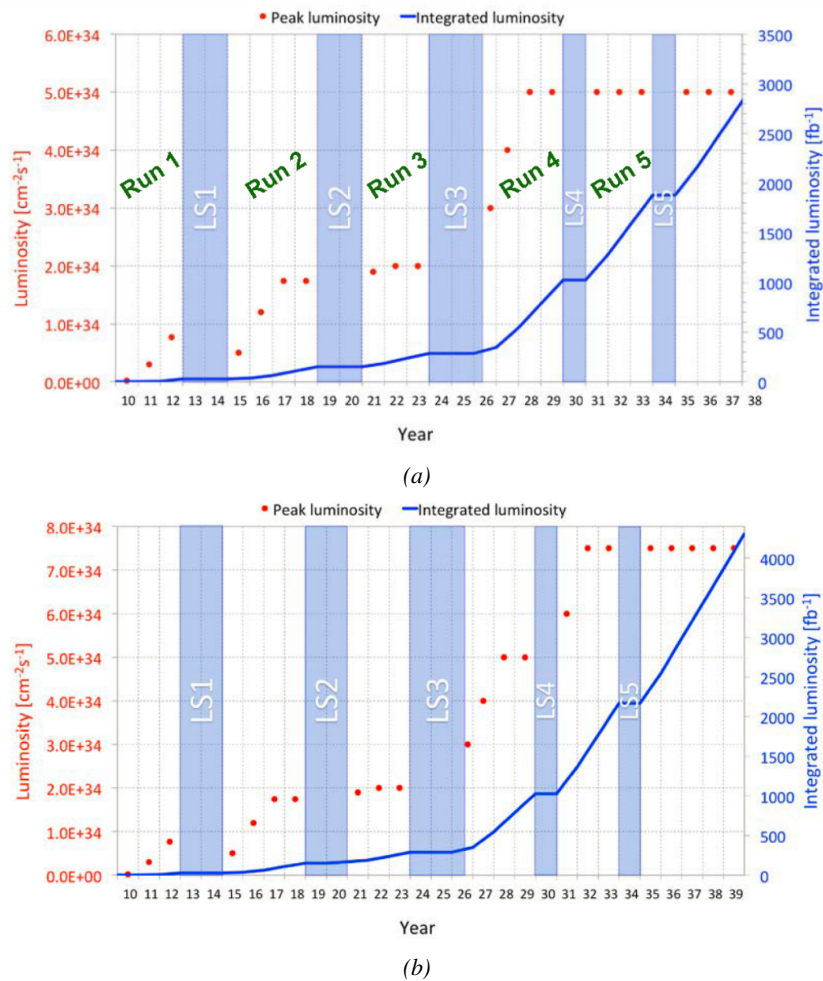


Figure 3.2: Detailed timeline projection of for LHC and HL-LHC operation until 2039 showing the evolution of the instantaneous and integrated luminosity as designed (Figure 3.2a) and in the ultimate case where the instantaneous luminosity is increased to $7.5 \times 10^{34} \text{ cm}^{-2}\text{s}^{-1}$ (Figure 3.2b) [160, 172].

The increase of irradiation close to the beam line will affect the background rate seen by the muon detectors in this area and tracking muons will prove to be difficult as this region is not yet equipped with all the detectors that were already foreseen for Phase-I. Improving this situation will come with the increase of hit numbers recorded along the particle track to reduce the ambiguity on

muon versus background detection. Moreover, the measurement of small production cross-section and/or decay branching ratio processes, such as the Higgs boson coupling to charge leptons, and in particular to muons, or the $B_s \rightarrow \mu^+ \mu^-$ decay, is of major interest and specific upgrades in the forward regions of the detector will be required to maximize the physics acceptance to the largest possible solid angle.

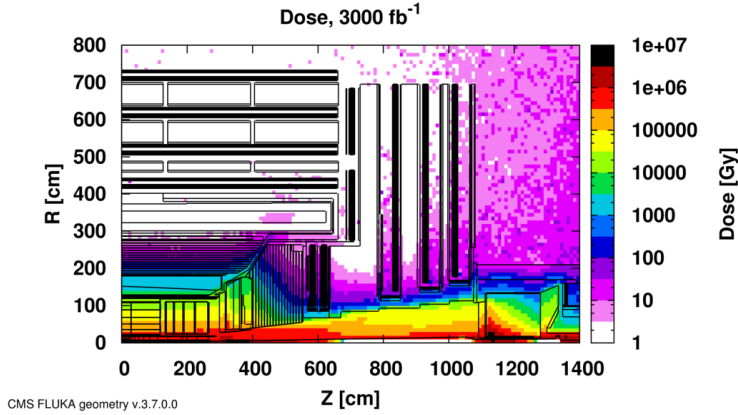


Figure 3.3: Absorbed dose in the CMS cavern after an integrated luminosity of 3000 fb. Using the interaction point as reference, R is the transverse distance from the beamline and Z is the distance along the beamline.

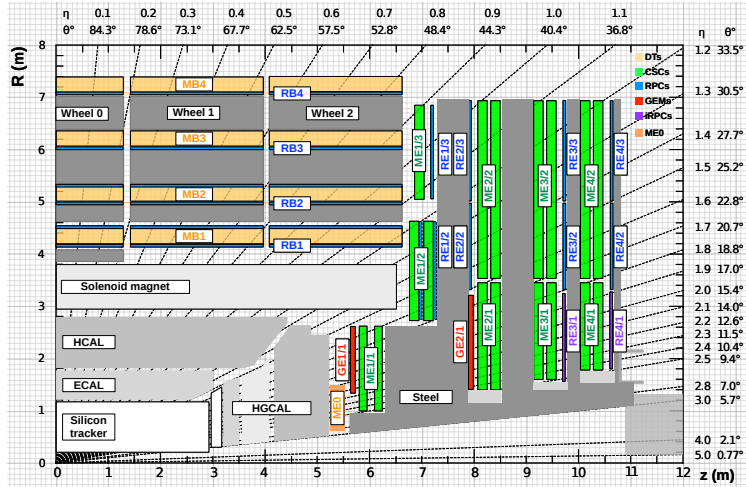


Figure 3.4: A quadrant of the muon system, showing DTs (yellow), RPCs (blue), and CSCs (green). The locations of new forward muon detectors for Phase-II are contained within the dashed box and indicated in red for GEM stations (ME0, GE1/I, and GE2/I) and dark blue for improved RPC (iRPC) stations (RE3/I and RE4/I).

To ensure proper trigger performance within the present coverage, the muon system will be completed with new chambers and the electronics of the present system will need to be upgraded to ensure an efficient triggering. Figure 3.4 shows the addition of Gas Electron Multiplier (GEM) and improved RPC (iRPC) in the pseudo-rapidity region $1.6 < |\eta| < 2.4$ to complete the redundancy of

the already existing CSCs as originally scheduled in the CMS Technical Proposal [173]. A first step into this direction will be taken by installing GEMs on the first endcap disk in position GE1/1 during LS2, during which preparations for the future installation of more GEMs and RPCs will take place by installing the needed services. During the YETS following LS2, iRPCs will be installed on the third and fourth endcap disks in position RE3/1 and RE4/1, and more GEMs will equip the second endcap in position GE2/1 and the inner layer, closest to the HCAL endcap called ME0 during LS3, finally completing the redundant coverage of the muon system and extending it a little by extending the reach to $|\eta| = 2.8$, the redundancy in the region $2.4 < |\eta| < 2.8$ being maintained by the 6 GEM layers contained in each ME0 detector that provide enough tracking points to efficiently reject neutron-induced background.

Nevertheless, the region beyond $|\eta| > 2.8$ and extending to $|\eta| = 5.0$ only is covered by the forward HCAL detectors and lack redundant muon detector coverage. Extensions of the tracker in the context of HL-LHC will increase its coverage up to $|\eta| = 4.0$ but the identification of muons and measurement of their energy with reasonable precision only using the tracker is nearly impossible. Thus, this increased tracker coverage range needs to be put in parallel with a matching muon detector and will open doors to multi-lepton final states in which leptons are likely to have a low transverse momentum and to be found near the beam line.

Finally, as the muon system is composed only of gaseous detectors, strong environmental concerns have risen over the last years as the European directives will restrict the use of fluorine based gas mixtures. Both the CSC and RPC subsystems, using CF_4 , $C_2H_2F_4$, or SF_6 , will need to adapt their working gas in order to strongly reduce the greenhouse potential of the mixtures released into the atmosphere due to gas leaks.

3.3 Necessity for improved electronics

Drift Tubes and Cathode Strip Chambers are important components used to identify and measure muons, especially thanks to their spatial resolution of the order of $100\ \mu m$. Nevertheless, the luminosity and irradiation during HL-LHC will cause serious event loss and ageing on the electronics of these subsystems that will comprise the triggering and data transferring needs of CMS. Thus, electronics upgrade are foreseen to address these expected problems. While only the RPCs' electronic system is able to operate under Phase-II requirements, DTs and CSCs will need to improve their trigger accept rate and latency to ensure that Level-1 trigger threshold stays at the same level [174], and DAQ data transfer rate, that respectively need to achieve a minimum of $500\ kHz$, get down to $12.5\ \mu s$ [175], and increase to $1082\ Gbit/s$ DTs and to $1026\ Gbit/s$ for CSCs. As of today, the Level-1 trigger accept rate of DTs doesn't reach $300\ kHz$ while this of CSCs is below $250\ kHz$ but the foreseen upgrades are expected to increase the rate way beyond the requirement in the of DTs and up to $4\ MHz$ for CSCs [171].

The first version of Minicrate electronics (MiC1) used by DTs don't allow for high enough trigger rate. In addition to this problem, it was showed that these electronics contain components that are not radiation hard enough to sustain HL-LHC conditions and thus, a too large number of channels may fail due to radiations. The MiC1 will be replaced on each detector by an improved version referred to as MiC2 while front-end electronics and high-voltage modules will not need any replacement. On the other hand, CSCs showed that there electronics would be able to live through the 10 years of Phase-II but the limited buffer depth might cause memory overflows and readout inefficiencies with a fraction of event loss ranging from 5 to more than 10% at an instantaneous

luminosity similar to which of HL-LHC depending on the expected background. Thus the replacement of CSCs' cathode front-end boards (CFEBs) by digital ones, DCFEBs, with deeper buffer would permit to make event loss negligible and satisfy HL-LHC requirements [171]. All these new DT and CSC electronics will be connected to the trigger electronics via optical links to ensure a faster communication.

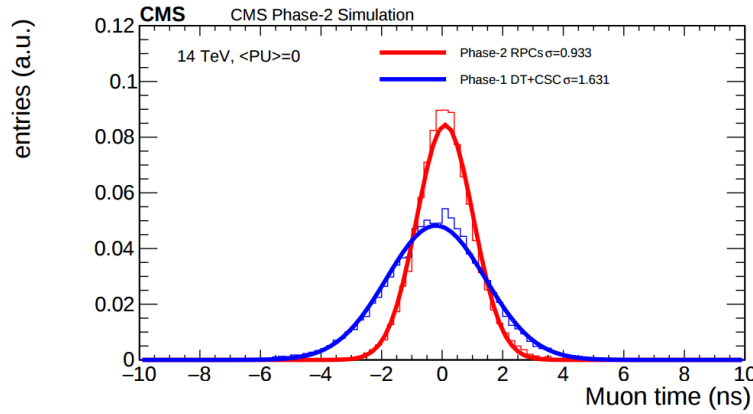


Figure 3.5: Comparison of the simulated time residuals in between reconstructed and true muon times without (blue) and with (red) the upgraded RPC link system.

The upgrade on the side of Resistive Plate Chambers will then not come from their on-board electronics but from the Link System located in the service cavern of CMS and that connects the front-end electronics data of RPCs into CMS trigger processors. The main motivation for such an upgrade is that the electronic board composing the link system are built using obsolete components and weak components that can easily suffer from the electromagnetic noise. These components may be the source of failing channels throughout Phase-II. Moreover, these link boards were originally designed only to match RPC digitized signals with the corresponding bunch crossing. Due to this feature, the time resolution of the full RPC chain is thus limited to 25 ns and does not exploit the full time resolution of the detectors. This would make the synchronization of the RPC system easier and allow to have a finer offline background removal within the 25 ns in between bunch crossings thanks to the order of magnitude gained in terms of time resolution.

Upgrading RPC link system will require the installation of 1376 new link boards and 216 control boards. The new boards will make use of the recent progress made with fast FPGAs and will be a great improvement to the ASICs formerly used as they will be able to process signals from several detectors in parallel. The benefit from using the full RPC time resolution thanks to the upgraded link system can be seen through Figure 3.5 where the resolution of the RPC system itself is better than which of DTs and CSCs that was used until now.

3.4 New detectors and increased acceptance

In the present muon system, the redundancy of was assured by RPCs used for their good timing performances. The extension of the muon system towards higher pseudo-rapidity in order to complete the redundancy in this very region and to contribute to the precision of muon momentum measurements will require muon chambers with a spatial resolution less or comparable to the contribution

¹⁷⁴⁴ muon of multiple scattering through the detector volume [161]. Most of the plausible physics is
¹⁷⁴⁵ covered only considering muons with $p_T < 100$ GeV hence, in order to match CMS requirements,
¹⁷⁴⁶ a spatial resolution of $\mathcal{O}(\text{few mm})$ will be necessary for the proposed new RPC stations while the
¹⁷⁴⁷ GEMs will need a resolution better than 1 mm, as showed by the simulation in Figure 3.6.

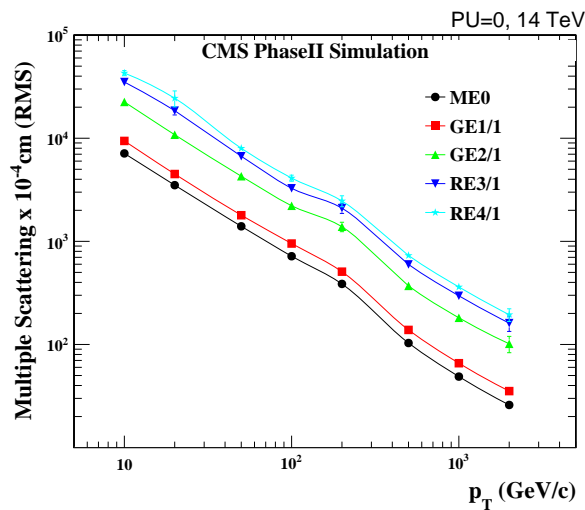


Figure 3.6: RMS of the multiple scattering displacement as a function of muon p_T for the proposed forward muon stations. All of the electromagnetic processes such as bremsstrahlung and magnetic field effect are included in the simulation.

¹⁷⁴⁸ 3.4.1 Gas electron multipliers

¹⁷⁴⁹ In the region closer to the interaction point where the spatial resolution is requested to be better
¹⁷⁵⁰ than 1 mm for the new detectors (at least for GE1/1 and ME0, GE2/1 being in the same order of
¹⁷⁵¹ requested spatial resolution than the new iRPCs that will equip the third and fourth endcaps), the
¹⁷⁵² choice has been made to use triple GEMs, micro pattern gaseous detectors, in the place of RPCs.
¹⁷⁵³ The GE1/1 project had been the first to be approved and demonstrators had been installed in CMS
¹⁷⁵⁴ already during LS1. The rest of the detectors will be installed during LS2 while the GE2/1 and ME0
¹⁷⁵⁵ projects are still under development. ME0, GE1/1 and GE2/1 will be installed respectively next to
¹⁷⁵⁶ the HCAL endcap, on the first and on the second muon endcap disks as can be seen from Figure 3.4.

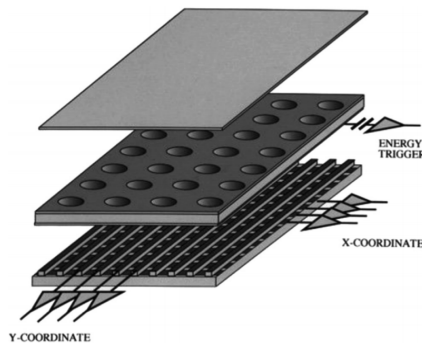


Figure 3.7: Schematics of a GEM showing the cathode on top, the GEM foil separating the gas volume into the drift region, in between the cathode and foil, and the induction region, in between the GEM foil and the anode, and the anode on which a 2D read-out is installed. A negative voltage is applied on the cathode while the anode is connected to the ground.

1757 Gas Electron multipliers are gaseous detectors [176] which gas volume is confined in between
 1758 2 planar electrodes, the anode serving as read-out panel. The gas volume is divided in 2 or more
 1759 regions by a single or multiple *GEM foils* as showed in Figure 3.7. These foils are very thin, of the
 1760 order of a few tens of μm , and are pierced with holes as can be seen in Figure 3.8. Both surfaces
 1761 of the GEM foils are clad with copper in order to apply a strong electric field in between each
 1762 side that will generate very strong potentials in the holes. The gas region contained in between
 1763 the cathode and the GEM foil is called the drift region as the electric field is not strong enough to
 1764 cause avalanches and thus start an amplification. The primary electrons drift toward the foil and are
 1765 accelerated and amplify by the very high potential within the holes, as showed in Figure 3.8. Then
 1766 the electrons reach the second drift region in which they will induce signal on the read-out located
 1767 on the anode. By restraining the amplification process at the level of the holes, the electrons can stay
 1768 in a very confined space and thus induce a very localized current, providing the GEMs with a very
 1769 good spatial resolution.

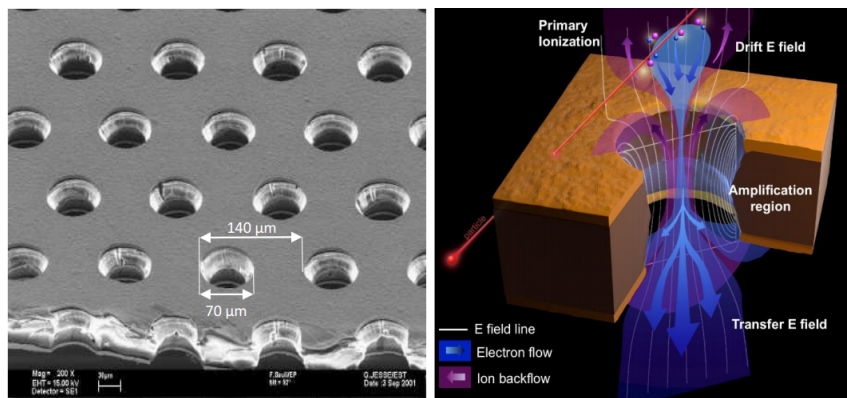


Figure 3.8: Left: Picture of a CMS GEM foil provided by a scanning electron microscope. Right: Representation of the electric field lines in a GEM hole and of the amplification that electrons and ions undergo in the hole's volume due to the very intense electric field.

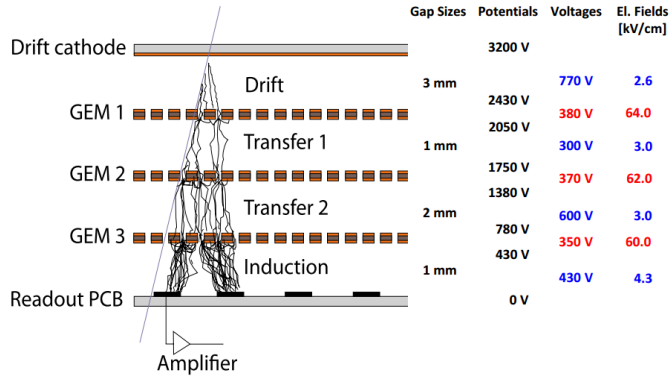


Figure 3.9: Schematic representation of CMS triple GEMs. The gas volume is divided into 4 areas. The drift area is the region where the primary electrons are created before being amplified a first time while passing through the first GEM foil. Then the process of drift and amplification is repeated twice in following two transfer areas and GEM foils. Finally, the charges have been amplified enough to induce current in the read-out strips while in the last drift area. The dimensions, potentials and electric fields are provided.

1770 In order to achieve a stronger amplification, the amplification process can be repeated several
 1771 times in a row. The GEMs that will be used in CMS are triple GEM detectors operated with a
 1772 70/30 gas mixture of Ar/CO₂. They contain 3 GEM foils and thus 3 electron amplifications, as
 1773 can be seen in Figure 3.9. The GEM foils used in CMS are 50 µm foils clad with 5 µm of copper
 1774 on each side. The foils are pierced with double-canonical holes which inner and outer diameters
 1775 are respectively 50 and 70 µm which are placed 140 µm from each other in an hexagonal pattern, as
 1776 showed in Figure 3.8. These detectors have a time resolution better than 10 ns and reach very good
 1777 spatial resolutions of less than 200 µrad as indeed the position of the hits is not measured along the
 1778 strips but following the azimuthal angle granularity of the radially organized trapezoidal strips.

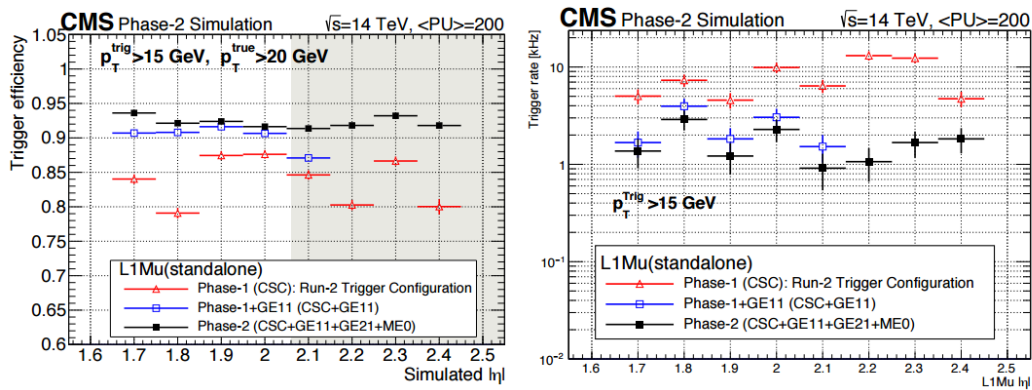


Figure 3.10: Simulated efficiency and rate of the standalone Level-1 muon trigger using tracks reconstructed in CSCs and all GEM stations compared with Phase-I values in the case where only CSCs are used or CSCs+GE1/I. The zones of inefficiency of the CSC subsystem are compensated by the addition of GEMs during Phase-II and the trigger rates is kept from increasing due to the high luminosity.

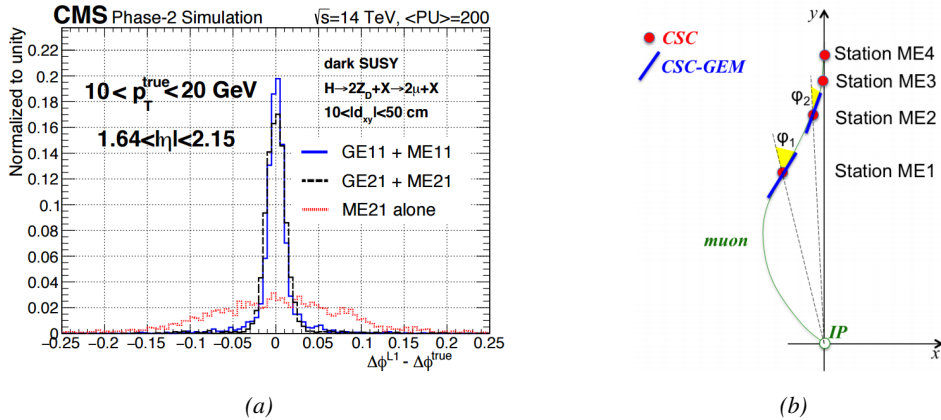


Figure 3.11: Figure 3.11a: Simulated resolution of the muon direction measurement $\Delta\phi$ with Phase-II conditions. In the second endcap station, the resolution is compared in the case of CSCs (ME2/1) alone and CSCs+GEMs (GE2/1+ME2/1) while a similar resolution measurement is given in the case of the first station (GE1/1+ME1/1). Figure 3.11b: The addition of GEM detectors on stations 1 and 2 (ME0 is considered to contribute to station station 1) as redundant system to CSCs allows to improve the muon momentum improvement through a more accurate measurement of the local bending angles ϕ_1 and ϕ_2 .

The GEM Upgrade is divided into 3 subsystems as GE1/1 was the first approved project [177] and that the detectors will already be installed during LS2. GE2/1 and ME0, on the other hand, will profit of the R&D knowledge and skills developed for GE1/1 while the requirements for each subsystem are different as they are not placed at the same distance from the interaction point. In this very forward region, a different position with respect to the center of the detector can change dramatically the conditions in which the detectors will have to be operated. In terms of rate capability, GE2/1, which is the furthest, is required to withstand 2.1 kHz/cm^2 while GE1/1 needs to be better than 10 kHz/cm^2 and ME0, better than 150 kHz/cm^2 . In terms of ageing with respect to charge deposition, ME0 needs to be certified to 840 mC/cm^2 , GE1/1 to 200 mC/cm^2 and GE2/1 only to 9 mC/cm^2 . All 3 detectors need to have a time resolution better than 10 ns and an angular resolution better than $500 \mu\text{rad}$.

On each GE1/1 ring, 36 super chambers, consisting of 2 single GEM layers and spanning 10° , will be installed covering the pseudo-rapidity region $1.6 < |\eta| < 2.2$ together with ME1/1 CSCs and the reach of the muon system will be improved thanks to the GE2/1 that will overlap with the GE1/1 and cover a region from $|\eta| > 1.6$ to $|\eta| < 2.4$ and complete the redundancy of ME2/1. The super chambers, built with 2 triple GEM layers each consisting of 4 single GEM modules due to the rather large surface of the GE2/1 chambers, that will be installed on the first ring of the second endcap will span 20° each, hence, a total of 72 chambers will be assembled to equip the muon system. Finally, the ME0 installed near the HCAL endcap will cover the region $2.0 < |\eta| < 2.8$ and this subsystem will consist in super modules of 6 layers of triple GEM detectors covering an azimuthal angle of 20° leading to the construction of 216 single detectors.

Adding the GEMs into the forward region of the muon system will allow to strongly enhance the Level-1 Trigger performance by reducing the inefficiency regions and the trigger rate as showed in Figure 3.10. Moreover, benefiting from the good spatial and angular resolution of the GEMs, the precision into the muon measurement will also be greatly improved by the addition of GEMs as can be seen from the simulation presented in Figure 3.11.

3.4.2 Improved forward resistive plate chambers

Figure 3.4 shows that the iRPCs that will equip the third and fourth endcap disks in position RE3/1 and RE4/1 will finally be the partners of the CSCs in position ME3/1 and ME4/1 and complete Phase-I plans but bringing the needed upgrades in the scope of Phase-II as the older chambers are not suitable to equip the forward region of CMS due to HL-LHC rates and charge deposition. By completing the redundancy, more track along the muon trajectory will be available and the lever arm will be improved. The benefits from extending the redundancy of the muon system with iRPCs to the forward most region is showed in Figure 3.12 in which the trigger efficiency is showed with and without RPCs in which it is possible to see that the efficiency of CMS trigger with the complete redundancy is improved is above 95% in the region $|\eta| > 1.8$ as the iRPCs help filling the holes in the CSC system.

The detectors that will be installed in the coming years will be similar to the already existing RPC system. 18 of the new chambers, each spanning 20° in φ around the beam axis with 96 radially oriented trapezoidal read-out strips, will cover each muon endcap disk leading to the production of 72 iRPCs. The main difference with the old RPC chambers is that these detectors will not have readout strips segmented in η as by using fast front-end electronics the strips will be read-out on both sides allowing for a radial spatial resolution of the order of 2 cm in order to contribute to the better reconstruction of muon in the forward region where the bending of muons by the magnetic field is low. This is motivated by the fact that, in the case a η segmentation was used, at least 5 pseudorapidity partitions would have been necessary to reach the minimal radial spatial resolution (≈ 20 cm). Having only one strip read-out from both along the chamber reduces by 60% the total number of channels and the necessary cabling and allows for a better spatial resolution. The strip pitch will range from 6.0 mm (5.9 mm) on the high pseudo-rapidity end to 12.3 mm (10.9 mm) on the low one on position RE3/1 (RE4/1). The spatial resolution in the direction perpendicular to the strips should reach approximately 3 mm, better than the minimal needed resolution (Figure 3.6), and the overall time resolution of the new installation will be equally 1.5 ns, as for the present due to the same link system being used.

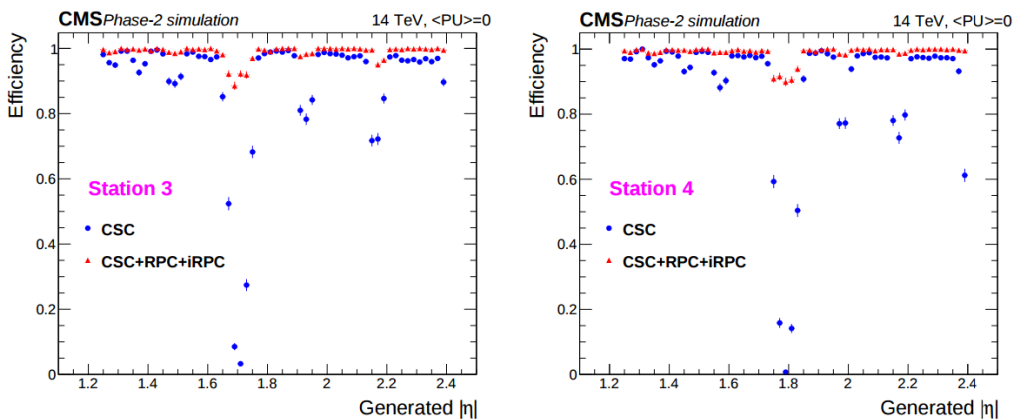


Figure 3.12: Simulation of the impact of RPC hit inclusion onto the local trigger primitive efficiency in station 3 (left) and station 4 (right). The contribution of iRPC starts above $|\eta| = 1.8$.

Nevertheless, having only a single strip instead of pseudo-rapidity segmentation will increase

the probability of double hits in the same channel. This probability was estimated to be low enough as it shouldn't exceed 0.7%. This estimation was made assuming an average hit rate per unit area of 600 Hz/cm^2 in the iRPCs (see Figure 3.13), a cluster size (average number of strips fired per muon) of 2, a strip active area of $158.4 \times 0.87 \text{ cm}^2$ and a safety factor 3 leading to an estimated rate per strip of 380 kHz corresponding to an average time interval of 2600 ns in between 2 consecutive hits. The time for a signal to go through the full strip length is about 10 ns to which can be added 1 ns of dead time and 2 TDC clock cycles of 2.5 ns for a minimal time interval of 16 ns necessary to avoid ambiguities. The probability of having ambiguous double hits in a strip in then the ratio in between this minimal time interval in between 2 consecutive hits and the average time interval estimated from the rate the detectors are subjected to.

The instantaneous luminosity at HL-LHC being very high, the rates at the level of the new chambers needed to be simulated in order to understand the necessary requirements for these detectors. The simulated results for different background components (neutrons, photons, electrons and positrons) are showed in Figure 3.13 assuming known sensitivities to these particles. It is showed that on average over the iRPC areas the rates would be of the order of 600 Hz/cm^2 (600 Hz/cm^2 seen in RE3/1 and 480 Hz/cm^2 in RE4/1) [178]. Thus, taking into account a safety factor of about 3, it was decided that improved RPCs should at least be certified for rates reaching 2 kHz/cm^2 which would be achieved thanks to several improvements on the design and on the electronics. The detectors design will be based on the existing RPC design as they will be double gaps. Similarly to the existing RPC system, the electrode material will be HPL although the thickness of the electrodes and of the gas gap will be reduced to 1.4 mm as a thinner gas gap leads to a decrease of deposited charge per avalanche as showed in Figure 3.14. The smaller the gas gap, the more the detector becomes sensitive to gap non-uniformities across the electrode planes making a gap of 1.4 mm a good compromise in between these two competing factors.

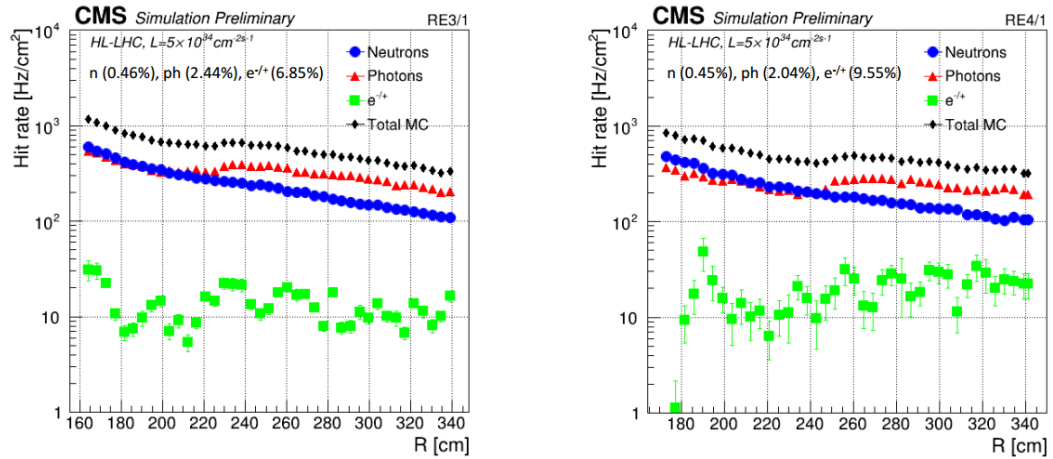


Figure 3.13: Expected hit rate due to neutrons, photons, electrons and positrons at HL-HLC instantaneou... luminosity of $5 \times 10^{34} \text{ cm}^{-2}\text{s}^{-1}$ in RE3/1 and RE4/1 chambers. The sensitivities of iRPCs used in the simulation for each particle are reported and differ from one endcap disk to another as the energies of the considered particles varies with the increasing distance from the interaction point.

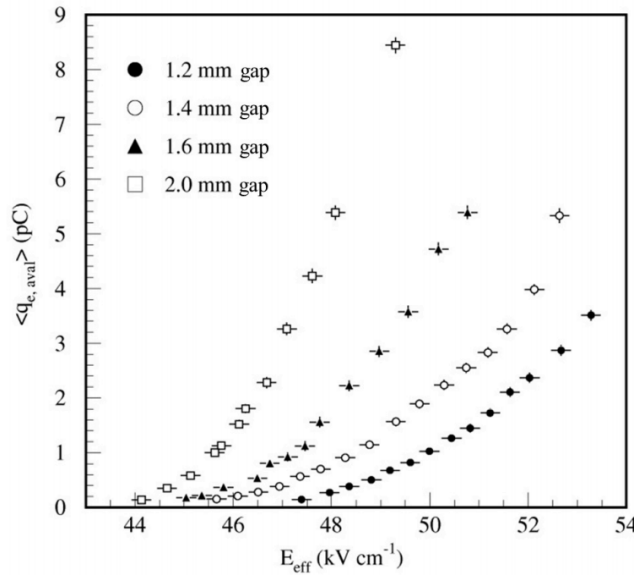


Figure 3.14: Measured average charge per avalanche as a function of the effective electric field for different gas gap thickness in double gap RPCs using HPL electrodes.

1857 A lower charge deposition inside of the detector volume means a slower ageing and a longer
 1858 lifetime for detectors subjected to high irradiation. But, in order to take advantage of the lower
 1859 detector gain, more sensitive electronics are required so that the part of gain that was formerly done
 1860 in the gas volume can be moved to the electronics. Achieving this with the technology developed
 1861 more than 10 years ago for the present system is not possible as the signal over noise ratio of such
 1862 electronics doesn't allow to detect charges as low as 10 fC. Moreover, the new front-end electronics
 1863 will need to be radiation hard to survive to more than 10 years of HL-LHC conditions. The new
 1864 technology that has been chosen is based on the PETIROC ASIC manufactured by OMEGA and is
 1865 a 64-channel ASIC called CMS RPCROC. The properties of these electronics will be discussed in
 1866 Chapter 6.

1867 3.4.3 Installation schedule

1868 The previous discussion on the different upgrade projects makes it clear that a lot of work is scheduled
 1869 for CMS to be ready at the end of LS3 for HL-LHC. Conducting all the upgrades of the muon system
 1870 together with upgrades of the other subsystems like the replacement of the Tracker and of part of the
 1871 ECAL, will prove to be very difficult as the opening of CMS to access the Barrel will be done by
 1872 fully opening the endcaps leaving only the first disk to be accessible. Thus, most subsystems have
 1873 planned early installation over LS2, and the following YETS until LS3 in order to give more space to
 1874 LS3 schedule.

1875 First of all, LS2 will see the installation of GE1/1 detectors, all the on-detector schedule of CSCs
 1876 and the installation of the necessary services for the improved RPCs to be installed later, such as
 1877 the HV and LV power supply lines, the gas and cooling lines or signal cables. CSCs will have a
 1878 huge work to do during LS2 as they will need to extract all of their detectors to refurbish them with
 1879 upgraded DCFEB and ALCT mezzanine boards. The GE1/1 services were installed during LS1

1880 together with a few demonstrator and only the detectors needs to be integrated into the first endcap
 1881 disk. The detectors are presently being built and tested at the different assembly site to prepare for a
 1882 smooth LS2 work.

1883 The work of GEMs will be continued during the following YETS during which is planned the
 1884 installation of the GE2/1 stations to only leave the ME0 to be installed during LS3. The iRPC
 1885 program will follow a similar path as the new detectors will be installed during the YETS preceding
 1886 LS3 in prevision of the fact that the endcap disks will not be accessible during LS3. This way, all the
 1887 subsystems, but DTs, made great effort on planing their installation and integration within CMS only
 1888 to have to deal with off-detector issues during the LS3 period, such as the replacement of ODMBs
 1889 and HV system in the case of CSCs or the upgrade of the RPC Link System. Finally, during LS3
 1890 are schedules the replacement of DT minicrates electronics and the installation and integration of
 1891 ME0 GEMs together with the HGCAL.

1892 3.5 Implications of the different upgrades on the Level-1 Trigger. 1893 Improvement of physics performance.

1894 The upgrades of the different subsystems will have a subsequent impact on the Level-1 Trigger.
 1895 Indeed, although its main scheme will not be affected, the efficiency of the trigger in efficiency
 1896 identifying muons and provide the DAQ with good and fast trigger that can cope with HL-LHC
 1897 instantaneous luminosity is a major improvement. In addition to the upgrade of the muon system in
 1898 terms of trigger accept rate and latency, the Level-1 Trigger will get extra information in including
 1899 the Tracker Trigger into its Muon Track Finder logic and combine the L1 Muon Trigger with Tracker
 1900 and Calorimeter Triggers to generate a Global L1 Trigger with a much better momentum resolution,
 1901 as showed in Figure 3.15.

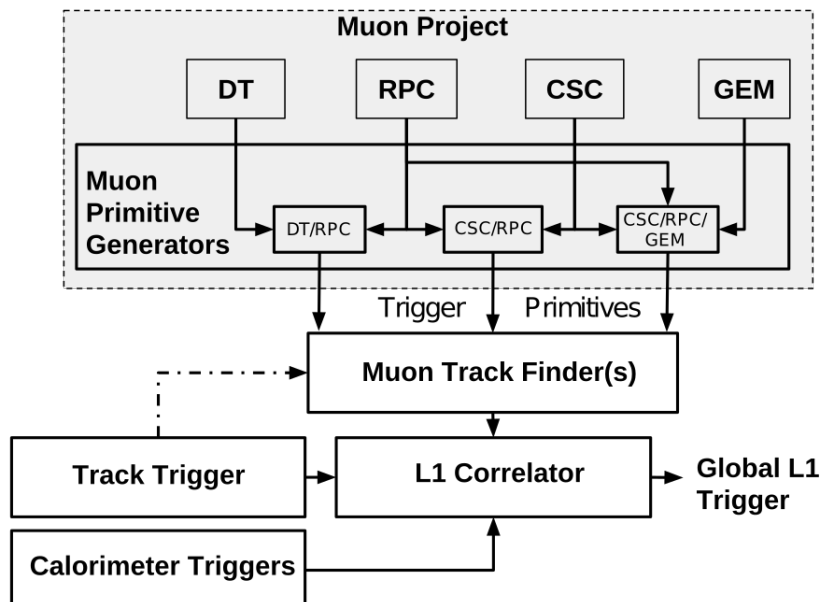


Figure 3.15: Data flow of the Level-1 Trigger during Phase-II operations.

In terms of muon trigger, 3 regions are considered due to their different track finding logic: the Barrel Muon Track Finder (BMTF), the Endcap Muon Track Finder (EMTF) for both the barrel and endcap regions, and finally the Overlap Muon Track Finder (OMTF) which concerns the pseudo-rapidity region in which there is a common coverage by both the barrel and endcap muon systems. This region can be seen in Figure 3.4 for $0.9 < |\eta| < 1.2$ and requires a specific more complex logic to provide with an efficient reconstruction of the muons due to the different orientation of the detectors and of the more complex magnetic field of this region that needs to be taken into account. The benefits of the upgrade for each of these track finders will be coming from different improvements and will be detailed sector by sector.

The main contribution to the improvement of the BMTF is the time resolution improvement of RPC link systems that will allow to take profit of the full 1.5 ns resolution of the detectors. From the perspective of RPCs only, this improvement will help reducing the neutron induced background and slightly improve the bunch crossing assignment. The upgrade of DT electronics is also to take into account as the trigger primitive generator will be renewed through the use of TDCs that will send the digitized signals directly to the back-end electronics instead of having an on-detector trigger logic as it will be the case until the end of Phase-I. The front data of both DTs and RPCs will be sent to the same back-end electronics. These upgrades were detailed in section 3.3 and will lead to a more robust operation of the trigger in the barrel region. Indeed, the combination of RPC hits together with DT primitives will bring improvement in the bunch crossing assignment and improve the efficiency of the trigger in between the wheels were the quality of DT primitives is the poorest. Moreover, having a redundant information is important in the case of failure and loss of efficiency of one of either subsystems.

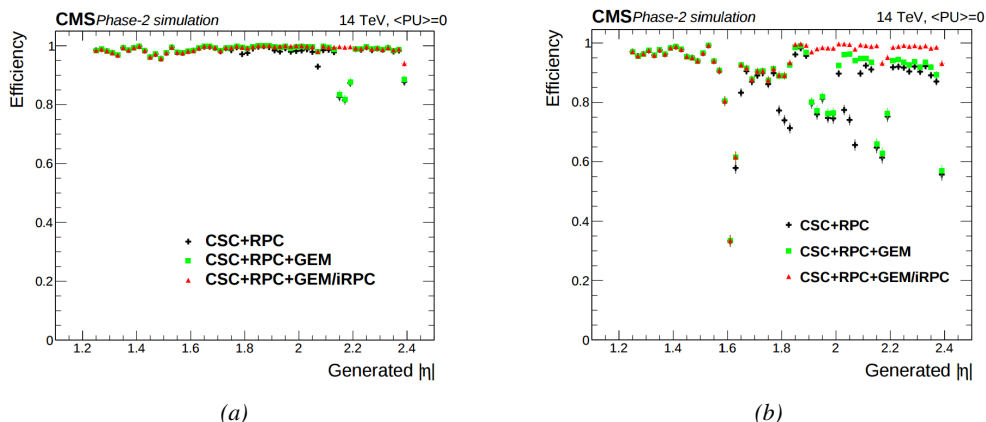


Figure 3.16: Efficiency of the L1 trigger in the endcap region after Phase-II upgrade in the case CSC/GEM/RPC hits are requested in at least 2 stations out of four (3.16a) and in all four stations (3.16b).

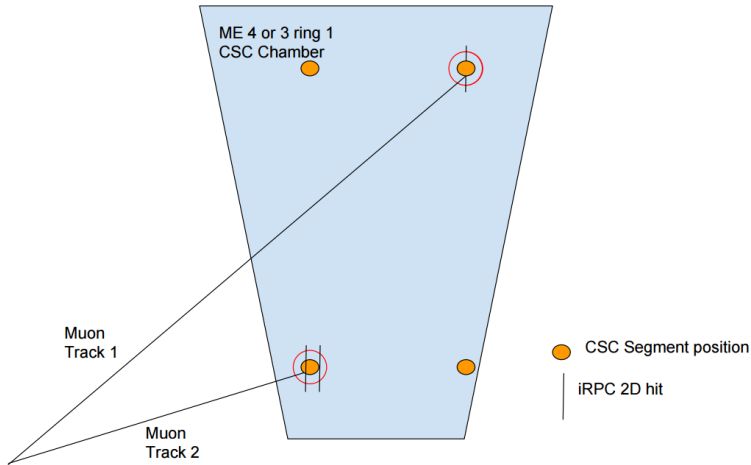


Figure 3.17: Resolution of the LCT ambiguous events thanks to the combination of CSC and iRPC readout data. Using CSCs only, 2 pairs of hits are possible.

With new detectors to cover the very forward region and the upgrade of RPC Link System, the EMTF will be greatly improved. The current EMTF already use more sophisticated algorithms by combining together RPC hits and CSC primitives and will also benefit from the improved time resolution of the RPC system. The GEMs, in stations 1 and 2, and the iRPCs, in stations 3 and 4, will be added into the EMTF algorithm. Both these contributions will help increasing the efficiency of the L1 trigger in the endcap region in one hand, as showed by Figure 3.16, and help lowering the L1 trigger rate in the other hand, especially in the most forward region. The improvement of the efficiency will come both from the better time resolution of RPC link boards and from the addition of more hits along the muon tracks and also a contribution from the GEMs to the lever arm of each track thanks to their high angular resolution.

The rate will be partly reduced in the forward region thanks to the better spatial resolution of iRPCs, with respect to the current RPC system, that will reduce the ambiguity brought by multiple local charged tracks in CSCs, as explained through Figure 3.17. Indeed, as the rates will increase, the probability to record more than a single local charged track will greatly increase. This is due to the fact that the trigger algorithm uses information from 3 consecutive bunch crossings to find muon tracks. It is estimated that with iRPCs operated at 95% efficiency the resolution of ambiguous events would be of the order of 99.7%.

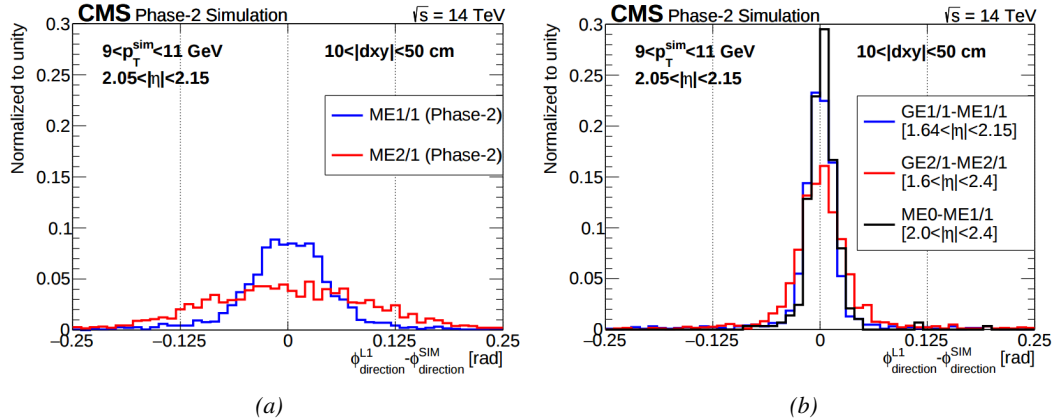


Figure 3.18: The angular resolution on reconstructed muon tracks in the GEM overlap region $2.0 < |\eta| < 2.15$ is compared for Phase-II conditions in the case CSC are alone (Figure 3.18a) and in the case the GEMs' data, including MEO, is combined to which of CSCs (Figure 3.18b).

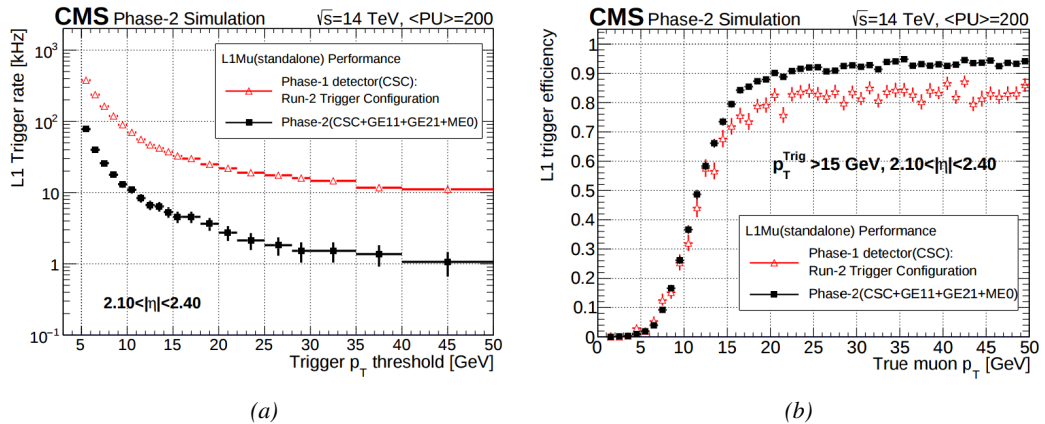


Figure 3.19: Comparison of L1 trigger performances for prompt muons with and without the addition of GEMs in the region $2.1 < |\eta| < 2.4$ at Phase-II conditions. GEMs would allow a reduction of the trigger accept rate by an order of magnitude (Figure 3.19a) while increasing the trigger efficiency (Figure 3.19b).

The addition of GEMs will improve greatly the measured muon momentum resolution by improving the global resolution of the direction of muon tracks, as can be seen in Figure 3.18, which will contribute to lowering the trigger rate and increase the efficiency, as can be seen from Figure 3.19 that focuses especially in the most challenging pseudo-rapidity region. Data from both CSCs and GEMs are combined into the OTMB to build on each station, GEM/CSC primitives matching space and time information from both subsystems.

Finally, the development of a track finder specific to the overlap region was already achieved during the Phase-I upgrade of the L1-Trigger [179]. Nevertheless, the improvements of DT spatial resolution and RPC timing will be carried and implemented into the OMTF.

1950 3.6 Ecofriendly gas studies

1951 Future strict restrictions in the use of certain gases will affect the gaseous detectors of several exper-
 1952 iment, including CMS. The European Commission adopted a new "F-gas regulation" in 2014 [180]
 1953 with the goal to strongly control and reduce the use of fluorinated gases with high Global Warm-
 1954 ing Potential (GWP). Using CF_4 , $C_2H_2F_4$ and SF_6 , both CSC and RPC subsystems will need to
 1955 address this problem by finding new gas mixture for the operation of their detectors. Finding a re-
 1956 placement for these gas component that were used for very specific reasons will be a great challenge.
 1957 Indeed, CSCs use CF_4 in order to enhance the longevity of the detectors, increase the drift velocity
 1958 of electrons and quench photons with a non-flammable gas mixture. RPCs use a mixture mainly
 1959 composed of $C_2H_2F_4$, or $R134a$, that features a high effective Townsend coefficient and the great
 1960 average fast charge allowing for operations with a high threshold, and contains a small fraction of
 1961 SF_6 that is used for its electronegative properties that prevents the development of delta-rays in the
 1962 gas volume that might trigger multiple ionization and avalanches.

	CSC	RPC
Greenhouse gases used	CF_4	$C_2H_2F_4$ and SF_6
Greenhouse gases fraction in the gas mixture	10%	95.2% and 0.3%
Global Warming Potential (relative to CO_2)	6500	1300 and 23900
Gas mixture re-circulation	Yes, 90%	Yes, 85%
Gas mixture replenishing rate (l/hr)	700	1100
F-gas recuperation	Yes, $\approx 40\%$	No
F-gas venting rate (l/hr)	42	1047 and 3.3
CO_2 -equivalent rate (m^3/h)	273	1440
Relative impact (entire muon system = 100%)	16%	84%

Table 3.1: Details of the greenhouse fluorinated gases used in CMS and of their GWP [171].

1963 Nevertheless, all these gases have a very high GWP, as reported in Table 3.1, and only few options
 1964 are left. The subsystems need to work on strongly decrease the loss of these gases due to leaks in the
 1965 gas system or completely change their gas mixture for more ecofriendly ones. Reducing the amount
 1966 of F-gas released in the atmosphere due to leaks on the current gas system will require installation
 1967 of a F-gas recuperation system on RPCs side and an upgrade of CSCs existing one in addition to
 1968 the repair of existing leaks. With such measures, it is expected that the total rate of greenhouses
 1969 gas vented in the atmosphere would represent only 1.6% of the current levels [171]. In the most
 1970 critical case the F-gas were to be banned, it would be necessary to have replacement mixtures to
 1971 operate CMS. CSC is presently investigating replacement for CF_4 such as CF_3I , C_4F_6 , IC_3F_6 ,
 1972 C_3F_8 or CHF_3 while RPCs, in collaboration with the ATLAS RPC group which uses the same gas
 1973 mixture and, hence, faces similar restrictions, have identified CF_3I ($GWP \leq 1$) and $C_3H_2F_4$ (GWP
 1974 ≤ 1), referred to as HFO-1234ze, as potential candidates with mixtures containing CO_2 but more
 1975 R&D needs to be conducted for both subsystems before concluding on the best alternative. No good
 1976 alternative to the present mixtures will require very efficient abatement system in CMS to burn and
 1977 convert the greenhouse gases into less harmful ones. This way, the air pollution would be strongly
 1978 reduced.

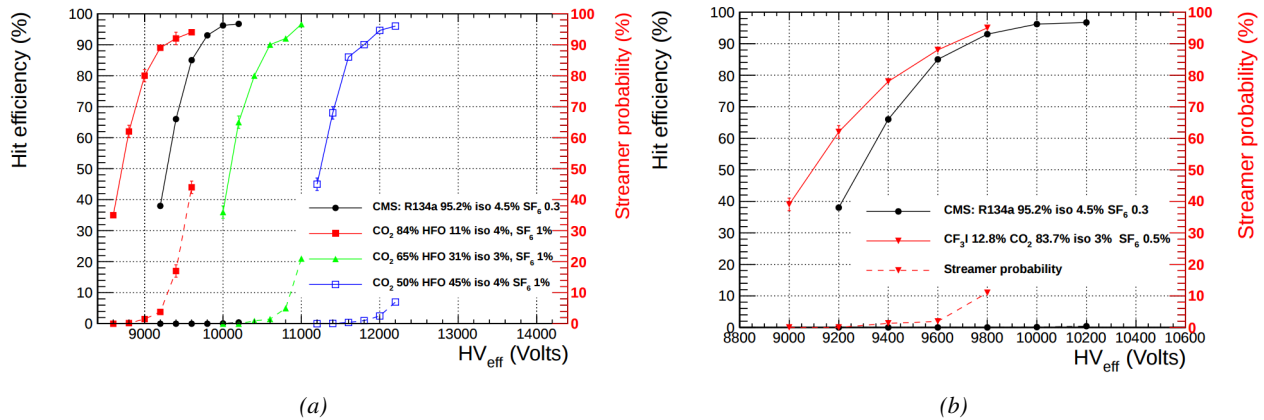


Figure 3.20: The efficiency (solid lines) and streamer probability (dashed lines) of HFO/CO₂ (Figure 3.20a) and CF₃I/CO₂ (Figure 3.20b) based gas mixtures as a function of the effective high-voltage are compared with the present CMS RPC gas mixture represented in black. The detector used for the study is a single gap RPC with similar properties than CMS RPCs. The streamer probability is defined as the proportion of events with a deposited charge greater than 20 pC.

1979 The status of RPC studies are presented in Figure 3.20 in which the performance (efficiency
 1980 and streamer probability) of an RPC operated with alternative gas mixtures is compared to the
 1981 present CMS RPC mixture. Although the efficiency of detectors operated with mixtures containing
 1982 CO₂/CF₃I or CO₂/HFO as a replacement for C₂H₂F₄ seem to reach similar levels than which of
 1983 the detectors operated with the present mixture, the new gas mixtures feature a streamer probability
 1984 (probability to have very large avalanches whose induced charge is greater than 20 pC) that far ex-
 1985 ceeds which of the present fluorinated mixture. The SF₆, being a component of the mixture added
 1986 in order to reduce the probability of large avalanches thanks to its electronegativity, doesn't seem
 1987 to prevent streamers as efficiently even when used at levels more than 3 times higher than with the
 1988 standard CMS RPC mixture. Nevertheless, it is important to note that these results were obtained
 1989 with a single gap RPC while the use of a double gap RPC would reduce the operation voltage by 200
 1990 to 300 V, lowering the induced charge. A compromise in between good efficiency and acceptable
 1991 level of streamer probability and the fine tuned composition of potential replacement gas mixtures
 1992 will be studied using a standard double-gap CMS RPC.

4

1993

1994

Physics of Resistive plate chambers

1995 A Resistive Plate Chamber (RPC) is a gaseous detector used in high-energy physics experiments
1996 as described in Chapter 3. It has been developed in 1981 by Santonico and Cardarelli [181], under
1997 the name of *Resistive Plate Counter*, as an alternative to the local-discharge spark counters pro-
1998 posed in 1978 by Pestov and Fedotovich [182, 183]. Working with spark chambers implied using
1999 high-pressure gas and high mechanical precision which the RPC simplified by formerly using a gas
2000 mixture of argon and butane flowed at atmospheric pressure and a constant and uniform electric
2001 field propagated in between two parallel electrode plates. Moreover, a significant increase in rate
2002 capability was introduced by the use of electrode plate material with high bulk resistivity, preventing
2003 the discharge from growing throughout the whole gas gap. Indeed, the effect of using resistive elec-
2004 trodes is that the constant electric field is locally canceled out by the development of the discharge,
2005 limiting its growth.

2006 Through its development history, different operating modes [184–186], gas mixtures [181, 186–
2007 191] and new detector designs [192–194] have been discovered, leading to further improvement of
2008 the rate capability of such a detector. The low developing costs and easily achievable large detection
2009 areas offered by RPCs, as well as the wide range of possible designs, made them a natural choice
2010 to as muon chambers and/or trigger detectors in multipurpose experiments such as CMS [161] or
2011 ATLAS [195], time-of-flight detectors in ALICE [196], calorimeter with CALICE [197] or even
2012 detectors for volcanic muography with ToMuVol [198].

2013 4.1 Principle

2014 RPCs are ionisation detectors composed of two parallel resistive plate electrodes in between which
2015 a constant electric field is set. The space in between the electrodes, referred to as *gap*, is filled with
2016 a dense gas that is used to generate primary ionization into the gas volume. The free charge carriers
2017 (electrons and cations) created by the ionization of the gas molecules are then accelerated towards the
2018 electrodes by the electric field, as shown in Figure 4.1 [199]. RPCs being passive detectors, a current
2019 on pick-up copper read-out placed outside of the gas volume is induced by the charge accumulation

2020 during the growth of the avalanche resulting from the acceleration of the charge carriers. As a
 2021 consequence, the time resolution of the detector is substantially increased as the output signal is
 2022 generated while the electrons are still in movement. The advantage of a constant electric field, over
 2023 multi-wire proportional chambers, is that the electrons are being fully accelerated from the moment
 2024 charge carriers are freed and feel the full strength of the electric field that doesn't depend on the
 2025 distance to the readout and that the output signal doesn't need for the electrons to be physically
 2026 collected.

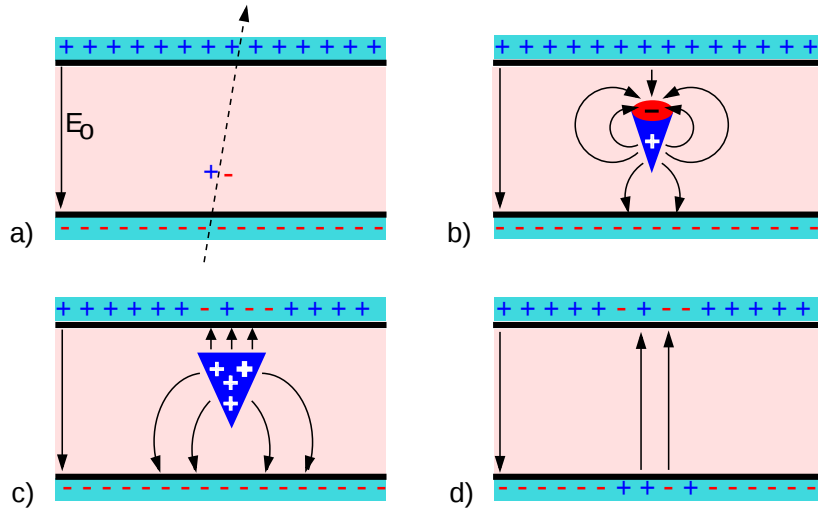


Figure 4.1: Different phases of the avalanche development in the RPC gas volume subjected to a constant electric field E_0 . a) An avalanche is initiated by the primary ionisation caused by the passage of a charged particle through the gas volume. b) Due to its growing size, the avalanche starts to locally influence the electric field. c) The electrons, lighter than the cations reach the anode first. d) The ions reach the cathode. While the charges have not recombined, the electric field in the small region around the avalanche stays affected and locally blinds the detector.

2027 After an avalanche developed in the gas, a time long compared to the development of a discharge
 2028 is needed to recombine the charge carriers in the electrode material due to their resistivity. This
 2029 property has the advantage of affecting the local electric field and avoiding sparks in the detector
 2030 but, on the other hand, the rate capability is intrinsically limited by the time constant τ_{RPC} of the
 2031 detector. Using a quasi-static approximation of Maxwell's equations for weakly conducting media,
 2032 it can be shown that the time constant τ_{RPC} necessary to the charge recombination at the interface
 2033 in between the electrode and the gas volume is given by the Formula 4.1 [200].

$$(4.1) \quad \tau_{RPC} = \frac{\epsilon_{electrode} + \epsilon_{gas}}{\sigma_{electrode} + \sigma_{gas}}$$

2034 A gas can be assimilated to vacuum, leading to $\epsilon_{gas} = \epsilon_0$ and $\sigma_{gas} = 0$, and the electrodes
 2035 permittivity and conductivity can be written as $\epsilon_{electrode} = \epsilon_r \epsilon_0$ and $\sigma_{electrode} = 1/\rho_{electrode}$,
 2036 showing the strong dependence of the time constant to the electrodes resistivity in Formula 4.2.

$$(4.2) \quad \tau_{RPC} = (\epsilon_r + 1)\epsilon_0 \times \rho_{electrode}$$

Very few materials with a low enough resistivity exist in nature. The resistivity targeted to build RPCs ranges from 10^9 to $10^{12} \Omega \cdot \text{cm}$. The most common RPC electrode materials are displayed in Table 4.1. When the doped glass and ceramics can offer short time constants of the order of 1 ms, the developing cost of such materials is quite high due to the very low demand. Thus, High-pressure laminate (HPL) is often the choice for high rate experiments using very large RPC detection areas. Other experiments working at cosmic muon fluxes can safely operate with ordinary float glass.

Material	$\rho_{\text{electrode}} (\Omega \cdot \text{cm})$	ϵ_r	$\tau_{\text{RPC}} (\text{ms})$
Float glass	10^{12}	~ 7	~ 700
High-pressure laminate	10^{10} to 10^{12}	~ 6	~ 6 to 600
Doped glass (LR S)	10^9 to 10^{11}	~ 10	~ 1 to 100
Doped ceramics (SiN/SiC)	10^9	~ 8.5	~ 1
Doped ceramics (Ferrite)	10^8 to 10^{12}	~ 20	~ 0.2 to 2000

Table 4.1: Properties of the most used electrode materials for RPCs.

4.2 Rate capability and time resolution of Resistive Plate Chambers

The electrode material plays a key role in the maximum intrinsic rate capability of RPCs. R&D is continuously being done to develop at always cheaper costs material with lower resistivity. Nevertheless, the amount of charge released, i.e. the size of the discharge, if reduced leads to a smaller blind area in the detector, increasing the rate capability of the detector. On the other hand, the drift velocity of electrons in the gas volume being quite stable with the applied electric field, the design of a detector and the associated read-out and pulse-processing electronics will be a major component of the time resolution of RPCs. Moreover, the sensitivity of the electronics will also help increasing the rate capability by lowering the gain the gas volume needs to be operated at, increasingly lowering the gas volume in which the signals will develop.

4.2.1 Operation modes

Being a gaseous detector using an accelerating electric field to amplify the signal of primary charge carriers, the RPC can be operated into different modes as the electric field intensity varies. Each mode offers different performances for such a detector, and it will be showed that the operating mode corresponding to the lowest electric field possible is best suited for high rate detectors working in collider experiments.

RPCs where developed early 1980s. At that time it was using an operating mode now referred to as *streamer mode*. Streamers are large discharges that develop in between the 2 electrodes enough to locally discharge the electrodes. If the electric field inside of the gas volume is strong enough, with electrons being fast compared to ions, a large and dense cloud of positive ions will develop nearby the anode and extend toward the cathode while the electrons are being collected, eventually leading to a streamer discharge due to the increase of field seen at the cathode. The field is then strong enough so that electrons are pulled out of the cathode. Electrodes, though they are a unique volume of resistive material, can be assimilated to capacitors. At the moment an electric field is applied in between their outer surfaces, the charge carriers inside of the volume will start moving leading to a situation where there is no voltage across the electrodes and a higher density of negative charges,

i.e. electrons, on the inner surface of the cathode. Finally, when a streamer discharge occurs, these electrons are partially released in the gas volume contributing to increase the discharge strength until the formation of a conductive plasma, the streamer. This can be understood through Figure 4.2 [184]. Streamer signals are very convenient in terms of read-out as no further amplification is required with output pulses amplitudes of the order of a few tens to few hundreds of mV as can be seen on Figure 4.3.

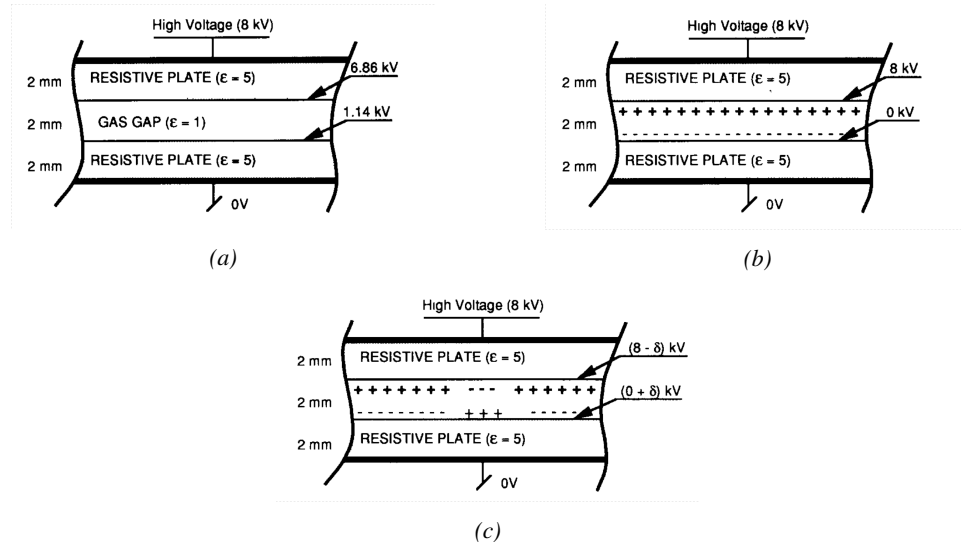


Figure 4.2: Movement of the charge carriers in an RPC. Figure 4.2a: Voltage across an RPC whose electrode have a relative permittivity of 5 at the moment the tension is applied. Figure 4.2b: After the charge carriers moved, the electrodes are charged and there is no voltage drop over the electrodes anymore. The full potential is applied on the gas gap only. Figure 4.2c: The streamer discharge initiated by a charged particle transports electrons and cations towards the anode and cathode respectively.

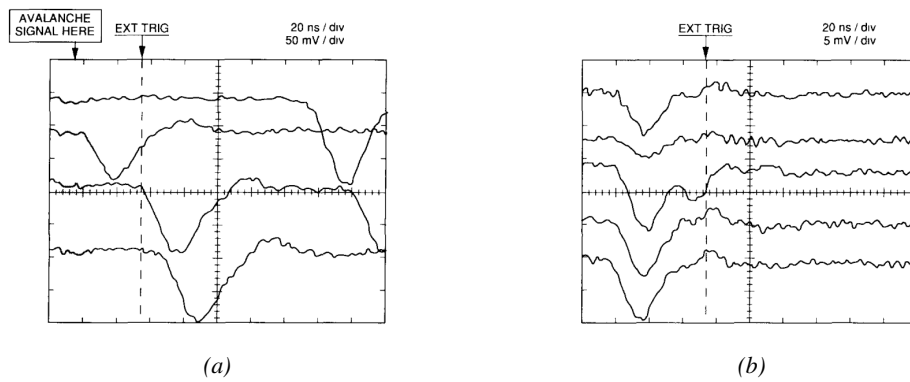


Figure 4.3: Typical oscilloscope pulses in streamer mode (Figure 4.3a) and avalanche mode (Figure 4.3b). In the case of streamer mode, the very small avalanche signal is visible.

When the electric field is reduced though, the electronic gain is small until the electrons get close enough to the anode and the positive ion cloud is much smaller. The electric field cannot rise to the

point a field emission of electrons on the cathode is possible. The resulting signal is weak, of the order of a few mv as shown on Figure 4.3, and requires amplification. This is the *avalanche mode* of RPC operation. This mode offers a higher rate capability by providing smaller discharges that don't affect the electrodes charge and are more locally contained in the gas volume as was demonstrated by Crotty with Figure 4.4 [184]. The detector only stays locally blind the time the charge carriers are recombined and there is no need for electrode recharge which is a long process affecting a large portion of the detector. Another advantage of avalanche signals over streamer is the great time consistency. Figure 4.3 shows very clearly that avalanche signals have a very small time jitter. Thus, using such a mode is a natural choice for experiments in which the detectors are required to have a high detection rate.

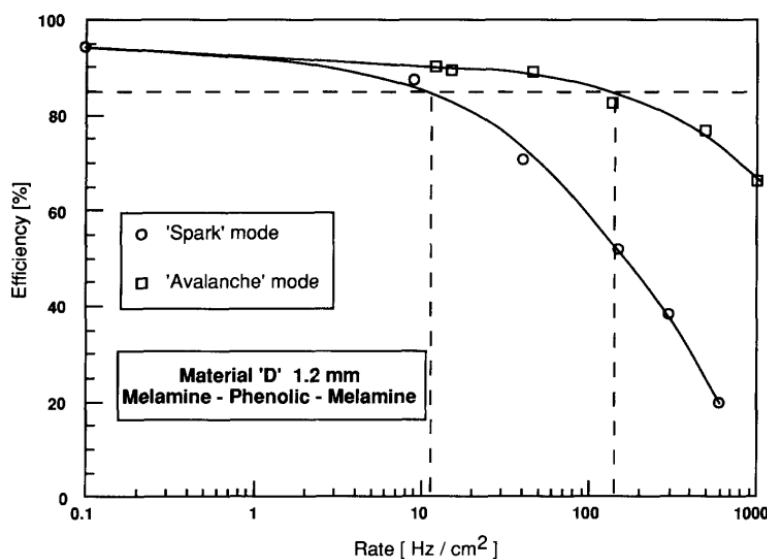


Figure 4.4: Rate capability comparison for the streamer and avalanche mode of operation. An order of magnitude in rate capability for a maximal efficiency drop of 10% is gained by using the avalanche mode over the streamer mode.

4.2.2 Standard gas mixture for RPCs operated in collider experiments

The first RPC working in streamer mode was operated with a 50/50 mixture of argon and butane [181], a standard mixture used at that time in multi-wire proportional chambers, taking profit of the good effective Townsend coefficient of argon to maximize the number of primary charge carriers freed in the gas by ionizing particles and of the quenching properties of butane. Before the discovery of the avalanche mode of RPC operation and concerned about the rate capability of RPCs operated in streamer mode, the performance improvement of the detectors through the increase of fast charge ratio in the signal development ,decreasing the charge induced per avalanche as can be seen through Figure 4.5, was studied by adding Freon based gases, such as CF_3Br , into the typical Ar/C_4H_{10} gas mixture was studied and showed that a lower induced charge could lead to an improvement the rate capability [187]. This consideration lead to the discovery of the avalanche mode which confirmed that the smaller the induced charge, the better the rate capability of the RPCs [184]. This discovery could happen thanks to the increased number of lower induced charge events allowed by adding a

²¹⁰¹ fraction of strong quencher in the gas mixture.

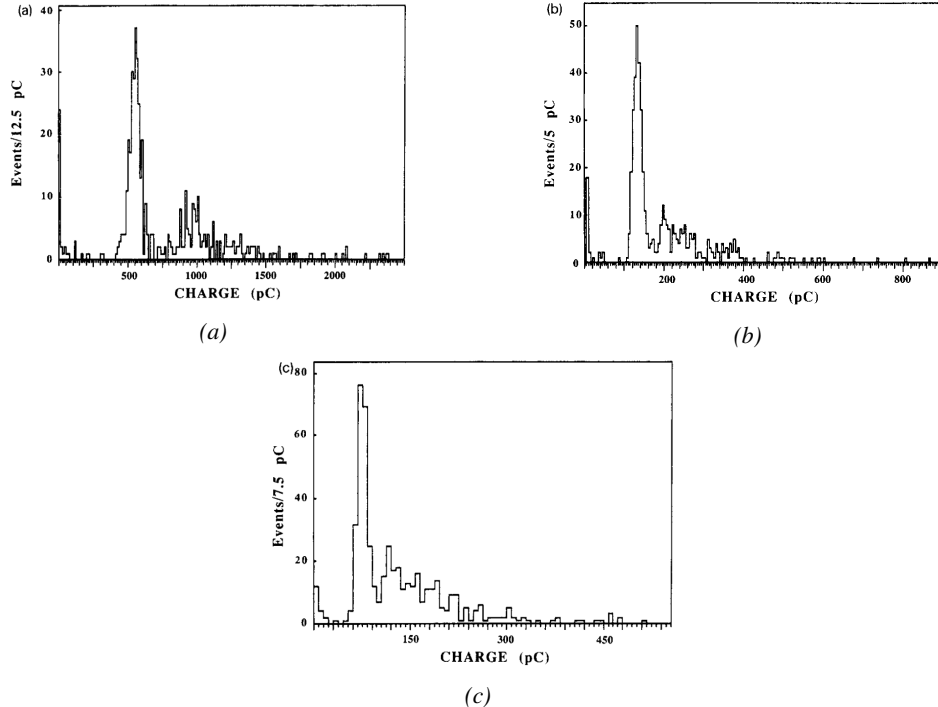


Figure 4.5: Comparison of the charge distribution of signals induced by cosmic muons in an RPC operated with a gas mixture of argon, butane and bromotrifluoromethane (CF_3Br). The Ar/C_4H_{10} is kept constant at 60/40 in volume while the total amount of CF_3Br in the mixture is varied: 0% (Figure 4.5a), 4% (Figure 4.5b) and 8% (Figure 4.5c) [187].

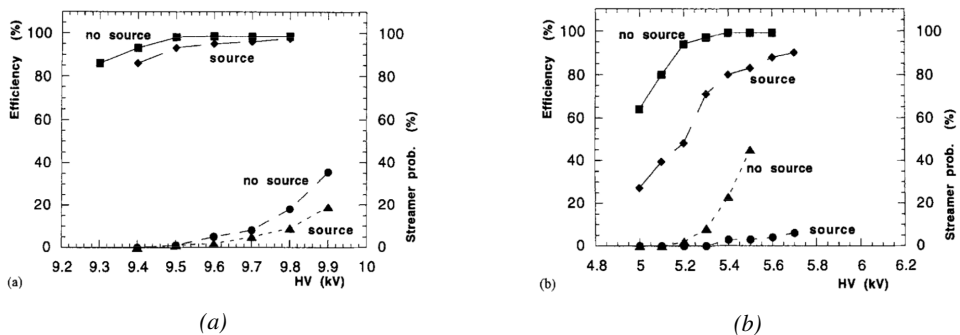


Figure 4.6: Comparison of the efficiency and streamer probability, defined as the fraction of events with an induced charge 10 times larger than that of the average avalanche, with and without irradiation by a 24 GBq ^{137}Cs source of an RPC successively operated with a 90/10 mixture $C_2H_2F_4/i-C_4H_{10}$ (Figure 4.6a) and a 70/5/10/15 mixture of $Ar/i-C_4H_{10}/CO_2/C_2H_2F_4$ (Figure 4.6b) [188].

²¹⁰² From this moment onward, more and more studies were conducted in order to find a gas mixture
²¹⁰³ that would allow for the best suppression of streamers for the benefit of low charge avalanches. Most

R&D groups working with narrow gaps started using freon-based gas mixtures while users of wide gap RPCs kept using Ar/CO_2 based mixtures. The differences in between narrow and wide gaps will be later discussed in Section 4.2.3. The CF_3Br having a high GWP, tetrafluoroethane ($C_2H_2F_4$) was preferred to it as more suitable ecofriendly gas in the middle of the 90s. An advantage of this new freon component is that it featured a high primary ionization and a low operating voltage, as reported by Cardarelli [186]. Thus, the new gas mixtures used were mainly composed of tetrafluoroethane alone with lower content of isobutane in order to reduce the flammability of the mixtures in the case it were to be used in accelerator experiments for safety reasons. Performance and models about such mixtures were discussed in papers of Abbrescia [188, 189] and showed a better suitability of such a gas mixture, with respect to argon based ones, for operations with high radiation backgrounds leading to a need for high rate capability of the detectors, as can be seen from Figures 4.6 and 4.7. Indeed, although the operating voltage of a tetrafluoroethane based mixture is higher than which of an argon based mixture but the efficiency under irradiation is more stable, the voltage range with negligible streamer probability is much wider, and the fast charge ratio available is much greater, providing with more stable operation of the detector.

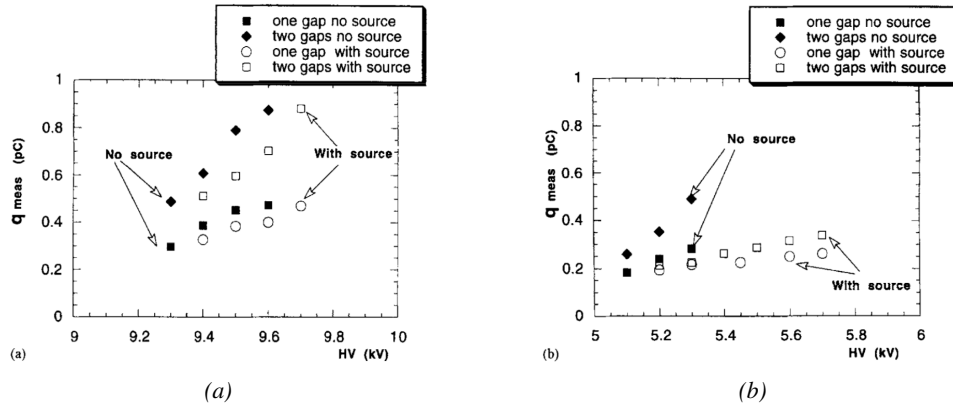


Figure 4.7: Comparison of the fast charge ratio with and without irradiation by a 24 GBq ^{137}Cs source of an RPC successively operated with a 90/10 mixture $C_2H_2F_4/i-C_4H_{10}$ (Figure 4.7a) and a 70/5/10/15 mixture of $Ar/i-C_4H_{10}/CO_2/C_2H_2F_4$ (Figure 4.7b). The results are provided for both single gap and double gap operation [188].

Aside of the improvement of the rate capability through linseed oil surface treatment of HPL electrodes, which allowed for a lower intrinsic noise rate and dark current of the detectors by improving the smoothness of the electrodes surface [201], it was later found that the streamers could be further suppressed by adding an electronegative compound into the gas mixture. The benefits of adding SF_6 in order to push the transitions from avalanche to streamers towards high voltages has been discussed in 1998 [190, 191] and eventually the high rate RPC destined to be used in accelerator physics would unanimously start using this compound into RPC gas mixtures. Being able to control the creation of streamers allows for slower ageing of the detector and lower power consumption as the currents driven by the electrodes consecutively to the induced charges would be smaller. In summary, the typical gas mixture RPCs are operated with is generally composed of the following 3 gas compounds, although, as mentioned in Chapter 3.6, research is being conducted into new more ecofriendly gas mixture using gases with a much lower Global Warming Potential:

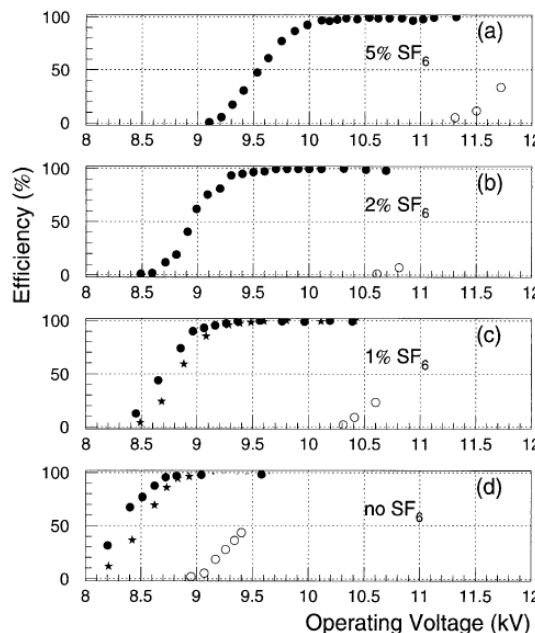
- Tetrafluoroethane ($C_2F_4H_2$), also referred to as *Freon* or *R134a*, is the principal compound

2132 of the RPC gas mixtures, with a typical fraction above 90%. It is used for its high effective
 2133 Townsend coefficient and the great average fast charge that allows to operate the detector
 2134 with a high threshold with respect to argon, for example, that has similar effective Townsend
 2135 coefficient but suffers from a lower fast charge. To operate with similar conditions, argon
 2136 would require a higher electric field leading to a higher fraction of streamers, thus limiting the
 2137 rate capability of the detector [188, 189].

- 2138
- 2139 • Isobutane ($i\text{-C}_4\text{H}_{10}$), only present in a few percent in the gas mixtures, is used for its UV
 2140 quenching properties [202] helping to prevent streamers due to UV photon emission during
 the avalanche growth.

2141

 - 2142 • Sulfur hexafluoride, (SF_6), simply referred to as SF_6 , is used in very little quantities for its
 2143 high electronegativity. Excess of electrons are being absorbed by the compound and streamers
 2144 are suppressed [190, 191]. Nevertheless, a fraction of SF_6 higher than 1% will not bring
 2145 any extra benefit in terms of streamer cancelation power but will lead to higher operating
 voltage [190], as can be understood through Figure 4.8.



2146 *Figure 4.8: Efficiency (circles and stars with 30 mV and 100 mV thresholds respectively) and streamer prob-
 2147 ability (open circles) as function of the operating voltage of a 2 mm single gap HPL RPC flushed with a gas
 2148 mixture containing (a) 5%, (b) 2%, (c) 1% and (d) no SF_6 [190].*

2149 In the last steps of R&D, the gas mixture of CMS RPCs was foreseen to be a 96.2/3.5/0.3 composition
 2150 of $\text{C}_2\text{H}_2\text{F}_4/i\text{-C}_4\text{H}_{10}/\text{SF}_6$ [203] but finally it was slightly changed into a 95.2/4.5/0.3 mixture
 2151 of the same gases [204]. A summary of the operation performance of the RPCs since the start of
 LHC and of CMS data taking is given in Figure 4.9 [205]. The performance of the detectors is
 regularly monitored and the operating voltages updated in order to obtain a very stable performance
 through time. Nevertheless, the detectors will face new challenges during Phase-II during which they

will exposed to more extreme radiation conditions. Description of the longevity tests with extreme irradiation and the conclusions regarding the operation of the present RPC system will be given in Chapter 5.

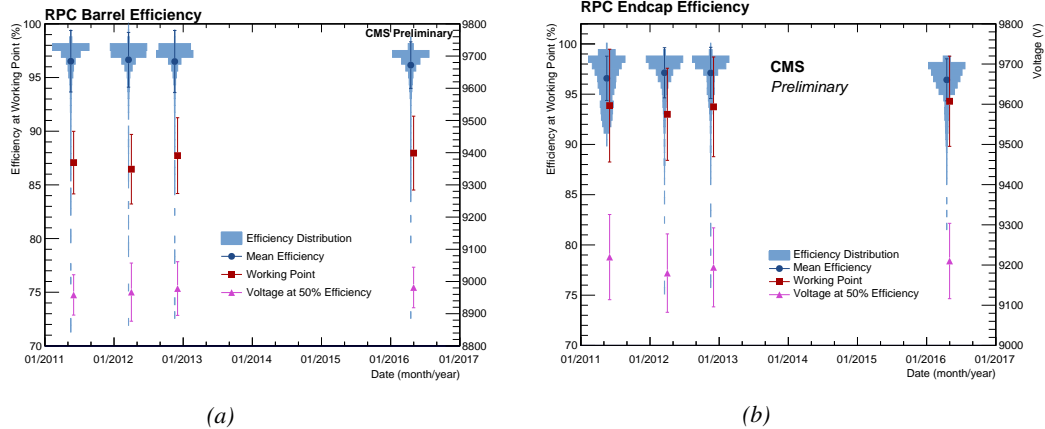


Figure 4.9: Evolution of the efficiency, working voltage, and voltage at 50% of maximum efficiency for CMS Barrel (Figure 4.9a) and Endcap (Figure 4.9b) RPCs obtained through yearly voltage scans since 2011. The working voltage of each RPC is updated after each voltage scan to ensure optimal operation [205].

It was already discussed that in the future, it is likely that the use of freon gases could be banned. As potential replacement for tetrafluoroethane was proposed the trifluoriodomethane (CF_3I), a molecule with similar properties than CF_3Br which was replaced by the tetrafluoroethane, and the 1,3,3,3-tetrafluoropropene ($C_3H_2F_4$ or HFO-1234re), a molecule with similar properties than the actual tetrafluoroethane and proposed as a replacement in refrigerating and air conditioning systems [206]. These 2 gases have stronger quenching properties than $C_2H_2F_4$ which means a much stronger electric field needs to be applied on the parallel electrodes of the RPCs in order to reach full efficiency. But the power supply system of CMS RPC is limited to 15 kV and so is ATLAS power supply system which is participating in a joined R&D. As can be seen from Figure 3.20, reducing the working voltage was achieved by mixing the potential replacements together with CO_2 . Introducing carbon dioxide into the mixture while keeping similar levels of isobutane and SF_6 increases the streamer probability and the best candidate identified for a compromise in between low enough working voltage and acceptable levels of streamers corresponds to a mixture containing 50% of CO_2 , 45% of HFO, 4% of isobutane and 1% of SF_6 but is not yet considered satisfactory. On the other hand, no good replacement for SF_6 has yet been identified. With its very high Global Warming Potential (23900), even small fraction of this gas in the mixture (it only represents 0.3% of CMS standard mixture but more than 5% of its overall GWP) substantially increase the danger for the environment. Although finding a replacement for this gas is less critical than for the tetrafluoroethane composing more than 90% of usual RPC standard mixtures, the problem will need to be addressed.

4.2.3 Detector designs and performance

Different RPC design have been used and each of them present its own advantages. Historically, the first type of RPC to have been developed is what is now referred to as *narrow gap* RPC [181, 207].

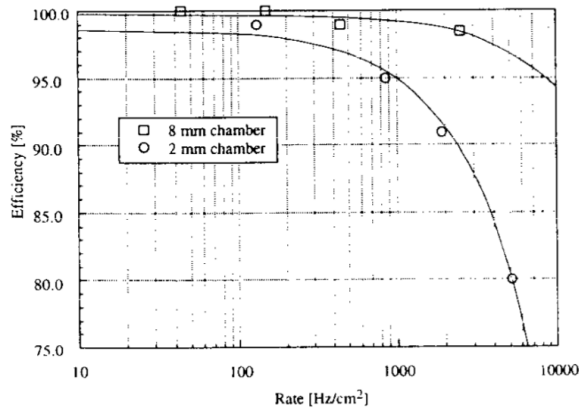


Figure 4.10: Comparison of the rate capability of 8 mm and 2 mm wide RPCs. The lines are linear fits on the data [207].

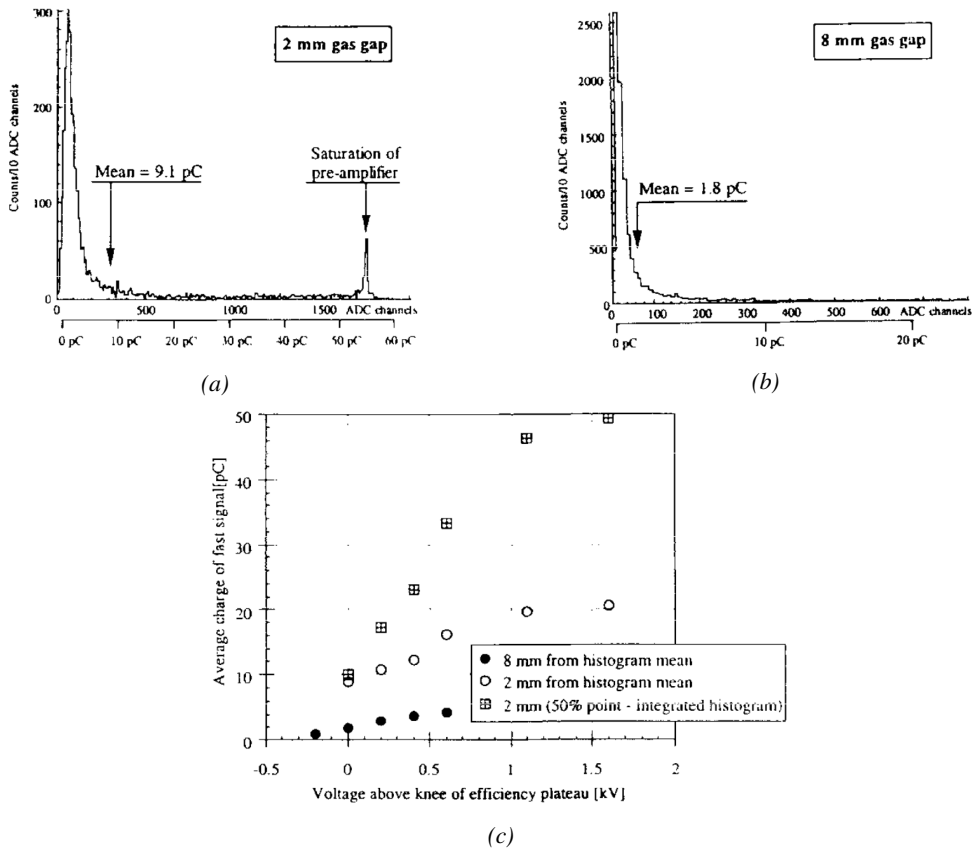


Figure 4.11: Distributions of the induced charge of fast signals on 2 mm (Figure 4.11a) and 8 mm (Figure 4.11b) RPCs exposed to a radiation rate of 100 Hz/cm^2 . Average induced charge of fast signals as a function of the high voltage applied on 2 mm and 8 mm RPCs (Figure 4.11c). In the case of the 2 mm RPC, a saturation of the pre-amplifier was observed. The average of the distribution is underestimated and the median is showed together with the average to account for this bias [207].

After the avalanche mode has been discovered [184], it has been showed that increasing the width of the gas gap lead to higher rate capability, due to lower charge deposition per avalanche, and lower power dissipation [207], as is showed in Figures 4.10 and 4.11. The distance in between the electrode being greater, a weaker electric field can be applied and a lower gain used as a longer gas volume will contribute to the signal induction on the read-out circuit. Nevertheless, by increasing the gas gap width, the time resolution of the detector decreases. This is a natural result if the increase of active gas volume in the detector is taken into account. Indeed, for a given detection threshold on the induced charge per signal, only the small fraction of gas closest to the cathode will provide enough gain to have a detectable signal. In the case of a wider gas volume, the active region is then larger and a larger time jitter is introduced with the variation of starting position of the avalanche, as discussed in [192] and showed in Figure 4.12.

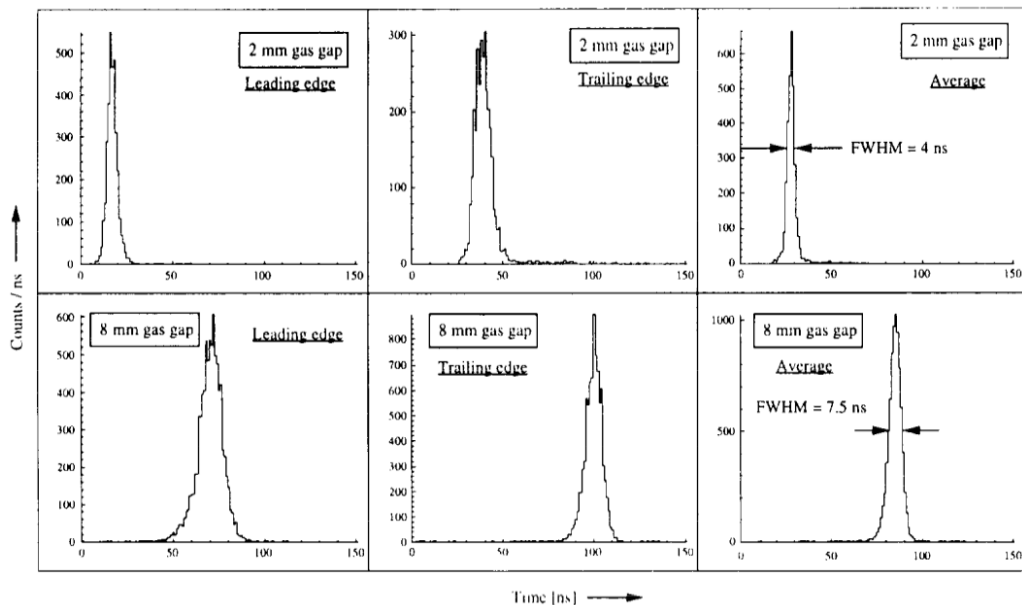


Figure 4.12: Time distributions of the leading, trailing, and average of both leading and trailing edges for 2 mm (top row) and 8 mm (bottom row) RPCs exposed to a 100 Hz/cm² radiation rate. The data was collected with RPCs operated at the voltage corresponding to the knee of the efficiency distribution, defined as the point where 95% of the maximum efficiency is obtained [207].

To improve both the time resolution and the rate capability, different methods were used trying to take advantage of both narrow and wide gap RPCs into a single design. Thus, double gap RPCs, combining two narrow gaps into a single detector to increase the effective sensitive volume, and multigap RPCs, which divided the large volume of a wide gap RPC into thinner sub-gaps by adding intermediate electrodes in between the cathode and anode to improve the time resolution by mimicking narrow gap RPCs, were developed starting from the middle of the 90s.

4.2.3.1 Double gap RPC

Made out of 2 narrow RPC detectors stacked on top of each other as shown in Figure 4.13, this detector layout, popularized by the two multipurpose experiments CMS [161] and ATLAS [195] at LHC, can be used as an OR system in which each individual chamber participates in the output signal

and increases the overall sensitive volume of the detector apparatus. Keeping the copper strip read-out system at the ground, CMS and ATLAS, due to different goals, have chosen different designs as CMS RPCs possess a 1D read-out while ATLAS RPCs offer a 2D read-out. The difference comes from placing the read-out in between the gaps, the anodes facing each other, or to have both RPC gaps in between 2 layers of read-out panels, one along the X-axis and one along the Y-axis, the cathodes facing each other.

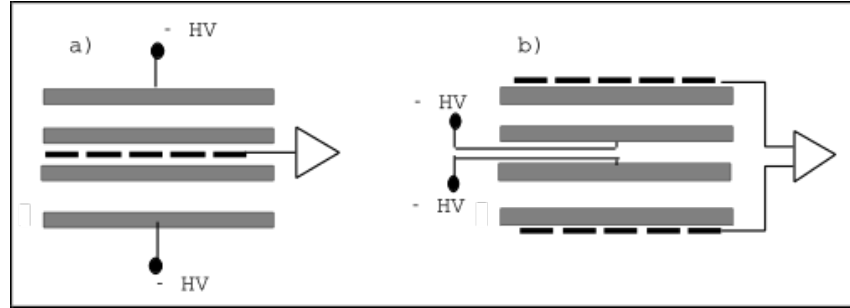


Figure 4.13: Possible double-gap RPC layouts: a) "standard" 1D double-gap RPC, as used in CMS experiment, where the anodes are facing each other and a 1D read-out plane is sandwiched in between them, b) double read-out double-gap RPC as used in ATLAS experiment, where the cathodes are facing each other and 2 read-out planes are used on the outer surfaces. This last layout can offer the possibility to use a 2D reconstruction by using orthogonal read-out planes.

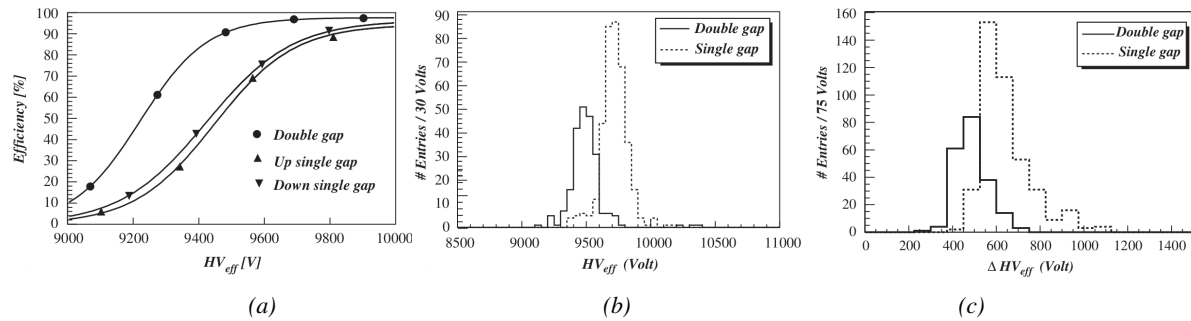
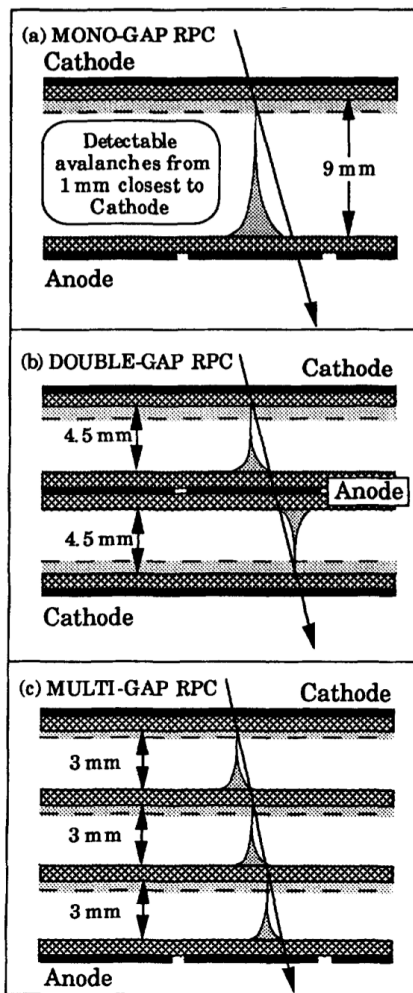


Figure 4.14: Comparison of performance of CMS double and single gap RPCs using cosmic muons [203]. Figure 4.14a: Comparison of efficiency sigmoids. Figure 4.14b: Voltage distribution at 95% of maximum efficiency. Figure 4.14c: $\Delta_{10\%}^{90\%}$ distribution.

The gain of such a detector is reduced by a factor 2 with respect to single-gap RPCs with an efficiency plateau reached at lower voltage, as visible on Figure 4.14, due to the two gas gaps contributing to the signal formation and offering a dynamic range closer to that of a wide gap RPC. A double gap is then fully efficient while the individual RPC gaps composing it are only 70 to 80% efficient. Naturally, by operating the double gap at a lower voltage, the rate capability is found to be increased as the induced charge per gap is then lower than in the case of a single gap detector also leading to a reduction of the streamer probability and a better extraction of the fast charge of the total signal as could be seen through previously presented Figure 4.7.

2213 **4.2.3.2 Multigap RPC (MRPC)**

2214 MRPCs are layouts in which floating sub electrode plates are placed into a wide gap RPC to divide
 2215 the gas volume and create a sum of narrow gaps [192, 193]. Similarly to the double gap RPC for
 2216 which the gain could be reduced by increasing the dynamic range, the multigap reduces the gain
 2217 while keeping a total dynamic range similar to which of a wide gap RPC by reducing the size of
 2218 each individual sub-gap composing the detector. The dynamic range, associated to the sensitive
 2219 volume, and the comparison of each detector layout to the wide gap RPC is showed in Figure 4.15.



2220 *Figure 4.15: Representation of different RPC layouts (wide gap on Figure (a), double gap on Figure (b)
 2221 and multigap on Figure (c)), of the corresponding sensitive volume in gray, and of the associated avalanche
 2222 size [193].*

2223 By operating the detector with thinner gaps, the time resolution is improved. Comparatively to
 2224 the time resolution presented in Figure 4.12 for the wide gap RPC of 8 mm, a complementary study
 2225 was conducted on multigaps using two 4 mm and four 2 mm subgaps and showed, via Figure 4.16,
 2226 an improvement of the time resolution with the reduction of the gap width and of the number of gaps

while the same sensitive volume was kept [193].

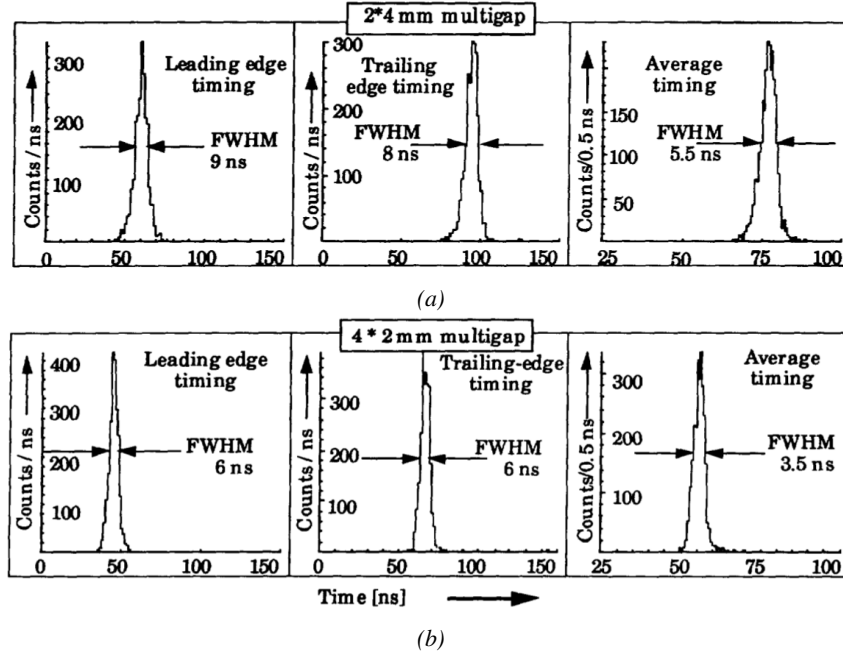


Figure 4.16: Time distributions of the leading, trailing, and average of both leading and trailing edges for multigap RPCs consisting in two 4 mm (Figure 4.16a) and four 2 mm (Figure 4.16b) exposed to a 100 Hz/cm^2 radiation rate. The data was collected with RPCs operated at the voltage corresponding to the knee of the efficiency distribution, defined as the point where 95% of the maximum efficiency is obtained [193].

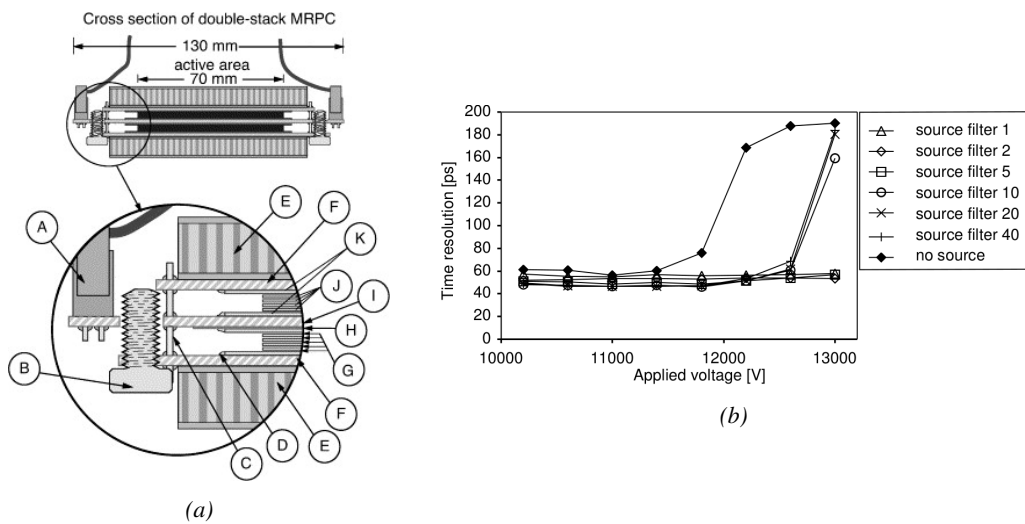


Figure 4.17: Presentation of a study of a possible ALICE MRPC cell using $250 \mu\text{m}$ gas gaps, $620 \mu\text{m}$ outer glass electrodes, and $550 \mu\text{m}$ inner floating electrodes (Figure 4.17a), and of its time resolution performance as a function of the applied high voltage for different radiation levels referred through different filter settings of the $740 \text{ GBq } ^{137}\text{Cs}$ source the former CERN GIF facility [208].

After the problem of streamers was solved by adding SF_6 into the gas mixture, the size of the MRPCs decreased as the research groups started applying the concept of dividing the gas volume into subvolumes to the narrow gap RPCs leading to the now widely used micro gap MRPCs. The time resolution of such a detector can reach of few tens of ps, with gas gaps of the order of a few hundred μm as showed in Figure 4.17 representing a single cell of ALICE Time-of-flight (ToF) system consisting of double MRPCs, as it was studied in the early 2000s [208].

Sometimes used as a double multigap RPC, taking advantage of the OR of double gap RPCs to both be able to operate a higher number of gaps while keeping a reasonable high voltage applied in between the cathode and anode and to further reduce the gain, the MRPC is mainly used as ToF detector [208–212] due to its excellent timing properties that allow to perform particle identification as explained by Williams in [213]. The principle of particle identification using ToF is simply the measurement of the velocity of a particle. Indeed, particles are defined by their mass (for the parameter of interest here, their electric charge being measured using the bending angle of the particles traveling through a magnetic field) and this mass can be calculated by measuring the velocity β and momentum of the particle:

$$(4.3) \quad \beta = \frac{p}{\sqrt{p^2 + m^2}}$$

Intuitively, it is trivial to understand that 2 different particles having the same momentum will have a different velocity due to the mass difference and thus a different flight time T_1 and T_2 through the detector and this is used to separate and identify particles. The better the time resolution of the ToF system used, the stronger will the separation be:

$$(4.4) \quad T = \frac{L}{v} = \frac{L}{c \cdot \beta}, \quad \Delta T = T_1 - T_2 = \frac{L}{c} \left(\sqrt{1 + m_1^2/p^2} - \sqrt{1 + m_2^2/p^2} \right) \cong (m_1^2 - m_2^2) \frac{L}{2cp^2}$$

An example of particle identification is given for the case of STAR experiment in Figure 4.18.

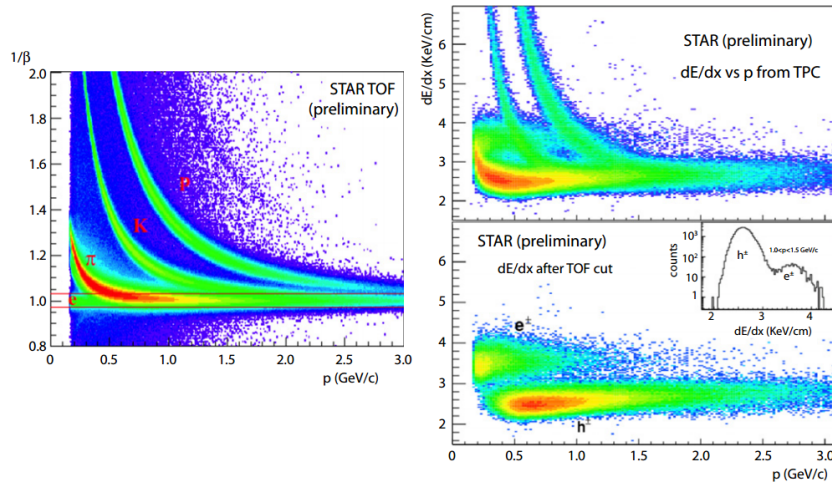


Figure 4.18: Particle identification applied to electrons in the STAR experiment. The identification is performed combining ToF and dE/dx measurements [213].

2245 Taking into account the distortion effect on the electric field inside of a MRPC built using micro
 2246 gaps due to the exposition to irradiation, distortion that can be understood by monitoring the current
 2247 drawn by the detector which should stay constant at constant electric field, another benefice of using
 2248 such small gas gaps is the strong reduction of the average avalanche volume and thus of the blind
 2249 spot on MRPCs leading to an improved rate capability. Multigaps can sustain backgrounds of several
 2250 kHz/cm² as demonstrated in Figure 4.19.

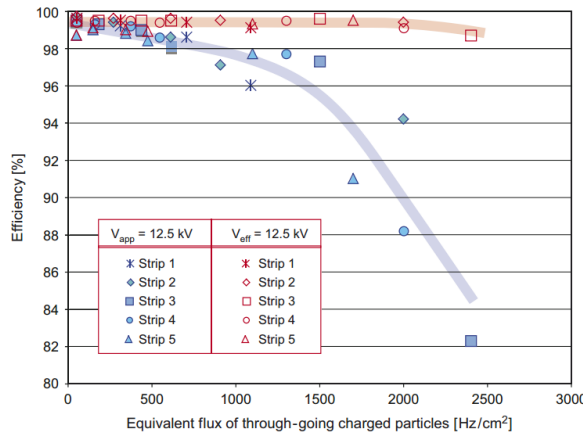


Figure 4.19: Comparison of the detector performance of ALICE ToF MRPC [214] at fixed applied voltage (in blue) and at fixed effective voltage (in red). The effective voltage is kept fixed by increasing the applied voltage accordingly to the current drawn by the detector.

2251 4.2.3.3 Charge distribution and performance limitations

2252 [This part could be moved in the next section of the chapter and deepened using the perspective
 2253 of the avalanche physics.]

2254 The direct consequence of the different RPC layouts is a variation of intrinsic time resolution of
 2255 the RPC as the gap size decreases and of the rate capability when the deposited charge per event is
 2256 spread over a larger number of amplification volumes, allowing for a reduction of the overall gain of
 2257 the detectors which is replaced by an on-electronics pre-amplification of the signals. in this sense,
 2258 an advantage is given to multigaps whose design use sub-millimeter gas volumes providing very
 2259 consistent signals.

2260 From the charge spectrum point of view, each layout has its own advantages. When the double-
 2261 gap has the highest induced over drifting charge ratio, as seen in Figure 4.20, the multigap has a
 2262 charge spectrum strongly detached from the origin, as visible in Figure 4.21. A high induced over
 2263 drifting charge ratio means that the double gap can be safely operated at high threshold or that at
 2264 similar threshold it can be operated with a twice smaller drifting charge, meaning a higher rate
 2265 capability if operated with sensitive enough electronics. On the other hand, the strong detachment
 2266 of the charge spectrum from the origin in the MRPC case allows to reach a higher efficiency with
 2267 increasing threshold as most of the induced charge is not low due to the convolution of several
 2268 single gap spectra. The range of stable efficiency increases with the number of gap, as presented in
 2269 Figure 4.22.

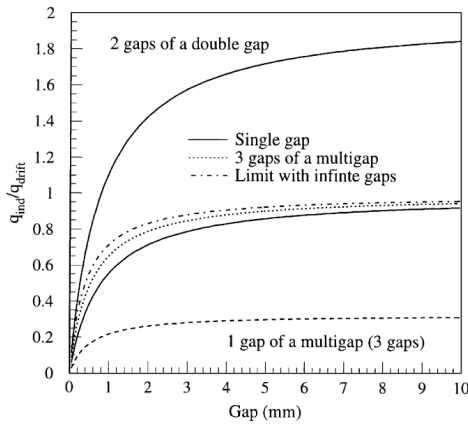


Figure 4.20: Ratio between total induced and drifting charge have been simulated for single gap, double-gap and multigap layouts [215]. The total induced charge for a double-gap RPC is a factor 2 higher than for a multigap.

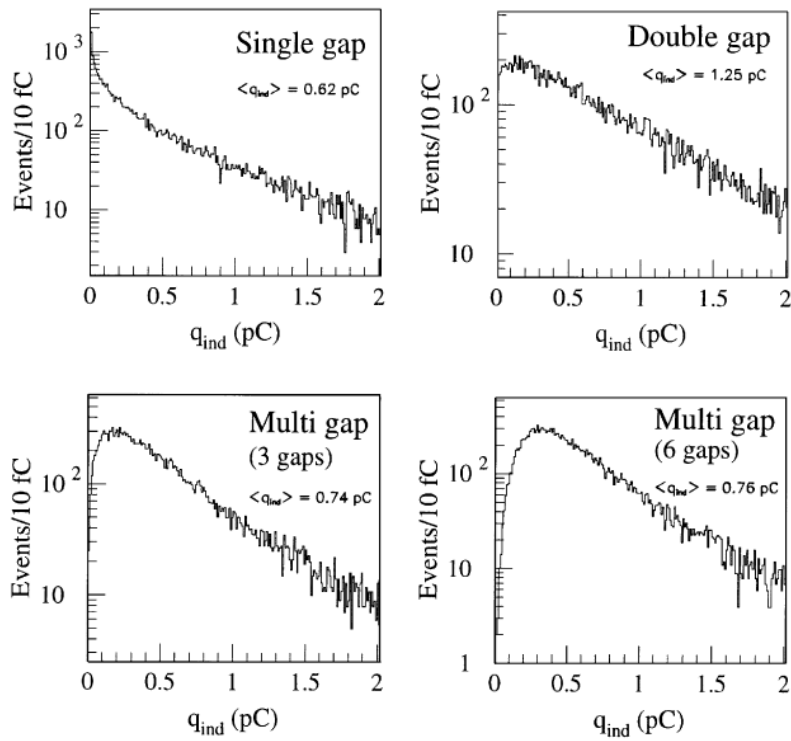


Figure 4.21: Charge spectra have been simulated for single gap, double-gap and multigap layouts [215]. It appears that when single gap shows a decreasing spectrum, double and multigap layouts exhibit a spectrum whose peak is detached from the origin. The detachment gets stronger as the number of gaps increases.

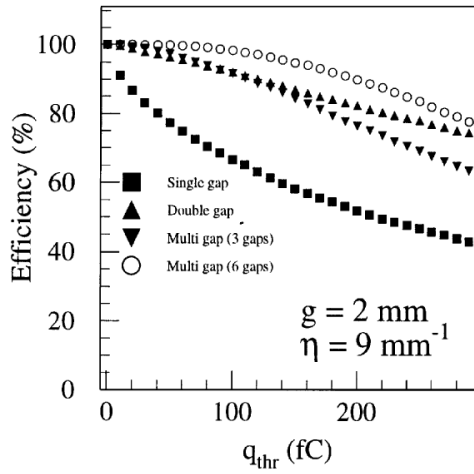


Figure 4.22: The maximal theoretical efficiency is simulated for single gap, double-gap and multigap layouts [215] at a constant gap thickness of 2 mm and using an effective Townsend coefficient of 9 mm^{-1} .

4.3 Signal formation

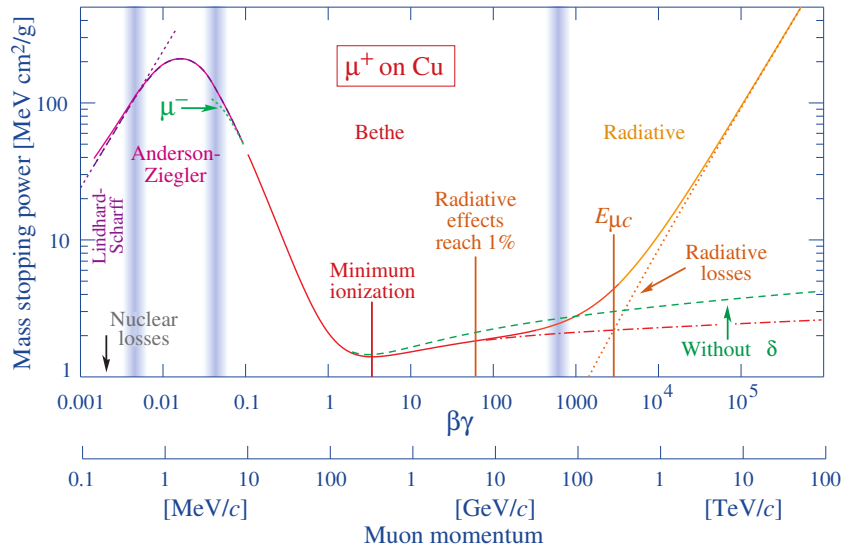


Figure 4.23: Mass stopping power as a function of $\beta\gamma = p/Mc$ for positive muons in copper [115]. The total stopping power is indicated with solid line and local components with dashed lines. The vertical bands are used to indicate boundaries between different approximations used at different energy range.

The physics of Resistive Plate Chambers still is far from being fully understood and work is regularly being accomplished in trying to model these detectors the best way possible by phenomenological models using well-defined physics [199, 216, 217]. These theoretical works have nevertheless lead to a better understanding of the key principles that account for RPCs signal formation. As previously

discussed, the typical mixture of such a detector is in great majority composed by a ionizing gas with some quenching properties and a low ionization potential to easily produce electrons, with the addition of UV quencher and electronegative compounds. The electronic avalanche formation will be triggered by a charged particle passing through the gas, typically a muon in the case of most uses of RPCs. The production of electrons in the gas of a detector is related to the energy lost by the incoming particle traveling through a material medium. The example of the mass stopping power of copper on muons is given in Figure 4.23 on which the different energy loss mechanisms at different energy ranges are visible. Once primary electrons have been freed in the gas volume, the electric field applied in between the electrodes of the RPC will make the charges move and there will be a competition in the gas in between the Townsend and attachment coefficient which describe the evolution of the number of electrons in an avalanche. While drifting through the gas, the electrons are also subjected to diffusion that will affect the evolution of the avalanches. Finally, when the avalanche is big enough, the accumulation of negative (electrons) and positive (ions) charges in the gas volume will start affecting the local electric field. This effect is known as space charge effect.

4.3.1 Energy loss at intermediate energies

Intuitively, a particle traveling through a medium will interact with its components, losing energy. When a muon travels through the gas of a gaseous detector, at the energy range usually observed, it interacts with the molecules of the gas leading to dissipation of the transferred energy in the form of inelastic diffusion or ionization. The photons and electron-ion pairs resulting from these interaction can trigger avalanches in the gas which will contribute to feed the avalanche growth thanks to the strong electric field applied in between the 2 electrodes of a RPC.

The mass stopping power of moderately relativistic ($0.1 \lesssim \beta\gamma \lesssim 1000$) heavy particles ($M \gg m_e$) traveling through a medium via excitation and ionization processes was studied by Bethe in 1930 [218] and is well described by the so called the Bethe Formula given in Equation 4.5.

$$(4.5) \quad \left\langle -\frac{dE}{dx} \right\rangle = K z^2 \frac{Z}{A} \frac{1}{\beta^2} \left(\frac{1}{2} \ln \frac{2m_e c^2 \beta^2 \gamma^2 W_{max}}{I^2} - \beta^2 - \delta(\beta\gamma) \right)$$

The different parameters used in this equation are

E	- incident particle energy γMc^2	MeV
x	- mass per unit area	g cm^{-2}
N_A	- Avogadro's number	$6.022\ 140\ 857(74) \times 10^{23} \text{ mol}^{-1}$
c	- speed of light in vacuum	$299\ 792\ 458 \text{ m s}^{-1}$
μ_0	- permeability of free space	$4\pi \times 10^{-7} \text{ N A}^{-2}$
ϵ_0	- permittivity of free space $\epsilon_0 = 1/\mu_0 c^2$	$8.854\ 187\ 817\dots \times 10^{-12} \text{ F m}^{-1}$
α	- fine structure constant $\alpha = e^2/4\pi\epsilon_0\hbar c$	$1/137.035\ 999\ 139(31)$
r_e	- classical electron radius $r_e = e^2/4\pi\epsilon_0 m_e c^2$	$2.817\ 940\ 3227(19) \text{ fm}$
e	- elementary charge of the electron	$-1.6021766208(98) \times 10^{-19} \text{ C}$
$m_e c^2$	- electron mass $\times c^2$	$0.510\ 998\ 9461(31) \text{ MeV}$
K	- constant defined as $K = 4\pi N_A r_e^2 m_e c^2$	$0.307\ 075 \text{ MeV mol}^{-1} \text{ cm}^2$
z	- charge number of incident particle	
Z	- atomic number of absorbing medium	
A	- atomic mass of absorbing medium	g mol^{-1}
β	- velocity of particle $\beta = v/c$	
γ	- Lorentz factor $\gamma = (1 - \beta^2)^{-1/2}$	

W_{max}	- maximum energy transfer through a single collision	MeV
I	- mean excitation energy of absorbing medium	eV
$\delta(\beta\gamma)$	- density effect correction to ionization energy loss	

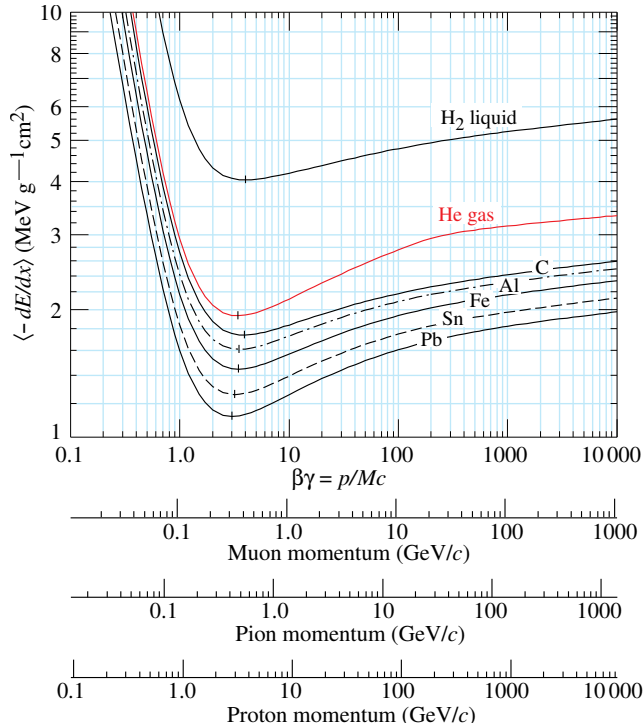


Figure 4.24: Mean mass stopping power for liquid hydrogen, as used in bubble chambers, gaseous helium, carbon, aluminum, iron, tin, and lead without the inclusion of radiative effect at higher $\beta\gamma$ necessary for pions and muons in denser materials [115].

In this equation, the maximum energy transfer W_{max} is defined as function of the incident particle mass M , expressed in MeV/c^2

$$(4.6) \quad W_{max} = \frac{2m_e c^2 \beta^2 \gamma^2}{1 + 2\gamma m_e / M + (m_e / M)^2}$$

and the mean excitation energy I depends on the absorber and its determination is non-trivial but recommendation are given by the International Commission on Radiation Units & Measurements (ICRU) based on experimental measurements and interpolations as showed in Figure 4.25.

For the case of copper, the mean stopping power is visible in Figure 4.23. The mean stopping power corresponding only to the Bethe range for other materials is given in Figure 4.24 and shows that $\langle -dE/dx \rangle$ is similar for each material with a slow decrease with Z . The factor affecting the equation the most is β as the dependence on M is introduced at higher energies in the logarithm via the max transfer energy per single collision but in most practice cases, only the dependence on β is considered as most of the relativistic particles are closed to the lowest mean energy loss rate and are

2311 referred to as minimum ionizing particles (mip's). The almost logarithmic relation in between the
 2312 mean energy loss rate for minimum ionizing particles and Z is showed in Figure 4.26.

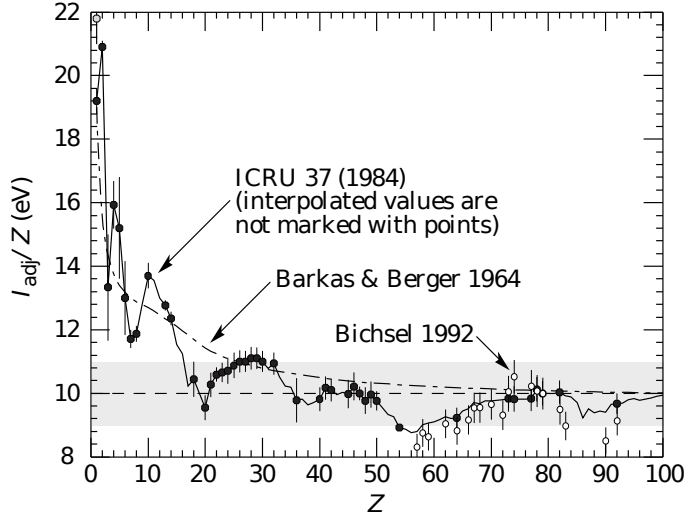


Figure 4.25: Mean excitation energies normalized to the atomic number as adopted by the ICRU [115, 219, 220].

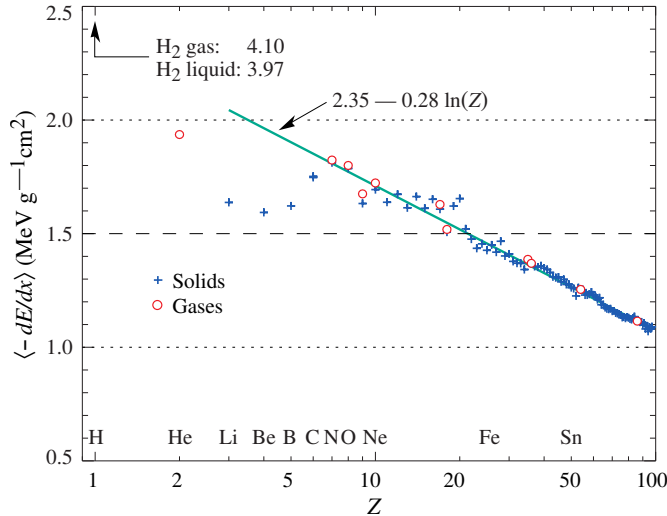


Figure 4.26: Mean mass stopping power at minimum ionization as a function of the atomic number [115].

2313 Finally, the term $\delta(\beta\gamma)/2$ corresponds to the density effect correction introduced to account for
 2314 the polarization of a real media that limits the spatial extension of the electric field of relativistic
 2315 particles. Indeed, as the energy of a particle increases, the associated electric field will flatten and
 2316 extend. Due to this effect, the distant collision contribution to Equation 4.5 will increase as $\ln(\beta\gamma)$
 2317 but the polarization of the media trunc this rise. At high energies, the correction is given by Equa-

2318 tion 4.7

$$(4.7) \quad \delta/2 \longrightarrow \ln(\hbar\omega_p/I) + \ln(\beta\gamma) - 1/2$$

2319 where $\hbar\omega_p$ represents the plasma energy that depends on the electron density of the media and
2320 the electron mass and can be calculated as $\sqrt{\rho\langle Z/A\rangle} \times 28.816$ eV. The introduction of this cor-
2321 rection term reduces the increase of the mean stopping power at higher energies as can be seen in
2322 Figure 4.23. Moreover, due to poorer electron density, the effect is less visible on gases than on
2323 liquids and solids has van be seen from Figure 4.24.

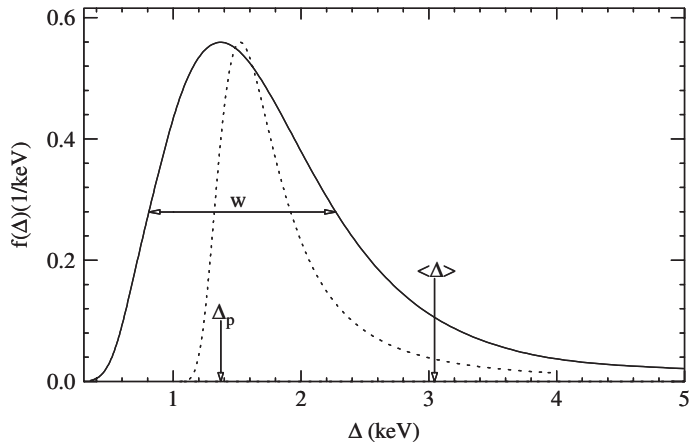


Figure 4.27: Example of straggling function $f(\Delta)$ of particles passing through 1.2 cm of Argon gas with a $\beta\gamma$ of 3.6 and represented with a solid line. The original Landau distribution is showed with a dashed line [221].

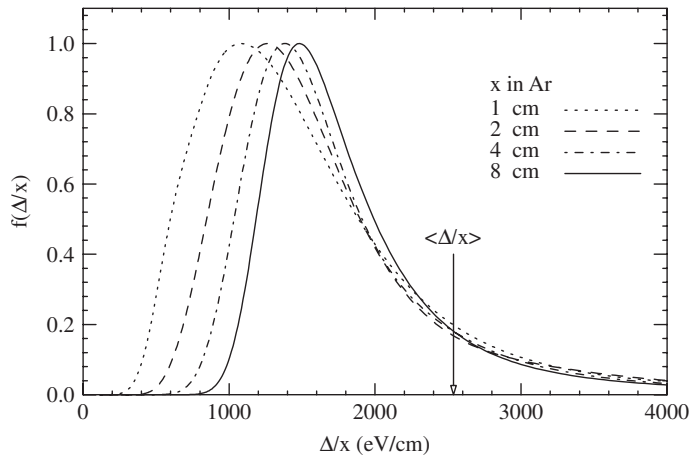


Figure 4.28: Evolution of straggling functions $f(\Delta)$ of particles passing through a volume of Argon gas with a $\beta\gamma$ of 3.6 with increasing thickness x [221].

2324 The mean energy loss per collision can be difficult to measure for low data samples and is not
2325 always representative of the energy loss distribution for a given incident particle energy. Hence, it is

2326 easier to access the most probable energy loss which is a lower value than than the average loss due
 2327 to the distribution of the energy transfer. This value is well described by a highly skewed Landau
 2328 distribution for detectors with "moderate" thickness x , expressed in g mol $^{-1}$. But for gas volumes,
 2329 a Landau distribution greatly underestimates the width w of the distribution and only succeeds to
 2330 provide with a correct value for the most probable energy loss, as showed in Figure 4.27. Thus,
 2331 the energy loss distribution is better represented by its most probable energy loss Δ_p and its full-
 2332 width-at-half-maximum (FWHM) w . As showed by Figure 4.28, the distribution is affected by
 2333 the thickness of the gas volume and the most probable energy loss normalized to the thickness is
 2334 increased and the width decreased, converging towards the Landau distribution, whereas the mean
 2335 energy loss is unchanged. Correction are brought to the original Landau equation in order to account
 2336 better for the number of collisions leading to an increased width of the energy loss distribution [221].

2337 In the case of gas mixtures, composed of several elements, using Bragg additivity it can be
 2338 understood that the mean energy loss of the mixture is the sum of the mean energy losses in each
 2339 individual element j layer of weight w_j .

$$(4.8) \quad \left\langle \frac{dE}{dx} \right\rangle = \sum w_j \left\langle \frac{dE}{dx} \right\rangle_j$$

2340 4.3.2 Primary ionization

2341 Using Bethe formula to understand the mean energy transfer of charged particle when traveling
 2342 through a gas volume give an intuition of the physics that affect the particle but doesn't provide a
 2343 detailed enough information about the individual ionizations along its tracks at a microscopic level.
 2344 In order to simulate efficiently an RPC and hence understand the processes governing avalanches
 2345 creation and growth, knowledge on the ionization process is necessary.

2346 To convert the energy loss rate into a number of primary ionizations was developed in 1980 the
 2347 Photo-Absorption Ionisation (PAI) model [222] based on the cross section of ionization of gas atoms
 2348 to real photons and the dielectric constant of the medium through which the charged particles are
 2349 going. Indeed, the interaction of charged particles with the gas molecules being of electromagnetic
 2350 nature, it is mediated by quasi-real photons and, hence, the cross section to photon ionization is
 2351 important to understand. This approach is nevertheless semi-classical as it relies on classical elec-
 2352 trodynamics and it only gives access to the energy transfer to the gas atoms and no information on
 2353 the energy dissipation and secondary emissions is available on the output of the model. The energy
 2354 transferred to the medium is not all used for ionization. For an energy deposition Δ , the number of
 2355 electron-ion pairs produced is:

$$(4.9) \quad \Delta = n_i W$$

2356 W corresponds to the mean work per pair production that depends on the medium and is greater
 2357 than the ionization potential leading to the conclusion that part of the transferred energy is dissipated
 2358 through other processes [217, 223]. In order to understand the energy dissipation and the secondary
 2359 emissions, the fine structure of each atom is taken into account. Through the PAI model, the incident
 2360 charged particle interacts is assumed to interact with the full atom rather than with a single electron.

2361 Although, considering that the particle interacts with a single electron, leads to the possibility
 2362 to study the excited state of the atom once the photo-electron has been emitted with an energy

corresponding to the transferred energy minus the binding energy of the electronic shell. The resulting vacancies in the electronic shell will be filled through emission of photons or Auger electrons and can contribute to further ionization or excitation in the gas volume. Fluorescence photons are usually not considered as they only constitute a very small fraction of secondary emissions [224]. Assuming that the transferred energy is absorbed in its totality by a single electronic shell, the PAI model was modified to include relaxations and constitute the new Photo-Absorption Ionisation with Relaxation (PAIR) model [224]. In this model, the cross section corresponding to the whole atom is re-expressed using a sum of partial cross sections corresponding to the different electronic shells. When one or more electrons are knocked out of the atom, the vacancies are filled by electrons of the shell above with relaxation by Auger electron emission. These processes happen in cascade from the inner shell to the outer one until all the vacancies are filled and the energy has been released.

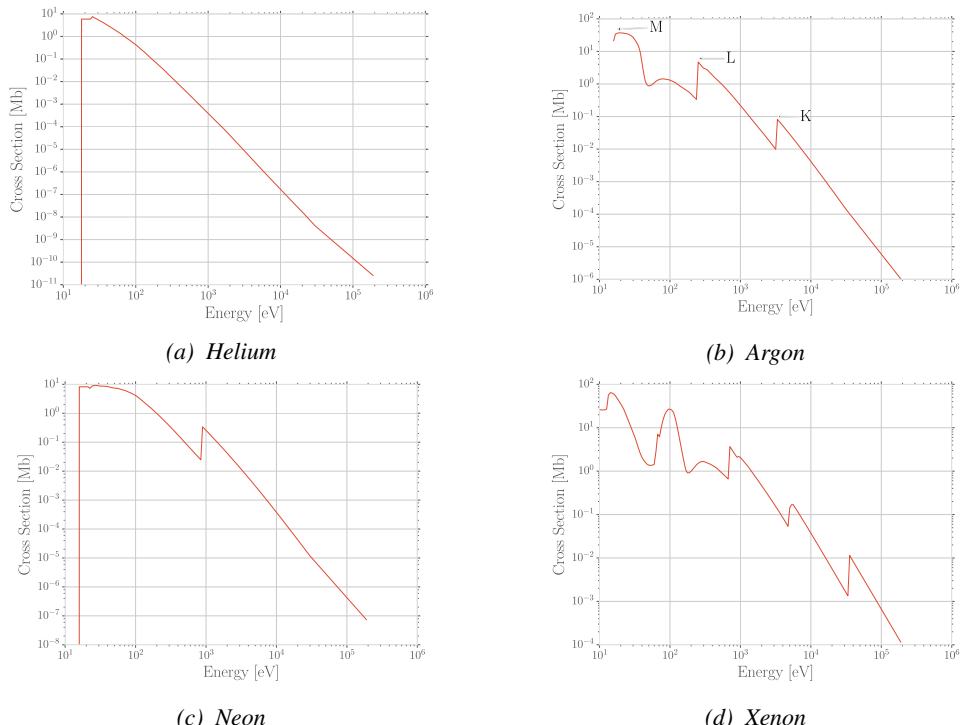


Figure 4.29: Photo-absorption cross section as computed by HEED for nobles gases with different electric shell numbers [217].

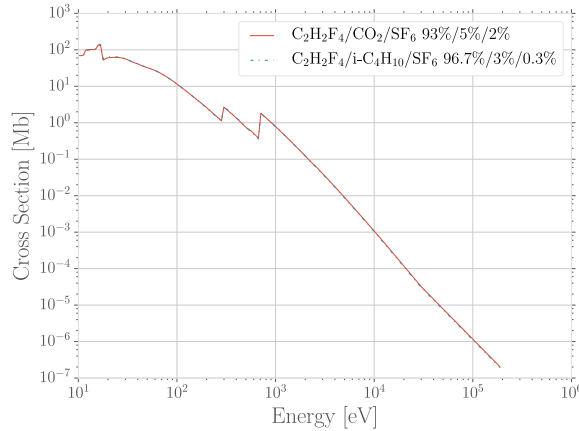


Figure 4.30: Photo-absorption cross section as computed by HEED for typical RPC gas mixtures [217]. The RPC mixture with CO₂ corresponds to the mixture used by CALICE SDHCAL [225] while the other one was foreseen for the experiment ATLAS [226] but has been changed since then.

This model is included in the program HEED developed at CERN [227] and called by Garfield, a program developed for the simulation of gaseous detectors. The results for the cross section for a few noble gases are given in Figure 4.29. It can be seen that for each shell, the cross section is increased. More complex patterns are seen with bigger atoms such as Xenon on Figure 4.29d. For gas mixtures, like the typical RPC mixtures, the cross section is showed in Figure 4.30. Both mixtures being mainly composed of C₂H₂F₄, the variations in between the 2 cross section profiles are very subtle and depends on the concentration of the other compounds.

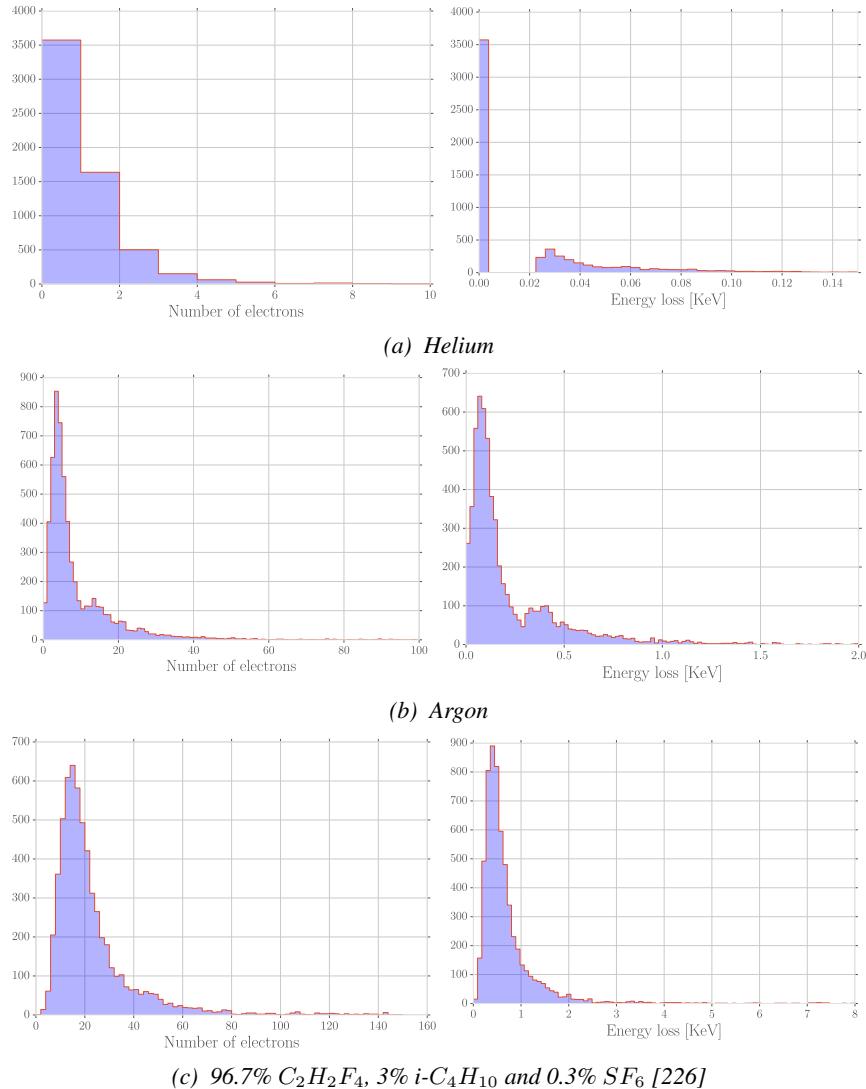


Figure 4.31: Distributions of number of electrons (left) and energy loss (right) for a 5 GeV/c muon passing through 1.2 mm of Helium (Figure 4.31a), Argon (Figure 4.31b) or a typical RPC gas mixture (Figure 4.31c) [217].

Once the cross section of interaction is known, it is possible to extract the distribution of energy loss and of the number of electron produced, as showed in Figure 4.31 for Helium, Argon, which is used in gaseous detectors, and for a typical RPC mixture [217]. The distributions are computed using HEED and show typical straggling function profiles with some complex structures that can be related to interaction of the incoming particle with the different electronic shells. Helium does not have a great photo-absorption cross-section according to Figure 4.29a and a muon will not be likely to lose a lot of energy and to create a lot of electrons whereas in a more complex atom like Argon, the cross-section is greater and will lead to a greater energy loss of muons and more electron produced. Finally, a complex gas mixture used in RPCs will offer an even greater cross-section, a wider energy loss distribution and will be able to produce more electrons. The same information is seen by looking

at the evolution of the mean number of cluster as a function of the lorentz factor associated to muons showed in Figure 4.32a. Indeed, the greater photo-absorption cross-section of RPC mixtures allow for a much greater amount of clusters to be created by charged particles. The size of these clusters is studied through Figure 4.32b which shows that, in most of the cases ($\approx 80\%$), the clusters only are composed of a single electron which is consistent with minimum ionizing particles.

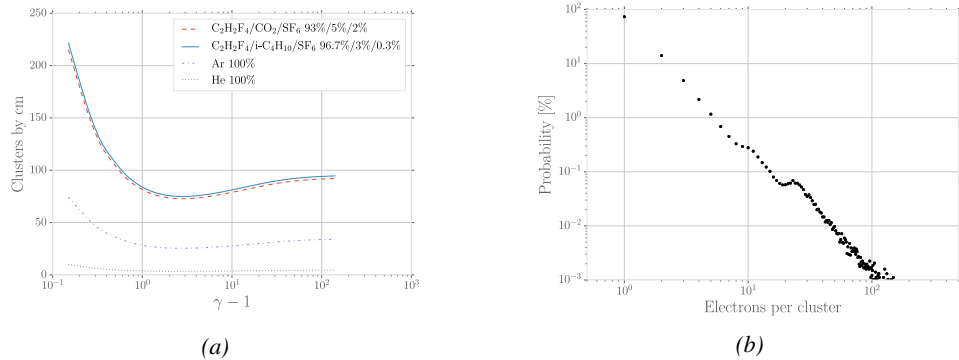


Figure 4.32: Figure 4.32a: Mean cluster density for muons through different gas volumes [217]. Figure 4.32b: Distribution of the number of electrons per cluster for a 5 GeV/c muon traveling through a mixture of 96.7% $C_2H_2F_4$, 3% $i-C_4H_{10}$ and 0.3% SF_6 [217, 226].

4.3.3 Development and propagation of avalanches

From the clusters released in the gas volume by the charged particles, free electrons will start drifting due to the electric applied in between the electrodes of the RPC. Gaining velocity and energy, these electrons in their turn will be able to ionize the gas. This process being repeated by all the produced electrons will trigger an avalanche to develop.

The growth of the avalanche can be intuitively understood as a competition between 2 effects. Due to their increasing energy, electrons have a probability to trigger new ionizations by interacting with gas molecules. On the other hand, before the minimal amount of energy is reached, the electrons can get attached to a gas molecule instead. These two effects can be described using a simple model in which the multiplication and attachment processes are given by the Townsend coefficient α and the attachment coefficient η , assuming that the history of previous interactions in the gas does not influence new interactions. This model simply takes into account probabilities to have at the gas depth z for a given number n of free electrons in the gas $n+1$ or $n-1$ electrons at the depth $z+dz$ (respectively $n\alpha dz$ and $n\eta dz$). Then, the mean number of electrons \bar{n} and cations \bar{p} can be written for single compound gases as

$$(4.10) \quad \frac{d\bar{n}}{dz} = (\alpha - \eta)\bar{n}, \quad \frac{d\bar{p}}{dz} = \alpha\bar{n}$$

which, assuming the initial conditions $\bar{n}(0) = 1$ and $\bar{p}(0) = 0$, lead to the mean number of electrons and cations at a depth z

$$(4.11) \quad \bar{n}(z) = e^{(\alpha-\eta)z}, \quad \bar{p}(z) = \frac{\alpha}{\alpha-\eta} \left(e^{(\alpha-\eta)z} - 1 \right)$$

²⁴¹³ The Townsend and attachment coefficient as a function of the applied electric field are given in
²⁴¹⁴ Figure 4.33 for a standard RPC gas mixture using Magboltz [228].

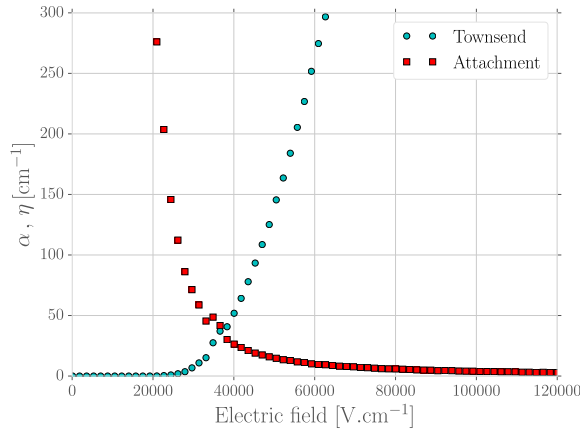


Figure 4.33: Townsend and attachment coefficient for a typical 96.7/3/0.3 mixture of $C_2H_2F_4/i-C_4H_{10}/SF_6$, at a temperature $T = 296.15\text{ K}$ and a pressure $P = 1013\text{ hPa}$ [217, 226].

²⁴¹⁵ Nevertheless, there are more to the avalanche growth than simply these two factors. Throughout
²⁴¹⁶ the 20th century, models have been developed to better understand the physics of discharges in gas.
²⁴¹⁷ In 1937, Furry developed a model to describe electromagnetic cascades [229] that would be used for
²⁴¹⁸ electron avalanches in gas during the 1950s. Furry realized that the use of a Poisson law to describe
²⁴¹⁹ the distribution of shower sizes could not be accurate as he understood that the events occurring in
²⁴²⁰ the development of a cascade are not independent from each other, as a Poisson law would suggest.
²⁴²¹ Indeed, part of the particles produce others and this process depends on both their original energy
²⁴²² and energy lost. Experimental results showed excess of small showers and an under estimate of very
²⁴²³ large ones. To solve this problem, Furry proposed a distribution of sizes of following the likelihood
²⁴²⁴ described in Equation 4.12, in which $\bar{n} = e^{\alpha z}$, compared with a Poisson law in Figure 4.34.

$$(4.12) \quad P(n, \bar{n}) = \bar{n}^{-1}(1 - \bar{n}^{-1})^{n-1}$$

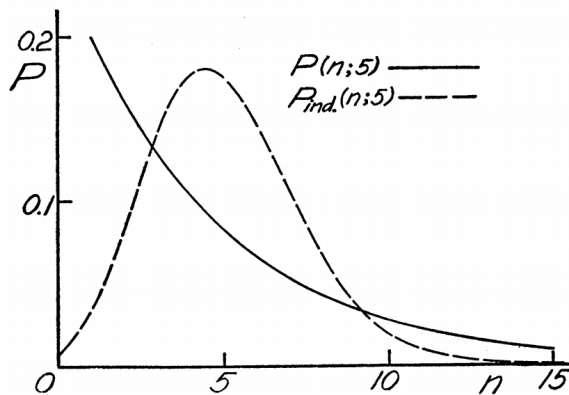


Figure 4.34: Comparison of the distribution law of Furry and the Poisson law for $\bar{n} = 5$ [229].

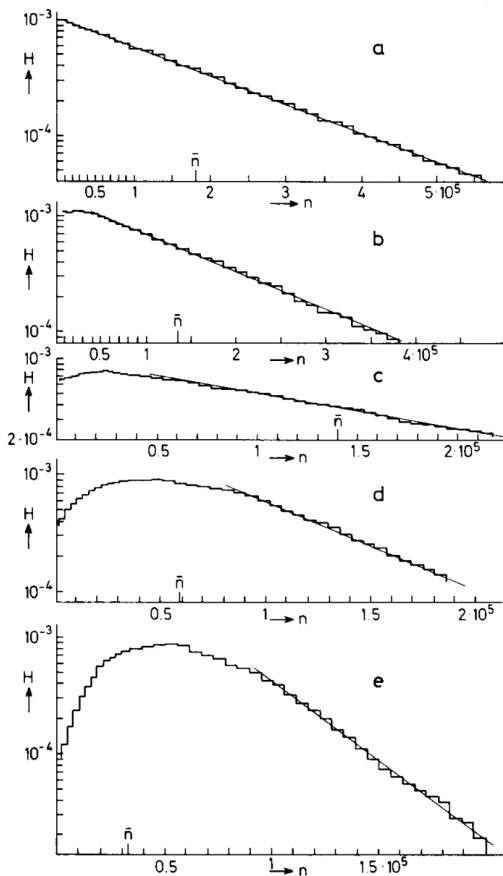


Figure 4.35: Single-electron avalanche size distribution in a proportionnal counter filled with methylal at different E/p values. (a) 70, (b) 76.5, (c) 105, (d) 186.5, (e) 426V/cm torr [230].

In this model, no extra energy is brought to the electrons in the showers, contrary to the case of a gaseous detector such as a RPC where an electric field accelerates them. Using the Furry model, Genz studied the fluctuations in electron avalanches in gaseous detectors [230]. Collisions leading to ionizations leave electrons with an energy much smaller than the ionization energy eU_i , where U_i is the ionization potential of a gas molecule. Hence, the electrons need to travel a distance $s = U_i/E$ along the electric field E to acquire a high enough energy to trigger a new ionization. For the probability of a new ionization to be independent from the path followed by the electrons since the previous ionization, the mean free path $1/\alpha$ of electrons in the gas has to be large compared to s and thus $E/\alpha \gg U_i$. The Townsend coefficient is related to the gas pressure leading to conditions on the value of E/p . Avalanches in gas are large compared to the showers Furry has studied in his original paper. For very large avalanche sizes, Equation 4.12 can be written as an exponential, as showed in Equation 4.13.

$$(4.13) \quad P(n, \bar{n}) = \bar{n}^{-1} e^{-n/\bar{n}}$$

This exponential behaviour is showed through Figure 4.35. In practice, to fully understand the avalanche growth, taking into account the path followed by electrons from one ionization to another

will become necessary. In the same paper, Genz then discusses models using Polya distributions to estimate the multiplication by looking at the size of the avalanche it self. Indeed, the number of charge carriers in the avalanche might become important enough to have an effect on the multiplication process. To account for this, it was proposed to use a varying Townsend coefficient such as described by Equation 4.14 depending on the position x in which θ is an empirical parameter leading to the probability distribution of Equation 4.15. In the limit case where θ goes to 0, the formula describes again the Furry model. But the data deviates from this model as well at large n values. Moreover, the introduction of an empirical parameters makes the model hard to interpret physically.

$$(4.14) \quad \alpha(n, x) = \alpha(x) \left(1 + \frac{\theta}{n}\right), \quad n > 0$$

$$(4.15) \quad P(n, x) = \frac{1 + \theta}{\bar{n}} \frac{1}{\theta!} \left(\frac{n(1 + \theta)}{\bar{n}}\right)^{\theta} e^{-\frac{n(1 + \theta)}{\bar{n}}}$$

In order to have a model that describes reality better, the introduction of the attachment into the model is an important step. Despite its limitations, the Furry model had the advantage to describe well avalanches occurring when the attachment could be ignored. This is only natural that this model was then extended to included attachment. This was done by Riegler, Lippmann and Veenhof [226] which showed that what was important was to consider both the Townsend coefficient describing the multiplication *and* the attachment coefficient, not only the effective multiplication coefficient $\bar{\alpha} = \alpha - \eta$. The probability to see an avalanche started by a single electron grow to a size n after having traveled a distance z through the gas is given by Equation 4.16.

$$(4.16) \quad \begin{aligned} P(n, z) = & P(n - 1, z) (n - 1)\alpha dz (1 - (n - 1)\eta dz) \\ & + P(n, z) (1 - n\alpha dz) (1 - n\eta dz) \\ & + P(n, z) n\alpha dz n\eta dz \\ & + P(n + 1, z) (1 - (n + 1)\alpha dz) (n + 1)\eta dz \end{aligned}$$

The first term of this probability that from a state with $n - 1$ electrons, only 1 multiplies while the others don't get attached. Both the second and third terms describes the probability that from a state with already n electrons the total number of electrons stay the same. On the second term, no electron gets attached nor multiplies while on the third term, 1 electron gets multiplied and 1 gets attached to compensate. Finally, the fourth term describes the probability to fall from a state with $n + 1$ to a state with n electrons due to the attachment of a single electron. At the first order, the evaluation of the previous expression leads to Equation 4.17 which general solution is given in Equation 4.18 in which are introduced the variables $\bar{n}(z)$, defined as in Equation 4.11, and $k = \eta/\alpha$ making explicit the fact that the distribution not only depends on the effective Townsend coefficient.

$$(4.17) \quad \frac{dP(n, z)}{dz} = -P(n, z)n(\alpha + \eta) + P(n - 1, z)(n - 1)\alpha + P(n + 1, z)(n + 1)\eta$$

$$(4.18) \quad P(n, z) = \begin{cases} k^{\frac{\bar{n}(z)-1}{\bar{n}(z)-k}}, & n = 0 \\ \bar{n}(z) \left(\frac{1-k}{\bar{n}(z)-k}\right)^2 \left(\frac{\bar{n}(z)-1}{\bar{n}(z)-k}\right)^{n-1}, & n > 0 \end{cases}$$

The example given through Figure 4.36 shows the importance of each individual process in the growth of avalanches and the fluctuation of their size. The values of α and η will influence the probability distribution, as can be seen from Figure 4.36a. Then, Figure 4.36b shows that the fluctuation really takes place within the very first interactions. Indeed, when the avalanche contains a large enough amount of charge carriers (a few hundreds), its size then increases like $e^{z(\alpha-\eta)}$.

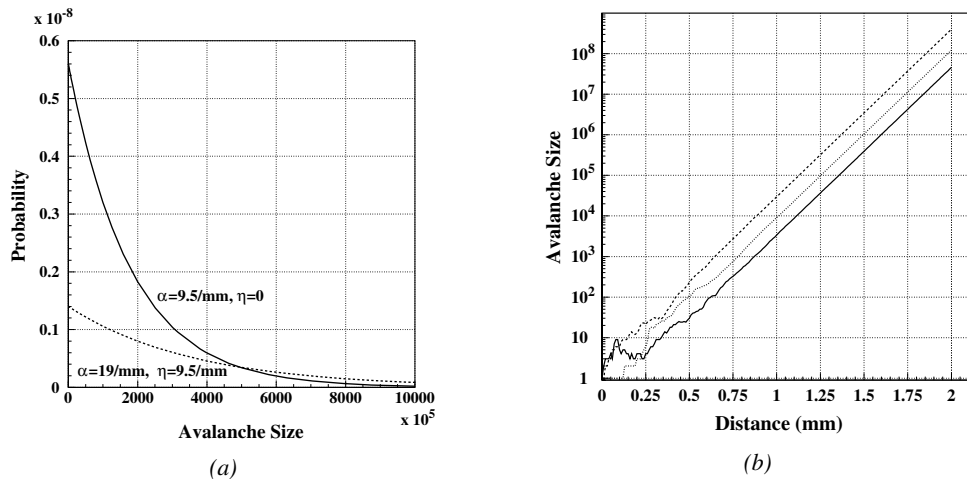


Figure 4.36: Figure 4.36a: Comparison of avalanche size distributions for different values of Townsend and attachment coefficients. The effective Townsend coefficient is the same for both distributions. Figure 4.36b: Fluctuation in avalanche size for avalanche started by a single electron with $\alpha = 13 \text{ mm}^{-1}$ and $\eta = 3.5 \text{ mm}^{-1}$ [226].

4.3.4 Drift and diffusion of the electron cloud

During the growth of avalanches, an electron cloud drifting along the electric field through the gas will undergo thermal diffusion due to random collisions with the gas molecules. This phenomenon can be studied using Maxwell-Boltzmann distribution whose mean is defined by the thermal energy of the cloud $\langle E \rangle = 3/2kT$ with an extra component coming from the constant drift motion. The drift of electrons along the field lines is usually observed on a macroscopic scale through which the speed can be assimilated to a constant v_D which corresponds to the mean drift speed over a large number of collisions in the gas.

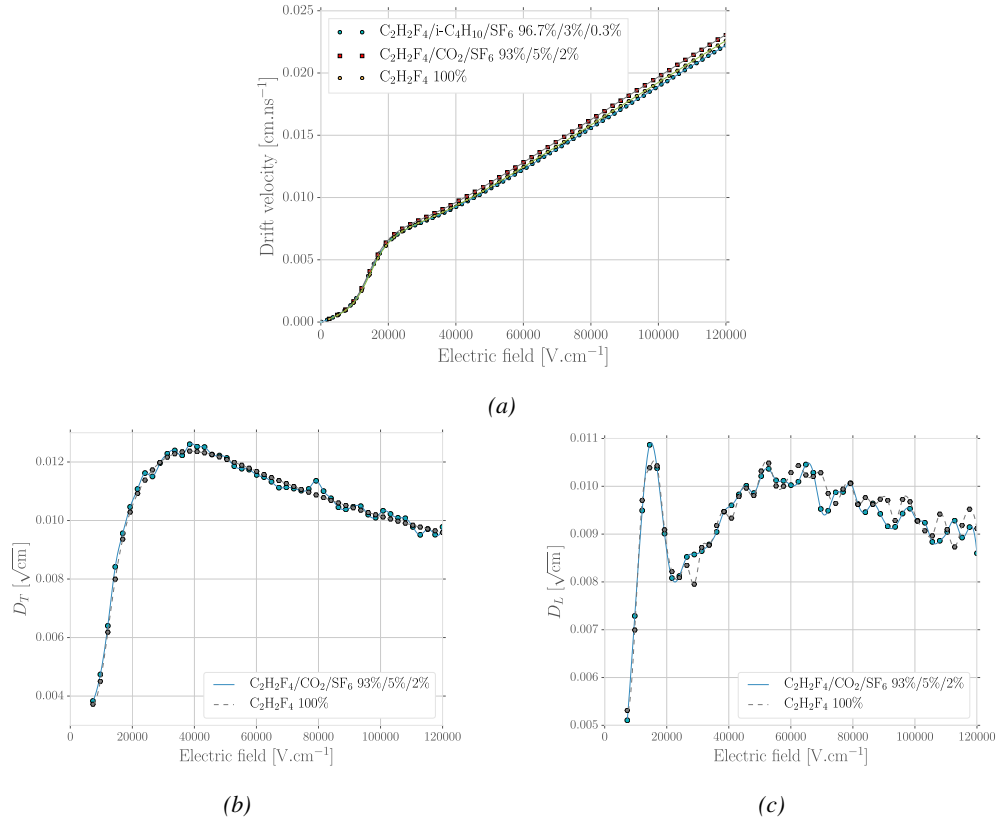


Figure 4.37: Figure 4.37a: Electron mean drift velocity v_D in pure C₂H₂F₄ and typical RPC gas mixtures. Figure 4.37b: Transverse diffusion coefficient in pure C₂H₂F₄ and a typical RPC gas mixture. Figure 4.37c: Longitudinal diffusion coefficient in pure C₂H₂F₄ and a typical RPC gas mixture. All results are given with a pressure $P = 760$ Torr and a temperature $T = 296.15$ K [217].

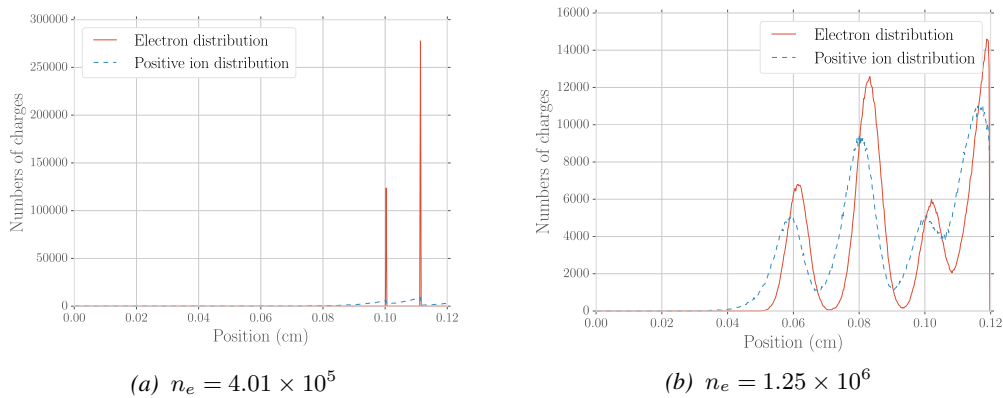


Figure 4.38: Comparison of the free charge carriers in the gas after a time $t = 7.90$ ns in the case where no diffusion is taken into account to simulate the avalanche (Figure 4.38a) and in the case where the diffusion is implemented (Figure 4.38b) [217].

Indeed, at the microscopic scale, the electrons are drifting over a distance δz while acquiring the corresponding kinetic energy $T = e_0 |\vec{E}| \delta z$ until they are slowed down by a collision in which they lose part of their energy. This process is repeated as long as electrons are free carriers. Starting from a point-like electron cloud, the Gaussian density distribution at \vec{r}_0 will be described by Formula 4.19 in which the width of the isotropic distribution is $\sigma = 2\bar{D}t$, with \bar{D} being a diffusion coefficient expressed in m^2/s [199].

$$(4.19) \quad \varphi(\vec{r}, t) = \frac{1}{(\sqrt{2\pi}\sigma(t))^3} \exp\left(-\frac{(\vec{r} - \vec{r}_0)^2}{2\sigma^2(t)}\right)$$

Now, if the constant drifting motion is added, the distribution is anisotropic and can be divided onto transversal (Formula 4.20) and longitudinal (Formula 4.21) terms, $\varphi(r, z, t) = \varphi_T(r, t)\varphi_L(z, t)$, with a cylindrical symmetry around the field axis [199]. The variables t and $\sigma_{T,L}(t)$ can be hidden to the profit of the diffusion coefficients by using the relations $v_D = l/t$ and $\sigma_{T,L}^2(t) = 2\bar{D}_{T,L}l/v_D$ and introducing new diffusion coefficients $D_{T,L} = \sqrt{2\bar{D}_{T,L}/v_D}$ in order to explicitly show the dependence of the Gaussian width in drifted distance l .

$$(4.20) \quad \varphi_T(r, t) = \frac{1}{D_T^2 l} \exp\left(-\frac{(r - r_0)^2}{2D_T^2 l}\right)$$

$$(4.21) \quad \varphi_L(z, t) = \frac{1}{\sqrt{2\pi l D_L}} \exp\left(-\frac{(z - z_0)^2}{2D_L^2 l}\right)$$

These coefficients, as well as the drift velocity of the electrons, can be calculated thanks to Magboltz as showed in Figure 4.37. The influence of the diffusion on the distribution of charge carriers throughout the gas volume is depicted in Figure 4.38. From very localised electron clusters in the gas in Figure 4.38a, a Gaussian diffusion is then visible in Figure 4.38b. Due to the interactions with gas molecules during the drift, diffusions can occur in the forward and backward direction. Electrons diffused backward will effectively drift over a longer distance and multiply more than electrons diffused forward that will see a shorter drift length. As an effect, the avalanche develops over a longer time and extends over a greater gas volume than in the case the electron cloud is considered as point like and without diffusion. Moreover, as a side effect to the longer growth of the avalanche due to backward longitudinal diffusion, the total production of electrons is increased.

4.3.5 Space charge effect & streamers

Now that have been considered the basic processes that influence the development of avalanches in a gaseous detector in the previous sections, it is now important to consider the influence of the charge carriers present in the avalanche on the electric field seen by the avalanche. Indeed, each charged particle induces an electric field and it is only natural that the increasing density of electrons and ions in the detector volume will affect the electric field. Thus, parameters such as the Townsend and attachment coefficients, drift velocity or diffusion coefficients will find themselves to be modified along the gas gap length due to this effect referred to as *space charge effect*. Figure 4.39 is a more detailed version of Figure 4.1 (b) in which three electric regions are distinguished [199]. When compared to the linear electric field of strength E_0 that is developed in between the detector's electrodes, the

2509 accumulation of negative charges (electrons) on the front of the avalanche will reinforce the effective
 2510 electric field in between the anode of the avalanche front. Deeper in the gas volume, the positive
 2511 charges (cations) slowly drift towards the cathode and can induce together with the avalanche front
 2512 opposite electric field loops. Finally, due to the density of positive charges, the electric field seen in
 2513 between the ions tails and the cathode charged with negative charges is on average stronger than E_0
 2514 and compensate for the locally reversed field E_2 . Lippmann roughly estimated by considering that
 2515 10^6 charges were contained in a sphere of radius $r_d = 0.1$ mm that the space charge effect could
 2516 change the electric field by 3% and the Townsend and attachment coefficient up to 14% [199, 217].

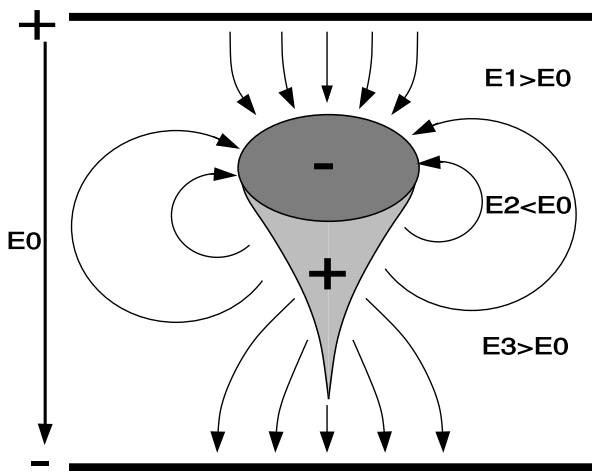


Figure 4.39: Schematic representation of an avalanche and of the electric field deformation it causes due to the local concentration of charge carriers [199].

2517 To account for the space charge effect, the electric potential and field of free charges are solved
 2518 and applied to each charges in the avalanche [199, 217]. As discussed by Français who has been
 2519 working on simulating RPCs similar to that used by the SDHCAL project of ILC, the computation
 2520 of these equations for each individual charge carrier to dynamically know the space charge field at
 2521 every stage of an avalanche development is a difficult task and would require far too much computa-
 2522 tion time and a solution is to pre-compute an interpolation table keeping an adequately large number
 2523 of values of the space charge field for each positions in space thanks to which the values stored in the
 2524 interpolation table become very close to the analytic solution and allow for a much faster simulation.
 2525

2526 The study of space charge effect through simulation shows that it can lead to a saturation of
 2527 the avalanche growth due to the deformation of the electric field, as showed through Figure 4.40.
 2528 Additionnally, a more precise understanding of the space charge effect is given through Figure 4.41
 2529 which looks at the distribution of charges and the distortion of the electric field at different steps of
 2530 the evolution of an avalanche in a RPC. At the moment a 5 GeV muon ionizes the gas, electron-ion
 2531 pairs are created in the gas in different clusters (Figure 4.41a). Later, the first clusters have reached
 2532 the anode while the clusters that where created the closest to the cathode are now big enough to start
 2533 influencing the electric field in the gap (Figure 4.41b). When a cluster is big enough, the electric field
 2534 in front of it locally increases a lot and contributes to a stronger but very localised multiplication. At
 2535 the same moment, the positive ions right behind the cluster avalanche front decrease the electric field,
 2536 saturating the electron multiplication on the tail of the electron cloud (Figure 4.41c). Finally, when

2537 all the electrons have reached the anode and are relaxing, the electric field still is very deformed
 2538 by the distribution of both positive and negative ions in the the gas volume closest to the anode
 2539 (Figure 4.41d).

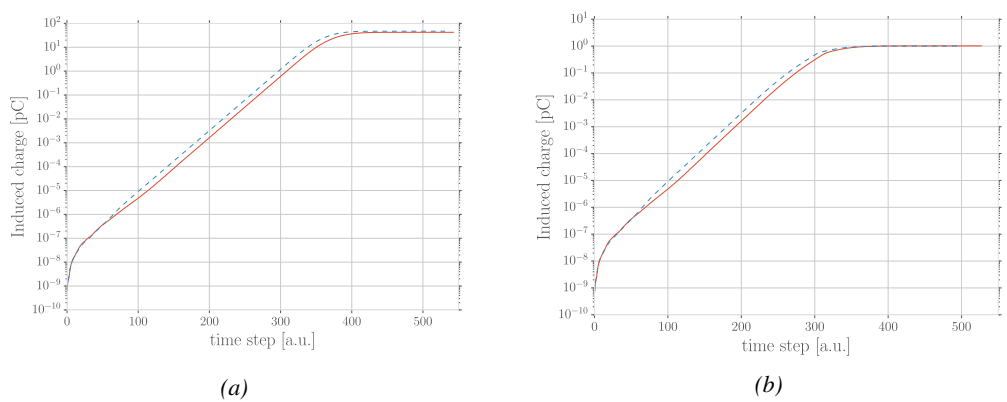


Figure 4.40: Evolution of the charge induced by an avalanche started by a single electron in a 1.2 mm thick RPC with an applied electric field of 54 kV/cm in the case space charge is not taken into account (Figure 4.40a) and in the case it is implemented into the simulation (Figure 4.40b). The total induced charge is correlated to the size of the avalanche [217].

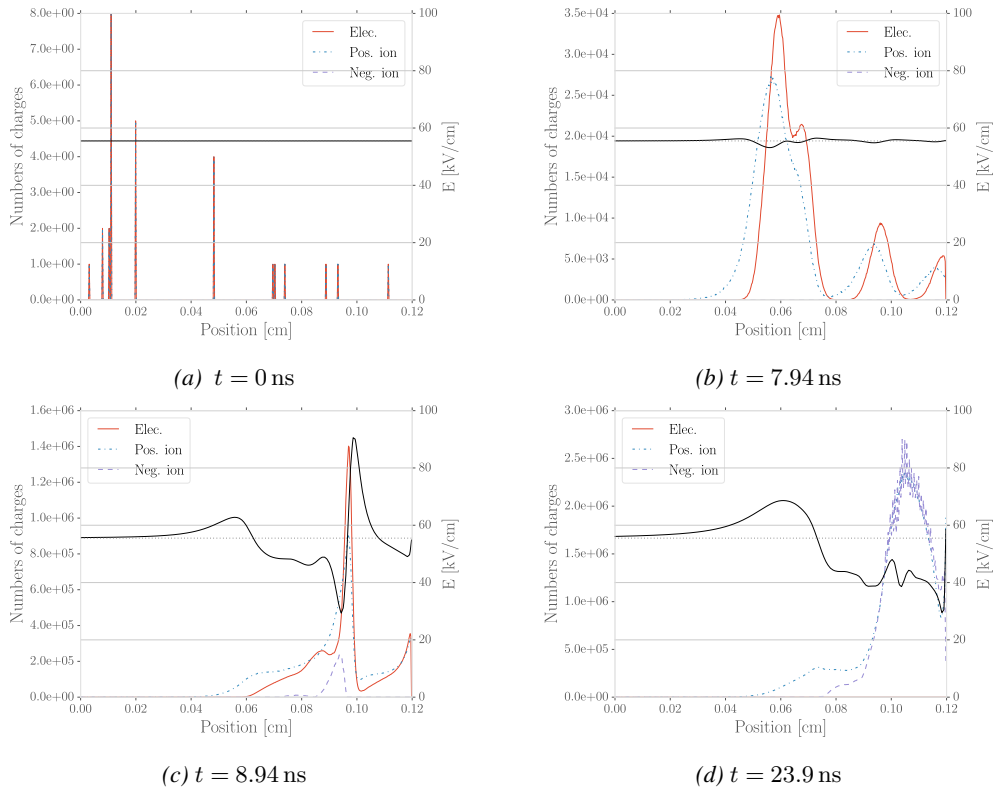


Figure 4.41: Distributions of charge carriers within the gas volume of a 1.2 mm thick RPC and the corresponding deformation of the electric field at different time steps with an applied electric field of 55.5 kV/cm [217].

2540 The electric field following the development of an avalanche can stay perturbed for a long time
 2541 with respect to the avalanche development due to the slow drift of the much heavier ions. This can
 2542 result in powerful secondary avalanches triggered by the fluctuation of the electric field together with
 2543 the emission of UV-photons leading to emission of electrons at the surface of the electrode. This is
 2544 a slow phenomenon compared to the development of avalanches. Experimentally, it is observed that
 2545 the stronger the electric field applied over the gap, the sooner after the avalanche, referred to as *pre-*
 2546 *cursor signal* in this context, and the stronger will the secondary avalanche be, possibly reaching the
 2547 streamer regime. This could be due to the amount of UV-photons emitted by the growing precursor.
 2548 These photons will be able to trigger new avalanches in a radius of a few mm around the precursor
 2549 by knocking electrons from the cathode by photoelectric effect. The strong distortions of the electric
 2550 field due to a large avalanche will be more likely to emit UV-photons as the electric field at the front
 2551 of the precursor avalanche will be large, providing the electrons with a larger energy. Eventually, the
 2552 new avalanches can grow to form streamers.

2553 4.4 Effect of atmospherical conditions on the detector's performance

2554

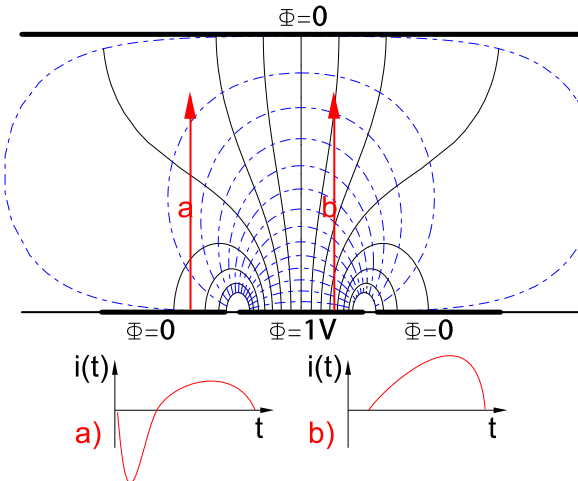


Figure 4.42: Representation of the weighting field in the volume of a RPC and the resulting induced current in the strip placed at 1 V and its neighbour connected to the ground. The induced current corresponds, as can be understood from Formula 4.22 [199].

2555 Accordingly to Ramo's theorem, the movement of charge carriers, and in particular, the movement
 2556 of a dense electron cloud toward the anode induces a current signal on one or more of the readout
 2557 electrodes (strips or pads). The ions on the other hand induce only a very small current as their
 2558 movement is much slower than which of the electrons. The current induced by n_{Cl} clusters of $N_j(t)$
 2559 charge carriers drifting at velocities $\vec{v}_{Dj}(t) = \vec{x}_j(t)$ at a time t is given by Formula 4.22 in which e_0
 2560 is the unit charge and \vec{E}_w is the weighting field.

$$(4.22) \quad i(t) = \sum_{j=1}^{n_{Cl}} \vec{E}_{wj}(\vec{x}_j(t)) \cdot \vec{v}_{Dj}(t) e_0 N_j(t)$$

2561 The weighting field, that has been schematised in Figure 4.42, corresponds to the electric field
 2562 that would be observed in the gas gap if a readout electrode is placed at a potential of 1 V while
 2563 keeping all the other electrodes grounded. Then the induced charge in the readout can be simply
 2564 obtained by integrating Formula 4.22 over the duration T of the signal, as given by Formula 4.23.

$$(4.23) \quad Q(t) = \int_0^T \sum_{j=1}^{n_{Cl}} \vec{E}_{wj}(\vec{x}_j(t)) \cdot \vec{v}_{Dj}(t) e_0 N_j(t)$$

2565 The signal induced in the readout of RPCs operated in avalanche mode is then sent into Front-
 2566 End Electronics in which they will be pre-amplified and discriminated. The discrimination and
 2567 digitization of signals in CMS FEE is described through Figure 4.43. On a first stage, analogic sig-
 2568 nals are amplified, following the curve given on Figure 4.44, and then sent to the Constant Fraction

2569 Discriminator (CFD) described in Figure 4.45. At the end of the chain, 100 ns long pulses are sent
 2570 in the LVDS output. The digital signals are both used as trigger for CMS and to evaluate the per-
 2571 formance of the detectors. The performance will depend on the applied HV, i.e. on the electric field
 2572 inside of the gas volume, but also on the threshold applied on the CFDs. Indeed, in order to reduce
 2573 the probability to measure noise, the threshold is set to a level where the noise is strongly suppressed
 2574 while the signals are not too affected. Typically, CMS FEEs are set to a threshold of 215 mV after
 2575 pre-amplification, corresponding to an input charge of about 140 fC.

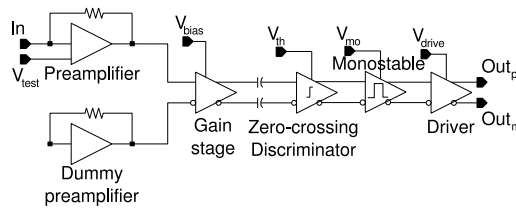


Figure 4.43: Schematics of CMS RPC FEE logic.

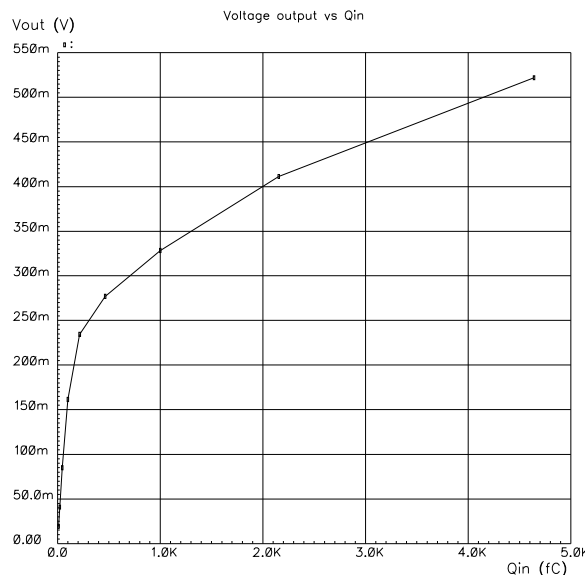


Figure 4.44: Equivalence in between the charge of the induced signal in input of the CMS FEE and the signal strength on the output of the pre-amplifier.

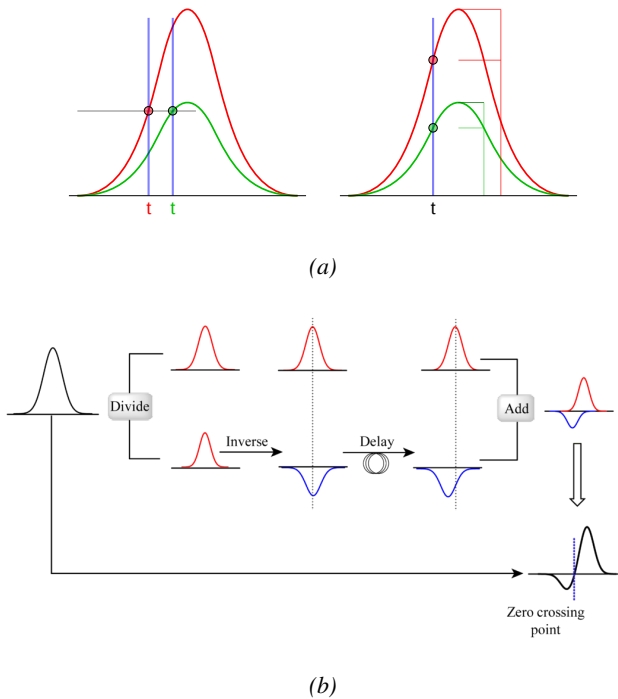


Figure 4.45: Description of the principle of a CFD. A comparison of threshold triggering (left) and constant fraction triggering (right) is shown in Figure 4.45a. Constant fraction triggering is obtained thanks to zero-crossing technique as explained in Figure 4.45b. The signal arriving at the input of the CFD is split into three components. A first one is delayed and connected to the inverting input of a first comparator. A second component is connected to the noninverting input of this first comparator. A third component is connected to the noninverting input of another comparator along with a threshold value connected to the inverting input. Finally, the output of both comparators is fed through an AND gate.

The performance of a detector is then simply measured relatively to which of a reference detector used as trigger as the ratio in between the number of events recorded in coincidence in the detector and the reference and the total amount of trigger events, $\epsilon = n_{events}/n_{triggers}$. An example of efficiency measured as a function of the effective voltage HV_{eff} is given in Figure 4.46 and can be fitted thanks to a sigmoidal function described as in Formula 4.24 and where ϵ_{max} is the maximal efficiency of the detector, λ is proportional to the slope at half maximum and HV_{50} is the value of the voltage when the efficiency reaches half of the maximum.

$$(4.24) \quad \epsilon(HV_{eff}) = \frac{\epsilon_{max}}{1 + e^{-\lambda(HV_{eff} - HV_{50})}}$$

CMS RPC also define two points on this sigmoid that called *knee* and *working point*. The corresponding voltages HV_{knee} is defined as the voltage at 95% of the maximum efficiency, and HV_{WP} is defined as in Formula 4.25.

$$(4.25) \quad HV_{WP} = HV_{knee} + \begin{cases} 100V & (\text{barrel}) \\ 150V & (\text{endcap}) \end{cases}$$

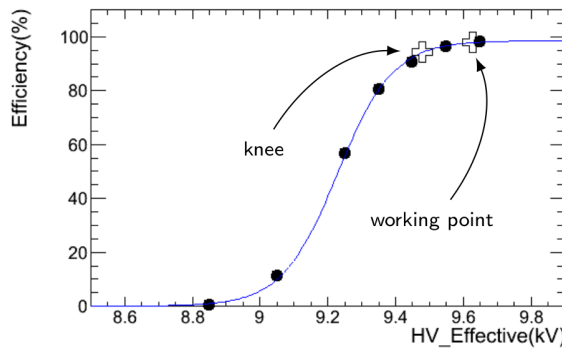


Figure 4.46: Typical efficiency sigmoid of a CMS RPC detector. The black dots correspond to the data, the blue line to the sigmoid fit and the opened cross to the knee and working extracted from the fit line.

Nevertheless, the voltage applied on a detector may vary due to a change in environmental conditions. Indeed, the variation of temperature and/or pressure will have effects on the gas density and the electrodes' resistivity which can be overcome by changing the electric field accordingly. The variation in temperature and pressure are depicted respectively in Figure 4.47 and Figure 4.48. A standard procedure to correct for temperature and pressure variations is to keep the factor $HV \cdot T/P$ constant using Formula 4.26 [231, 232] with reference values for T_0 and P_0 . For example, CMS uses $T_0 = 293.15$ K and $P_0 = 965$ hPa.

$$(4.26) \quad HV_{app} = HV_{eff} \frac{P_0}{P} \frac{T}{T_0}$$

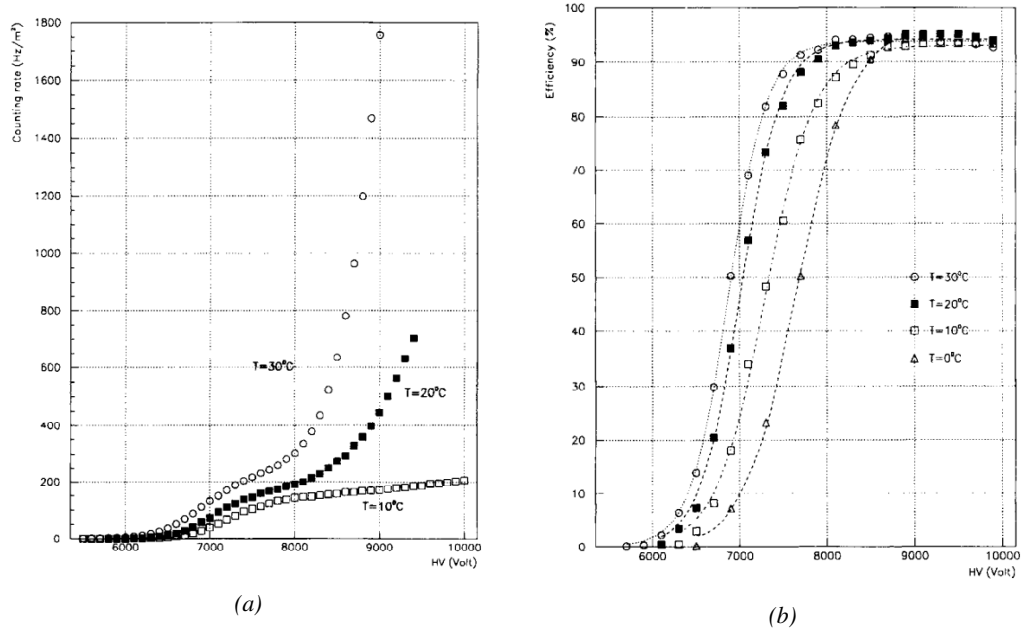


Figure 4.47: Effect of the temperature variation on the rate (Figure 4.47a) and the efficiency (Figure 4.47b) of a RPC [231].

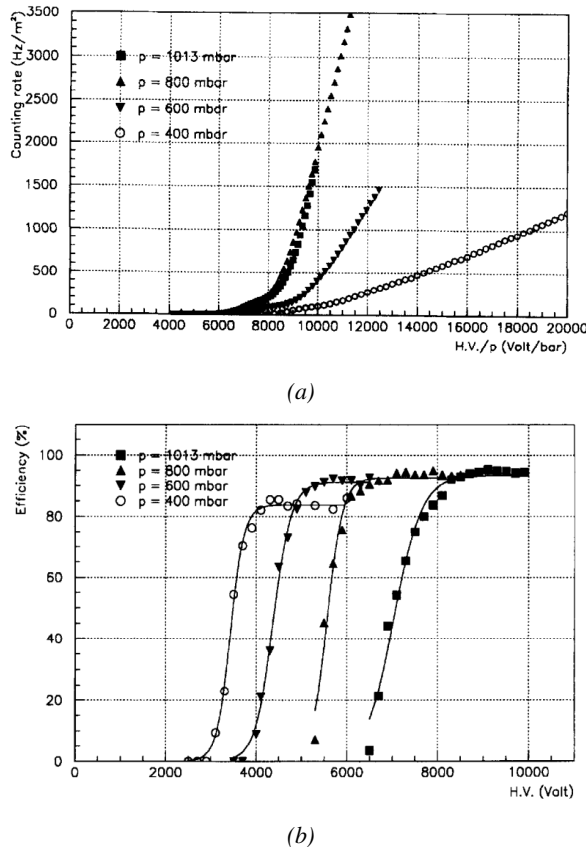


Figure 4.48: Effect of the pressure variation on the rate (Figure 4.48a) and the efficiency (Figure 4.48b) of a RPC [232].

It was actually found that such a simple procedure would overcorrect the applied voltage in the case the variations of temperature or pressure were too important [233–236]. CMS, considering that the temperature variations in the detector cavern were very small, decided only to improve the pressure correction, giving rise to Formula 4.27 [233] while on the other hand, ATLAS decided to have a more robust correction for both parameters and uses Formula 4.28 instead [236]. The coefficients α , in the case of CMS, and α, β , in the case of ATLAS, are extracted from fit on available dataset obtained during the operation of the detectors.

$$(4.27) \quad HV_{app} = HV_{eff} \left(1 - \alpha + \alpha \frac{P_0}{P} \right) \frac{T}{T_0}, \quad \alpha = 0.8$$

$$(4.28) \quad HV_{eff} = HV_{app} \left(1 + \alpha \frac{\Delta T}{T_0} \right) \left(1 - \beta \frac{\Delta P}{P_0} \right), \quad \alpha = 0.5, \beta = 0.71$$

5

2600

2601

2602

Longevity studies and Consolidation of the present CMS RPC subsystem

2603 The RPC system, located in both barrel and endcap regions, provides a fast, independent muon trigger
2604 with a looser p_T threshold over a large portion of the pseudo-rapidity range ($|\eta| < 1.6$). During
2605 HL-LHC operations the expected conditions in terms of background and pile-up will make the iden-
2606 tification and correct p_T assignment a challenge for the muon system. The goal of RPC upgrade is to
2607 provide additional hits to the Muon System with more precise timing. All this information will be
2608 elaborated by the Trigger System in a global way enhancing the performance of the trigger in terms
2609 of efficiency and rate control. The RPC Upgrade is based on two projects: an improved Link Board
2610 System and the extension of the RPC coverage up to $|\eta| = 2.4$.

2611 The Link Board System is responsible for the processing, the synchronization and the zero-
2612 suppression the signals coming from the RPC FEBs. The Link Board components have been pro-
2613 duced between 2006 and 2007 and will be subjected to ageing and failure on a long term scale. An
2614 upgraded Link Board System will overcome the ageing problems and will allow for a more precise
2615 timing information to the RPC hits from 25 to 1.5 ns.

2616 In order to develop an improved RPC that fulfills CMS requirements, an extensive R&D program is
2617 being conducted. The benefits of adding two new RPC layers in the innermost ring of stations 3 and
2618 4 will be mainly observed in the neutron-induced background reduction and efficiency improvement
2619 for both trigger and offline reconstruction.

2620 The coverage of the RPC System up to higher pseudo-rapidity $|\eta| = 2.1$ was part of the original
2621 CMS TDR. Nevertheless, the expected background rates being higher than the certified rate capabili-
2622 ty of the present CMS RPCs in that region and the budget being limited, RPCs were restricted to a
2623 shorter range. Even though the iRPC technology that will equip the extension of the Muon System
2624 will be different than the current CMS RPC technology, it is necessary to certify the rate capability
2625 and longevity of the existing detectors as the radiation level will increase together with the increase
2626 of instantaneous luminosity of the LHC. For this purpose, spare RPC detectors built but not installed
2627 in CMS have been installed in different irradiation facilities, first of all, to certify the detectors to the

new levels of irradiation they will be subjected to and, finally, to study their ageing and certify their good operation throughout the HL-LHC program.

5.1 Testing detectors under extreme conditions

The upgrade from LHC to HL-LHC will increase the peak luminosity from $10^{34} \text{ cm}^{-2} \text{ s}^{-1}$ to reach $5 \times 10^{34} \text{ cm}^{-2} \text{ s}^{-1}$, increasing in the same way the total expected background to which the RPC System will be subjected to. Mainly composed of low energy gammas, neutrons, and electrons and positrons from p - p collisions, but also of low momentum primary and secondary muons, punch-through hadrons from calorimeters, and particles produced in the interaction of the beams with collimators, the background will mostly affect the regions of CMS that are the closest to the beam line, i.e. the RPC detectors located in the endcaps.

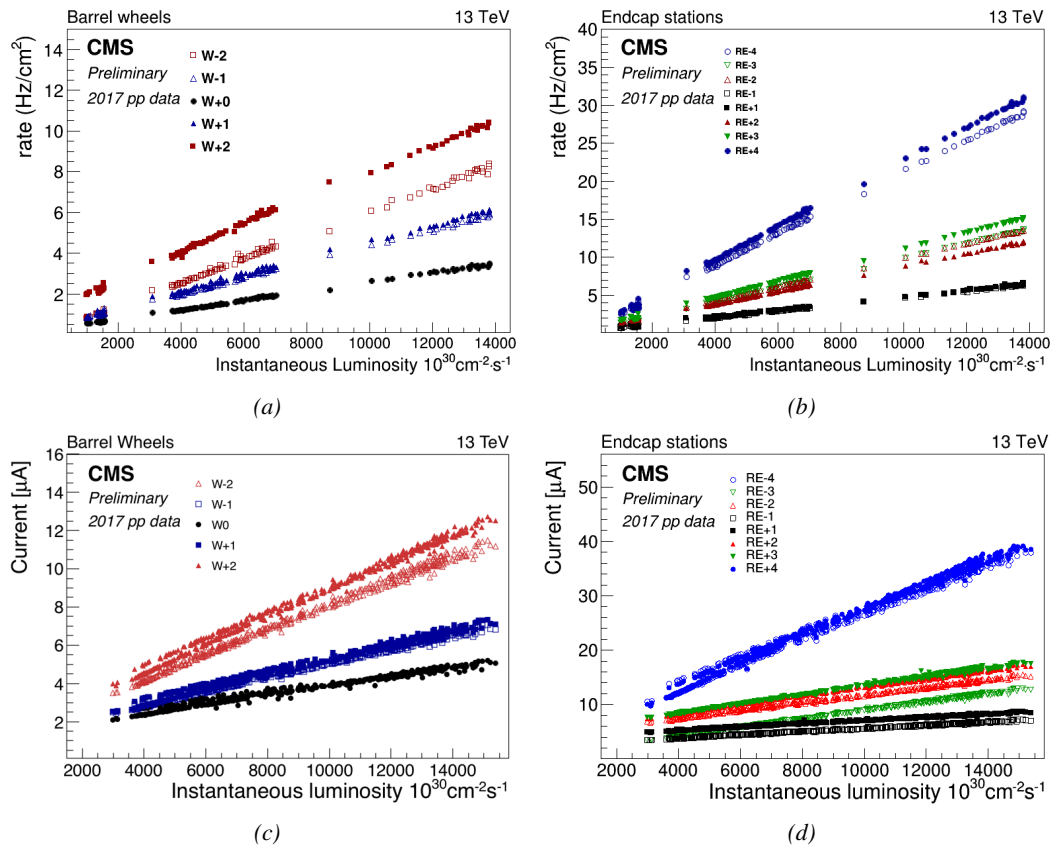


Figure 5.1: Mean RPC Barrel (left column) and Endcap (right column) rate (top row) and current (bottom row) as a function of the instantaneous luminosity as measured in 2017 p - p collision data.

Data collected over 2017, presented through Figure 5.1, allows to study the values of the background rate in all the RPC System. This was achieved thanks to a monitoring of the rates in each RPC rolls, where rolls correspond to the pseudo-rapidity partitioning of the readout electronics, and of the current in each HV channel. A linear dependence in between the mean rate or current with

instantaneous luminosity is showed in selected runs with identical LHC running parameters. In Figure 5.2, a linear extrapolation of the distribution of the background hit rate per unit area as well as the integrated charge is showed at a HL-LHC condition. The maximum rate per unit area in the endcap detectors at HL-LHC conditions is expected to be of the order of 600 Hz/cm^2 while the charge deposition should exceed 800 mC/cm^2 . The detectors will then be certified up to an irradiation of 840 mC/cm^2 . These extrapolations are provided with a required safety factor 3 for the certification study.

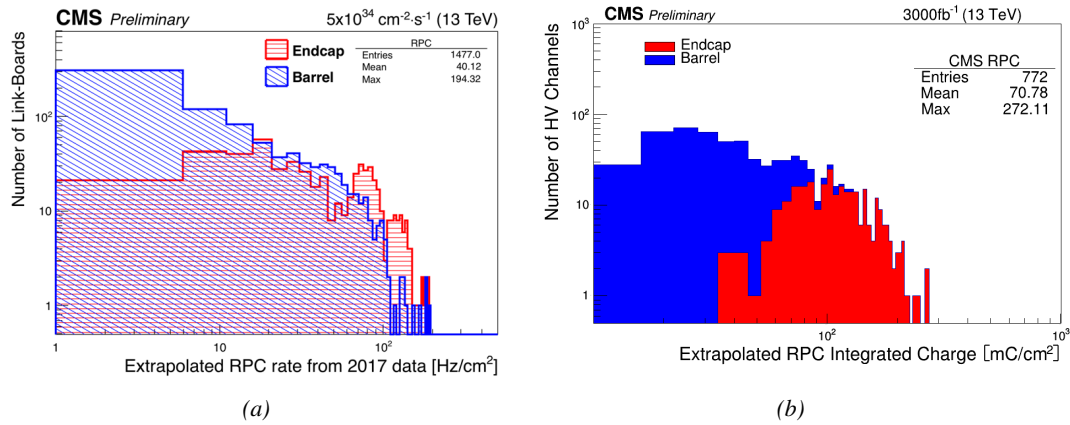


Figure 5.2: Figure 5.2a: The hit rate per region (Barrel, Endcap) is linearly extrapolated to HL-LHC highest instantaneous luminosity ($5 \times 10^{34} \text{ cm}^{-2} \text{ s}^{-1}$) using the rate as a function of instantaneous luminosity recorded by RPCs in 2017 showing a linear dependence. Figure 5.2b: The integrated charge per region (Barrel, Endcap) is extrapolated to HL-LHC integrated luminosity (3000 fb^{-1}) using the data accumulated in 2016 in every HV channels.

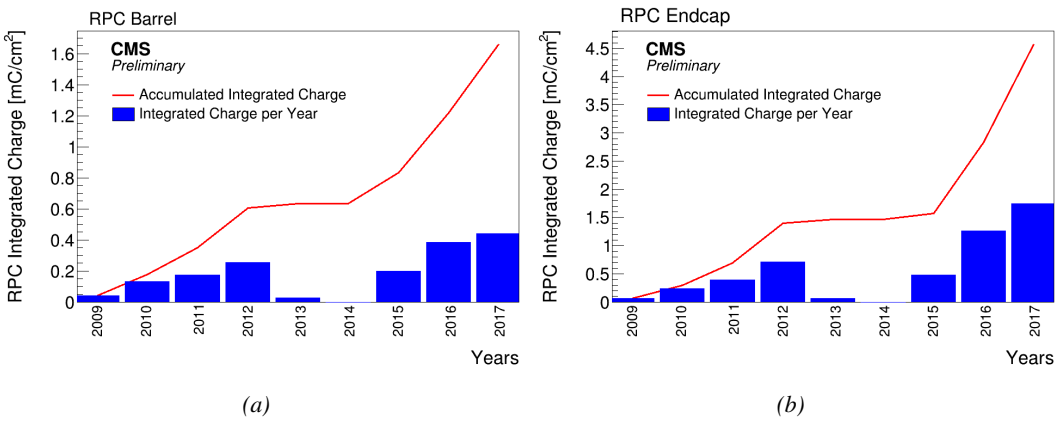


Figure 5.3: CMS RPC mean integrated charge in the Barrel region (Figure 5.3a) and the Endcap region (Figure 5.3b). The integrated charge per year is shown in blue. The red curve shows the evolution of the accumulated integrated charge through time. The blank period in 2013 and 2014 corresponds to LS1. The total integrated charge for the entire operation period (Oct.2009 - Dec.2017) is estimated to be about 1.66 mC/cm^2 in the Barrel and 4.58 mC/cm^2 in the Endcap.

In the past, extensive long-term tests were carried out at several gamma and neutron facilities

certifying the detector performance. Both full size and small prototype RPCs have been irradiated with photons up to an integrated charge of $\sim 0.05 \text{ C/cm}^2$ and $\sim 0.4 \text{ C/cm}^2$ respectively and were certified for rates reaching 200 Hz/cm^2 [237, 238]. Since the beginning of Run-I until December 2017, the RPC system provided stable operation and excellent performance and did not show any ageing effects for a maximum integrated charge in a detector of the order of 0.01 C/cm^2 - the average being of the order of 2 mC/cm^2 in the Barrel and 5 mC/cm^2 in the Endcap, closer to the beam line, as can be seen from Figure 5.3 - and a peak luminosity reaching $1.4 \times 10^{34} \text{ cm}^{-2} \text{ s}^{-1}$ during 2017 data taking period.

To perform the necessary studies on the present CMS RPC detectors, facilities offering the possibility to irradiate the chambers are necessary in order to recreate HL-LHC conditions or stronger and study their performance through time. Such facilities exist at CERN and were exploited to conduct this study. A first series of preliminary studies were conducted in the former gamma facility of CERN (GIF) before its dismantlement. This preliminary study was used as a stepping stone towards the building of a more powerful irradiation fully dedicated to longevity studies of CMS and ATLAS subsystems in the perspective of HL-LHC. The period of preliminary work has also been a key moment in the elaboration and improvement of data acquisition, offline analysis and online monitoring tools that are extensively used in the new gamma irradiation facility.

5.1.1 GIF

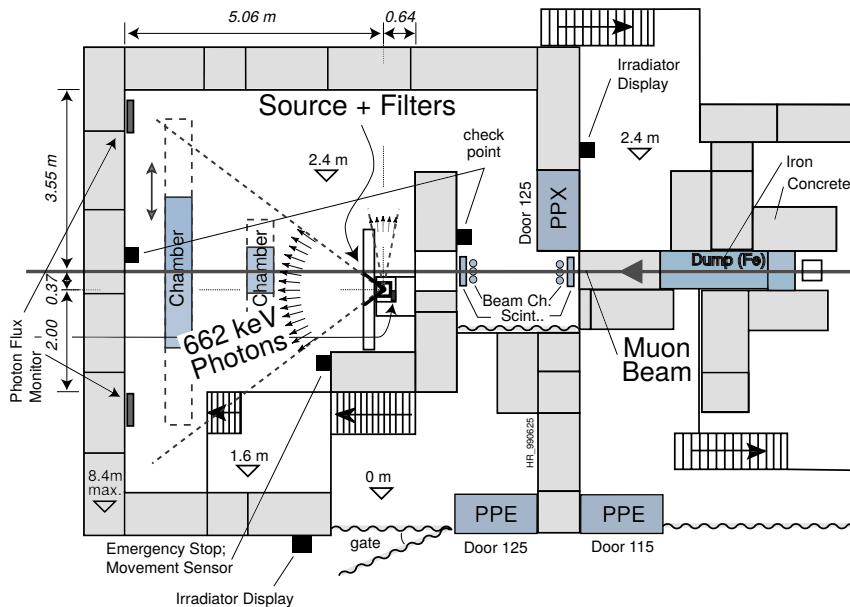


Figure 5.4: Layout of the test beam zone called X5c GIF at CERN. Photons from the radioactive source produce a sustained high rate of random hits over the whole area. The zone is surrounded by 8 m high and 80 cm thick concrete walls. Access is possible through three entry points. Two access doors for personnel and one large gate for material. A crane allows installation of heavy equipment in the area.

Located in the SPS West Area at the downstream end of the X5 test beam, the Gamma Irradiation Facility (GIF) was a test area in which particle detectors were exposed to a particle beam in presence of an adjustable gamma background [239]. Its goal was to reproduce background conditions these

detectors would suffer in their operating environment at LHC. GIF layout is showed in Figure 5.4. Gamma photons are produced by a strong ^{137}Cs source installed in the upstream part of the zone inside a lead container. The source container includes a collimator, designed to irradiate a $6 \times 6 \text{ m}^2$ area at 5 m maximum to the source. A thin lens-shaped lead filter helps providing with a uniform out-coming flux in a vertical plane, orthogonal to the beam direction. The photon rate is controlled by further lead filters allowing the maximum rate to be limited and to vary within a range of four orders of magnitude. Particle detectors under test are then placed within the pyramidal volume in front of the source, perpendicularly to the beam line in order to profit from the homogeneous photon flux. Adjusting the background flux of photons can then be done by using the filters and choosing the position of the detectors with respect to the source.

As described on Figure 5.5, the ^{137}Cs source emits a 662 keV photon in 85% of the decays. An activity of 740 GBq was measured on the 5th of March 1997. To estimate the strength of the flux in 2014, was considered the nuclear decay through time associated to the Cesium source whose half-life is well known ($t_{1/2} = (30.05 \pm 0.08) \text{ y}$). The GIF tests were done in between the 20th and the 31st of August 2014, i.e. at a time $t = (17.47 \pm 0.02) \text{ y}$ resulting in an attenuation of the activity from 740 GBq in 1997 to 494 GBq in 2014.

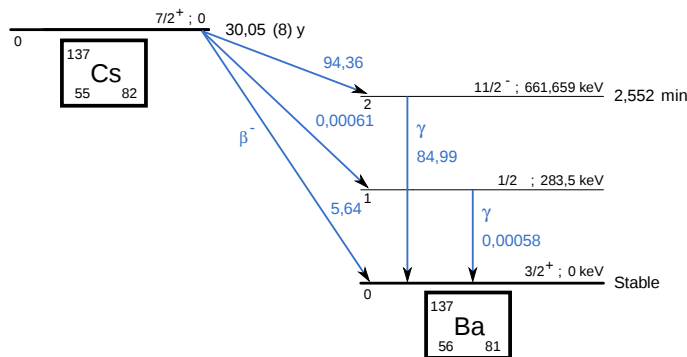


Figure 5.5: ^{137}Cs decays by β^- emission to the ground state of ^{137}Ba (BR = 5.64%) and via the 662 keV isomeric level of ^{137}Ba (BR = 94.36%) whose half-life is 2.55 min.

5.1.2 GIF++

The new Gamma Irradiation Facility (GIF++), located in the SPS North Area at the downstream end of the H4 test beam, has replaced its predecessor during LS1 and has been operational since spring 2015 [240]. Like GIF, GIF++ features a ^{137}Cs source of 662 keV gamma photons, their fluence being controlled with a set of filters of various attenuation factors. The source provides two separated large irradiation areas for testing several full-size muon detectors with homogeneous irradiation, as presented in Figure 5.6.

The source activity was measured to be about 13.5 TBq in March 2016. The photon flux being far greater than HL-LHC expectations, GIF++ provides an excellent facility for accelerated ageing tests of muon detectors. The source is situated in a bunker designed to perform irradiation test along a muon beam line, the muon beam being available during selected periods throughout the year. The H4 beam, providing the area with muons with a maximum momentum of about 150 GeV/c, passes through the GIF++ zone and is used to periodically study the performance of the detectors placed under long term irradiation. Its flux is of $104 \text{ particles/s/cm}^2$ focused in an area similar to

2701 $10 \times 10 \text{ cm}^2$. Therefore, with properly adjusted filters, one can simulate the background expected at
 2702 HL-LHC and study the performance and ageing of muon detectors in HL-LHC environment.

2703

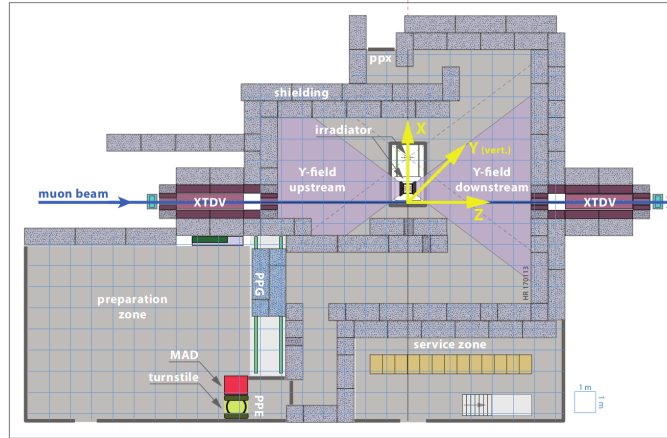


Figure 5.6: Floor plan of the *GIF++* facility. When the facility downstream of the *GIF++* takes electron beam, a beam pipe is installed along the beam line (z -axis). The irradiator can be displaced laterally (its center moves from $x = 0.65 \text{ m}$ to 2.15 m), to increase the distance to the beam pipe.

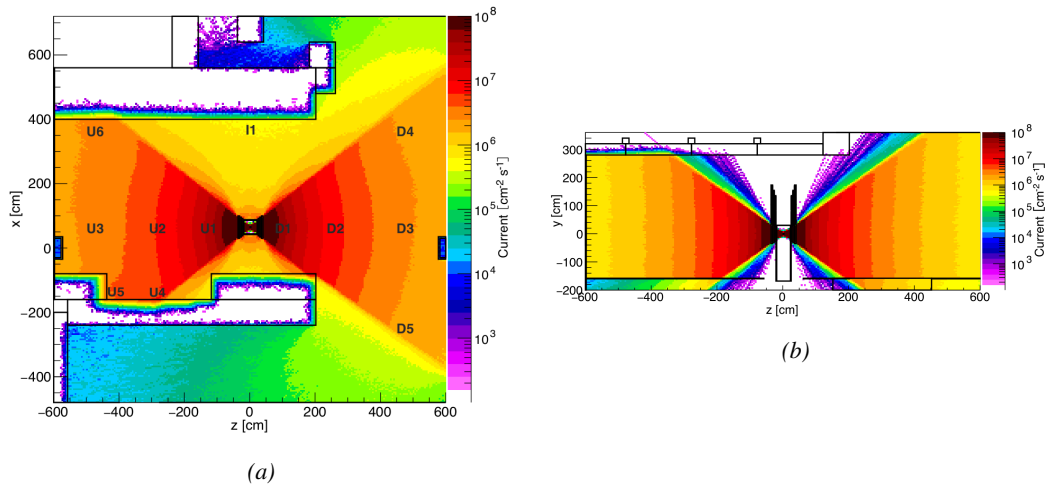


Figure 5.7: Simulated unattenuated current of photons in the xz plane (Figure 5.7a) and yz plane (Figure 5.7b) through the source at $x = 0.65 \text{ m}$ and $y = 0 \text{ m}$ [241]. With angular correction filters, the current of 662 keV photons is made uniform in xy planes.

2704 The gamma current as simulated with GEANT4 is presented in Figure 5.7 in which the labels
 2705 UN, DN, with $N \in [1 : 5]$ and I1 correspond to the position of different Radiation Monitoring
 2706 (RADMON) sensors dedicated to measuring the irradiation in the bunker area [241]. According to
 2707 the simulation results, that agree within 12% to the doses measured with the RADMONs, the RPCs
 2708 that will be tested in *GIF++* can expect a maximal gamma current of the order of 2 to 5×10^6

2709 $\text{cm}^{-2} \text{s}^{-1}$ assuming they will always stay in a region in between sensor U5 and the back wall of the
 2710 upstream area.

2711 5.2 Preliminary studies at GIF

2712 5.2.1 RPC test setup

2713 During summer 2014, preliminary tests have been conducted in the GIF area on an endcap chamber
 2714 of type RE4/2 and labeled RE-4-2-BARC-161 produced for the extension of the endcap with a
 2715 fourth disk in 2013. This chamber has been placed into a trolley covered with a tent. The position
 2716 of the RPC inside the tent and of the tent with respect to the source in the bunker are described in
 2717 Figure 5.8. The goal of the study were to have a preliminary understanding of the rate capability
 2718 of the present technology used in CMS. It was decided to measure the efficiency of the RPC under
 2719 irradiation at detecting cosmic muons as, at the time of the tests, the beam not operational anymore.
 2720 Three different absorber settings were used and compared to the case where the detector was not ir-
 2721 radated in order to study the evolution of the performance of the detector with increasing exposition
 2722 to gamma radiation. First of all, measurements were done with fully opened source. To complete
 2723 this preliminary study, the gamma flux has been attenuated by a factor 2, a factor 5 and finally the
 2724 source was shut down. Was measured the efficiency of the RPC at detecting the cosmic muons in
 2725 coincidence with a cosmic trigger as well as the background rate as seen by the detectors.

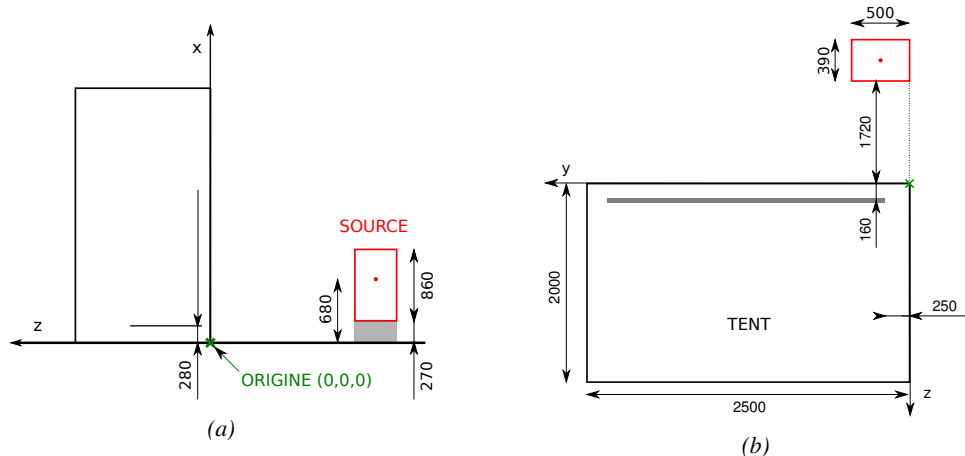


Figure 5.8: Description of the RPC setup. Dimensions are given in mm. A tent containing RPCs is placed at 1720 mm from the source container. The source is situated in the center of the container. RE-4-2-BARC-161 chamber is 160 mm inside the tent. This way, the distance between the source and the chambers plan is 2060 mm. Figure 5.8a provides a side view of the setup in the xz plane while Figure 5.8b shows a top view in the yz plane.

2726 The trigger system was composed of 2 plastic scintillators and was placed in front of the setup
 2727 with an inclination of 10° with respect to the detector plane in order to look at cosmic muons. Using
 2728 this particular trigger layout, showed in Figure 5.9, leads to a cosmic muon hit distribution into the
 2729 chamber similar to the one of Figure 5.10. Measured without gamma irradiation, two peaks can
 2730 be seen on the profile of readout partition B, centered on strips 52 and 59. Section 5.2.2 will help
 2731 us understand that these two peaks are due respectively to forward and backward coming cosmic

²⁷³² particles where forward coming particles are first detected by the scintillators and then the RPC
²⁷³³ while the backward coming muons are first detected in the RPC.



Figure 5.9: RE-4-2-BARC-161 chamber is inside the tent as described in Figure 5.8. In the top right, the two scintillators used as trigger can be seen. This trigger system has an inclination of 10° relative to horizontal and is placed above half-partition B2 of the RPCs. PMT electronics are shielded thanks to lead blocks placed in order to protect them without stopping photons from going through the scintillators and the chamber.

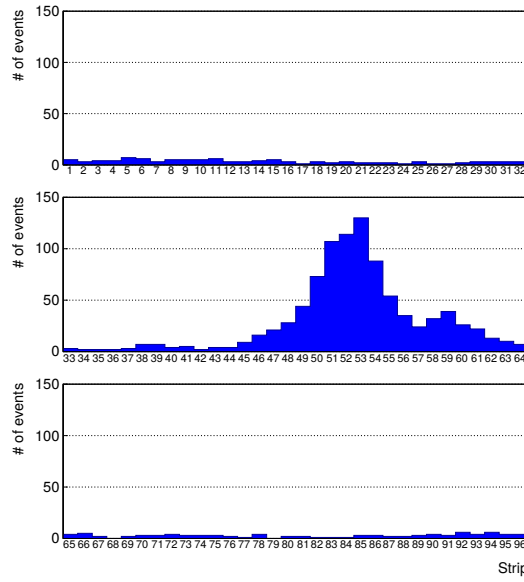


Figure 5.10: Hit distributions over all 3 partitions of RE-4-2-BARC-161 chamber is showed. Top, middle and bottom figures respectively correspond to partitions A, B, and C. The profiles show that some events still occur in other half-partitions than B2, which corresponds to strips 49 to 64, in front of which the trigger is placed, contributing to the inefficiency of detection of cosmic muons. In the case of partitions A and C, the very low amount of data can be interpreted as noise. On the other hand, it is clear that a little portion of muons reach the half-partition B1, corresponding to strips 33 to 48.

2734 The data taking is then performed thanks to a CEAN TDC module of type V1190A [242] to
 2735 which is connected the digitized output of the RPC Front-End Board, as described in Figure 5.11a
 2736 and the trigger signal from the telescope. The communication with the computer is performed thanks
 2737 to a CAEN communication module of type V1718 [243]. In order to control the rates recorded by
 2738 the detector, the digitized RPC signals are also sent to scalers as described in Figure 5.11b. The
 2739 C++ DAQ software used in GIF was developed as an early attempt towards the understanding of
 2740 the CAEN libraries and the data collected by the TDCs was saved into .dat files is analysed with
 2741 an algorithm computing parameters such as efficiency, hit profile, cluster size, or gamma and noise
 2742 rates which was developed with C++ as well. Finally, histograms and curves are produced using
 2743 ROOT.

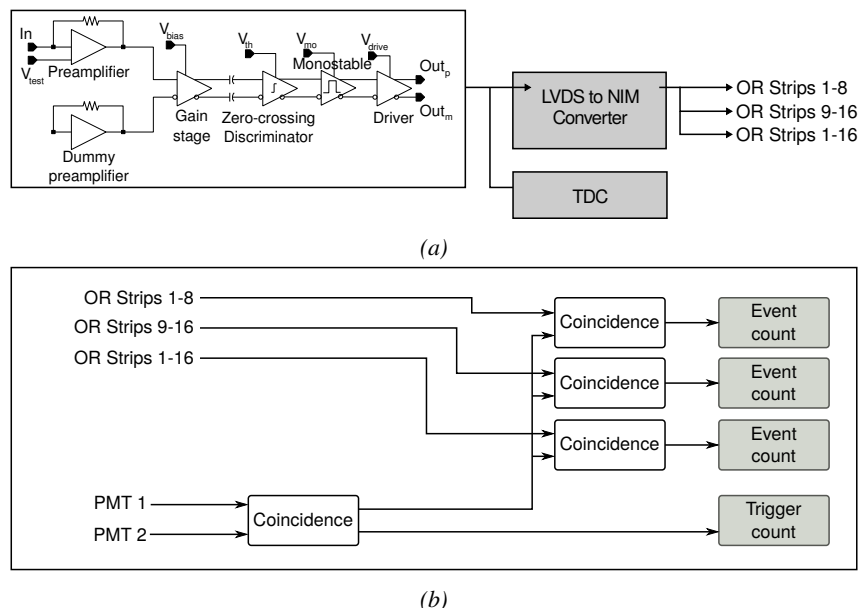


Figure 5.11: Signals from the RPC strips are shaped by the FEE described on Figure 5.11a. Output LVDS signals are then read-out by a TDC module connected to a computer or converted into NIM and sent to scalers. Figure 5.11b describes how these converted signals are put in coincidence with the trigger.

2744 5.2.2 Geometrical acceptance of the setup layout to cosmic muons

2745 In order to profit from a constant gamma irradiation, the detectors inside of the GIF bunker need
 2746 to be placed in a plane orthogonal to the beam line. The muon beam that used to be available was
 2747 meant to test the performance of detectors under test. This beam not being active anymore, an other
 2748 solution to test detector performance had to be used. Thus, it has been decided to use cosmic muons
 2749 detected through a telescope composed of two scintillators. Lead blocks were used as shielding to
 2750 protect the photomultipliers from gammas as can be seen from Figure 5.9.

2751 An inclination of $\sim 10^\circ$ has been given to the cosmic telescope to maximize the muon flux. A
 2752 good compromise had to be found between good enough muon flux and narrow enough hit distribution
 2753 to be sure to contain all the events into only one half partitions as required from the limited
 2754 available readout hardware. It was then foreseen to detect muons and read them out only from
 2755 half-partition B2, the last 16 channels of readout partition B (i.e. strips 49 to 64). Nevertheless,

a consequence of the misplaced trigger, that can be seen as a loss of events in half-partition B1 (strips 33 to 48) in Figure 5.10, is an inefficiency. The observed inefficiency of approximately 20% highlighted in Figure 5.12 by comparing the performance of chamber RE-4-2-BARC-161 as measured prior to the study at GIF and at GIF without irradiation seems too important, compared to the 12.7% of data contained into the first 16 strips observed on Figure 5.10, to only be explained by the geometrical acceptance of the setup itself. Simulations have been conducted to show how the setup brings inefficiency.

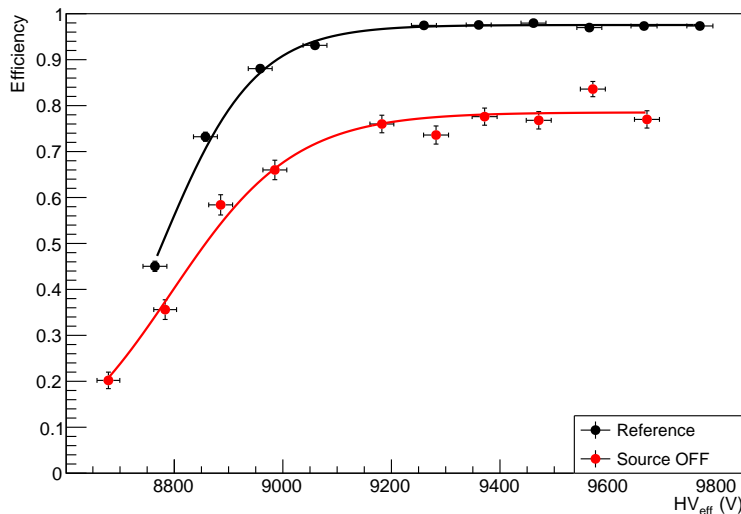


Figure 5.12: Results are derived from data taken on half-partition B2 only. On the 18th of June 2014, data has been taken on chamber RE-4-2-BARC-161 at CERN building 904 (Prevessin Site) with cosmic muons providing us a reference efficiency plateau of $(97.54 \pm 0.15)\%$ represented by a black curve. A similar measurement has been done at GIF on the 21st of July with the same chamber giving a plateau of $(78.52 \pm 0.94)\%$ represented by a red curve.

5.2.2.1 Description of the simulation layout

The layout of GIF setup has been reproduced, only roughly using Figure 5.9 due to the lack of measures, and incorporated into a C++ Monte Carlo (MC) simulation to study the geometrical acceptance of the telescope projected onto the readout strips [244]. A 3D view of the simulated layout is given into Figure 5.13. Muons are generated randomly in a horizontal plane located at a height corresponding to the lowest point of the PMTs. This way, the needed size of the plane in order to simulate events happening at very large azimuthal angles (i.e. $\theta \approx \pi$) can be kept relatively small while the total number of muon tracks to propagate is kept relatively small. The muon flux is designed to follow the usual $\cos^2\theta$ distribution for cosmic particles. The goal of the simulation is to look at muons that pass through the telescope composed of the two scintillators and define their distribution onto the RPC read-out plane. During the reconstruction, the read-out plane is then divided into read-out strips and each muon track is assigned to a strip.

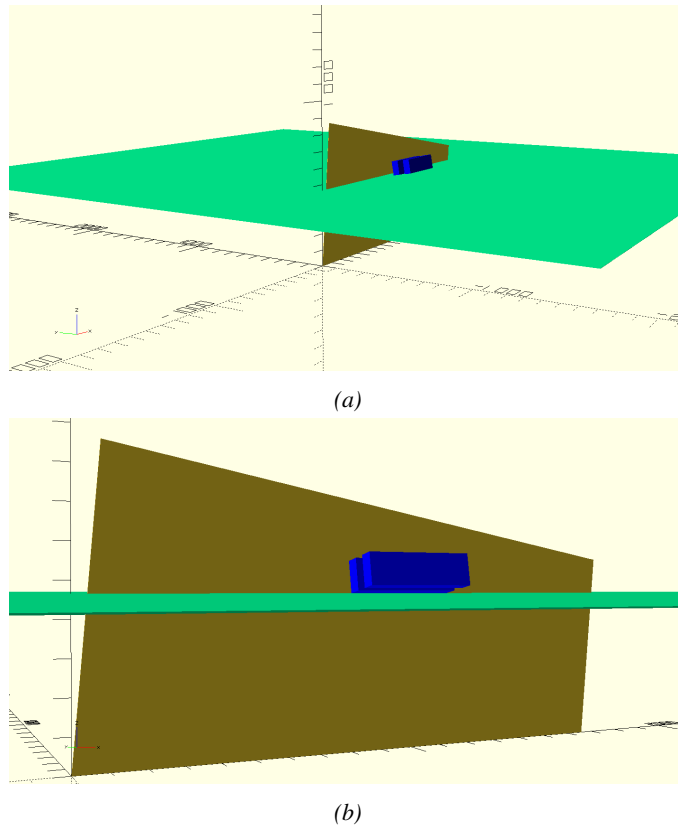


Figure 5.13: Representation of the layout used for the simulations of the test setup. The RPC read-out plane is represented as a yellow trapezoid while the two scintillators as blue cuboids looking at the sky. The green plane corresponds to the muon generation plane within the simulation. Figure 5.8a shows a global view of the simulated setup. Figure 5.8b shows a zoomed view that allows to see the 2 scintillators as well as the full RPC plane.

2775 5.2.2.2 Simulation procedure

2776 $N_\mu = 10^8$ muons are randomly generated inside the muon plane with an azimuthal angle θ chosen
 2777 to follow a $\cos^2\theta$ distribution. Infinite planes are associated to each surface of the scintillators.
 2778 Knowing the muon position into the muon generation plane and its direction allows, by assuming
 2779 that muons travel in a straight line, to compute the intersection of the muon track with these planes.
 2780 Applying conditions to the limits on the contours of the scintillators' faces then gives an answer to
 2781 whether or not the muon passed through the scintillators. In the case the muon was not *detected* into
 2782 both scintillators, the simulation discards the muon and generates a new one.

2783 On the contrary, if the muon is labeled as good, its position within the RPC read-out plane
 2784 is computed and the corresponding strip, determined through geometrical tests, gets a *hit*. Muon
 2785 hits fill different histograms whether they are associated to forward or backward coming muons.
 2786 A discrimination is performed according to their direction components. An (x, y, z) position into
 2787 the generation plane as well as a $(\theta; \phi)$ pair are associated to each generated muon providing with
 2788 information on the direction the track follows. This way, muons satisfying the condition $0 \leq \phi < \pi$
 2789 are labeled as *backward* coming muons while muons satisfying $\pi \leq \phi < 2\pi$ as *forward* coming

2790 muons.

2791 **5.2.2.3 Results and limitations**

2792 The output from the simulation is given in Figure 5.14 in which the distribution is showed for all
 2793 muons but also for the separate contributions of forward and backward coming muons. The strip
 2794 number is here given in a range of 1 to 32 corresponding to the 32 strips contained in each RPC
 2795 read-out partition, without taking into account the fact that partition B of an RPC correponds, by
 2796 convention, to strips 33 to 64. Comparing the number of muons recorded respectively in the first 16
 2797 strips and the in all of the 32 strips of the RPC read-out panel, it can be established than, out of the
 2798 total amount of muons that have passed through the telescope and reached the RPC, 16.8% where to
 2799 be detected in the 16 first strip of the read-out plane corresponding to half partition B1. This brings
 2800 a geometrical inefficiency of the same amount that can then be used to correct the data by scaling up
 2801 by a factor $c_{geo} = 1/(1 - 0.168)$ the maximum efficiency measured during data taking.

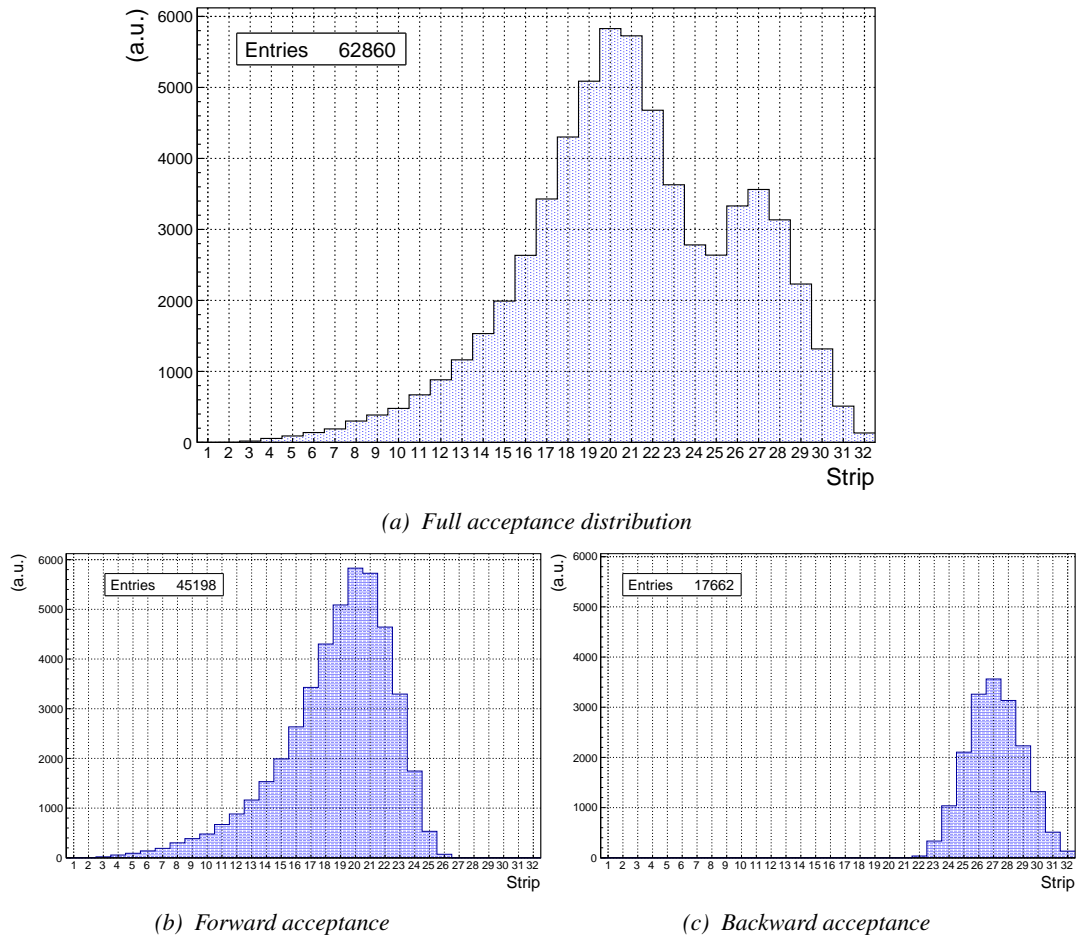


Figure 5.14: Geometrical acceptance distribution as provided by the Monte Carlo simulation.

2802 Nevertheless, it is difficult to evaluate a systematical uncertainty on this geometrical correction

for different reasons. First of all, even though the dimensions of the scintillators and of the RPC are well known, the position of each element of the setup with respect to one another was not measured. It was then necessary, using known dimensions, to extract the positions of each element from Figure 5.9 with unknown uncertainty. The inclination is also roughly measured to be 10° and even if the position of each peak, distant in the simulation of 7 strips, tends to confirm this assumption, the geometrical inefficiency would be affected by a variation of the inclination angle. Introducing in the simulation an error of $\pm 2^\circ$ would lead to a correction factor $c_{geo} = 1.20^{+0.04}_{-0.03}$ that allows for a good improvement of the efficiency measured in GIF, as can be seen from Figure 5.15. GIF measurement is in agreement with the reference curve within statistical errors.

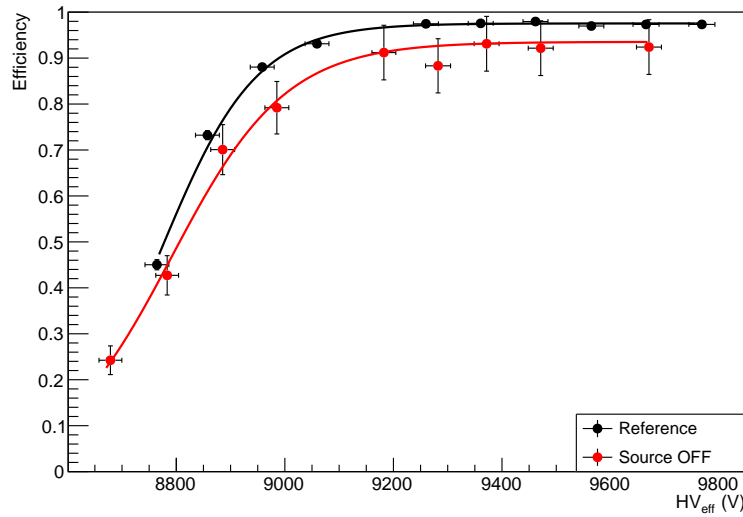


Figure 5.15: Correction of the efficiency without source. The efficiency after correction gets much closer to the Reference measurement performed before the study in GIF by reaching a plateau of $(93.52 \pm 2.64)\%$.

Further corrections could be also be brought as it can easily be understood that the distribution showed through Figure 5.14a differs from the measured hit profile showed in Figure 5.10. The contributions of forward and backward muon indicate that 28.1% of the total geometrical acceptance should contribute to detecting backward muons whereas it is measured that the hit profile contains 22.0% of backward data only. This estimation of the backward versus forward content in the data was done through a fit using a sum of two skew distribution, one acting on the forward muon peak while the other acts on the backward muon fit, as showed in Figure 5.16. Although a skew distribution lacks physical interpretation, it allows to easily fit such kind of data. A description of a skew distribution, as the product of a gaussian and a sigmoid (Formula 5.1), is given through Formula 5.2.

$$(5.1) \quad g(x) = A_g e^{\frac{-(x-\bar{x})^2}{2\sigma^2}}, \quad s(x) = \frac{A_s}{1 + e^{-\lambda(x-x_i)}}$$

$$(5.2) \quad sk(x) = g(x) \times s(x) = A_{sk} \frac{e^{\frac{-(x-\bar{x})^2}{2\sigma^2}}}{1 + e^{-\lambda(x-x_i)}}$$

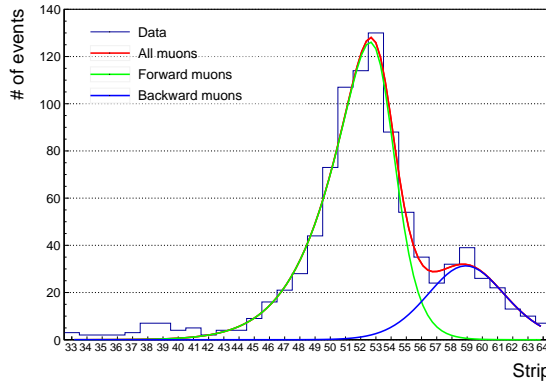


Figure 5.16: Hit distributions over read-out partition B of RE-4-2-BARC-161 chamber together with skew distribution fits corresponding to forward and backward coming muons.

From the obvious difference in between geometrical simulation and data, it is necessary to realize that the geometrical acceptance and the hit profile are two distinct information. When the geometrical acceptance only provides with the information about what the detector can expect to see in a perfect world where all muons are detected in the exact same way independently from their energy, angle of incidence, fluctuation of the detector gain due to complexe avalanche development, thresholds applied on the scintillators and on the RPC FEEs to reduce the noise, the cross-talk and corresponding spread of the induced charge observed on the read-out strips, the hit profile provides the final product of all the previously mentioned contributions and can greatly differ from purely geometrical considerations. A full physics analysis involving softwares such as GEANT would be required to further refine the correction on the measured efficiency at GIF.

5.2.3 Photon flux at GIF

In order to understand and evaluate the γ flux in the GIF area, simulations had been conducted at the time GIF was opened for research purposes [239]. Table 5.1 presented in this article gives the γ flux for different distances D to the source. The simulation was done using GEANT and a Monte Carlo N-Particle (MCNP) transport code, and the flux F is given with the estimated error from these packages expressed in %.

Nominal ABS	Photon flux F [$\text{cm}^{-2} \text{s}^{-1}$]			
	at $D = 50 \text{ cm}$	at $D = 155 \text{ cm}$	at $D = 300 \text{ cm}$	at $D = 400 \text{ cm}$
1	$0.12 \times 10^8 \pm 0.2\%$	$0.14 \times 10^7 \pm 0.5\%$	$0.45 \times 10^6 \pm 0.5\%$	$0.28 \times 10^6 \pm 0.5\%$
2	$0.68 \times 10^7 \pm 0.3\%$	$0.80 \times 10^6 \pm 0.8\%$	$0.25 \times 10^6 \pm 0.8\%$	$0.16 \times 10^6 \pm 0.6\%$
5	$0.31 \times 10^7 \pm 0.4\%$	$0.36 \times 10^6 \pm 1.2\%$	$0.11 \times 10^6 \pm 1.2\%$	$0.70 \times 10^5 \pm 0.9\%$

Table 5.1: Total photon flux ($E\gamma \leq 662 \text{ keV}$) with statistical error predicted considering a ^{137}Cs activity of 740 GBq at different values of the distance D to the source along the x-axis of irradiation field [239].

The simulation does not provide with an estimated flux at the level of the RPC under test. First of all, it is necessary to extract the value of the flux from the available data contained in the original paper and then to estimate the flux in 2014 at the time the experimentation took place. In the case of a pointlike source emitting isotropic and homogeneous gamma radiations, the gamma flux F at a

2841 distance D from the source with respect to a reference point situated at D_0 where a known flux F_0
 2842 is measured will be expressed like in Formula 5.3, assuming that the flux decreases as $1/D^2$, where
 2843 c is a fitting factor that can be written from Formula 5.3 as Formula 5.4. Finally, using Equation 5.4
 2844 and the data of Table 5.1, with $D_0 = 50$ cm as reference point, Table 5.2 can be built. It is interesting
 2845 to note that c for each value of D doesn't depend on the absorption factor.

$$(5.3) \quad F^{ABS} = F_0^{ABS} \times \left(\frac{cD_0}{D} \right)^2$$

$$(5.4) \quad c = \frac{D}{D_0} \sqrt{\frac{F^{ABS}}{F_0^{ABS}}} , \quad \Delta c = \frac{c}{2} \left(\frac{\Delta F^{ABS}}{F^{ABS}} + \frac{\Delta F_0^{ABS}}{F_0^{ABS}} \right)$$

Nominal ABS	Correction factor c		
	at $D = 155$ cm	at $D = 300$ cm	at $D = 400$ cm
1	$1.059 \pm 0.70\%$	$1.162 \pm 0.70\%$	$1.222 \pm 0.70\%$
2	$1.063 \pm 1.10\%$	$1.150 \pm 1.10\%$	$1.227 \pm 0.90\%$
5	$1.056 \pm 1.60\%$	$1.130 \pm 1.60\%$	$1.202 \pm 1.30\%$

Table 5.2: Correction factor c is computed thanks to Formula 5.4 taking as reference $D_0 = 50$ cm and the associated flux F_0^{ABS} for each absorption factor available in table 5.1.

2846 For the range of D/D_0 values available, it is possible to use a simple linear fit to get the evolution
 2847 of c that can be expressed as $c(D/D_0) = aD/D_0 + b$. Using Formula 5.5, but neglecting the
 2848 uncertainty on D that will only be used when extrapolating the values for the position of the RPC
 2849 under test whose position is not perfectly known, the results showed in Figure 5.17 is obtained.
 2850 Figure 5.17b confirms that using only a linear fit to extract c is enough as the evolution of the rate
 2851 that can be obtained superimposes well on the simulation points.

$$(5.5) \quad F^{ABS} = F_0^{ABS} \left(a + \frac{bD_0}{D} \right)^2 , \quad \Delta F^{ABS} = F^{ABS} \left[\frac{\Delta F_0^{ABS}}{F_0^{ABS}} + 2 \frac{\Delta a + \Delta b \frac{D_0}{D} + \Delta D \frac{bD_0}{D^2}}{a + \frac{bD_0}{D}} \right]$$

2852 In the context of the 2014 GIF tests, the RPC read-out plane is located at a distance $D = 206$ cm
 2853 from the source. Moreover, to estimate the strength of the flux in 2014 it is necessary to consider the
 2854 nuclear decay through time assiciated to the Cesium source whose half-life is well known ($t_{1/2} =$
 2855 (30.05 ± 0.08) y). The very first source activity measurement has been done on the 5th of March
 2856 1997 while the GIF tests where done in between the 20th and the 31th of August 2014, i.e. at a time
 2857 $t = (17.47 \pm 0.02)$ y resulting in an attenuation of the activity from 740 GBq in 1997 to 494 GBq in
 2858 2014. All the needed information to extrapolate the expected flux through the detector at the moment
 2859 of GIF preliminary tests has now been assembled, leading to Table 5.3. By assuming a sensitivity of
 2860 the RPC to γ of 2×10^{-3} , the order of magnitude of the expected hit rate per unit area would be of
 2861 the order of the kHz for the fully opened source, as reported in the last column of the table.

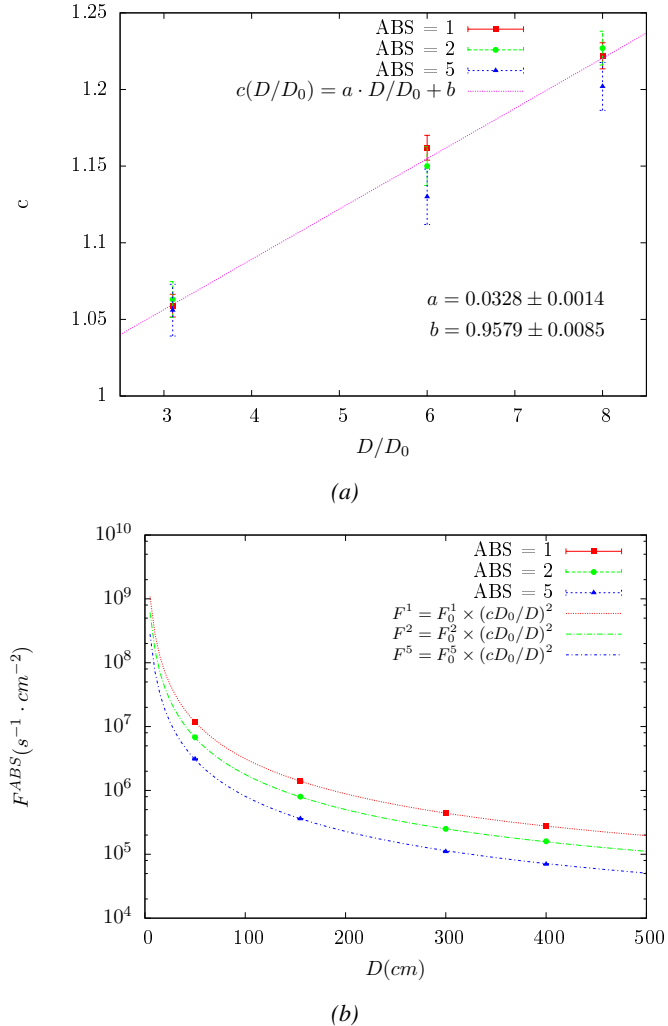


Figure 5.17: Figure 5.17a shows the linear approximation fit performed on data extracted from table 5.2. Figure 5.17b shows a comparison of Formula 5.5 with the simulated flux using a and b given in figure 5.17a in formulae 5.3 and the reference value $D_0 = 50$ cm and the associated flux for each absorption factor F_0^{ABS} from table 5.1

Nominal ABS	Photon flux F [$\text{cm}^{-2} \text{s}^{-1}$]			Rate [Hz/cm^2] at $D^{2014} = 206$ cm
	at $D_0^{97} = 50$ cm	at $D^{97} = 206$ cm	at $D^{2014} = 206$ cm	
1	$0.12 \times 10^8 \pm 0.2\%$	$0.84 \times 10^6 \pm 1.2\%$	$0.56 \times 10^6 \pm 1.2\%$	1129 ± 14
2	$0.68 \times 10^7 \pm 0.3\%$	$0.48 \times 10^6 \pm 1.2\%$	$0.32 \times 10^6 \pm 1.2\%$	640 ± 8
5	$0.31 \times 10^7 \pm 0.4\%$	$0.22 \times 10^6 \pm 1.2\%$	$0.15 \times 10^6 \pm 1.2\%$	292 ± 4

Table 5.3: The data at D_0 in 1997 is taken from [239]. Using Formula 5.5, the flux at D , including an error of 1 cm, can be estimated in 1997. Then, taking into account the attenuation of the source activity, the flux at D can be estimated at the time of the tests in GIF in 2014. Assuming a sensitivity of the RPC to γ s = 2×10^{-3} , an estimation of the hit rate per unit area is obtained.

The goal of the study will be to have a good measurement of the intrinsic performance without source irradiation. Then, taking profit of the two working absorbers, at absorbtion factors 5 (300 Hz) and 2 (~ 600 Hz) the goal will be to show that the detectors fulfill the performance certification of CMS RPCs. Finally, a first idea of the performance of the detectors at higher background will be provided with absorbtion factor 1 (no absorbtion and >1 kHz).

5.2.4 Results and discussions

The data taking at GIF has been conducted in between the 21st and the 31st of August, 2014. Data has been collected with both source OFF and ON using three different absorber settings (ABS 5, 2 and 1) in order to vary the irradiation on the RPC. For each source setting, two HV scans have been performed with two different trigger settings. During a first scan the trigger sent to the TDC module was the coincidence of the two scintillators composing the telescope while during a second scan the trigger was a pulse coming from a pulse generator in order to measure the noise or gamma rate seen by the chamber. Indeed, using a pulse allows to trigger at moments not linked to any physical event and, hence, to obtain a *RANDOM* trigger on noise and gamma events to measure the associated rates, the probability to have a pulse in coincidence with a cosmic muon being negligible.

From the cosmic trigger scans, a summary of the efficiencies and corresponding cluster sizes is showed in Figure 5.18. The efficiency curves with Source ON show a shift with respect to the case without irradiation. With ABS 5, the general shape of the efficiency curve stays unchanged whereas a clear alteration of the performance is observed at ABS 2 and ABS 1. From the cluster size results, a reduction of the cluster size under irradiation can be oberved at equivalent efficiency. This effect can be due to the perturbation of the electric field by the strong rate of gamma particles starting avalanches in the gas volume of the detector.

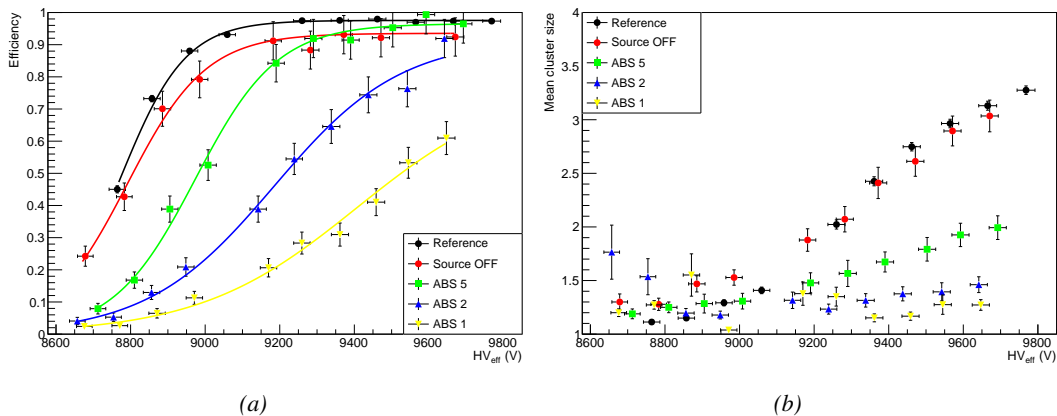


Figure 5.18: Efficiency (Figure 5.18a) and cluster size (Figure 5.18b) of chamber RE-4-2-BARC-161 measured at GIF with Source OFF (red) and Source ON using different absorber settings: ABS 5 (green), ABS 2 (blue) and ABS 1 (yellow). The results are compared to the Reference values obtained with cosmics.

It is necessary to study the evolution of the performance of the chamber with the increasing rate. In Figure 5.19a, the noise rate when the source is OFF stays low but increases at voltages above 9500 V. The rise of the noise rate in the detector can be related to the increased streamer probability observed with such a large electric field. The rates with source ON measured at GIF all show a

similar behaviour until a high voltage of approximately 9400 V at which the rate of ABS 5 saturates, corresponding to the chamber reaching full efficiency. It is important to note that, even though the rates look similar independently from the gamma flux, relatively to the efficiency of the chamber, the rate actually increases with increasing flux at equivalent efficiency. A rough way to measure the rate effectively observed by the detector for each source setting would be to normalize the measured rates to the efficiency of the detector. This exercise was done with Figure 5.19b from which constant fits were done on Source ON data in order to extract the rate the chamber was subjected to.

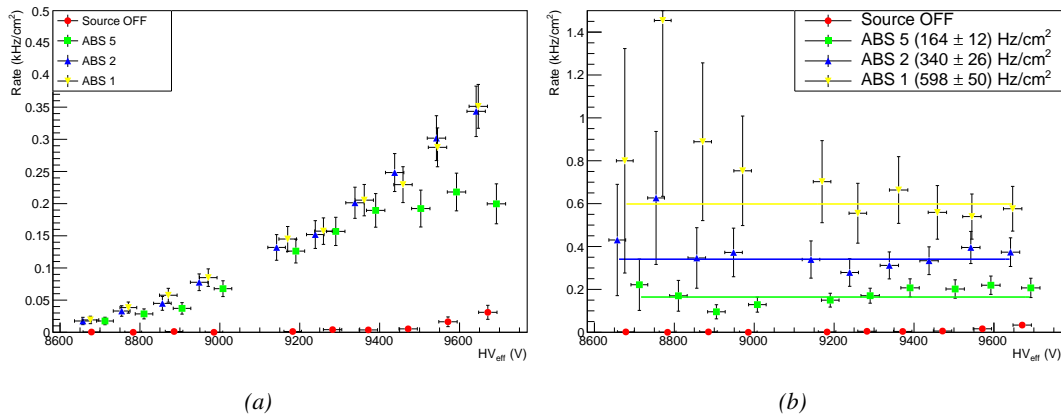


Figure 5.19: Rates in chamber RE-4-2-BARC-161 measured at GIF with Source OFF (red) and Source ON using different absorber settings: ABS 5 (green), ABS 2 (blue) and ABS 1 (yellow). On Figure 5.19b, the rates of Figure 5.19a were normalized to the measured efficiency and constant fits are performed on Source ON data showing the gamma rate in the chamber.

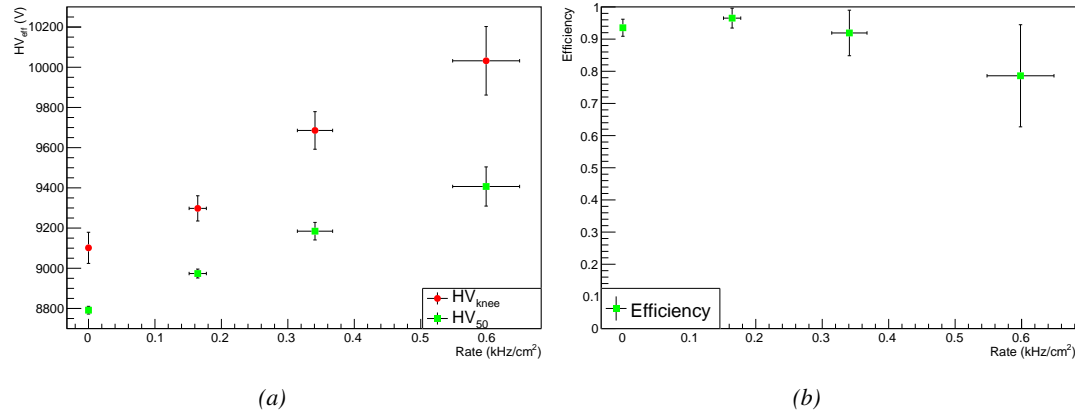


Figure 5.20: Evolution of the voltages at half maximum and at 95% of the maximum efficiency (Figure 5.20a), and of the maximum efficiency (Figure 5.20b) as a function of the rate in chamber RE-4-2-BARC-161. The data is extracted from the fits in Figures 5.18a and 5.19b.

The results need to be taken with care as a better estimation of the rate would have been to push the detector towards higher voltages to reach the efficiency plateau for each absorber configuration

and only then extract the measured rate at working voltage, defined as in Formula 4.25. Nevertheless, using this method to estimate the rate the chamber is subjected to, it is possible to look at the evolution of the HV_{50} and HV_{knee} (the working voltage being defined to be 150 V above the knee in the endcap) as a function of the increasing rate as showed in Figure 5.20. The results from GIF suggest that at a rate of 600 Hz/cm^2 the working voltage of the chamber is increased by a thousand V while the efficiency is reduced to approximately 80%, although the result still is consistent with an efficiency better than 90% due to the large error on the measurement. Moreover, it is likely that the rates obtained through fitting on normalized values is underestimated. Indeed, monitoring the current in the 3 gaps composing a CMS endcap RPC (Figure 5.21) while knowing the rate, the charge deposition per avalanche q_γ can be computed.

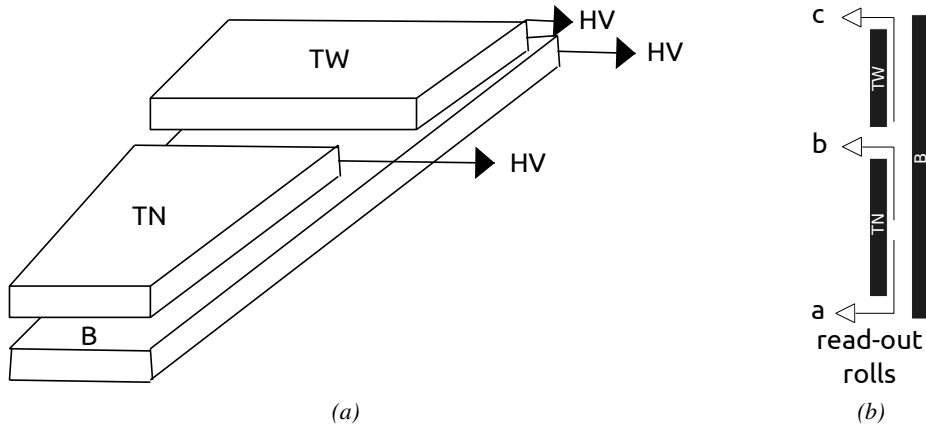


Figure 5.21: Presentation of a double-gap endcap RPC with its 3 RPC gaps. Due to the partitioning of the read-out strips into 3 rolls, the TOP layer of gap is divided into 2 gaps: TOP NARROW (TN) and TOP WIDE (TW). The BOTTOM (B) only consists in 1 gap.

A charge is expressed in C which is consistent with a current density, expressed in A/cm^2 , divided by a rate per unit area, expressed in Hz/cm^2 . The current driven by the RPC is assumed to be due to the irradiation, hence, to the avalanches developing in the gas volume due to the photons of the Cesium source. On the other hand, the rate is supposed to be a measure of the number of photons interacting with the detector. This way, it comes that the charge deposition per avalanche is expressed like $q_\gamma = J_{mon}/R_\gamma$, J_{mon} being the monitored current density and R_γ the measured γ rate. The current density is computed as the sum of the current density measured on the top gap layer and of which measured in the bottom gap layer, $J_{mon} = (I_{mon}^{TW} + I_{mon}^{TN})/(A_{TW} + A_{TN}) + I_{mon}^B/A_B$, $A_{B,TN,TW}$ being the active area and $I_{mon}^{B,TN,TW}$ the monitored currents of the gaps. According to Figure 5.22, the charge deposition per avalanche consistently converges to a value of the order of 50 pC for each absorber setting which corresponds to a value more than twice greater than what reported in literature for CMS detectors [245, 246] indicating that the rates could have been wrongly evaluated during the short study performed at GIF. An increase of the γ rate by a factor 2 would be consistent with the expected rates calculated in Table 5.3, assuming the sensitivity to γ to be of the order of 2×10^{-3} .

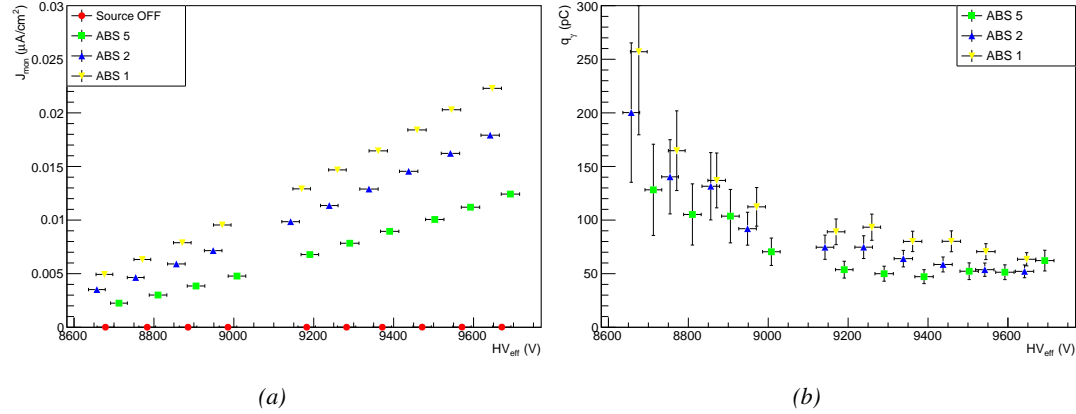


Figure 5.22: Current density and charge deposition per gamma avalanche, defined as the current density normalized to the measured rate taken from Figure 5.19a as a function of the effective high voltage in chamber RE-4-2-BARC-161 measured at GIF with Source ON using different absorber settings: ABS 5 (green), ABS 2 (blue) and ABS 1 (yellow).

Overall, working at GIF has been a rewarding experience as it offered CMS RPC R&D team the possibility to start developing the necessary skills and tools that would become the core of GIF++ experiment. The quality of the results can be argued both due to the little robustness of the experimental setup and the lack of available statistics to draw conclusions from, bringing large errors on the final result. The confrontation of the data to known results pointed to a failure in correctly measuring the γ rate at working voltage and, hence, to an overestimation of the charge per avalanche and of the drift of working voltage with increasing rate. Nevertheless, the prototypes of DAQ and offline analysis tools proved to be reliable.

5.3 Longevity tests at GIF++

5.3.1 Selection and characterization of CMS RPCs for longevity at GIF++

First proposed in 2009 [247], the new Gamma Irradiation Facility of CERN was thought in the perspective of future upgrades of PHC that would bring detectors to be operated in a high irradiation environment. GIF++ would thus provide all LHC R&D teams working on behalf of the different LHC experiment with a facility to perform longevity studies using a very intense Cesium gamma source.

In the specific case of CMS RPC, the longevity studies imply a constant irradiation of selected detectors in order to accumulate a charge equivalent to what is expected during HL-LHC, i.e. a charge of $0.8 \text{ C}/\text{cm}^2$ according to Figure 5.2 including a safety factor 3, while other detectors are left non irradiated to be used as references. Throughout the irradiation campaign, the performance of the irradiated and reference detectors will be periodically probed using the high intensity H4 muon beam. Dedicated test beam periods will be used to measure the efficiency and γ rate at the level of the detectors with different source absorber settings to have access to the rate capability of CMS RPCs, that needs to be certified above $600 \text{ Hz}/\text{cm}^2$, and to identify signs of ageing in the case the performance of the irradiated detectors diverges from those of the reference detectors with increasing accumulated charge. Other than the performance of the detectors, signs of ageing

2947 could come from increasing dark current that would be related to local ageing of the electrodes
 2948 triggered by the fluoridric acid (*HF*) production in an irradiated environment. *HF* is produced
 2949 by the decomposition of $C_2H_2F_4$ molecules during the charge multiplication process and leads to
 2950 increased dark current and noise in Bakelite RPCs treated with linseed oil. This effect is strongly
 2951 reinforced by the presence of UV photons [248, 249]. A close monitoring of the current driven by
 2952 the detectors will then be necessary as well as dedicated periodical electrode resistivity measurement
 2953 and chromatography measurement on the gas exhaust.

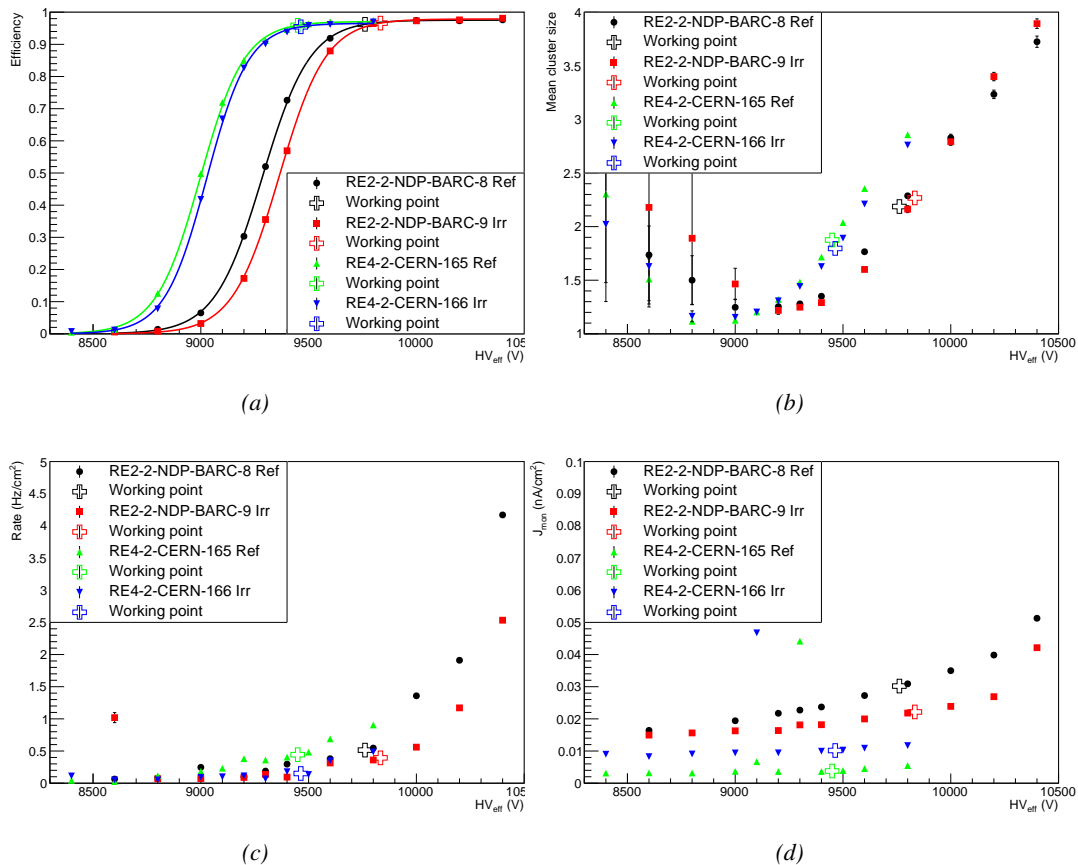


Figure 5.23: Characterization of CMS RPC detectors foreseen to be used at Gif++ for longevity studies of the present system. Using cosmic muons, efficiency (Figure 5.23a) and cluster size (Figure 5.23b) were measured as well as noise rate (Figure 5.23c) and current density (Figure 5.23d). For each detector, the working voltage, defined as in Formula 4.25, was extracted from sigmoid fits performed in Figure 5.23a and the values of efficiency, cluster size, noise rate and current density at this voltage are reported using open crosses.

2954 As the maximum background is found in the endcap, the choice naturally was made to focus
 2955 the Gif++ longevity studies on endcap chambers. Most of the RPC system was installed in 2007.
 2956 Nevertheless, the large chambers in the fourth endcap (RE4/2 and RE4/3) have been installed during
 2957 LS1 in 2014. The Bakelite of these two different productions having different properties, four spare
 2958 chambers of the present system were selected. From the original CMS RPC system, two RE2/2
 2959 spares were selected along two RE4/2 spares from the newest detectors. Having two chambers of

2960 each type allows to always keep one of them non irradiated as reference. Due to the limited gas
 2961 flow in GIF++, the RE4 chamber remained non-irradiated until end of November 2016 where the
 2962 longevity studies could finally be started on those chambers.

2963 The performance of the chambers prior to the start of the longevity campaign has been char-
 2964 acterized in Ghent before being shipped to CERN to be installed in GIF++. The results of the
 2965 characterization are showed in Figure 5.23 and summarized in Table 5.4. A clear difference in per-
 2966 formance for both types of chambers is observed as the working voltages of the newest chambers,
 2967 of type RE4, are 300 to 400 V lower to the older chambers indicating that the gap thickness of RE4
 2968 detectors could be thinner. This conclusion could as well be supported by the lower cluster size at
 2969 working voltages that also are smaller in RE4 chambers. Even though the measured currents are
 2970 low, RE4 detectors draw less current without irradiation than RE2 detectors pointing to a difference
 2971 in electrode resistivity that were produced at different moments. Efficiency and noise rate levels are
 2972 of the same order of magnitude for both type of RPCs.

RPC	RE2-2-NPD-BARC-08	RE2-2-NPD-BARC-09	RE4-2-CERN-165	RE4-2-CERN-166
Used as	Reference	Irradiation	Reference	Irradiation
HV_{WP} [V]	(9762 \pm 6)	(9833 \pm 6)	(9449 \pm 5)	(9464 \pm 5)
Efficiency at WP	(96.2 \pm 0.3)	(96.6 \pm 0.3)	(95.9 \pm 0.3)	(95.5 \pm 0.3)
Cluster size at WP	(2.19 \pm 0.04)	(2.27 \pm 0.05)	(1.88 \pm 0.04)	(1.80 \pm 0.04)
Noise at WP [Hz/cm ²]	(0.51 \pm 0.01)	(0.39 \pm 0.01)	(0.44 \pm 0.00)	(0.15 \pm 0.01)
J^{WP} [pA/cm ²]	(30.1 \pm 0.1)	(22.2 \pm 0.1)	(3.8 \pm 0.0)	(10.2 \pm 0.0)

Table 5.4: Summary of the characterization measurement performed in Ghent on CMS RPC detectors foreseen to be used at GIF++ for longevity studies of the present system. For each detector, the working voltage, defined as in Formula 4.25, was extracted from sigmoid fits performed in Figure 5.23a and the values of efficiency, cluster size, noise rate and current density at this voltage are reported.

5.3.2 RPC test setup

2973 For an easy manipulation of the detectors, a trolley with a structure containing slots in which the
 2974 RPCs can be slid vertically and referred to as T1 was used. In this position, each chamber is in a
 2975 plane perpendicular to the beam line and the source flux as can be seen through Figure 5.24, receiving
 2976 a uniform irradiation. Moreover the trolley allows for easy movement of the system. Indeed, the
 2977 position of trolley varies according to the period of the year.

2978 During the dedicated test beam periods during which GIF++ longevity experiments are in control
 2979 of the muon beam, the trolley is placed in the upstream region of the bunker, in the beam line, as
 2980 described through Figure 5.24a. The CMS RPC detectors are the ones being further away from the
 2981 source on this side of the source as other detectors need to be certified at higher background rates. An
 2982 additional trolley, referred to as T3, containing iRPCs and tracking RPCs is placed in between the
 2983 source and the trolley containing present CMS RPCs. Indeed, iRPCs need to be certified at higher
 2984 rates and thus need to be placed closer to the source to receive a stronger irradiation using the same
 2985 absorber settings. The space on T1 being limited, the tracking RPCs used for extra offline informa-
 2986 tion during the analysis are placed on the same trolley than iRPCs and are kept at full efficiency at
 2987 all time to reconstruct muon tracks in correlate them with hits recorded in T1 chambers. The beam
 2988 trigger system is composed of 2 scintillators placed outside on each side of the bunker and of a third
 2989 scintillator placed in between T1 and the wall of the bunker along the beam line.

2990 However, most of the year, T1 is placed in the so called *ageing position* corresponding to the

furthest position from the source outside of the beam line, which needs to stay clear during periods where GIF++ doesn't have the control of the beam so that a beam tube can be installed through the bunker, as can be seen in Figure 5.24b. The reason for placing the chambers as far as possible from the source comes from the too high irradiation delivered by the source during the irradiation periods where all the other experiment having placed detectors into the bunker requires to integrate as much charge as possible. Hence, the source is operated with any absorbers. On the contrary, during the test beam periods, all the groups working in GIF++ are interested in operating the source using various absorber settings to study the performance of their detectors under different irradiation conditions. The time spent with a source fully opened and during which the RPCs of T1 are kept at a standby voltage of 6500 V much lower than what necessary to grow avalanches in the gas is then small compared to the time spent with other source settings and during which data can be taken.

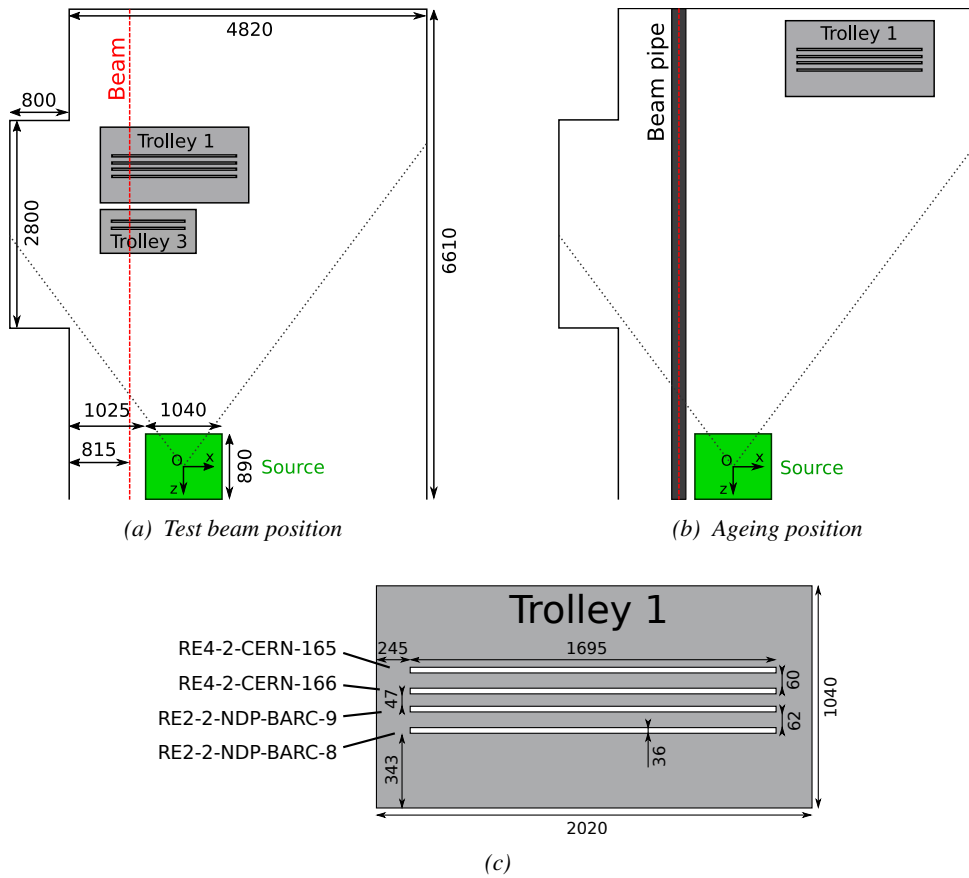


Figure 5.24: CMS RPC setup inside of GIF++ bunker during test beam (Figure 5.24a) and ageing periods (Figure 5.24b). The space in between the RPCs and the source is usually used by other detectors while the space in between T1 and the upstream wall is not filled. Due to the presence of the beam pipe, the trolley is moved away from the beam line during irradiation periods and placed further away from the source for less intense irradiation. The position of the trolley can vary due to the use of the space by other setups and is then not exact. In the contrary, the position of the chambers in the trolley is fixed and given in Figure 5.24c.

From the bunker area, the detectors are connected to the service area, visible in Figure 5.6, through the wooden floor tanks to long cable. The service area hosts all the high and low voltage power

3005 supplies, the TDCs and computers used for data acquisition and preliminary offline analysis used
 3006 to fill the Detector Control Software (DCS) webpage, referred to as WebDCS, with Data Quality
 3007 Monitoring (DQM) histograms useful for the shifters on duty in the control room located further in
 3008 the building, away from the beam lines, as well as the gas system required for the gaseous detectors
 3009 installed in GIF++ [250]. The detectors read-out is, as in the case of GIF, connected to V1190A
 3010 VME TDCs communicating with the DAQ computer thanks to a V1718 VME bridge manufactured
 3011 by CAEN. Moreover, a constant monitoring of all the environmental parameters, in different points
 3012 of the bunker area, gas parameters, to control its composition, temperature and pressure, and of the
 3013 voltages and currents delivered by the power supplies is performed and displayed on the homepage
 3014 of the WebDCS interface.

3015 5.3.3 GIF++ data flow

3016 At GIF++, the CMS RPC R&D experiment collects different types of data coming from the detectors
 3017 monitored parameters, such as voltage and currents, the gas, source, and environmental parameters,
 3018 and, of course, the TDC data in which are collected the actual muon and gamma physics. These
 3019 different data source compose 3 different data flows as presented in Figure 5.25.

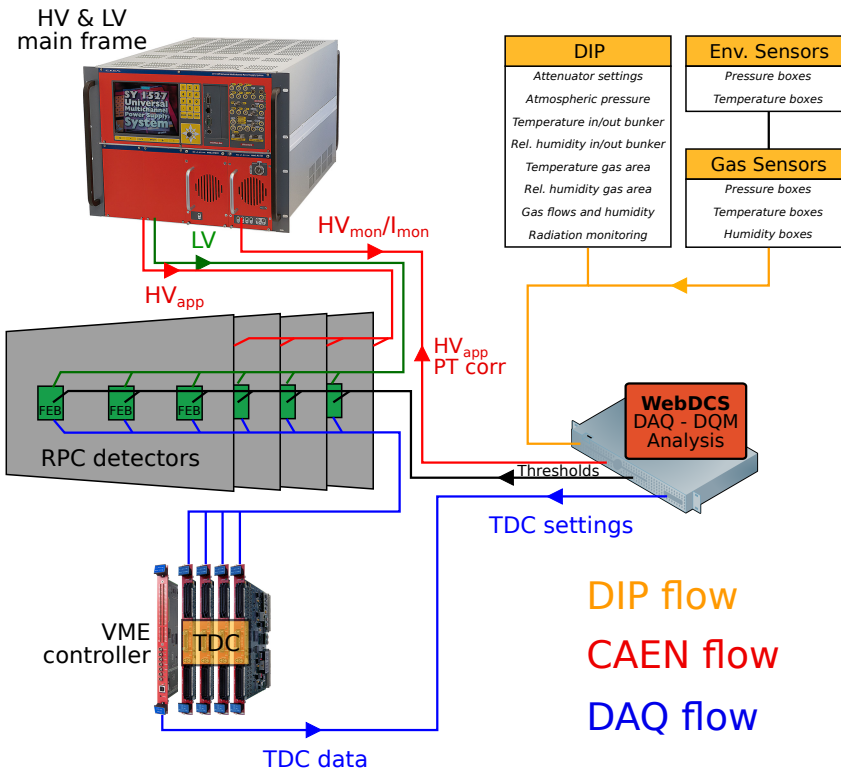


Figure 5.25: Visualtion of the main data flows in GIF++. The yellow flow lines corresponds to the DIP flow used for source, environmental and gas information. The red flow lines are for the CAEN flow through which the WebDCS communicates the voltages to be applied on the detectors using pressure and temperature information and retrieves the monitored voltages and currents. Finally, the blue flow lines corresponds to the DAQ flow through which the RPC data is collected from the TDCs by the computer.

3020 The *DIP flow*, DIP being a communication system allowing for exchange of real-time information
 3021 between systems, concerns all the data coming from the gas composition, temperature and
 3022 humidity, the environmental temperature and pressure, the source settings and the radiation monitoring
 3023 sensors. The experimental area is in charge of measuring, storing and distributing the data
 3024 of interest for all of the users of the facility (source settings, radiation monitoring, gas composition
 3025 at the exit of the gas mixer and general environmental information). Retrieving this data is done by
 3026 accessing to the database of the experimental hall in which GIF++ is located through DIP communica-
 3027 tion. More specific data such as gas flow, temperature and humidity at the level of the detectors
 3028 (upstream and downstream of the detectors) as well as environmental parameters are at the charge
 3029 of the users. For this reason, several pressure, temperature and humidity sensors were installed on
 3030 the gas distribution system of the RPC trolleys. The corresponding data flow, although not related
 3031 to DIP itself, is saved together with the DIP data into the local CMS RPC database and displayed
 3032 on the front page of the WebDCS together with alerts in the case the values measured are out of
 3033 optimal working range. The data is particularly important to perform the PT correction described in
 3034 Section 4.4 of Chapter 4 and keep stable the effective voltage of the detectors. Monitoring history
 3035 plots are made using JavaScript are also displayed for an easy access to past information, as
 3036 showed in Figure 5.26.

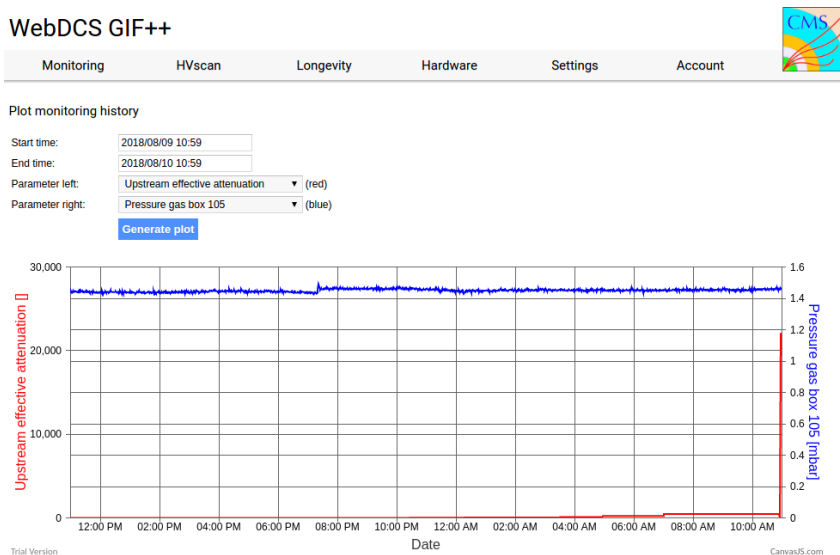


Figure 5.26: *DIP monitoring history accessed through GIF++ WebDCS interface.*

3037 The data flow related to the monitoring of detector high voltages and currents, referred to as
 3038 *CAEN flow* as a reference to the manufacturer of power supplies, is retrieved thanks to computer
 3039 to main frame communications. Indeed, during the operations (irradiation or beam period), these
 3040 values can be accessed directly through the bus of the main frame hosting the high voltage supplies.
 3041 Finally, the DAQ flow concerns all data acquired through the use of the TDCs, i.e. all the muon or
 3042 gamma data recorded by the detectors under test at GIF++.

3043 5.3.4 Measurements performed during beam periods

3044 As previously described, two types of measurement are performed on the chambers during beam
 3045 periods. On one hand, it is interesting to measure the efficiency of the RPCs with increasing voltage
 3046 with different source absorber settings but on the other hand, it is important to correlate the efficiency
 3047 information to the gamma rate seen by the chambers at the voltages that were scanned for efficiency.
 3048 The choice was made to separate efficiency measurements from rate measurements to better manage
 3049 time and data volume. In both cases, TDC data recorded during so called *HV scans* is divided into
 3050 *runs*, one for each high voltage point, whose data is stored into ROOT files. The TDC settings
 3051 used during both these scans as well as the ROOT data structure are detailed in Section A.4.2 of
 3052 Appendix A.

3053 The goal of both efficiency and rate scans is to measure the rate capability of the detectors but
 3054 also to monitor any degradation of the performance due to ageing. This way, during test beam
 3055 periods the efficiency and corresponding gamma background are measured to correlate the evolution
 3056 of rate capability at different stages of irradiation. In the absence of other signs of ageing, a reduction
 3057 of the rate capability could be related to an increase of the electrodes resistivity.

3058 5.3.4.1 Efficiency scans

3059 The HV scans performed to specifically measure the muon detection efficiency under different ir-
 3060 radiation conditions follow a standardized procedure. Data using the DAQ is taken at the same 12
 3061 HV points for all chambers, ranging from 9 kV to 10.1 kV by steps of 100 V. For each HV run, a
 3062 minimum of 5000 muon beam triggers, provided by the coincidence of the 3 scintillators, is required
 3063 in order to accumulate enough statistics for a reliable computation of the efficiency of the detectors.
 3064 In addition to the 4 RPCs held on T1, 2 tracking RPCs installed on T3 are kept at a fixed voltage of
 3065 9.7 kV to provide the analysis software [251] with beam position information to exclude off-track
 3066 signals. The tracking RPCs, whose design is based on which of CMS RPCs, are double gap detectors
 3067 featuring 2 mm HPL electrodes and 2 mm gas gaps. Finally, the monitored currents and voltages are
 3068 recorded in histograms along the TDC data in a different ROOT file for each run.

3069 HV scans are taken for different source settings as the goal is to irradiate all the detectors with a
 3070 minimal rate of 600 Hz/cm². Usually, a full study of the performance of the detectors is performed
 3071 with Source OFF, and then with 9 absorber settings that attenuate the nominal gamma flux by factors
 3072 from more than 200 to only 3, settings with fully opened source being avoided with RPCs in test
 3073 beam position. Adjusting the gamma flux is possible thanks to the 3 layers of absorbers featured on
 3074 the Cesium source [252].

3075 5.3.4.2 Rate scans

3076 These background measurement are performed using a similar HV scan procedure than in the case
 3077 of efficiency measurements. The HV scan in test beam period will be taken fewer HV points than
 3078 for the efficiency scans as the region of interest is located around the knee and efficiency plateau
 3079 of the detectors in order to extract through linear interpolation the value of the rate at the working
 3080 voltage deduced from the efficiency scan. Thus, these scans are performed only on 6 HV points
 3081 ranging from 9.5 kV to 10 kV. Rate scans are substantially heavier than efficiency scans. Indeed, a
 3082 good estimation of the rate requires a long enough integrated time worth of data. The way data is
 3083 collected, detailed in Appendix A, makes the DAQ search for data stored in the TDC buffers prior to
 3084 the trigger signal. The time window from which the data is collected ranges in between only 25 ns

3085 to more than $50\ \mu\text{s}$. The Cesium source delivering a consistent gamma flux, it was decided than a
 3086 total integrated time of $0.2\ \text{s}$ would be enough to have a reliable calculation of the γ rate. This is
 3087 achieved by taking 20,000 random trigger pulses delivered by a pulse generator at a frequency of
 3088 $300\ \text{Hz}$ while extracting $10\ \mu\text{s}$ of data from the buffers for each trigger.

3089 Separating rate measurements from efficiency measurement was motivated by the inconsistency
 3090 of the muon beam provided in GIF++. Using periods without beam to measure rates with a good
 3091 statistics allows for faster study programs. Moreover, depending on the muon strength that can
 3092 strongly vary due to users placed upstream of GIF++ and using magnets, the number of muon de-
 3093 livered per beam spill can make the accumulation of 20,000 events too long for the other users of
 3094 GIF++. Hence, efficiency scans are performed with lower statistics and the time window from which
 3095 the data is extracted is strongly reduced (400ns for efficiency scans versus $10\ \mu\text{s}$ for rate scans) to
 3096 keep the data size to its bare minimum.

3097 5.3.4.3 Offline analysis and Data Quality Monitoring

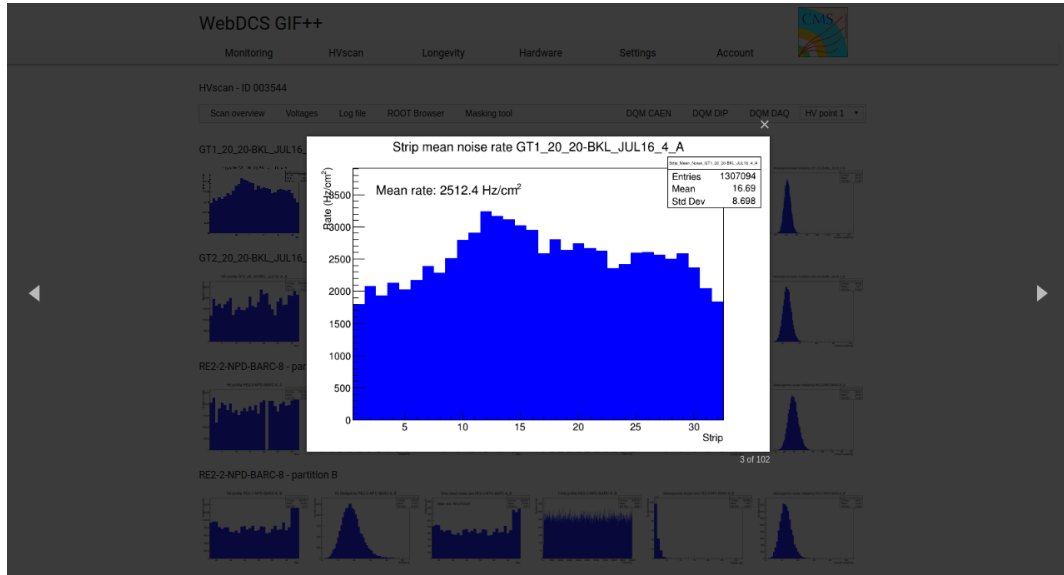


Figure 5.27: Example of DQM page available on CMS WebDCS in GIF++. Here is presented the rate measured in one of the tracking chambers, namely GT1_20_20-BKL_JUL16_4. The DQM page allows to click on each histogram to extend its view and to navigate through the histograms thanks to the left and right arrows.

3098 The data recorded during efficiency and rate scans always consist in two ROOT files per run, a run
 3099 corresponding to a HV point. One of the files corresponds to the TDC data, a collection of hits
 3100 per active channel on the read-out of the RPCs, while the second is the CAEN main frame data,
 3101 offering a monitoring of the currents and high voltages. This data is systematically analysed at the
 3102 end of each scan thanks to the Offline Analysis tool of GIF++, detailed in Appendix B, that produces
 3103 histograms such as hit, rate and time profiles, hit multiplicities, gamma cluster sizes or multiplicities
 3104 for the DQM display of the WebDCS, as showed in Figure 5.27. More histograms can be accessed
 3105 through the ROOT browser included in the WebDCS, as showed in Figure 5.28. Moreover, the
 3106 analysis performed thanks to the Offline tool is definitive in the case of evaluating the rates from rate

3107 scans. On the contrary, the algorithm for efficiency calculation is kept simple and approximative in
3108 the tool as including taking into the analysis requires manual adjustment for each individual scan.

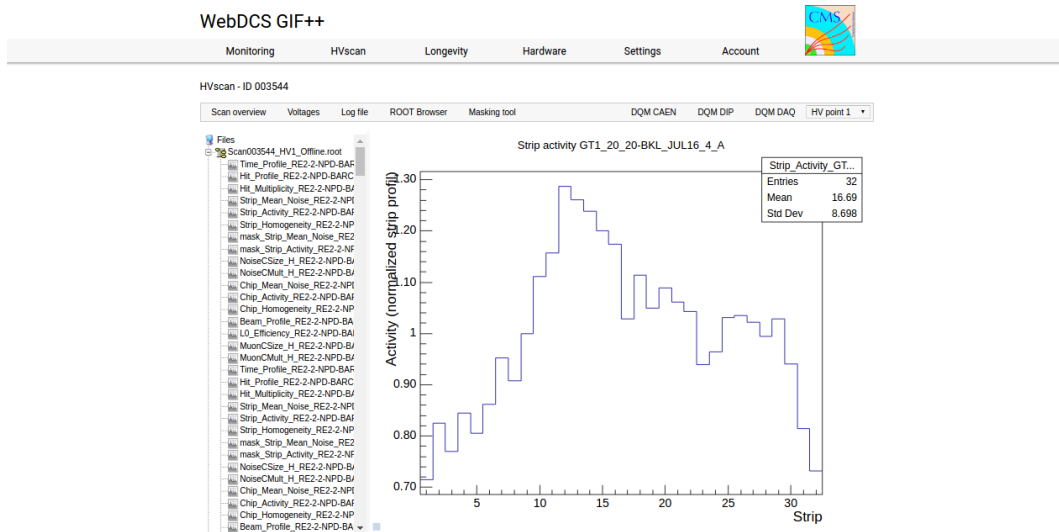


Figure 5.28: Example of DQM ROOT Browser page available on CMS RPC WebDCS in GIF++. Here is presented the strip activity profile, defined as the rate profile normalized to the mean rate, in one of the tracking chambers, namely GT1_20_20-BKL_JUL16_4. Available ROOT files and histograms can be browsed thanks to the left panel showing the directory and files structures.

5.3.5 Measurements performed during irradiation periods

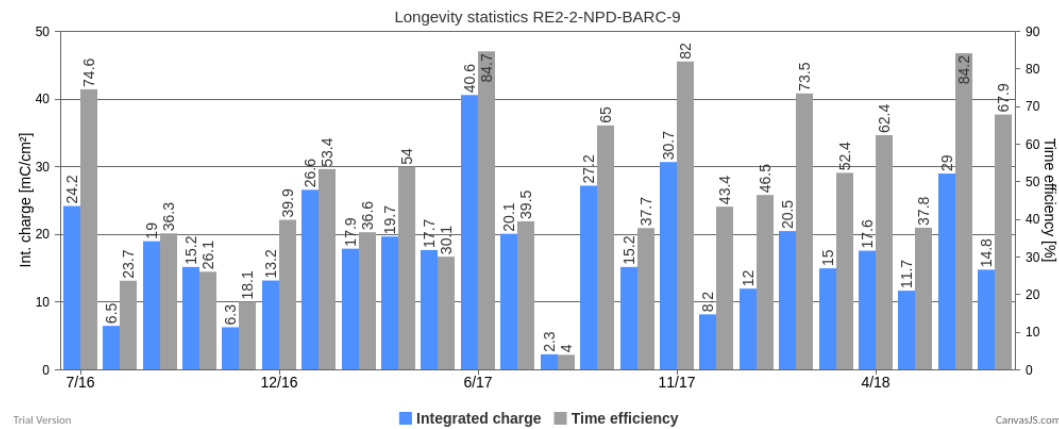


Figure 5.29: Longevity statistics of chamber RE2-2-NPD-BARC-9 in GIF++. For each month since July 2017, the integrated charge (in blue) as well as the time efficiency of irradiation (in gray) is reported.

Even though test beam periods are stressful times has an extensive data taking planing needs to be finalized in a short amount of time, the biggest amount of data comes from irradiation periods.

Indeed, when T1 is moved back to its ageing position in between each test beam periods, data is recorded at any time the source can be switched ON for irradiation. Indeed, other experiments in the area might prevent the source from staying opened continuously. As an example, the time efficiency of irradiation of CMS RPC detectors in Gif++ is presented in Figure 5.29.

Several types of measurement are performed throughout the irradiation period. Indeed, as long as the detectors are being irradiated, a monitoring of the currents is performed to evaluate the corresponding integrated charge considering the irradiation time. Moreover, the corresponding gamma rates need to be measured on a regular basis. Ageing signs can be understood through an increase of the detector noise correlated with an increased dark current. For this purpose, HV scans are performed to measure the noise with increasing voltage and the dark currents. Another way to highlight ageing is through the loss of rate capability of the detectors. During irradiation periods this can be looked through thanks to HV scans performed at various source settings, which are referred to as *source scans*. The loss in rate capability could be understood by a saturation of the measured at higher gamma flux. This effect could be correlated with an increase of the electrodes resistivity. The resistivity is then measured periodically during the year, generally before or after test beam periods by the use of Argon breakdown technic.

5.3.5.1 Longevity scans

The main activity of irradiation periods consist in the *longevity scans* during which the currents of the irradiated chambers are continuously monitored. The two irradiated chambers, RE2-2-NPD-BARC-09 and RE4-2-CERN-166, are both brought to a voltage of 9.8 kV while the source flux can vary depending on the need of experiments using the facility. The currents are recorded on each active gas volume and each gap contribution is then translated into the mean chamber integrated charge as can be seen from Figure 5.30. At the end of each longevity scan the integrated charge accumulated in each chamber is used to update the summary plots providing the collaboration with official results to be spread.

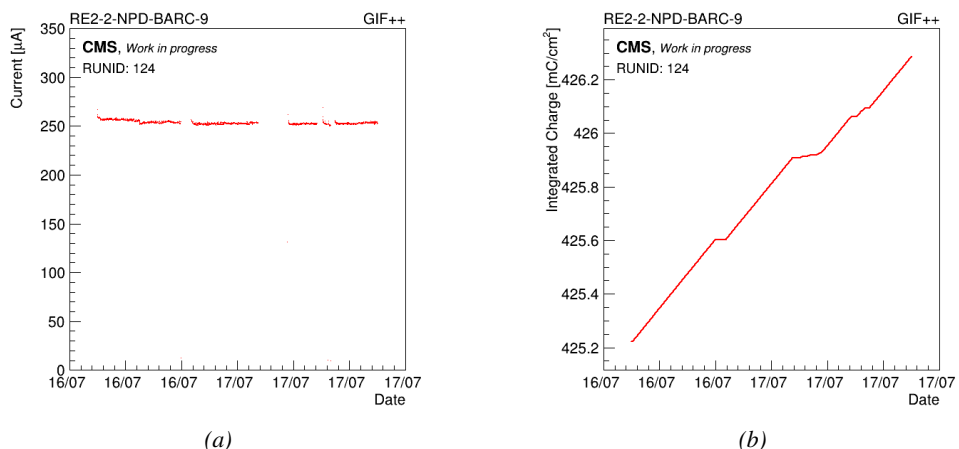


Figure 5.30: Example of current monitoring (Figure 5.30a) and of corresponding integrated charge (Figure 5.30b) of chamber RE2-2-NPD-BARC-09. The decrease of current are related to a decrease of the voltage due to the daily rate scan procedure or to periods during which the source was turned OFF.

5.3.5.2 Daily rate monitoring scans

Every night during longevity scans, the DAQ is used to perform *daily rate scans*. These scans aim at keeping track of the gamma rate measured in the irradiated RPCs during longevity but is also measured the noise rate at standby voltage and this, for each gap individually. The procedure for these HV scans consist in 9 runs for which 50,000 random triggers are requested, corresponding to 0.5 s of total integrated time.

- 1- All gaps are first left at the irradiation voltage of 9.8 kV to measure the γ rate.
- 2- Then all gaps are brought to the standby voltage of 6.5 kV to measure the noise rate of the full detectors.
- 3- Both top gaps (TW and TN) are brought to a voltage equivalent to an OFF status, i.e. 1 kV so that the noise contribution of only the bottom gap at standby voltage can be measured.
- 4- The bottom gaps are ramped up toward the working voltage of 9.8 kV to measure their contribution to the gamma rate estimation.
- 5-8 The steps 3 and 4 are repeated on TN and then on TW, keeping the bottom and the top gap which is not of interest at a voltage of 1 kV. This way, the individual contribution to the noise and gamma rates are known.
- 9- Finally, both TW and TN are brought to working voltage while the bottom gap is left at 1 kV to measure the gamma rate for the full top layer at once.

Finally, the voltages of all gaps are brought back to working voltage for the longevity program to continue until the next daily scan.

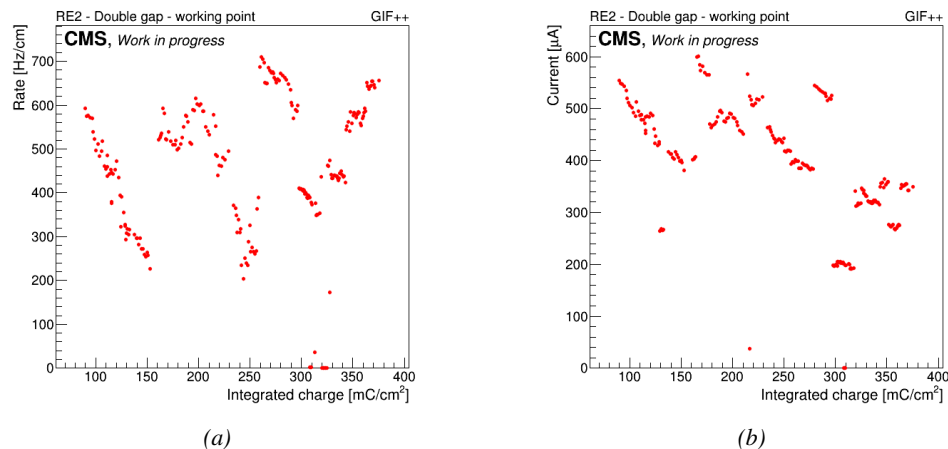


Figure 5.31: Example of rate (Figure 5.31a) and current (Figure 5.31b) monitoring of chamber RE2-2-NPD-BARC-09 with increasing integrated charge. The variations of rate and current are correlated and corresponds to change of source irradiation, gas flow, gas humidity, or environmental conditions.

Naturally, as this data is taken using Gif++ DAQ, 2 ROOT files containing the DAQ data and CAEN data are created for each runs in the exact same way than for efficiency or rate scans taken during test beam periods but while the currents are still monitored by the longevity scan and saved

3160 into GIFT++ database for an easy evaluation of the currents to the integrated charge. The Offline
 3161 Analysis tool provides then the DQM page with histograms and daily values can be assembled in
 3162 long term monitoring plots to study the variations of rate and current with increasing integrated
 3163 charge, as presented in Figure 5.31. The rates on every single read-out channel is also tracked to
 3164 control their activity with increasing integrated charge and, this way, understand the appearance of
 3165 hot spots through noisy channels, as showed in Figure 5.32.

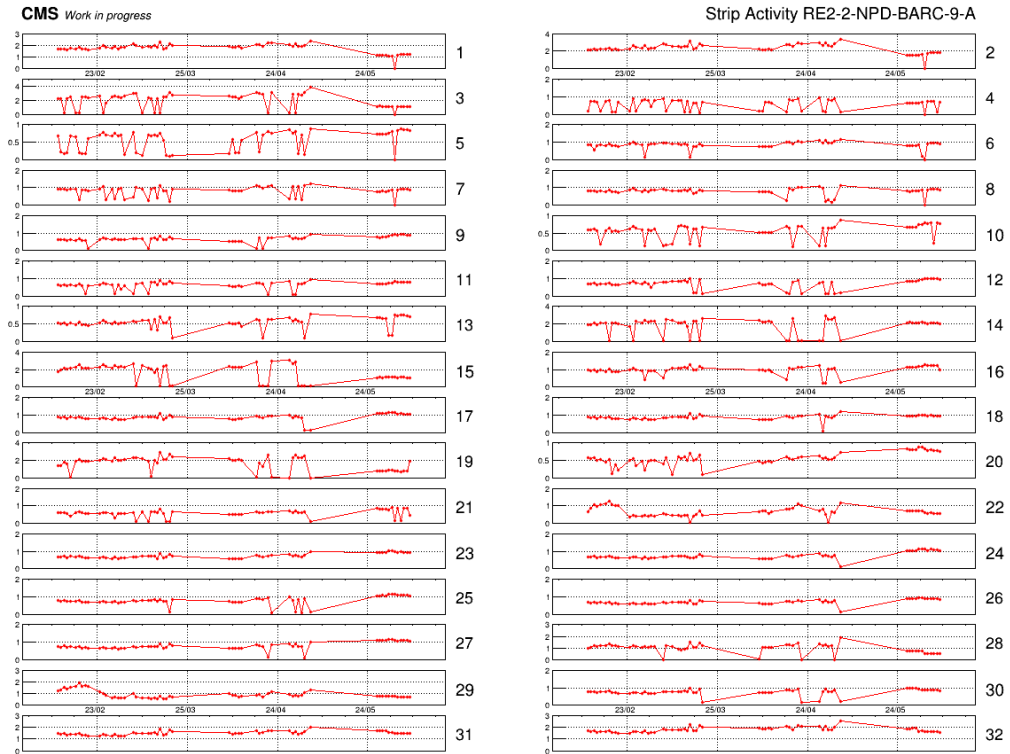


Figure 5.32: Example of strip activity of chamber RE2-2-NPD-BARC-09 monitoring through time. The activity of a strip is defined as the rate of the individual channel normalized to the mean rate measured in the corresponding read-out partition.

3166 5.3.5.3 Weekly noise monitoring scans

3167 Once a week, the source is turned OFF for the CMS RPC to make a noise scan, which consist into
 3168 a HV scan composed of 7 runs and involving both the irradiated but also the reference chambers,
 3169 providing with a weekly monitoring of the evolution of the irradiated chambers noise and dark
 3170 current. The first run is taken at standby voltage for all chambers while the next 6 runs are taken
 3171 with voltages ranging from 9.4 to 9.9 kV in order to have for both type of chambers, RE2 and RE4, a
 3172 coverage of the noise rate in the voltage region in which the efficiency rises and reaches the plateau.

3173 5.3.5.4 Weekly source scans

3174 Directly following the weekly noise scans, HV rate scans are organised at 3 different source settings,
 3175 usually corresponding to ABS 6.8, 4.6 and 3.3. The procedure of these HV scans is strictly similar to

3176 which of weekly noise scans, involving the four RPCs in order to have a weekly comparison of the
 3177 values recorded in every chambers. Measuring with all detectors at the same time allows to get rid
 3178 of potential systematics that might make the rates (noise or gamma) vary from one measurement to
 3179 another. If such systematic effect occurs, it will be observed in all detectors.

3180 **5.3.5.5 Weekly current scans**

3181 The previously detailed daily rate scans, but also the weekly noise and source scans are interesting
 3182 tools to look at an increase of noise rates and dark currents or at a loss of rate capability and point
 3183 to an increase of surface resistivity of the electrodes through the absorption of fluoridric acid. Nev-
 3184 ertheless, periodically measuring the currents on wider high voltage ranges allows to have access
 3185 to the ohmic part of the current driven by the detectors related to the electrodes resistance. This is
 3186 why precise current scans, consisting only in measuring the current driven through the 4 detectors,
 3187 are performed each week. The scan procedure consists in 131 high voltage steps in between 500 V
 3188 and 10 kV by steps of 100 V until the standby voltage of 6.5 kV is reached and then by steps of
 3189 50 V. The current increase in between 500 V and the voltage where charge multiplication starts to
 3190 occur is only driven by the resistance of the detector to current and thus increases linearly. A fit on
 3191 this linear increase of the currents in the range before charge multiplication occurs gives access to
 3192 the resistance of the system electrodes/gas. If any variation of the electrode resistance occurs, the
 3193 global resistance will increase and so will the current. Technically, these scans will record a ROOT
 3194 file per HV step that will have the same format than the CAEN ROOT file saved during other HV
 3195 scans and is also analysed using the Offline Analysis tool to provide with DQM histograms as well
 3196 as standardised I/V tables.

3197 **5.3.5.6 Resistivity measurements**

3198 Aside of the parameters monitored to spot ageing, the resistivity of the HPL planes is measured
 3199 regularly before or after test beam periods through high voltage scans of the detectors operated
 3200 with pure Argon. The electric field strength at which Argon breaks down being well known, the
 3201 breakdown voltage in the detectors is measured and gives an information about the resistance of the
 3202 electrodes, as above the breakdown voltage Argon turns into a conductive plasma and thus does not
 3203 offer electric resistance anymore, which then can be used to calculate the resistivity of the electrode
 3204 material. The Argon line in GIF++ are not kept humid and thus this measurement is not performed
 3205 too often to make sure the electrodes don't dry out, leading to an increase of the electrode resistivity.

3206 **5.3.6 Results and discussions**

3207 Since 2015, CMS RPCs have been irradiated in GIF++ with the goal to reach a total integrated
 3208 charge per irradiated detector of 0.84 C/cm^2 while certifying the detectors to a rate capability of
 3209 600 Hz/cm^2 . As of today, the RE2 and RE4 chambers respectively achieved 51 and 26% of the
 3210 total irradiation program. A few years of irradiation are expected before reaching the end of the
 3211 longevity study and a final answer on whether the detector will be able to live through HL-LHC or
 3212 not. A negative answer to this question would probably lead to solutions to replace the detectors
 3213 before HL-LHC or to improve the shielding of these detectors against background radiation in CMS
 3214 cavern, which could be a more sustainable solution.

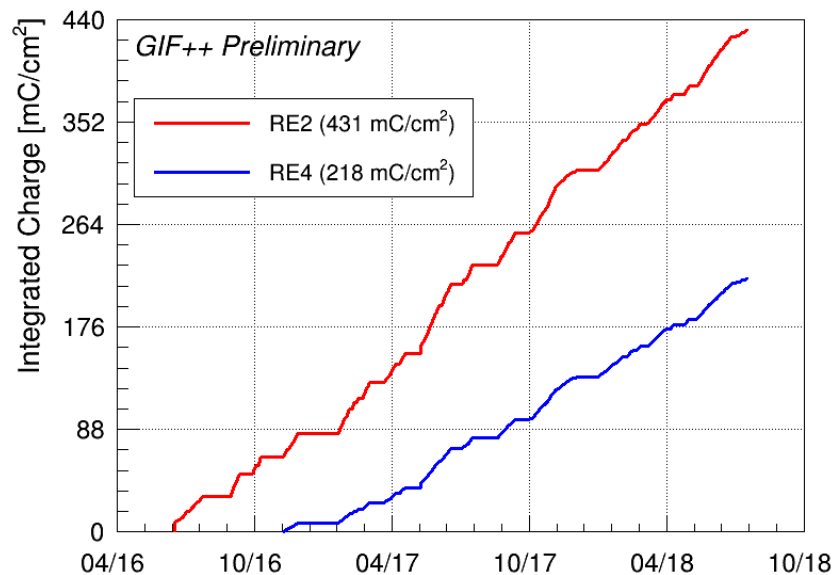


Figure 5.33: Total integrated charge in the irradiated RPCs, RE2–2–NPD–BARC–9 and RE4–2–CERN–165, before starting August 2018 test beam period. The irradiation of the RE2 chamber started in June 2016 while the RE4 chamber couldn't be irradiated before November 2016.

6

3215

3216

3217

Improved RPC investigation and preliminary electronics studies

3218 The extension in the endcap of the RPC sub-system towards higher pseudo-rapidity will bring the
3219 new detectors to be exposed to much more intense background radiations due to the proximity of
3220 the detectors with the beam line. The challenge will be to produce high counting rate detectors
3221 with limited ageing rate to ensure a stable operation of the detector over a period longer than 10
3222 years. In Chapter 4 was discussed the influence of the detector design (number and thickness of
3223 gas volumes, OR system, etc...) on the charge deposition and rate capability. Nevertheless, this
3224 question can also be addressed from the electronics point of view as a better signal to noise ratio
3225 would also mean the possibility to greatly lower the charge threshold on the signals to be detected,
3226 allowing to use the detector at lower gain, hence lowering the charge deposition per avalanche in the
3227 gas volume. Cardarelli showed that the production of low-noise fast FEE could help decreasing the
3228 charge deposition per avalanche at working voltage by an order of magnitude virtually increasing
3229 the life expectancy of such a detector in the same way [253].

3230 **6.1 FEE candidate for the production of iRPCs**

3231 The extension of the third or fourth endcap disks with improved RPCs has been presented in
3232 Chapter 3 together with the expected background levels and the needed requirements from such
3233 detectors to bring out the full potential of the CMS detector by strongly reducing the detection rate
3234 thanks to a more precise reconstruction of the events of interest. An important piece of these iRPCs
3235 will be the Front-End Electronics that will be equipped on the chambers. A fast, low-jitter and low
3236 charge sensitive electronics will help in further reducing the charge deposition in the detector by
3237 making it possible to operate at lower gain.

3238 In the context of the CMS Muon Upgrade, two FEE solutions have been considered to equip the
3239 iRPCs. The baseline for the RPC upgrade is based on the PETIROC ASIC, initially for Time-of-
3240 flight (ToF) applications. A back-up solution is also under study and focuses on a new low-noise

3241 preamplifier designed in INFN laboratories in Rome to replace the preamplification stage of the
 3242 already existing CMS RPC Front-End Board.

3243 The FEEs that are foreseen to equip the new RPCs need to be able to detect charges as small as
 3244 10 fC. Not only the new electronics need to be fast and reliable, they also should be able to sustain
 3245 the high radiation the detectors will be subjected to in the region closest to the beam.

3246 6.1.1 CMS RPCROC: the RPC upgrade baseline

3247 Designed by Weeroc, a spin-off company from the french OMEGA laboratory, the PETIROC 2A
 3248 consists in a fast and low jitter 32-channel ASIC originally developed to read-out Silicon Photomul-
 3249 tiplier (SiPM) in ToF applications and that allows for precise time measurements [254, 255]. The
 3250 ASIC uses an AMS 350 ns SiGe technology. The block diagram of the ASIC is showed on Fig-
 3251 ure 6.1. A 10-bit DAC allows to adjust the trigger level in a dynamical range spanning from 0.5 to
 3252 a few tens of photoelectrons and a 6-bit DAC to adjust the response of each individual channel to
 3253 similar a level.

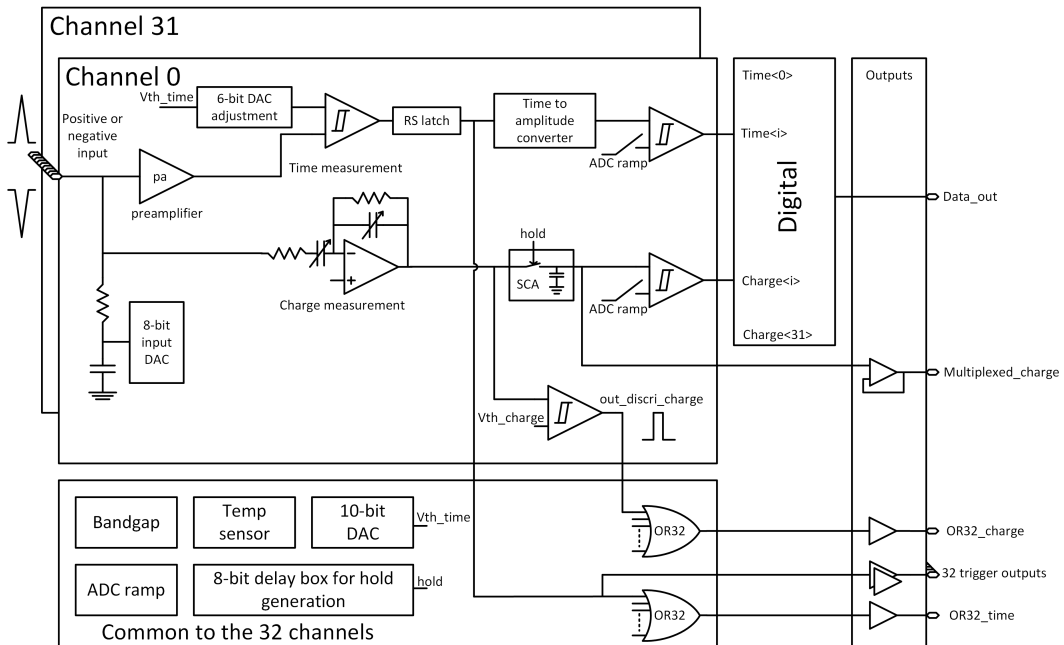


Figure 6.1: PETIROC 2A block diagram.

3254 Nevertheless, in order to adapt this ASIC to CMS, modifications were brought to the PETIROC [171].
 3255 In the new CMS RPCROC, the measurement of the charge will be performed by a TimeOverTech-
 3256 nique, taking profit of the capacity the ASIC has in measuring both the leading and trailing edges of the
 3257 input signals. The dynamic range will be expanded towards lower values to allow for the detection
 3258 of charges as low as 10 fC. Due to the radiation levels that are foreseen at the level of the iRPCs, the
 3259 SiGe technology will be replaced by the Taiwan Semiconductor Manufacturing Company (TSMC)
 3260 130 nm CMOS, to increase its radiation hardness while keeping fast pre-amplification and discrimi-
 3261 nation with a very low jitter that can reach less than 20 ps if no internal clock is used, as can be seen
 3262 from Figure 6.2. The ASIC is associated with an FPGA which purpose is to measure time thanks to

3263 a TDC with a time resolution of 50-100 ps developed by Tsinghua University and that will provide
 3264 a measurement of the signal position along the strip with a precision of a few cm by measuring the
 3265 signal timing on both ends of the strips. In order to read-out all 96 strips, 3 ASICs and 3 TDCs, each
 3266 having an increased number of 64-channels, are hosted on a FEB attached to the chamber.

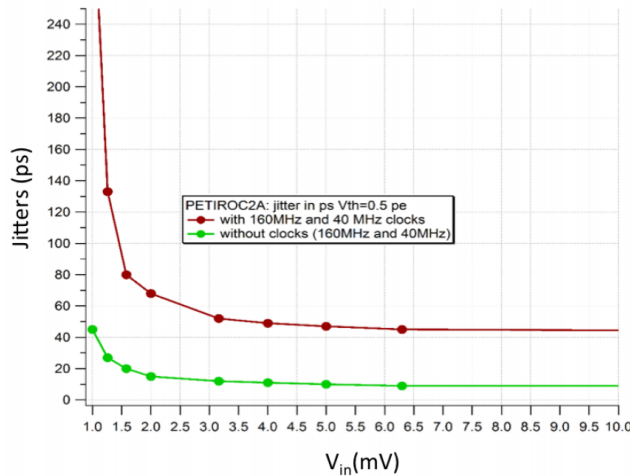


Figure 6.2: The PETIROC time jitter as a function of the input signal amplitude, measured with and without internal clocks.

3267 6.1.2 INFN Front-End Electronics: a robust back-up solution

3268 6.2 Preliminary tests at CERN

7

3269

3270

Conclusions and outlooks

3271 **7.1 Conclusions**

3272 **7.2 Outlooks**

A

3273

3274

A data acquisition software for CAEN VME TDCs

3275

3276 Certifying detectors in the perspective of HL-LHC required to develop tools for the GIF++ expe-
3277 riment. Among them was the C++ Data Acquisition (DAQ) software that allows to make the commu-
3278 nications in between a computer and TDC modules in order to retrieve the RPC data [256]. In this
3279 appendix, details about this software, as of how the software was written, how it functions and how
3280 it can be exported to another similar setup, will be given.

3281 A.1 GIF++ DAQ file tree

3282 GIF++ DAQ source code is fully available on github at [https://github.com/afagot/GIF_](https://github.com/afagot/GIF_DAQ)
3283 DAQ. The software requires 3 non-optional dependencies:

- 3284 • CAEN USB Driver, to mount the VME hardware,
- 3285 • CAEN VME Library, to communicate with the VME hardware, and
- 3286 • ROOT, to organize the collected data into a TTree.

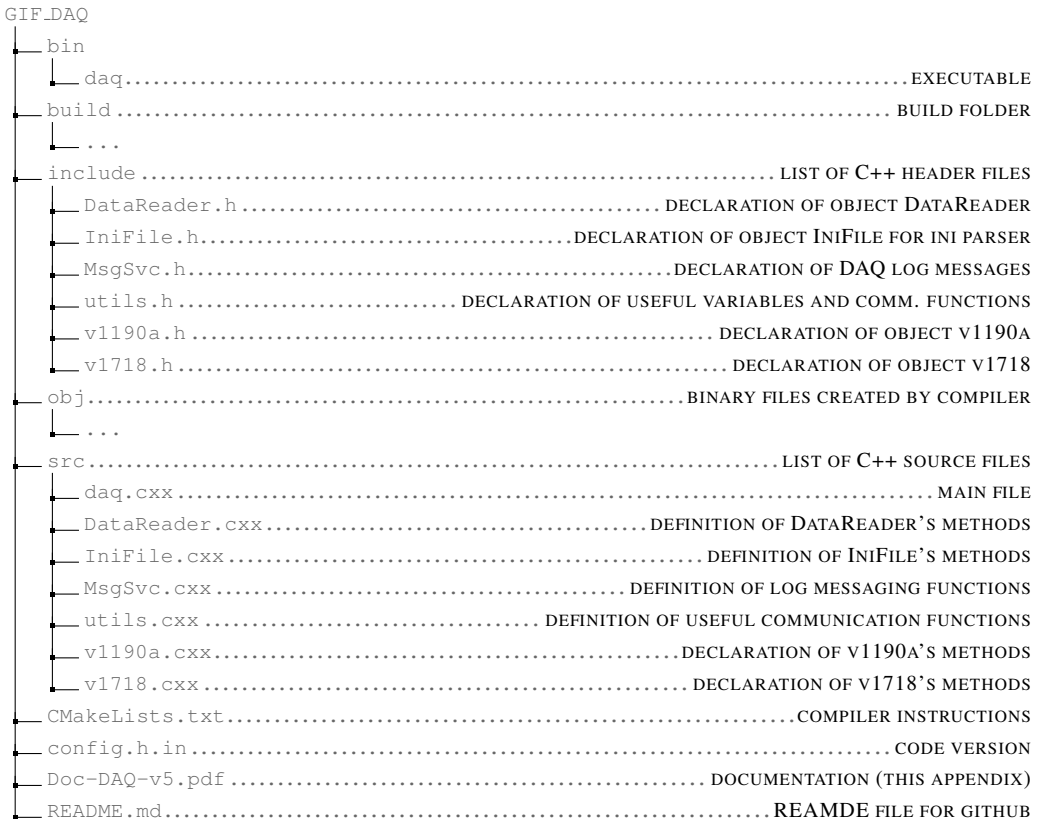
3287 The CAEN VME library will not be packaged by distributions and will need to be installed man-
3288 ually. To compile the GIF++ DAQ project via a terminal, from the DAQ folder use the command:

```
3289 mkdir build
3290 cd build
3291 cmake ..
3292 make install
```

3291 The source code tree is provided below along with comments to give an overview of the files' con-
3292 tent. The different objects created for this project (`v1718`, `v1190a`, `IniFile` & `DataReader`) will be

3293 described in details in the following sections.

3294



3295

A.2 Usage of the DAQ

3296 GIF++ DAQ, as used in GIF++, is not a standalone software. Indeed, the system being more com-
 3297 plexe, the DAQ only is a sub-layer of the software architecture developped to control and monitor
 3298 the RPCs that are placed into the bunker for performance study in an irradiated environment. The top
 3299 layer of GIF++ is a Web Detector Control System (webDCS) application. The DAQ is only called
 3300 by the webDCS when data needs to be acquired. The webDCS operates the DAQ through command
 3301 line. To start the DAQ, the webDCS calls:

3302

3303 bin/daq /path/to/the/log/file/in/the/output/data/folder

3304 where /path/to/the/log/file/in/the/output/data/folder is the only argument required. This
 3305 log file is important for the webDCS as this file contains all the content of the communication of the
 3306 webDCS and the different systems monitored by the webDCS. Its content is constantly displayed
 3307 during data taking for the users to be able to follow the operations. The communication messages
 3308 are normally sent to the webDCS log file via the functions declared in file MsgSvc.h, typically
 3309 MSG_INFO(string message).

3310

3311 A.3 Description of the readout setup

3312 The CMS RPC setup at GIF++ counts 5 V1190A Time-to-Digital Converter (TDC) manufactured
 3313 by CAEN [242]. V1190A are VME units accepting 128 independent Multi-Hit/Multi-Event TDC
 3314 channels whose signals are treated by 4 100 ps high performance TDC chips developed by CERN
 3315 / ECP-MIC Division. The communication between the computer and the TDCs to transfer data is
 3316 done via a V1718 VME master module also manufactured by CAEN and operated from a USB
 3317 port [243]. These VME modules are all hosted into a 6U VME 6021 powered crate manufactured by
 3318 W-Ie-Ne-R than can accommodate up to 21 VME bus cards [257]. These 3 components of the DAQ
 3319 setup are shown in Figure A.1.

3320

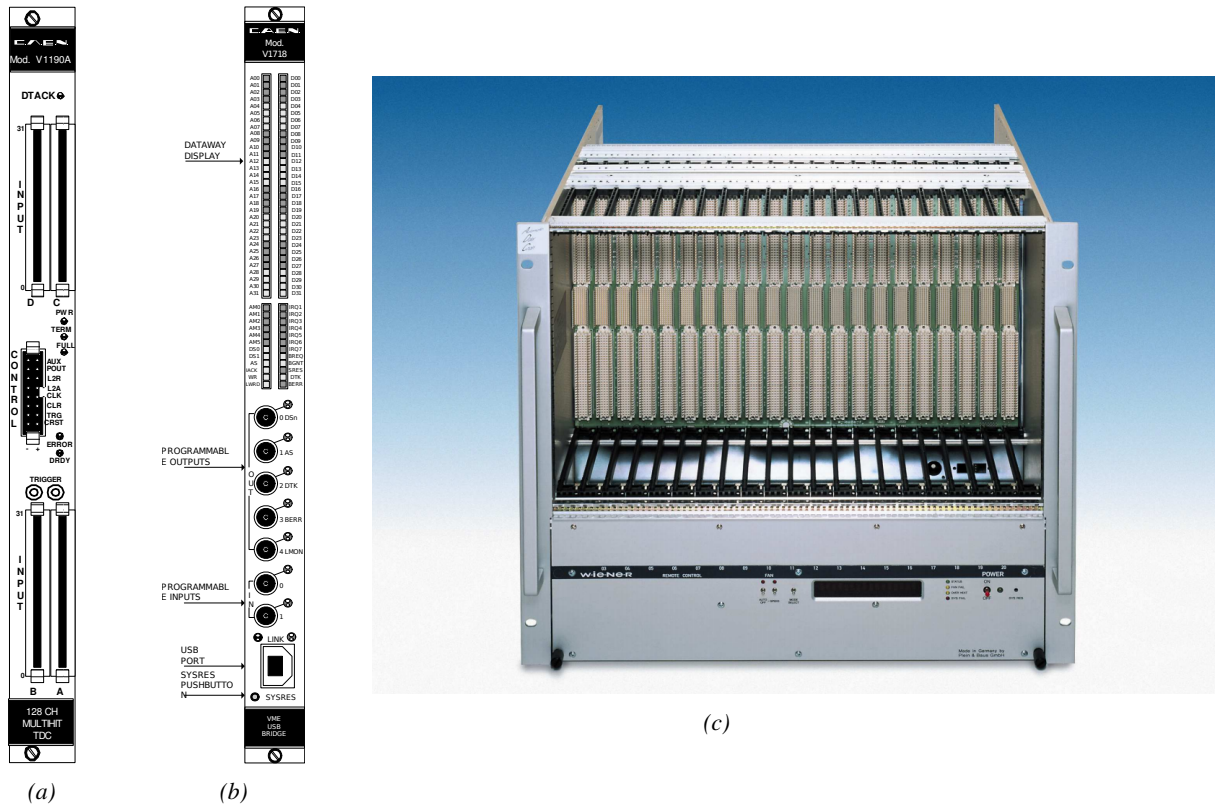


Figure A.1: (A.1a) View of the front panel of a V1190A TDC module [242]. (A.1b) View of the front panel of a V1718 Bridge module [243]. (A.1c) View of the front panel of a 6U 6021 VME crate [257].

3321 A.4 Data read-out

3322 To efficiently perform a data readout algorithm, C++ objects to handle the VME modules (TDCs
 3323 and VME bridge) have been created along with objects to store data and read the configuration file
 3324 that comes as an input of the DAQ software.

3325

A.4.1 V1190A TDCs

The DAQ used at GIF takes profit of the *Trigger Matching Mode* offered by V1190A modules. This setting is enabled through the method `v1190a::SetTrigMatching (int ntdcs)` where `ntdcs` is the total number of TDCs in the setup this setting needs to be enabled for (Source Code A.1). A trigger matching is performed in between a trigger time tag, a trigger signal sent into the TRIGGER input of the TDC visible on Figure A.1a, and the channel time measurements, signals recorded from the detectors under test in our case. Control over this data acquisition mode, explained through Figure A.2, is offered via 4 programmable parameters:

- **match window:** the matching between a trigger and a hit is done within a programmable time window. This is set via the method
`void v1190a::SetTrigWindowWidth(Uint windowHeight, int ntdcs)`
- **window offset:** temporal distance between the trigger tag and the start of the trigger matching window. This is set via the method
`void v1190a::SetTrigWindowWidth(Uint windowHeight, int ntdcs)`
- **extra search margin:** an extended time window is used to ensure that all matching hits are found. This is set via the method
`void v1190a::SetTrigSearchMargin(Uint searchMargin, int ntdcs)`
- **reject margin:** older hits are automatically rejected to prevent buffer overflows and to speed up the search time. This is set via the method
`void v1190a::SetTrigRejectionMargin(Uint rejectMargin, int ntdcs)`

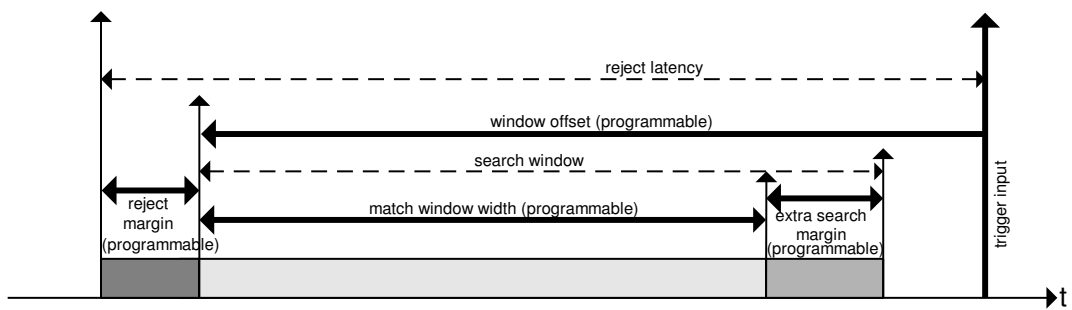


Figure A.2: Module V1190A Trigger Matching Mode timing diagram [242].

Each of these 4 parameters are given in number of clocks, 1 clock being 25 ns long. It is easy to understand at this level that there are 3 possible functioning settings:

- **1:** the match window is entirely contained after the trigger signal,
- **2:** the match window overlaps the trigger signal, or
- **3:** the match window is entirely contained before the trigger signal as displayed on Figure A.2.

In both the first and second cases, the sum of the window width and of the offset can be set to a maximum of 40 clocks, which corresponds to 1 μ s. Evidently, the offset can be negative, allowing

3353 for a longer match window, with the constraint of having the window ending at most 1 μ s after the
3354 trigger signal. In the third case, the maximum negative offset allowed is of 2048 clocks (12 bit) cor-
3355 responding to 51.2 μ s, the match window being strictly smaller than the offset. In the case of GIF++,
3356 the choice has been made to use this last setting by delaying the trigger signal. During the studies
3357 performed in GIF++, both the efficiency of the RPCs, probed using a muon beam, and the noise or
3358 gamma background rate are monitored. The extra search and reject margins are left unused.

3359 To probe the efficiency of RPC detectors, the trigger time tag is provided by the coïncidence of
3360 scintillators when a bunch of muons passes through GIF++ area is used to trigger the data acquisi-
3361 tion. For this measurement, it is useful to reduce the match window width only to contain the muon
3362 information. Indeed, the delay in between a trigger signal and the detection of the corresponding
3363 muon in the RPC being very contant (typically a few tens of ns due to jitter and cable length), the
3364 muon signals are very localised in time. Thus, due to a delay of approximalety 325 ns in between
3365 the muons and the trigger, the settings were chosen to have a window width of 24 clocks (600 ns)
3366 centered on the muon peak thanks to a negative offset of 29 clocks (725 ns).

3367 On the otherhand, monitoring the rates don't require for the DAQ to look at a specific time window.
3368 It is important to integrate enough time to have a robust measurement of the rate as the number of
3369 hits per time unit. The triggering signal is provided by the pulse generator integrated into the com-
3370 munication module V1718 at a frequency of 100 Hz to ensure that the data taking occurs in a random
3371 way, uncorrelated with beam physics, to probe only the irradiation spectrum on the detectors. The
3372 match window is set to 400 clocks (10 μ s) and the negative offset to 401 clocks as it needs to exceed
3373 the value of the match window.

3374

3375 The v1190a object, defined in the DAQ software as in Source Code A.1, offers the possil-
3376 ity to store all TDCs in the readout setup into a single object containing a list of hardware ad-
3377 dresses (addresses to access the TDCs' buffer through the VME crate) and each constructor and
3378 method acts on the list of TDCs to set the different acquisition parameters as describe above.
3379 The type of trigger matching is chosen with `v1190a::SetTrigMatching()` and the time substrac-
3380 tion, used to have a time measurement referring to the beggining of the time window, is set by
3381 `v1190a::SetTrigTimeSubtraction()`. Then, the wiwdow width and offset are respectively set
3382 thanks to `v1190a::SetTrigWindowWidth()` and `v1190a::SetTrigWindowOffset()`. The rejection
3383 and extra search margin, even if left unused and hence set to a default value of 0, can be set through
3384 `v1190a::SetTrigRejectionMargin()` and `v1190a::SetTrigSearchMargin()`. These methods are
3385 then called in `v1190a::SetTrigConfiguration()` that uses the information contained in the config-
3386 uration file `IniFile *iniFile` to set the different TDC parameters. A thorough explaination of the
3387 content of the configuration file is provided in Section A.5.2.

3388

3389 Among the other methods of class `v1190a` can be found a set of the detection mode (`v1190a::SetTDC`
3390 `DetectionMode()`), of the TDC time resolution (`v1190a::SetTDCResolution()`), of the dead time
3391 in between two consecutive signals recorded into a single channel (`v1190a::SetTDCDeadTime()`) or
3392 of the maximal number of signals that can be recorded per event (`v1190a::SetTDCEventSize()`). To
3393 help with setting these parameters, `enum` were used (`EdgeMode`, `Resolution`, `DeadTime` and `HitMax`
3394 are defined in `include/v1190a.h`).

```

3395
class v1190a
{
    private :
        long             Handle;
        vector<Data32>   Address;
        CVDataWidth      DataWidth;
        CVAAddressModifier AddressModifier;

    public:

        v1190a(long handle, IniFile *inifile, int ntdcs);
        ~v1190a();
        Data16 write_op_reg(Data32 address, int code, string error);
        Data16 read_op_reg(Data32 address, string error);
        void Reset(int ntdcs);
        void Clear(int ntdcs);
        void TestWR(Data16 value,int ntdcs);
        void CheckTDCStatus(int ntdcs);
        void CheckCommunication(int ntdcs);
        void SetTDCTestMode(Data16 mode,int ntdcs);
        void SetTrigMatching(int ntdcs);
        void SetTrigTimeSubtraction(Data16 mode,int ntdcs);
        void SetTrigWindowWidth(Uint windowHeight,int ntdcs);
        void SetTrigWindowOffset(Uint windowOffset,int ntdcs);
        void SetTrigSearchMargin(Uint searchMargin,int ntdcs);
        void SetTrigRejectionMargin(Uint rejectMargin,int ntdcs);
        void GetTrigConfiguration(int ntdcs);
        void SetTrigConfiguration(IniFile *inifile,int ntdcs);
        void SetTDCDetectionMode(Data16 mode,int ntdcs);
        void SetTDCResolution(Data16 lsb,int ntdcs);
        void SetTDCDeadTime(Data16 time,int ntdcs);
        void SetTDCHeadTrailer(Data16 mode,int ntdcs);
        void SetTDCEventSize(Data16 size,int ntdcs);
        void SwitchChannels(IniFile *inifile,int ntdcs);
        void SetIRQ(Data32 level, Data32 count,int ntdcs);
        void SetBlockTransferMode(Data16 mode,int ntdcs);
        void Set(IniFile *inifile,int ntdcs);
        void CheckStatus(CVErrorCodes status) const;
        int ReadBlockD32(Uint tdc, const Data16 address,
                         Data32 *data, const Uint words, bool ignore_berr);
        Uint Read(RAWData *DataList,int ntdcs);
};

3396

```

3397 *Source Code A.1: Description of C++ object v1190a.*

3398 The detection mode corresponds to the type of edge detection the TDC will be using to
 3399 record the data. The TDCs can record the time stamp of the leading edge alone, of the trailing edge
 3400 alone, of both or they can operate in pair mode, meaning that the leading edge is recorded together
 3401 with the time difference in between leading and trailing edges. This last mode is not very practical
 3402 for the case of GIFT++ measurements as the information is coded into a single words in the TDC's
 3403 buffer, putting strong constraints on the time window and duration of the input signals. Indeed,
 3404 when recording the edges individually (single edge or both edges), a 32-bit word, of which 18 are
 3405 used to provide the time information alone, is stored into memory for each signal edge. With the
 3406 pair mode, instead of having one 32-bit word per edge, only a single 32-bit word is written of which
 3407 12 are used for the leading edge time information and 6 for the width of the pulse, as described on
 3408 p73 of reference [242]. This way, even though the pair mode is convenient to use as it automatically

3409 correlates a leading edge with the corresponding signal width in a single word, it is advised to be
 3410 careful when using it and to be aware of the extra time constraints (for both leading time and signal
 3411 width) that will come for choosing this setting. If it is necessary to work with large input signals,
 3412 the mode recording both edges will be preferred to the pair mode and the association of a leading
 3413 and trailing edges pair will then be performed offline by the user. Then, the time resolution is to be
 3414 chosen in a range from 100 to 800 ps, the dead time in a range from 5 to 100 ns, and the maximal
 3415 number of hits per event in a range from 0 to 128 with the possibility to choose to have no limits.

3416 A.4.2 DataReader

3417 Enabled thanks to `v1190a::SetBlockTransferMode()`, the data transfer is done via Block Transfer
 3418 (BLT). Using BLT allows to transfer a fixed number of events called a *block*. This is used together
 3419 with an Almost Full Level (AFL) of the TDCs' output buffers, defined through `v1190a::SetIRQ()`.
 3420 This AFL gives the maximum amount of 32735 words (16 bits, corresponding to the depth of a TDC
 3421 output buffer) that can be written in a buffer before an Interrupt Request (IRQ) is generated and seen by
 3422 the VME Bridge V1718, which sends a `BUSY` signal intended to stopping the data acquisition during
 3423 the transfer of the content of each TDC buffers before resuming. For each trigger, 6 words or more
 3424 are written into the TDC buffer:

- 3425 • **a global header** providing information of the event number since the beginning of the data
 3426 acquisition,
- 3427 • **a TDC header** which is enabled thanks to `v1190a::SetTDCHeadTrailer()`,
- 3428 • **the TDC data (if any)**, 1 for each hit recorded during the event, providing the channel and the
 3429 time stamp associated to the hit,
- 3430 • **a TDC error** providing error flags,
- 3431 • **a TDC trailer** which is enabled thanks to `v1190a::SetTDCHeadTrailer()`,
- 3432 • **a global trigger time tag** that provides the absolute trigger time relatively to the last reset,
 3433 and
- 3434 • **a global trailer** providing the total word count in the event.

3435 CMS RPC FEEs provide with 100 ns long LVDS output signals that are injected into the TDCs'
 3436 input. Any avalanche signal that gives a signal above the FEEs threshold is thus recorded by the
 3437 TDCs as a hit within the match window. Each hit is assigned to a specific TDC channel with a time
 3438 stamp, with a precision of 100 ps. The reference time, $t_0 = 0$, is provided by the beginning of the
 3439 match window. Thus for each trigger, coming from a scintillator coincidence or the pulse generator,
 3440 a list of hits is stored into the TDCs' buffers and will then be transferred into a ROOT Tree.
 3441 When the BLT is used, it is easy to understand that the maximum number of words that have been set
 3442 as AFL will not be a finite number of events or, at least, the number of events that would be recorded
 3443 into the TDC buffers will not be a multiple of the block size. In the last BLT cycle to transfer data,
 3444 the number of events to transfer will most probably be lower than the block size. In that case, the
 3445 TDC can add fillers at the end of the block but this option requires to send more data to the computer
 3446 and is thus a little slower. Another solution is to finish the transfer after the last event by sending a
 3447 bus error that states that the BLT reached the last event in the pile. This method has been chosen in

3448 GIF++.

3449 Due to irradiation, an event in GIF++ can count up to 300 words per TDC. A limit of 4096 words
 3450 (12 bits) has been set to generate IRQ which represent from 14 to almost 700 events depending on
 3451 the average of hits collected per event. Then the block size has been set to 100 events with enabled
 3452 bus errors. When an AFL is reached for one of the TDCs, the VME bridge stops the acquisition by
 3453 sending a BUSY signal.

3454

3455 The data is then transferred one TDC at a time into a structure called `RAWData` (Source Code A.2).
 3456 Note that the structure as presented here is used when a single edge detection is used as there is only
 3457 one time stamp list associated to the hits. When using detection on both edges, a second time stamp
 3458 list could be added and when using pair detection, a list with the signal width could be added instead.

3459

```
3460   struct RAWData {
 3461     vector<int>                   *EventList;
 3462     vector<int>                   *NHitsList;
 3463     vector<int>                   *QFlagList;
 3464     vector<vector<int> >   *ChannelList;
 3465     vector<vector<float> >   *TimeStampList;
 3466 }
```

3461

Source Code A.2: Description of data holding C++ structure `RAWData`.

```
3462   class DataReader
 3463   {
 3464     private:
 3465       bool              StopFlag;
 3466       IniFile *iniFile;
 3467       Data32          MaxTriggers;
 3468       v1718            *VME;
 3469       int              nTDCs;
 3470       v1190a           *TDCs;
 3471       RAWData          TDCData;

 3472     public:
 3473       DataReader();
 3474       virtual ~DataReader();
 3475       void             SetIniFile(string inifilename);
 3476       void             SetMaxTriggers();
 3477       Data32           GetMaxTriggers();
 3478       void             SetVME();
 3479       void             SetTDC();
 3480       int             GetQFlag(Uint it);
 3481       void             Init(string inifilename);
 3482       void             FlushBuffer();
 3483       void             Update();
 3484       string           GetFileName();
 3485       void             WriteRunRegistry(string filename);
 3486       void             Run();
 3487 }
```

3463

Source Code A.3: Description of C++ object `DataReader`.

3464

3465 In order to organize the data transfer and the data storage, an object called `DataReader` was
 3466 created (Source Code A.3). On one hand, it has `v1718` and `v1190a` objects as private members for
 3467 communication purposes, such as VME modules settings via the configuration file `*iniFile` or data

3467 read-out through `v1190a::Read()` and on the other hand, it contains the structure `RAWData` that allows
 3468 to organise the data in vectors reproducing the tree structure of a ROOT file.
 3469 Each event is transferred from `TDCData` and saved into branches of a ROOT `TTree` as 3 integers
 3470 that represent the event ID (`EventCount`), the number of hits read from the TDCs (`nHits`), and the
 3471 quality flag that provides information for any problem in the data transfer (`qflag`), and 2 lists of
 3472 `nHits` elements containing the fired TDC channels (`TDCCh`) and their respective time stamps (`TDCTS`),
 3473 as presented in Source Code A.4. The ROOT file file is named using information contained into
 3474 the configuration file, presented in section A.5.2. The needed information is extracted using method
 3475 `DataReader::GetFileName()` and allow to build the output filename format `ScanXXXXXX_HVX_DAQ.root`
 3476 where `ScanXXXXXX` is a 6 digit number representing the scan number into GIF++ database and `HVX`
 3477 the HV step within the scan that can be more than a single digit. An example of ROOT data file is
 3478 provided with Figure A.3.

```
3479
  RAWData TDCData;
  TFile *outputFile = new TFile(outputFileName.c_str(), "recreate");
  TTree *RAWDataTree = new TTree("RAWData", "RAWData");

  int EventCount = -9;
  int nHits = -8;
  int qflag = -7;
  vector<int> TDCCh;
  vector<float> TDCTS;

  RAWDataTree->Branch("EventNumber", &EventCount, "EventNumber/I");
  RAWDataTree->Branch("number_of_hits", &nHits, "number_of_hits/I");
  RAWDataTree->Branch("Quality_flag", &qflag, "Quality_flag/I");
  RAWDataTree->Branch("TDC_channel", &TDCCh);
  RAWDataTree->Branch("TDC_TimeStamp", &TDCTS);

  //...
  //Here read the TDC data using v1190a::Read() and place it into
  //TDCData for as long as you didn't collect the requested amount
  //of data.
  //...

  for(Uint i=0; i<TDCData.EventList->size(); i++) {
    EventCount = TDCData.EventList->at(i);
    nHits = TDCData.NHitsList->at(i);
    qflag = TDCData.QFlagList->at(i);
    TDCCh = TDCData.ChannelList->at(i);
    TDCTS = TDCData.TimeStampList->at(i);
    RAWDataTree->Fill();
  }
}
```

3481 *Source Code A.4: Highlight of the data transfer and organisation within `DataReader::Run()` after the data
 has been collected into `TDCData`.*

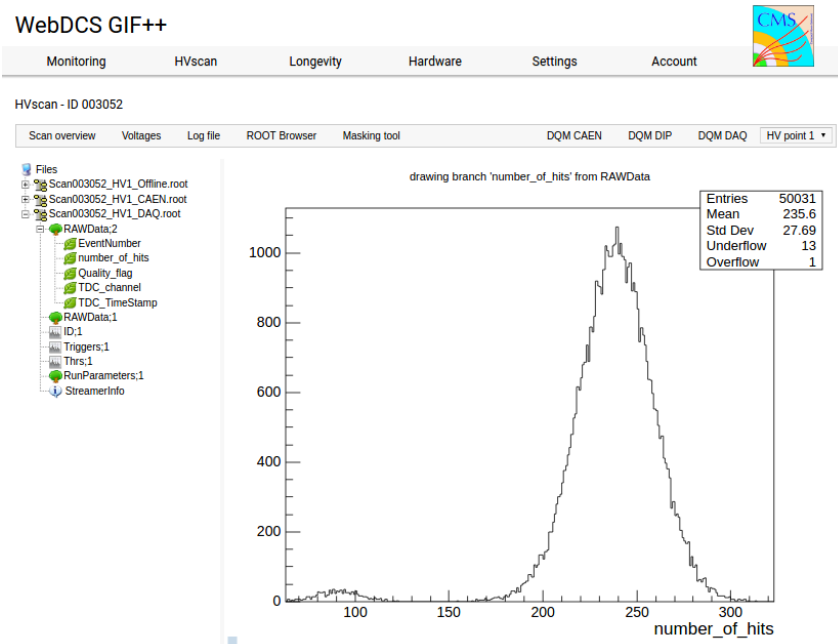


Figure A.3: Structure of the ROOT output file generated by the DAQ. The 5 branches (EventNumber, number_of_hits, Quality_flag, TDC_channel and TDC_TimeStamp) are visible on the left panel of the ROOT browser. On the right panel is visible the histogram corresponding to the variable nHits. In this specific example, there were approximately 50k events recorded to measure the gamma irradiation rate on the detectors. Each event is stored as a single entry in the TTree.

3482 A.4.3 Data quality flag

3483 Among the parameters that are recorded for each event, the quality flag is determined on the fly
 3484 by checking the data recorded by every single TDC. An `enum` called `QualityFlag` was written to
 3485 associate the key `GOOD` to the integer 1 and `CORRUPTED` to 0. From method `v1190a::Read()`, it can
 3486 be understood that the content of each TDC buffer is readout one TDC at a time. Entries are created
 3487 in the data list for the first TDC and then, when the second buffer is readout, events corresponding
 3488 to entries that have already been created to store data for the previous TDC are added to the existing
 3489 list element. On the contrary, when an event entry has not been yet created in the data list, a new
 3490 entry is created.

3491 It is possible that each TDC buffer contains a different number of events. In cases where the first
 3492 element in the buffer list is an event for corresponds to a new entry, the difference in between the
 3493 entry from the buffer and the last entry in the data list is recorded and checked. If it is greater than 1,
 3494 what should never be the case, the quality flag is set to `CORRUPTED` for this TDC and an empty entry
 3495 is created in the place of the missing ones. Missing entries are believe to be the result of a bad hold
 3496 on the TDC buffers at the moment of the readout. Indeed, the software hold is effective only on 1
 3497 TDC at a time and no solution as been found yet to completely block the writting in the buffers when
 3498 an IRQ is received.

3499 At the end of each BLT cycle, the ID of the last entry stored for each TDC buffer is not recorded.
 3500 When starting the next cycle, if the first entry in the pile corresponds to an event already existing
 3501 in the list, the readout will start from this list element and will not be able to check the difference

3502 in between this entry's ID and the one of the last entry that was recorded for this TDC buffer in
 3503 the previous cycle. In the case events were missing, the flag stays at its initial value of 0, which is
 3504 similar to CORRUPTED and it is assumed that then this TDC will not contribute to number_of_hits,
 3505 TDC_channel or TDC_TimeStamp. Finally, since there will be 1 RAWData entry per TDC for each event
 3506 (meaning nTDCs entries, referring to DataReader private attribute), the individual flags of each TDC
 3507 will be added together. The final format is an integer composed nTDCs digits where each digit is the
 3508 flag of a specific TDC. This is constructed using powers of 10 like follows:

3509 TDC 0: QFlag = $10^0 \times \text{QualityFlag}$

3510 TDC 1: QFlag = $10^1 \times \text{QualityFlag}$

3511 ...

3512 TDC N: QFlag = $10^N \times \text{QualityFlag}$

3513 and the final flag to be with N digits:

3514 QFlag = n....3210

3515 each digit being 1 or 0. Below is given an example with a 4 TDCs setup.

3516 If all TDCs were good : QFlag = 1111,

3517 but if TDC 2 was corrupted : QFlag = 1011.

3518 When data taking is over and the data contained in the dynamical RAWData structure is transferred
 3519 to the ROOT file, all the 0s are changed into 2s by calling the method DataReader::GetQFlag().
 3520 This will help translating the flag without knowing the number of TDCs beforehand. Indeed, a flag
 3521 111 could be due to a 3 TDC setup with 3 good individual TDC flags or to a more than 3 TDC setup
 3522 with TDCs those ID is greater than 2 being CORRUPTED, thus giving a 0.

3523 The quality flag has been introduced quite late, in October 2017 only, to the list of GIFT++ DAQ
 3524 parameters to be recorded into the output ROOT file. Before this addition, the missing data, corrupting
 3525 the quality for the offline analysis, was contributing to artificially fill data with lower multiplicity.
 3526 Looking at TBranch number_of_hits provides an information about the data of the full GIFT++
 3527 setup. When a TDC is not able to transfer data for a specific event, the effect is a reduction of the
 3528 total number of hits recorded in the full setup, this is what can be seen from Figure A.4. After offline
 3529 reconstruction detector by detector, the effect of missing events can be seen in the artificially filled
 3530 bin at multiplicity 0 shown in Figure A.5. Nonetheless, for data with high irradiation levels, as it is
 3531 the case for Figure A.5a, discarding the fake multiplicity 0 data can be done easily during the offline
 3532 analysis. At lower radiation, the missing events contribution becomes more problematic as the mul-
 3533 tiplicity distribution overlaps the multiplicity 0 and that in the same time the proportion of missing
 3534 events decreases. Attempts to fit the distribution with a Poisson or skew distribution function were
 3535 not conclusive and this very problem has been at the origin of the quality flag that allows to give a
 3536 non ambiguous information about each event quality.

3537

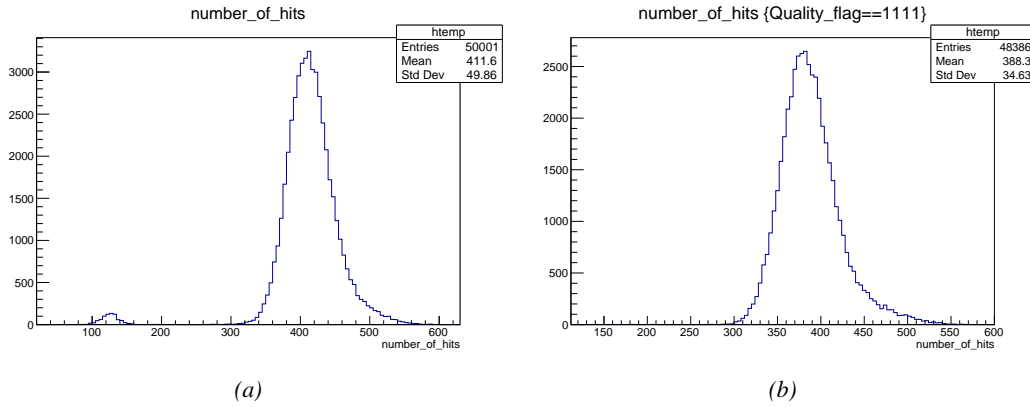


Figure A.4: The effect of the quality flag is explained by presenting the content of TBranch `number_of_hits` of a data file without `Quality_flag` in Figure A.4a and the content of the same TBranch for data corresponding to a `Quality_flag` where all TDCs were labelled as `GOOD` in Figure A.4b taken with similar conditions. It can be noted that the number of entries in Figure A.4b is slightly lower than in Figure A.4a due to the excluded events.

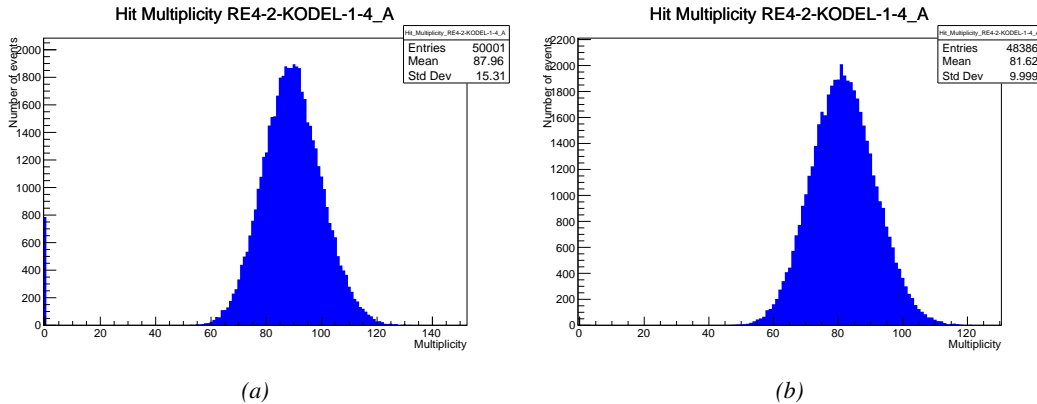


Figure A.5: Using the same data as previously showed in Figure A.4, the effect of the quality flag is explained by presenting the reconstructed hit multiplicity of a data file without `Quality_flag` in Figure A.5a and the reconstructed content of the same RPC partition for data corresponding to a `Quality_flag` where all TDCs were labelled as `GOOD` in Figure A.5b taken with similar conditions. The artificial high content of bin 0 is completely suppressed.

3538 A.5 Communications

3539 To ensure data readout and dialog in between the machine and the TDCs or in between the webDCS
 3540 and the DAQ, different communication solutions were used. First of all, it is important to have a
 3541 module to allow the communication in between the TDCs and the computer from which the DAQ
 3542 operates. When this communication is effective, shifters using the webDCS to control data taking
 3543 can thus send instructions to the DAQ.

3545 **A.5.1 V1718 USB Bridge**

3546 In the previous section, the data transfer as been discussed. The importance of the `v1718` object
 3547 (Source Code A.5), used as private member of `DataReader`, was not explicited. VME master
 3548 modules are used for communication purposes as they host the USB port that connects the pow-
 3549 ered crate buffer to the computer were the DAQ is installed. From the source code point of view,
 3550 this object is used to control the communication status, by reading the returned error codes with
 3551 `v1718::CheckStatus()`, or to check for IRQs coming from the TDCs through `v1718::CheckIRQ()`.
 3552 To ensure that triggers are blocked at the hardware level, a NIM pulse is sent out of one of the two
 3553 first programmable outputs of the module (`v1718::SendBUSY()`) to the VETO of the coincidence
 3554 module where the trigger signals originate. As long as this signal is ON, no trigger can reach the
 3555 TDCs anymore. Finally, used in the case of noise and background measurements in which the trig-
 3556 ger needs not to be provided by the muon beam but by an uncorrelated source, a pulse generator
 3557 is enabled with `v1718::RDMTriggerPulse()`. The "random" pulse is sent through the third and
 3558 fourth outputs of the module. Both the BUSY signal and the random pulse are shaped in the method
 3559 `v1718::SetPulsers()` where the number of pulses to be generated, their width, as well as the period
 3560 of the pulse generator is defined.

3561

```
class v1718{
    private:
        int             Handle;
        Data32          Data;           // Data
        CVIRQLevels     Level;         // Interrupt level
        CVAddressModifier AM;          // Addressing Mode
        CVDataWidth     DataSize;       // Data Format
        Data32          BaseAddress;   // Base Address

    public:
        v1718(IniFile *inifile);
        ~v1718();
        long            GetHandle(void) const;
        int             SetData(Data16 data);
3562        Data16          GetData(void);
        int             SetLevel(CVIRQLevels level);
        CVIRQLevels     GetLevel(void);
        int             SetAM(CVAddressModifier am);
        CVAddressModifier GetAM(void);
        int             SetDataSize(CVDataWidth datasize);
        CVDataWidth     GetDataSize(void);
        int             SetBaseAddress(Data16 baseaddress);
        Data16          GetBaseAddress(void);
        void            CheckStatus(CVErrorCodes status) const;
        bool            CheckIRQ();
        void            SetPulsers(UINT RDM_Frequency);
        void            SendBUSY(PulserLevel level);
        void            RDMTriggerPulse(PulserLevel level);
};
```

3563

Source Code A.5: Description of C++ object v1718.

3564 **A.5.2 Configuration file**

3565 The DAQ software takes as input a configuration file written using INI standard [258]. This file is
 3566 partly filled with the information provided by the shifters when starting data acquisition using the
 3567 webDCS, as shown by Figure A.6. This information is written in section [**General**] and will later
 3568 be stored in the ROOT file that contains the DAQ data as can be seen from Figure A.3. Indeed,
 3569 another `TTree` called `RunParameters` as well as the 2 histograms `ID`, containing the scan number,
 3570 start and stop time stamps, and `Triggers`, containing the number of triggers requested by the shifter,
 3571 are available in the data files. Moreover, `ScanID` and `HV` are then used to construct the file name
 3572 thanks to the method `DataReader::GetFileName()`.

Chamber	RE2-2-NPD-BARC-8	RE4-2-CERN-105	RE2-2-NPD-BARC-9	RE4-2-CERN-105	RE4-2-KODEL-1-4	Max triggers
HV _{eff} 1	8600	8500	8600	8500	6500	
HV _{eff} 2	8700	8600	8700	8600	6600	
HV _{eff} 3	8800	8700	8800	8700	6700	
HV _{eff} 4	8900	8800	8900	8800	6800	
HV _{eff} 5	9000	8900	9000	8900	6900	
HV _{eff} 6	9100	9000	9100	9000	7000	
HV _{eff} 7	9200	9100	9200	9100	7100	
HV _{eff} 8	9300	9200	9300	9200	7200	
HV _{eff} 9	9400	9300	9400	9300	7300	
HV _{eff} 10	9500	9400	9500	9400	7400	

Figure A.6: WebDCS DAQ scan page. On this page, shifters need to choose the type of scan (Rate, Efficiency or Noise Reference scan), the gamma source configuration at the moment of data taking, the beam configuration, and the trigger mode. These information will be stored in the DAQ ROOT output. Are also given the minimal measurement time and waiting time after ramping up of the detectors is over before starting the data acquisition. Then, the list of HV points to scan and the number of triggers for each run of the scan are given in the table underneath.

3573 The rest of the information is written beforehand in the configuration file template, as explicated
 3574 in Source Code A.6, and contains the hardware addresses to the different VME modules in the
 3575 setup as well as settings for the TDCs. As the TDC settings available in the configuration file are not
 3576 supposed to be modified, an improvement would be to remove them from the configuration file and
 3577 to hardcode them inside of the DAQ code itself or to place them into a different INI file that would
 3578 host only the TDC settings to lower the probability for a bad manipulation of the configuration file
 3579 that can be modified from one of webDCS' menus.

3580

```
[General]
TdcS=4
ScanID=$scanid
HV=$HV
RunType=$runtype
MaxTriggers=$maxtriggers
Beam=$beam
[VMEInterface]
Type=V1718
BaseAddress=0xFF0000
Name=VmeInterface
int_trig_freq=100
[TDC0]
Type=V1190A
BaseAddress=0x00000000
Name=Tdc0
StatusA00-15=1
StatusA16-31=1
StatusB00-15=1
StatusB16-31=1
StatusC00-15=1
StatusC16-31=1
StatusD00-15=1
StatusD16-31=1
[TDC1]
Type=V1190A
BaseAddress=0x11110000
Name=Tdc1
StatusA00-15=1
StatusA16-31=1
StatusB00-15=1
StatusB16-31=1
StatusC00-15=1
StatusC16-31=1
StatusD00-15=1
StatusD16-31=1
3581
[TDC2]
Type=V1190A
BaseAddress=0x22220000
Name=Tdc2
StatusA00-15=1
StatusA16-31=1
StatusB00-15=1
StatusB16-31=1
StatusC00-15=1
StatusC16-31=1
StatusD00-15=1
StatusD16-31=1
[TDC3]
Type=V1190A
BaseAddress=0x44440000
Name=Tdc3
StatusA00-15=1
StatusA16-31=1
StatusB00-15=1
StatusB16-31=1
StatusC00-15=1
StatusC16-31=1
StatusD00-15=1
StatusD16-31=1
[TDCErrors]
TriggerExtraSearchMargin=0
TriggerRejectMargin=0
TriggerTimeSubtraction=0b1
TdcDetectionMode=0b01
TdcResolution=0b10
TdcDeadTime=0b00
TdcHeadTrailer=0b1
TdcEventSize=0b1001
TdcTestMode=0b0
BLTMode=1
```

Source Code A.6: INI configuration file template for 4 TDCs. In section [General], the number of TDCs is explicitated and information about the ongoing run is given. Then, there are sections for each and every VME modules. There buffer addresses are given and for the TDCs, the list of channels to enable is given. Finally, in section [TDCSettings], a part of the TDC settings are given.

```

3582 typedef map< const string, string > IniFileData;

3583 class IniFile{
    private:
        bool          CheckIfComment(string line);
        bool          CheckIfGroup(string line, string& group);
        bool          CheckIfToken(string line, string& key, string& value);
        string         FileName;
        IniFileData   FileData;
        int           Error;

    public:
        IniFile();
        IniFile(string filename);
        virtual      ~IniFile();

        // Basic file operations
        void          SetFileName(string filename);
        int           Read();
        int           Write();
        IniFileData   GetFileData();

        // Data readout methods
        Data32 addressType(string groupname, string keyname, Data32 defaultvalue);
        long          intType(string groupname, string keyname, long defaultvalue);
        long long    longType(string groupname, string keyname, long long
        ↵ defaultvalue);
        string         stringType(string groupname, string keyname, string defaultvalue);
        float         floatType(string groupname, string keyname, float defaultvalue);

        // Error methods
        string         GetErrorMsg();
};

3584 
```

Source Code A.7: Description of C++ object IniFile used as a parser for INI file format.

3585 In order to retrieve the information of the configuration file, the object `IniFile` has been developed
 3586 to provide an INI parser, presented in Source Code A.7. It contains private methods returning a
 3587 boolean to check the type of line written in the file, whether a comment, a group header or a key line
 3588 (`IniFile::CheckIfComment()`, `IniFile::CheckIfGroup()` and `IniFile::CheckIfToken()`). The
 3589 key may sometimes be referred to as *token* in the source code. Moreover, the private element
 3590 `FileData` is a map of `const` string to string that allows to store the data contained inside the
 3591 configuration file via the public method `IniFile::GetFileData()` following the formatting (see
 3592 method `IniFile::Read()`):

```

3593     string group, token, value;
    // Get the field values for the 3 strings.
    // Then concatenate group and token together as a single string
    // with a dot separation.
    token = group + "." + token;
    FileData[token] = value;

```

3595 More methods have been written to translate the different keys into the right variable format
 3596 when used by the DAQ. For example, to get a **float** value out of the configuration file data, knowing
 3597 the group and the key needed, the method `IniFile::floatType()` can be used. It takes 3 arguments
 3598 being the group name and key name (both `string`), and a default **float** value used as exception in
 3599 the case the expected combination of group and key cannot be found in the configuration file. This
 3600 default value is then used and the DAQ continues on working after sending an alert in the log file for
 3601 further debugging.

3602

3603 A.5.3 WebDCS/DAQ intercommunication

3604 When shifters send instructions to the DAQ via the configuration file, it is the webDCS itself that
 3605 gives the start command to the DAQ and then the 2 softwares use inter-process communication
 3606 through file to synchronise themselves. This communication file is represented by the variable `const`
 3607 `string __runstatuspath`.

3608 On one side, the webDCS sends commands or status that are readout by the DAQ:

- 3609 • INIT, status sent when launching a scan and read via function `CtrlRunStatus(...)`,
- 3610 • START, command to start data taking and read via function `CheckSTART()`,
- 3611 • STOP, command to stop data taking at the end of the scan and read via function `CheckSTOP()`,
3612 and
- 3613 • KILL, command to kill data taking sent by user and read via function `CheckKILL()`. Note that
3614 the DAQ doesn't stop before the current ROOT file is safely written and saved.

3615 and on the other, the DAQ sends status that are controled by the webDCS:

- 3616 • DAQ_RDY, sent with `SendDAQReady()` to signify that the DAQ is ready to receive commands
3617 from the webDCS,
- 3618 • RUNNING, sent with `SendDAQRunning()` to signify that the DAQ is taking data,
- 3619 • DAQ_ERR, sent with `SendDAQError()` to signify that the DAQ didn't receive the expected com-
3620 mand from the webDCS or that the launch command didn't have the right number of argu-
3621 ments,
- 3622 • RD_ERR, sent when the DAQ wasn't able to read the communication file, and
- 3623 • WR_ERR, sent when the DAQ wasn't able to write into the communication file.

3624 A.5.4 Example of inter-process communication cycle

3625 Under normal conditions, the webDCS and the DAQ processes exchange commands and status via
 3626 the file hosted at the address `__runstatuspath`, as explained in subsection A.5.3. An example of
 3627 cycle is given in Table A.1. In this example, the steps 3 to 5 are repeated as long as the webDCS tells
 3628 the DAQ to take data. A data taking cycle is the equivalent as what is called a *Scan* in GIFT++ jargon,

3629 referring to a set a runs with several HV steps. Each repetition of steps 3 to 5 is then equivalent to a
 3630 single *Run*.

3631 At any moment during the data taking, for any reason, the shifter can decide that the data taking
 3632 needs to be stopped before it reached the end of the scheduled cycle. Thus at any moment on the
 3633 cycle, the content of the inter-process communication file will be changed to `KILL` and the DAQ will
 3634 shut down right away. The DAQ checks for `KILL` signals every 5s after the TDCs configuration is
 3635 over. So far, the function `CheckKILL()` has been used only inside of the data taking loop of method
 3636 `DataReader::Run()` and thus, if the shifter decides to KILL the data taking during the TDC con-
 3637 figuration phase or the HV ramping in between 2 HV steps, the DAQ will not be stopped smoothly
 3638 and a *force kill* command will be sent to stop the DAQ process that is still awake on the computer.
 3639 Improvements can be brought on this part of the software to make sure that the DAQ can safely
 3640 shutdown at any moment.

3641

step	actions of webDCS	status of DAQ	<code>__runstatuspath</code>
1	launch DAQ ramp voltages ramping over wait for currents stabilization	readout of IniFile configuration of TDCs	INIT
2		configuration done send DAQ ready wait for <code>START</code> signal	DAQ_RDY
3	waiting time over send <code>START</code>		START
4	wait for run to end monitor DAQ run status	data taking ongoing check for <code>KILL</code> signal	RUNNING
5		run over send <code>DAQ_RDY</code> wait for next DCS signal	DAQ_RDY
6	ramp voltages ramping over wait for currents stabilization		DAQ_RDY
3	waiting time over send <code>START</code>		START
4	wait for run to end monitor DAQ run status	update IniFile information data taking ongoing check for <code>KILL</code> signal	RUNNING
5		run over send <code>DAQ_RDY</code> wait for next DCS signal	DAQ_RDY
7	send command <code>STOP</code>	DAQ shuts down	STOP

Table A.1: Inter-process communication cycles in between the webDCS and the DAQ through file string signals.

A.6 Software export

3642 In section A.2 was discussed the fact that the DAQ as written in its last version is not a standalone
 3643 software. It is possible to make it a standalone program that could be adapted to any VME setup

3645 using V1190A and V1718 modules by creating a GUI for the software or by printing the log messages
3646 that are normally printed in the webDCS through the log file, directly into the terminal. This
3647 method was used by the DAQ up to version 3.0 moment where the webDCS was completed. Also, it
3648 is possible to check branches of DAQ v2.X to have example of communication through a terminal.
3649 DAQ v2.X is nonetheless limited in its possibilities and requires a lot of offline manual interventions
3650 from the users. Indeed, there is no communication of the software with the detectors' power
3651 supply system that would allow for a user a predefine a list of voltages to operate the detectors at
3652 and loop over to take data without any further manual intervention. In v2.X, the data is taken for a
3653 single detector setting and at the end of each run, the softwares asks the user if he intends on taking
3654 more runs. If so, the software invites the user to set the operating voltages accordingly to what is
3655 necessary and to manual update the configuration file in consequence. This working mode can be a
3656 very first approach before an evolution and has been successfully used by colleagues from different
3657 collaborations.

3658 For a more robust operation, it is recommended to develop a GUI or a web application to interface
3659 the DAQ. Moreover, to limit the amount of manual interventions, and thus the probability to make
3660 mistakes, it is also recommended to add an extra feature into the DAQ by installing the HV Wrapper
3661 library provided by CAEN of which an example of use in a similar DAQ software developped by a
3662 master student of UGent, and called TinyDAQ, is provided on UGent's github. Then, this HV Wrapper
3663 will help you communicating with and give instructions to a CAEN HV powered crate and can
3664 be added into the DAQ at the same level where the communication with the user was made in DAQ
3665 v2.X. In case you are using another kind of power system for your detectors, it is stringly adviced to
3666 use HV modules or crates that can be remotely controloled via a using C++ libraries.

3667

B

3668

3669

Details on the offline analysis package

3670 The data collected in GIF++ thanks to the DAQ described in Appendix A is difficult to interpret by
3671 a human user that doesn't have a clear idea of the raw data architecture of the ROOT data files. In
3672 order to render the data human readable, a C++ offline analysis tool was designed to provide users
3673 with detector by detector histograms that give a clear overview of the parameters monitored during
3674 the data acquisition [251]. In this appendix, details about this software in the context of GIF++, as
3675 of how the software was written and how it functions will be given.

3676 B.1 GIF++ Offline Analysis file tree

3677 GIF++ Offline Analysis source code is fully available on github at https://github.com/aafagot/GIF_OfflineAnalysis. The software requires ROOT as non-optionnal dependency
3678 as it takes ROOT files in input and write an output ROOT file containing histograms. To compile the
3679 GIF++ Offline Analysis project is compiled with cmake. To compile, first a build/ directory must
3680 be created to compile from there:
3681

```
3682     mkdir build
 3683     cd build
 3684     cmake ..
 3685     make
 3686     make install
```

3684 To clean the directory and create a new build directory, the bash script cleandir.sh can be used:

```
3685
 3686     ./cleandir.sh
```

3687 The source code tree is provided below along with comments to give an overview of the files' con-
3688 tent. The different objects created for this project (`Infrastructure`, `Trolley`, `RPC`, `Mapping`, `RPCHit`,
3689 `RPCCluster` and `Inifile`) will be described in details in the following sections.

3690

```

GIF_OfflineAnalysis
├── bin
│   └── offlineanalysis ..... EXECUTABLE
├── build..... CMAKE COMPILATION DIRECTORY
└── ...
    ├── include..... LIST OF C++ HEADER FILES
    │   ├── Cluster.h..... DECLARATION OF OBJECT RPCCLUSTER
    │   ├── Current.h..... DECLARATION OF GETCURRENT ANALYSIS MACRO
    │   ├── GIFTrolley.h..... DECLARATION OF OBJECT TROLLEY
    │   ├── Infrastructure.h..... DECLARATION OF OBJECT INFRASTRUCTURE
    │   ├── IniFile.h..... DECLARATION OF OBJECT INI FILE FORINI PARSER
    │   ├── Mapping.h..... DECLARATION OF OBJECT MAPPING
    │   ├── MsgSvc.h..... DECLARATION OF OFFLINE LOG MESSAGES
    │   ├── OfflineAnalysis.h..... DECLARATION OF DATA ANALYSIS MACRO
    │   ├── RPCTracker.h..... DECLARATION OF OBJECT RPC
    │   ├── RPCHit.h..... DECLARATION OF OBJECT RPCHIT
    │   ├── types.h..... DEFINITION OF USEFUL VARIABLE TYPES
    │   └── utils.h..... DECLARATION OF USEFUL FUNCTIONS
    ├── obj..... BINARY FILES CREATED BY COMPILER
    └── ...
        ├── src..... LIST OF C++ SOURCE FILES
        │   ├── Cluster.cc..... DEFINITION OF OBJECT RPCCLUSTER
        │   ├── Current.cc..... DEFINITION OF GETCURRENT ANALYSIS MACRO
        │   ├── GIFTrolley.cc..... DEFINITION OF OBJECT TROLLEY
        │   ├── Infrastructure.cc..... DEFINITION OF OBJECT INFRASTRUCTURE
        │   ├── IniFile.cc..... DEFINITION OF OBJECT INI FILE FORINI PARSER
        │   ├── main.cc..... MAIN FILE
        │   ├── Mapping.cc..... DEFINITION OF OBJECT MAPPING
        │   ├── MsgSvc.cc..... DECLARATION OF OFFLINE LOG MESSAGES
        │   ├── OfflineAnalysis.cc..... DECLARATION OF DATA ANALYSIS MACRO
        │   ├── RPCTracker.cc..... DECLARATION OF OBJECT RPC
        │   ├── RPCHit.cc..... DECLARATION OF OBJECT RPCHIT
        │   └── utils.cc..... DEFINITION OF USEFUL FUNCTIONS
        ├── cleandir.sh..... BASH SCRIPT TO CLEAN BUILD DIRECTORY
        ├── CMakeLists.txt..... SET OF INSTRUCTIONS FOR CMAKE
        ├── config.h.in..... DEFINITION OF VERSION NUMBER
        └── README.md..... README FILE FOR GITHUB

```

3691

B.2 Usage of the Offline Analysis

3692

In order to use the Offline Analysis tool, it is necessary to know the Scan number and the HV Step of the run that needs to be analysed. This information needs to be written in the following format:

3694

3695

```
Scan00XXXX_HVY
```

3696

3697

where XXXX is the scan ID and Y is the high voltage step (in case of a high voltage scan, data will be taken for several HV steps). This format corresponds to the base name of data files in the database

3698 of the Gif++ webDCS. Usually, the offline analysis tool is automatically called by the webDCS at
 3699 the end of data taking or by a user from the webDCS panel if an update of the tool was brought.
 3700 Nonetheless, an expert can locally launch the analysis for tests on the Gif++ computer, or a user can
 3701 get the code on its local machine from github and download data from the webDCS for its own anal-
 3702 ysis. To launch the code, the following command can be used from the `GIF_OfflineAnalysis` folder:

3703

```
3704 bin/offlineanalysis /path/to/Scan00XXXX_HVY
```

3705 where, `/path/to/Scan00XXXX_HVY` refers to the local data files. Then, the offline tool will by itself
 3706 take care of finding all available ROOT data files present in the folder, as listed below:

3707

- `Scan00XXXX_HVY_DAQ.root` containing the TDC data as described in Appendix A.4.2 (events,
 hit and timestamp lists), and
- `Scan00XXXX_HVY_CAEN.root` containing the CAEN mainframe data recorded by the monitor-
 ing tool webDCS during data taking (HVs and currents of every HV channels). This file is
 created independently of the DAQ.

3712

B.2.1 Output of the offline tool

3713

B.2.1.1 ROOT file

3714

The analysis gives output ROOT datafiles that are saved into the data folder and called using the
 3715 naming convention `Scan00XXXX_HVY_Offline.root`. Inside those, a list of `TH1` histograms can be
 3716 found. Its size will vary as a function of the number of detectors in the setup as each set of histograms
 3717 is produced detector by detector. For each partition of each chamber, can be found:

3718

- `Time_Profile_Tt_Sc_p` shows the time profile of all recorded events (number of events per
 time bin),
- `Hit_Profile_Tt_Sc_p` shows the hit profile of all recorded events (number of events per chan-
 nel),
- `Hit_Multiplicity_Tt_Sc_p` shows the hit multiplicity (number of hits per event) of all recorded
 events (number of occurrences per multiplicity bin),
- `Time_vs_Strip_Profile_Tt_Sc_p` shows the 2D time vs strip profile of all recorded events
 (number of events per time bin per strip),
- `Strip_Mean_Noise_Tt_Sc_p` shows noise/gamma rate per unit area for each strip in a se-
 lected time range. After filters are applied on `Time_Profile_Tt_Sc_p`, the filtered version
 of `Hit_Profile_Tt_Sc_p` is normalised to the total integrated time and active detection area
 of a single channel,
- `Strip_Activity_Tt_Sc_p` shows noise/gamma activity for each strip (normalised version of
 previous histogram - strip activity = strip rate / average partition rate),
- `Strip_Homogeneity_Tt_Sc_p` shows the *homogeneity* of a given partition ($\text{homogeneity} = \exp(-\text{strip rates standard deviation}(\text{strip rates in partition}/\text{average partition rate}))$),

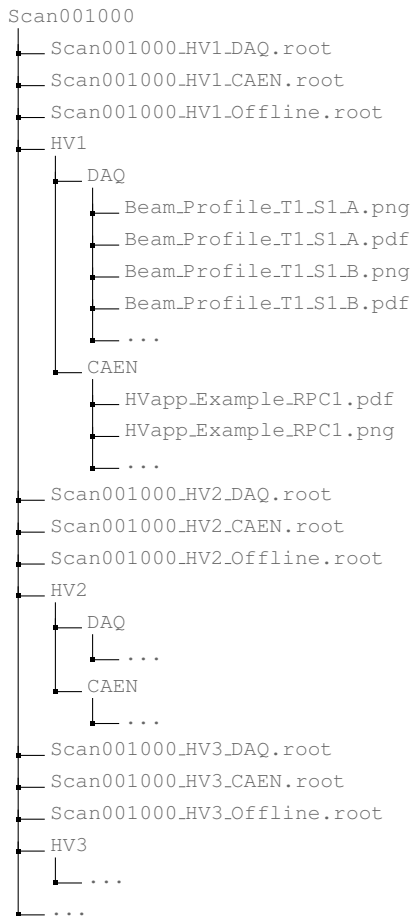
- 3734 ● `mask_Strip_Mean_Noise_Tt_Sc_p` shows noise/gamma rate per unit area for each masked
 3735 strip in a selected time range. Offline, the user can control the noise/gamma rate and decide to
 3736 mask the strips that are judged to be noisy or dead. This is done via the *Masking Tool* provided
 3737 by the webDCS,
- 3738 ● `mask_Strip_Activity_Tt_Sc_p` shows noise/gamma activity per unit area for each masked
 3739 strip with respect to the average rate of active strips,
- 3740 ● `NoiseCSize_H_Tt_Sc_p` shows noise/gamma cluster size, a cluster being constructed out of
 3741 adjacent strips giving a signal at the *same time* (hits within a time window of 25 ns),
- 3742 ● `NoiseCMult_H_Tt_Sc_p` shows noise/gamma cluster multiplicity (number of reconstructed
 3743 clusters per event),
- 3744 ● `Chip_Mean_Noise_Tt_Sc_p` shows the same information than `Strip_Mean_Noise_Tt_Scp` us-
 3745 ing a different binning (1 chip corresponds to 8 strips),
- 3746 ● `Chip_Activity_Tt_Sc_p` shows the same information than `strip_Activity_Tt_Scp` using
 3747 chip binning,
- 3748 ● `Chip_Homogeneity_Tt_Sc_p` shows the homogeneity of a given partition using chip binning,
- 3749 ● `Beam_Profile_Tt_Sc_p` shows the estimated beam profile when taking efficiency scan. This
 3750 is obtained by filtering `Time_Profile_Tt_Sc_p` to only consider the muon peak where the
 3751 noise/gamma background has been subtracted. The resulting hit profile corresponds to the
 3752 beam profile on the detector channels,
- 3753 ● `Efficiency_Fake_Tt_Ss_p` shows the efficiency given by fake hits by probing outside the
 3754 peak in an uncorrelated window as wide as the peak window,
- 3755 ● `Efficiency_Peak_Tt_Ss_p` shows the efficiency given by hits contained in the peak window,
- 3756 ● `PeakCSize_H_Tt_Sc_p` shows the cluster size that was estimated using all the hits in the peak
 3757 window,
- 3758 ● `PeakCMult_H_Tt_Sc_p` shows the cluster multiplicity that was estimated using all the hits in
 3759 the peak window,
- 3760 ● `L0_Efficiency_Tt_Sc_p` shows the level 0 muon efficiency that was estimated **without** muon
 3761 tracking after correction,
- 3762 ● `MuonCSize_H_Tt_Sc_p` shows the level 0 muon cluster size that was estimated **without** muon
 3763 tracking after correction, and
- 3764 ● `MuonCMult_H_Tt_Sc_p` shows the level 0 muon cluster multiplicity that was estimated **without**
 3765 muon tracking after correction.

3766 In the histogram labels, *t* stands for the trolley number (1 or 3), *c* for the chamber slot label in
 3767 trolley *t* and *p* for the partition label (A, B, C or D depending on the chamber layout) as explained
 3768 in Chapter 5.3.

3769

3770 In the context of GIF++, an extra script called by the webDCS is called to extract the histograms
 3771 from the ROOT files. The histograms are then stored in PNG and PDF formats into the corresponding
 3772 folder (a single folder per HV step, so per ROOT file). An example of histogram organisation is
 3773 given bellow for an hypothetical scan 001000 with at least 3 HV steps and whose chamber located in
 3774 slot 1 of trolley 1 is called *Example_RPC1* and has at least 2 read-out partitions A and B. The goal is
 3775 to then display the histograms graphs on the Data Quality Monitoring (DQM) page of the webDCS,
 3776 as presented in Figure 5.27, in order for the users to control the quality of the data taking at the end
 3777 of data taking.

3778



3779

B.2.1.2 CSV files

3780 Moreover, up to 4 CSV files can be created depending on which ones of the 3 input files were in the
 3781 data folder:

3782
 3783

- `Offline-Corrupted.csv`, is used to keep track of the amount of data that was corrupted and removed from old data format files that don't contain any data quality flag.

- 3784 ● `Offline-Current.csv`, contains the summary of the currents and voltages applied on each
3785 RPC HV channel.
- 3786 ● `Offline-L0-EffCl.csv`, is used to write the efficiencies, cluster size and cluster multiplicity
3787 of efficiency runs. Note that `L0` refers here to *Level 0* and means that the results of efficiency and
3788 clusterization are a first approximation calculated without performing any muon tracking in
3789 between the different detectors. This offline tool provides the user with a preliminar calcula-
3790 tion of the efficiency and of the muon event parameters. Another analysis software especially
3791 dedicated to muon tracking is called on selected data to retrieve the results of efficiency and
3792 muon clusterization using a tracking algorithm to discriminate noise or gamma from muons
3793 as muons are the only particles that pass through the full setup, leaving hits than can be used
3794 to reconstruct their tracks.
- 3795 ● `Offline-Rate.csv`, is used to write the noise or gamma rates measured in the detector readout
3796 partitions.

3797 Note that these 4 CSV files are created along with their *headers* (`Offline-[...]-Header.csv`
3798 containing the names of each data columns) and are automatically merged together when the offline
3799 analysis tool is called from the webDCS, contrary to the case where the tool is runned locally from
3800 the terminal as the merging bash script is then not called. Thus, the resulting files, used to make
3801 official plots, are:

- 3802 ● `Corrupted.csv`,
- 3803 ● `Current.csv`,
- 3804 ● `L0-EffCl.csv`.
- 3805 ● `Rate.csv`.

3806 **B.3 Analysis inputs and information handling**

3807 The usage of the Offline Analysis tool as well as its output have been presented in the previous sec-
3808 tion. It is now important to dig further and start looking at the source code and the inputs necessary
3809 for the tool to work. Indeed, other than the raw ROOT data files that are analysed, more information
3810 needs to be imported inside of the program to perform the analysis such as the description of the
3811 setup inside of GIFT++ at the time of data taking (number of trolleys, of RPCs, dimensions of the
3812 detectors, etc...) or the mapping that links the TDC channels to the coresponding RPC channels in
3813 order to translate the TDC information into human readable data. Two files are used to transmit all
3814 this information:

- 3815
- 3816 ● `Dimensions.ini`, that provides the necessary setup and RPC information, and
- 3817 ● `ChannelsMapping.csv`, that gives the link between the TDC and RPC channels as well as the
3818 *mask* for each channel (masked or not?).

3819 B.3.1 Dimensions file and IniFile parser

3820 GIF++ CMS RPC setup consists in detectors held into trolleys inside of the GIF++ bunker. Each of
 3821 these detector may have a read-out segmented to cover different pseudo-rapidity range once intalled
 3822 in CMS. The segmentation of the read-out is referred to as "partitions". This input file, present in
 3823 every data folder, allows the analysis tool to know of the number of active trolleys, the number of
 3824 active RPCs in those trolleys, and the details about each RPCs such as the number of RPC gaps, the
 3825 number of pseudo-rapidity partitions, the number of strips per partion or the dimensions. To do so,
 3826 there are 3 types of groups in the INI file architecture. Groups are sections of the INI file content
 3827 starting with a title encapsulated in between square brackets. A first general group, appearing only
 3828 once at the head of the document, gives information about the number of active trolleys as well
 3829 as their IDs, as presented in Source Code B.1. For each active trolley, a group similar to Source
 3830 Code B.2 can be found containing information about the number of active detectors in the trolley
 3831 and their IDs. Each trolley group as a `Tt` name format, where `t` is the trolley ID. Finally, for each
 3832 detector stored in slots of an active trolley, there is a group providing information about their names
 3833 and dimensions, as shown in Source Code B.3. Each slot group as a `TtSs` name format, where `s` is
 3834 the slot ID of trolley `t` where the active RPC is hosted.

```
3835    [General]
3836    nTrolleys=2
3837    TrolleysID=13
```

Source Code B.1: Example of `[General]` group as might be found in `Dimensions.ini`. In GIF++, only 2 trolleys are available to hold RPCs and place them inside of the bunker for irradiation. The IDs of the trolleys are written in a single string as "13" and then read character by character by the program.

```
3838    [T1]
3839    nSlots=4
      SlotsID=1234
```

Source Code B.2: Example of trolley group as might be found in `Dimensions.ini`. In this example, the file tells that there are 4 detectors placed in the holding slots of the trolley `T1` and that their IDs, written as a single string variable, are 1, 2, 3 and 4.

```
3840    [T1S1]
      Name=RE2-2-NPD-BARC-8
      Partitions=3
      Gaps=3
      Gap1=BOT
      Gap2=TN
      Gap3=TW
      AreaGap1=11694.25
      AreaGap2=6432
      AreaGap3=4582.82
      Strips=32
      ActiveArea-A=157.8
      ActiveArea-B=121.69
      ActiveArea-C=93.03
```

Source Code B.3: Example of slot group as might be found in `Dimensions.ini`. In this example, the file provides information about a detector named `RE2-2-NPD-BARC-8`, having 3 pseudo-rapidity readout partitions and stored in slot `S1` of trolley `T1`. This is a CMS RE2-2 type of detector. This information will then be used for example to compute the rate per unit area calculation.

3842 This information is read-out and stored in a C++ object called `IniFile`, that parses the information
 3843 of the INI input file and stores it into a local buffer for later use. This INI parser is the exact
 3844 same one that was previously developed for the GIF++ DAQ and described in Appendix A.5.2.

3845 B.3.2 TDC to RPC link file and Mapping

3846 The same way the INI dimension file information is stored using `map`, the channel mapping and
 3847 mask information making the link in between TDC channels and RPC strips is stored and accessed
 3848 through `map`. First of all, the mapping CSV file is organised into 3 columns separated by tabulations:

3850	RPC_channel	TDC_channel	mask
------	-------------	-------------	------

3851 using as formatting for each field:

3852	TSCCC	TCCC	M
------	-------	------	---

3854 TSCCC is a 5-digit integer where `T` is the trolley ID, `s` the slot ID in which the RPC is held inside
 3855 the trolley `T` and `ccc` is the RPC channel number, or *strip* number, that can take values up to
 3856 3-digits depending on the detector,

3857 TCCC is a 4 digit integer where `T` is the TDC ID to which the RPC is connected, `ccc` is the TDC
 3858 channel number linked to the RPC strip that can take values in between 0 and 127, and

3859 M is a 1-digit integer indicating if the channel should be considered (`M = 1`) or discarded (`M = 0`)
 3860 during analysis. Note that the absence of a third column is interpreted by the mapping file
 3861 parser as `M = 1` by default.

3862 This mapping and masking information is readout and stored thanks to the object `Mapping`, presented
 3863 in Source Code B.4. Similarly to `IniFile` objects, this class has private methods to provide
 3864 with parser rules. The first one, `Mapping::CheckIfNewLine()` is used to find the newline character
 3865 '`\n`' or return character '`\r`' (depending on which kind of operating system interacted with the file).
 3866 Finding and identifying a newline or return character is used for the simple reason that the masking
 3867 information has been introduced only during the year 2017 but the channel mapping files exist since
 3868 2015 and the very beginning of data taking at GIF++. This means that in the older data folders,
 3869 before the upgrade, the channel mapping file only had 2 columns, the RPC channel and the TDC
 3870 channel. For compatibility reasons, this method helps controlling the character following the readout
 3871 of the 2 first fields of a line. In case any end of line character is found, no mask information is present
 3872 in the file and the default `M = 1` is used. On the contrary, if the next character was a tabulation or a
 3873 space, the mask information is present.

3874 Once the 3 fields have been readout, the second private method `Mapping::CheckIfTDCCh()` is
 3875 used to control that the TDC channel is an existing TDC channel by checking its format. Finally,
 3876 the information is stored into 3 different maps (`Link`, `ReverseLink` and `Mask`) thanks to the public
 3877 method `Mapping::Read()`. `Link` allows to get the RPC channel by knowing the TDC channel while
 3878 `ReverseLink` does the opposite by returning the TDC channel by knowing the RPC channel. Finally,
 3879 `Mask` returns the mask associated to a given RPC channel.

```

3880 typedef map<Uint,Uint> MappingData;

3881 class Mapping {
3882     private:
3883         bool          CheckIfNewLine(char next);
3884         bool          CheckIfTDCCh(Uint channel);
3885         string        FileName;
3886         MappingData  Link;
3887         MappingData  ReverseLink;
3888         MappingData  Mask;
3889         int           Error;
3890
3891     public:
3892         Mapping();
3893         Mapping(string baseName);
3894         ~Mapping();
3895
3896         void SetFileName(const string filename);
3897         int  Read();
3898         Uint GetLink(Uint tdcchannel);
3899         Uint GetReverse(Uint rpcchannel);
3900         Uint GetMask(Uint rpcchannel);
3901     };

```

3882 *Source Code B.4: Description of C++ object Mapping used as a parser for the channel mapping and mask file.*

3883 B.4 Description of GIF++ setup within the Offline Analysis tool

3884 In the previous section, the tool input files have been discussed. The dimension file information is
 3885 stored in a map hosted by the `IniFile` object. But this information is then used to create a series of
 3886 new objects that helps defining the GIF++ infrastructure directly into the Offline Analysis. Indeed,
 3887 from the `RPC`, to the more general `Infrastructure`, every element of the GIF++ infrastrucutre is
 3888 recreated for each data analysis based on the information provided in input. All this information
 3889 about the infrastructure will be used to assign each hit signal to a specific strip channel of a specific
 3890 detector, and having a specific active area. This way, rate per unit area calculation is possible.
 3891

3892 B.4.1 RPC objects

3893 `RPC` objects have been developped to represent physical active detectors in GIF++ at the moment
 3894 of data taking. Thus, there are as many `RPC` objects created during the analysis than there were
 3895 active `RPCs` tested during a run. Each `RPC` hosts the information present in the corresponding INI
 3896 slot group, as showed in B.3, and organises it using a similar architecture. This can be seen from
 3897 Source Code B.5.

3898 To make the object more compact, the lists of gap labels, of gap active areas and strip active
 3899 areas are stored into `vector` dynamical containers. `RPC` objects are always contructed thanks to the
 3900 dimension file information stored into the `IniFILE` and their ID, using the format `TtSs`. Using the
 3901 `RPC` ID, the constructor calls the methods of `IniFILE` to initialise the `RPC`. The other constructors
 3902 are not used but exist in case of need. Finally, some getters have been written to access the different
 3903 private parameters storing the detector information.

3904

3905 B.4.2 Trolley objects

3906 Trolley objects have been developed to represent physical active trolleys in GIF++ at the moment
3907 of data taking. Thus, there are as many trolley objects created during the analysis than there were
3908 active trolleys hosting RPCs under test during a run. Each Trolley hosts the information present in
3909 the corresponding INI trolley group, as shown in B.2, and organises it using a similar architecture.
3910 In addition to the information hosted in the INI file, these objects have a dynamical container of `RPC`
3911 objects, representing the active detectors the active trolley was hosting at the time of data taking.
3912 This can be seen from Source Code B.6.

3913 Trolley objects are always constructed thanks to the dimension file information stored into the
3914 `IniFILE` and their ID, using the format `Tt`. Using the Trolley ID, the constructor calls the methods
3915 of `IniFILE` to initialise the Trolley. Retrieving the information of the RPC IDs via `SlotsID`, a new
3916 `RPC` is constructed and added to the container `RPCs` for each character in the ID string. The other
3917 constructors are not used but exist in case of need. Finally, some getters have been written to access
3918 the different private parameters storing the trolley and detectors information.

3919

3920 B.4.3 Infrastructure object

3921 The `Infrastructure` object has been developed to represent the GIF++ bunker area dedicated to
3922 CMS RPC experiments. With this very specific object, all the information about the CMS RPC
3923 setup within GIF++ at the moment of data taking is stored. It hosts the information present in the
3924 corresponding INI general group, as shown in B.1, and organises it using a similar architecture. In
3925 addition to the information hosted in the INI file, this object has a dynamical container of `Trolley`
3926 objects representing the active trolleys in GIF++ area, themselves containing `RPC` objects. This can
3927 be seen from Source Code B.7.

3928 The `Infrastructure` object is always constructed thanks to the dimension file information stored
3929 into the `IniFILE`. Retrieving the information of the trolley IDs via `TrolleysID`, a new `Trolley` is
3930 constructed and added to the container `Trolleys` for each character in the ID string. By extension,
3931 it is easy to understand that the process described in Section B.4.2 for the construction of RPCs
3932 takes place when a trolley is constructed. The other constructors are not used but exist in case of
3933 need. Finally, some getters have been written to access the different private parameters storing the
3934 infrastructure, trolleys and detectors information.

```

3935 class RPC{
3936     private:
3937         string name;           //RPC name as in webDCS database
3938         Uint nGaps;          //Number of gaps in the RPC
3939         Uint nPartitions;    //Number of partitions in the RPC
3940         Uint nStrips;        //Number of strips per partition
3941         vector<string> gaps; //List of gap labels (BOT, TOP, etc...)
3942         vector<float> gapGeo;   //List of gap active areas
3943         vector<float> stripGeo; //List of strip active areas
3944
3945     public:
3946         RPC();
3947         RPC(string ID, IniFile* geofile);
3948         RPC(const RPC& other);
3949         ~RPC();
3950         RPC& operator=(const RPC& other);
3951
3952         string GetName();
3953         Uint GetNGaps();
3954         Uint GetNPartitions();
3955         Uint GetNStrips();
3956         string GetGap(Uint g);
3957         float GetGapGeo(Uint g);
3958         float GetStripGeo(Uint p);
3959     };

```

3937 *Source Code B.5: Description of C++ objects RPC that describe each active detectors used during data taking.*

```

class Trolley{
    private:
        Uint nSlots; //Number of active RPCs in the considered trolley
        string SlotsID; //Active RPC IDs written into a string
        vector<RPC*> RPCs; //List of active RPCs
    public:
        Trolley();
        Trolley(string ID, IniFile* geofile);
        Trolley(const Trolley& other);
        ~Trolley();
        Trolley& operator=(const Trolley& other);
3938
        Uint GetNSlots();
        string GetSlotsID();
        Uint GetSlotID(Uint s);
        RPC* GetRPC(Uint r);
        void DeleteRPC(Uint r);
3939
        //Methods to get members of RPC objects stored in RPCs
        string GetName(Uint r);
        Uint GetNGaps(Uint r);
        Uint GetNPartitions(Uint r);
        Uint GetNStrips(Uint r);
        string GetGap(Uint r, Uint g);
        float GetGapGeo(Uint r, Uint g);
        float GetStripGeo(Uint r, Uint p);
    };

```

3939 *Source Code B.6: Description of C++ objects Trolley that describe each active trolley used during data taking.*

```

class Infrastructure {
    private:
        Uint             nTrolleys;   //Number of active Trolleys in the run
        string          TrolleysID;  //Active trolley IDs written into a string
        vector<Trolley*> Trolleys;  //List of active Trolleys (struct)

    public:
        Infrastructure();
        Infrastructure(IniFile* geofile);
        Infrastructure(const Infrastructure& other);
        ~Infrastructure();
        Infrastructure& operator=(const Infrastructure& other);

        Uint    GetNTrolleys();
        string GetTrolleysID();
        Uint    GetTrolleyID(Uint t);

3940        Trolley* GetTrolley(Uint t);
        void    DeleteTrolley(Uint t);

        //Methods to get members of GIFTrolley objects stored in Trolleys
        Uint    GetNSlots(Uint t);
        string GetSlotsID(Uint t);
        Uint    GetSlotID(Uint t, Uint s);
        RPC*   GetRPC(Uint t, Uint r);

        //Methods to get members of RPC objects stored in RPCs
        string GetName(Uint t, Uint r);
        Uint    GetNGaps(Uint t, Uint r);
        Uint    GetNPartitions(Uint t, Uint r);
        Uint    GetNStrips(Uint t, Uint r);
        string GetGap(Uint t, Uint r, Uint g);
        float  GetGapGeo(Uint t, Uint r, Uint g);
        float  GetStripGeo(Uint t, Uint r, Uint p);
    };

```

Source Code B.7: Description of C++ object Infrastructure that contains the full information about CMS RPC experiment in GIF++.

3942 B.5 Handeling of data

3943 As discussed in Appendix A.4.2, the raw data uses a `TTree` architecture where every entry is related
3944 to a trigger signal provided by a muon or a random pulse, whether the goal of the data taking was to
3945 measure the performance of the detector or the noise/gamma background respectively. Each of these
3946 entries, referred also as events, contain a more or less full list of hits in the TDC channels to which
3947 the detectors are connected. To this list of hits corresponds a list of time stamps, marking the arrival
3948 of the hits within the TDC channel.

3949 The infrastructure of the CMS RPC experiment within `GIF++` being defined, combining the raw
3950 data information with the information provided by both the mapping/mask file and the dimension
3951 file allows to build new physical objects that will help in computing efficiency or rates.

3952 B.5.1 RPC hits

3953 The raw data stored in the ROOT file as output of the GIFT++ DAQ, is readout by the analysis tool
 3954 using the structure `RAWData` presented in Source Code B.9 that differs from the structure presented
 3955 in Appendix A.4.2 as it is not meant to hold all of the data contained in the ROOT file. In this sense,
 3956 this structure is in the case of the offline analysis tool not a dynamical object and will only be storing
 3957 a single event contained in a single entry of the `TTree`.

3958

```
class RPCHit {
  private:
    Uint Channel;      //RPC channel according to mapping (5 digits)
    Uint Trolley;     //0, 1 or 3 (1st digit of the RPC channel)
    Uint Station;     //Slot where is held the RPC in Trolley (2nd digit)
    Uint Strip;        //RPC strip where the hit occurred (last 3 digits)
    Uint Partition;   //Readout partition along eta segmentation
    float TimeStamp;  //Time stamp of the arrival in TDC

  public:
    RPCHit();
    RPCHit(Uint channel, float time, Infrastructure* Infra);
    RPCHit(const RPCHit& other);
    ~RPCHit();
    RPCHit& operator=(const RPCHit& other);

    Uint GetChannel();
    Uint GetTrolley();
    Uint GetStation();
    Uint GetStrip();
    Uint GetPartition();
    float GetTime();
};

typedef vector<RPCHit> HitList;
typedef struct GIFHitList {HitList rpc[NTROLLEYS][NSLOTS][NPARTITIONS];}
  ↪ GIFHitList;

bool SortHitbyStrip(RPCHit h1, RPCHit h2);
bool SortHitbyTime(RPCHit h1, RPCHit h2);
```

3960

Source Code B.8: Description of C++ object `RPCHit`.

3961

```
struct RAWData{
  int iEvent;          //Event i
  int TDCHits;        //Number of hits in event i
  int QFlag;           //Quality flag list (1 flag digit per TDC)
  vector<Uint> *TDCCh; //List of channels giving hits per event
  vector<float> *TDCTS; //List of the corresponding time stamps
};
```

3962

Source Code B.9: Description of C++ structure `RAWData`.

3963 Each member of the structure is then linked to the corresponding branch of the ROOT data tree,
 3964 as shown in the example of Source Code B.10, and using the method `GetEntry(int i)` of the ROOT
 3965 class `TTree` will update the state of the members of `RAWData`.

3966 The data is then analysed entry by entry and to each element of the TDC channel list, a `RPCHit` is
 3967 constructed by linking each TDC channel to the corresponding RPC channel thanks to the Mapping

3968 object. The information carried by the RPC channel format allows to easily retrieve the trolley and
 3969 slot from which the hit was recorded (see section B.3.2). Using these 2 values, the readout partition
 3970 can be found by knowing the strip channel and comparing it with the number of partitions and strips
 3971 per partition stored into the `Infrastructure` object.

```
3972
3973   TTree* dataTree = (TTree*)dataFile.Get("RAWData");
      RAWData data;

      dataTree->SetBranchAddress("EventNumber", &data.iEvent);
      dataTree->SetBranchAddress("number_of_hits", &data.TDCNHits);
      dataTree->SetBranchAddress("Quality_flag", &data.QFlag);
      dataTree->SetBranchAddress("TDC_channel", &data.TDCCh);
      dataTree->SetBranchAddress("TDC_TimeStamp", &data.TDCTS);
```

3974 *Source Code B.10: Example of link in between RAWData and TTree.*

3975 Thus `RPCHit` objects are then stored into 3D dynamical list called `GIFHitList` (Source Code B.8)
 3976 where the 3 dimensions refer to the 3 layers of the readout in `GIF++`: in the bunker there are *trolleys*
 3977 (*T*) holding detectors in *slots* (*S*) and each detector readout is divided into 1 or more pseudo-rapidity
 3978 *partitions* (*P*). Using these 3 information allows to assign an address to each readout partition and
 3979 this address will point to a specific hit list.

3980

3981 B.5.2 Clusters of hits

3982 All the hits contained in the ROOT file have been sorted into the different hit lists through the
 3983 `GIFHitList`. At this point, it is possible to start looking for clusters. A cluster is a group of adjacent
 3984 strips getting hits within a time window of 25 ns. These strips are then assumed to be part of the same
 3985 physical avalanche signal generated by a muon passing through the chamber or by the interaction of
 3986 a gamma stopping into the electrodes of the RPCs.

3987 To keep the cluster information, `RPCCluster` objects have been defined as shown in Source
 3988 Code B.11. Using the information of each individual `RPCHit` taken out of the hit list, it stores
 3989 the cluster size (number of adjacent strips composing the cluster), the first and last hit, the center for
 3990 spatial reconstruction and finally the start and stop time stamps as well as te time spread in between
 3991 the first and last hit.

3992

3993 To investigate the hit list of a given detector partition, the function `Clusterization()` defined
 3994 in `include/Cluster.h` needs the hits in the list to be time sorted. This is achieved by calling func-
 3995 tion `sort()` of library `<algorithm>` using the comparator `SortHitbyTime(RPCHit h1, RPCHit h2)`
 3996 defined in `include/RPCHit.h` that returns `true` if the time stamp of hit *h1* is lower than that of *h2*.
 3997 A first isolation of strips is made only based on time information. All the hits within the 25 ns win-
 3998 dow are taken separately from the rest. Then, this sub-list of hits is sorted this time by ascending
 3999 strip number, using this time the comparator `SortHitbyStrip(RPCHit h1, RPCHit h2)`. Finally, the
 4000 groups of adjacent strips are used to construct `RPCCluster` objects that are then stored in a temporary
 4001 list of clusters that is at the end of the process used to know how many clusters were reconstructed
 4002 and to fill their sizes into an histogram that will allows to know the mean size of muon or gamma
 4003 clusters. This method to group hits together into clusters is limited as no systematic study of the
 4004 average avalanche time development into TDC hits was performed and that there is no correlation

4005 of both spatial and time information to make the first selection of hits. Due to this, two clusters
 4006 developping consecutively next to each other during a total time longer to 25 ns could be wrongly
 4007 grouped as a cluster composed of the first developed cluster plus a part of the second cluster while
 4008 the rest of the second cluster would be placed in a second truncated cluster. This kind of event
 4009 is not likely but needs to be taken into account nonetheless. A possible improvement would be to
 4010 identify clusters in a 2D space whose dimensions are time and strip. In this 2D space, the cluster
 4011 could be geometrically identified as isolated groups of adjacent strips receiving a hit at a similar time.
 4012

```

4012
4013   class RPCCluster{
4014     private:
4015       Uint ClusterSize; //Size of cluster #ID
4016       Uint FirstStrip; //First strip of cluster #ID
4017       Uint LastStrip; //Last strip of cluster #ID
4018       float Center; //Center of cluster #ID ((first+last)/2)
4019       float StartStamp; //Time stamp of the earliest hit of cluster #ID
4020       float StopStamp; //Time stamp of the latest hit of cluster #ID
4021       float TimeSpread; //Time difference between earliest and latest hits
4022           //of cluster #ID
4023
4024     public:
4025       RPCCluster();
4026       RPCCluster(HitList List, Uint cID, Uint cSize, Uint first, Uint firstID);
4027       RPCCluster(const RPCCluster& other);
4028       ~RPCCluster();
4029       RPCCluster& operator=(const RPCCluster& other);
4030
4031       Uint GetID();
4032       Uint GetSize();
4033       Uint GetFirstStrip();
4034       Uint GetLastStrip();
4035       float GetCenter();
4036       float GetStart();
4037       float GetStop();
4038       float GetSpread();
4039   };
4040
4041   typedef vector<RPCCluster> ClusterList;
4042
4043   //Other functions to build cluster lists out of hit lists
4044   void BuildClusters(HitList &cluster, ClusterList &clusterList);
4045   void Clusterization(HitList &hits, TH1 *hcSize, TH1 *hcMult);
  
```

4014

Source Code B.11: Description of C++ object Cluster.

4015 B.6 DAQ data Analysis

4016 All the ingredients to analyse GIFT++ data have been introduced. This section will focus on the
 4017 different part of the analysis performed on the data, from determining the type of data the tool is
 4018 dealing with to calculate the hit and cluster rate per unit area in each detector or reconstructing
 4019 muon or gamma clusters.

4020 B.6.1 Determination of the run type

4021 In GIF++, both the performance of the detectors in detecting muons in an irradiated environment
 4022 and the gamma or noise background can be independantly measured. These correspond to different
 4023 run types and hence, to different TDC settings giving different data to look at.

4024 In the case of performance measurements, the trigger for data taking is provided by the coin-
 4025 cidence of several scintillators when muons from the beam passing through the area are detected.
 4026 Data is collected in a 600 ns wide window centered around the arrival of muons in the RPCs. The
 4027 expected time distribution of hits is shown in Figure B.1a. The muon peak is clearly visible in the
 4028 center of the distribution and is to be extracted from the gamma background that composes the flat
 4029 part of the distribution.

4030 On the other hand, gamma background or noise measurements are focussed on the non muon
 4031 related physics and the trigger needs to be independant from the muons to give a good measurement
 4032 of the gamma/noise distribution as seen by the detectors. The trigger is then provided by a pulse
 4033 generated by the DAQ at a frequency of 100 Hz whose pulse is not likely to be on time with a muon.
 4034 In order to increase the integrated time without increasing proportionnaly the acquisition time, the
 4035 width of the acquisition windows are increased to 10 μ s. The time distribution of the hits is expected
 4036 to be flat, as shown by Figure B.1b.

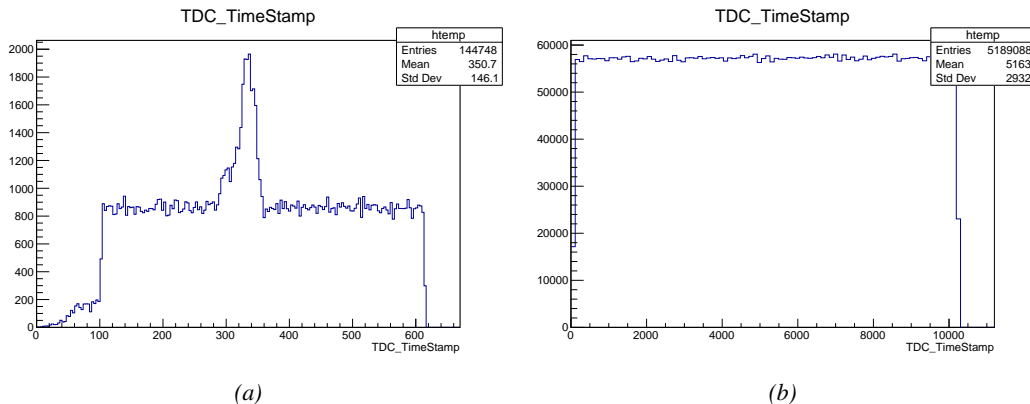


Figure B.1: Example of expected hit time distributions in the cases of efficiency (Figure B.1a) and noise/gamma rate per unit area (Figure B.1b) measurements as extracted from the raw ROOT files. The unit along the x-axis corresponds to ns. The fact that "the" muon peak is not well defined in Figure B.1a is due to the contribution of all the RPCs being tested at the same time that don't necessarily have the same signal arrival time. Each individual peak can have an offset with the ones of other detectors. The inconsistancy in the first 100 ns of both time distributions is an artefact of the TDCs and are systematically rejected during the analysis.

4037 The ROOT files include a `TTree` called `RunParameters` containing, among other things, the infor-
 4038 mation related to the run type. The run type can then be accessed as described by Source Code B.12
 4039 and the function `IsEfficiencyRun()` is then used to determine if the run file is an efficiency run or,
 4040 on the contrary, another type of run (noise or gamma measurement).

4041 Finally, the data files will have a slightly different content whether it was collected before or after
 4042 October 2017 and the upgrade of the DAQ software that brought a new information into the ROOT
 4043 output. This is discussed in Appendix A.4.3 and implies that the analysis will differ a little depending
 4044 on the data format. Indeed, as no information on the data quality is stored, in older data files, the cor-
 4045 rections for missing events has to be done at the end of the analysis. The information about the type

4046 of data format is stored in the variable **bool** `isNewFormat` by checking the list of branches contained
 4047 in the data tree via the methods `TTree::GetListOfBranches()` and `TCollection::Contains()`.

```
4048
4049   TTree* RunParameters = (TTree*)dataFile.Get("RunParameters");
4050   TString* RunType = new TString();
4051   RunParameters->SetBranchAddress("RunType", &RunType);
4052   RunParameters->GetEntry(0);
```

4050 *Source Code B.12: Access to the run type contained in `TTree* RunParameters`.*

4051 **B.6.2 Beam time window calculation for efficiency runs**

4052 Knowing the run type is important first of all to know the width of the acquisition window to be used
 4053 for the rate calculation and finally to be able to seek for muons. Indeed, the peak that appears in the
 4054 time distribution for each detectors is then fitted to extract the most probable time window in which
 4055 the tool should look for muon hits. The data outside of this time window is then used to evaluate the
 4056 noise or gamma background the detector was subjected to during the data taking. Computing the
 4057 position of the peak is done calling the function `SetBeamWindow()` defined in file `src/RPCHit.cc` that
 4058 loops a first time on the data. The data is first sorted in a 3D array of 1D histograms (`GIFH1Array`, see
 4059 `include/types.h`). Then the location of the highest bin is determined using `TH1::GetMaximumBin()`
 4060 and is used to define a window in which a gaussian fit will be applied to compute the peak width.
 4061 This window is a 80 ns defined by Formula B.1 around the central bin.

$$(B.1a) \quad t_{center}(ns) = bin \times width_{bin}(ns)$$

$$(B.1b) \quad [t_{low}; t_{high}] = [t_{center} - 40; t_{center} + 40]$$

4062 Before the fit is performed, the average number of noise/gamma hits per bin is evaluated using
 4063 the data outside of the fit window. Excluding the first 100 ns, the average number of hits per bin
 4064 due to the noise or gamma is defined by Formula B.2 after extracting the amount of hits in the time
 4065 windows $[100; t_{low}]$ and $[t_{high}; 600]$ thanks to the method `TH1::Integral()`. This average number
 4066 of hits is then subtracted to every bin of the 1D histogram, in order to *clean* it from the noise or
 4067 gamma contribution as much as possible to improve the fit quality. Bins where $\langle n_{hits} \rangle$ is greater
 4068 than the actual bin content are set to 0.

$$(B.2a) \quad \Delta t_{noise}(ns) = 600 \overbrace{-t_{high} + t_{low}}^{-80ns} - 100 = 420ns$$

$$(B.2b) \quad \langle n_{hits} \rangle = width_{bin}(ns) \times \frac{\sum_{t=100}^{t_{low}} + \sum_{t=t_{high}}^{600}}{\Delta t_{noise}(ns)}$$

4069 Finally, the fit parameters are extracted and saved for each detector in 3D arrays of **float**
 4070 (`muonPeak`, see `include/types.h`), a first one for the mean arrival time of the muons, `PeakTime`,
 4071 a second for the height or strength of the peak, `PeakHeight`, and a third one for the width of the
 4072 peak, `PeakWidth`. The width is on purpose chosen to be wider than the peak and defined as 6σ of the
 4073 gaussian fit, for a peak range being as given by Formula B.3.

$$(B.3) \quad [t_{low}^{peak}; t_{high}^{peak}] = [t_{center}^{peak} - 3\sigma; t_{center}^{peak} + 3\sigma]$$

4074 For a finer analysis, it is advised to determine more precisely the width of the peak to exclude
 4075 as much noise or background hits as possible. The same settings are applied to every partitions of
 4076 the same detector. To determine which one of the detector's partitions is directly illuminated by the
 4077 beam, the peak height of each partition is compared and the highest one is then used to define the
 4078 peak settings.

4079 It is not possible to identify the particles causing the hits, hence muons, background gamma
 4080 particles or even noise could be responsible of hits within the time window. To be able to account
 4081 for this effect, the peak width extracted from the fit on the peak will also be used to define a fake
 4082 time window, uncorrelated to the muon peak and in which a fake efficiency, contribution from both
 4083 background and noise, will be measured. This window corresponds to the time range described in
 4084 Formula B.4.

$$(B.4) \quad [t_{low}^{fake}; t_{high}^{fake}] = [600 - 6\sigma; 600]$$

4085 B.6.3 Data loop and histogram filling

4086 3D arrays of histogram are created to store the data and display it on the DQM of GIF++ webDCS
 4087 for the use of shifters. The dimensions correspond to the different layers held into the GIF++ infras-
 4088 tructure (trolleys `T` containing RPCs or *slots* `s` each being divided into read-out partitions `p`). These
 4089 histograms, presented in section B.2.1.1, are filled while looping on the data. Before starting the
 4090 analysis loop, it is necessary to control the entry quality for the new file formats featuring `QFlag`. If
 4091 the `QFlag` value for this entry shows that 1 TDC or more have a `CORRUPTED` flag, then this event is
 4092 discarded. The loss of statistics is low enough to be neglected. `QFlag` is controlled using the func-
 4093 tion `IsCorruptedEvent()` defined in `src/utils.cc`. As explained in Appendix A.4.3, each digit of
 4094 this integer represent a TDC flag that can be either 1 or 2. Each 2 is the sign of a `CORRUPTED` state.
 4095 Then, the data is accessed entry by entry in the ROOT `TTree` using `RAWData` and each hit in the hit
 4096 list is assigned to a detector channel and saved in the corresponding histograms. As described in
 4097 Source Code B.13, in the first part of the analysis, in which the loop over the ROOT file's content is
 4098 performed, the different steps are:

4099 **1- RPC channel assignment and control:** a check is done on the RPC channel extracted thanks
 4100 to the mapping via the method `Mapping::GetLink()`. If the channel is not initialised and is 0, or if
 4101 the TDC channel is not contained in a range in between X000 and X127, X being the TDC ID, the
 4102 hit is discarded. This means there was a problem in the mapping. Often a mapping problem leads to
 4103 the failure of the offline tool.

4104 **2- Creation of a `RPCHit` object:** to easily get the trolley, slot and partition in which the hit has
 4105 been assigned, this object is particularly helpful.

4106 **3- General histograms are filled:** the hit is filled into the time distribution, global hit distribution
 4107 and time versus strip histograms, and if the arrival time is within the first 100 ns, it is discarded and
 4108 nothing else happens and the loop proceeds with the next hit in the list, going back to step 1.

4109

```

for(int h = 0; h < data.TDCCh->size(); h++) {
    Uint tdcchannel = data.TDCCh->at(h);
    Uint rpcchannel = RPCChMap->GetLink(tdcchannel);
    float timestamp = data.TDCTS->at(h);
    //Get rid of the hits in channels not considered in the mapping
    if(rpcchannel != NOCHANNELLINK) {
        RPCHit hit(rpcchannel, timestamp, GIFInfra);
        Uint T = hit.GetTrolley();
        Uint S = hit.GetStation()-1;
        Uint P = hit.GetPartition()-1;
        //Fill the time and hit profiles
        TimeProfile_H.rpc[T][S][P]->Fill(hit.GetTime());
        HitProfile_H.rpc[T][S][P]->Fill(hit.GetStrip());
        TimeVSChanProfile_H.rpc[T][S][P]->Fill(hit.GetStrip(),hit.GetTime());
        //Reject the 100 first ns due to inhomogeneity of data
        if(hit.GetTime() >= TIMEREJECT) {
            Multiplicity.rpc[T][S][P]++;
            if(IsEfficiencyRun(RunType)) {
                //Define peak time range for efficiency calculation
                float lowlimit_eff = PeakTime.rpc[T][S][P]
                    - PeakWidth.rpc[T][S][P];
                float highlimit_eff = PeakTime.rpc[T][S][P]
                    + PeakWidth.rpc[T][S][P];
                bool peakrange = (hit.GetTime() >= lowlimit_eff
                    && hit.GetTime() < highlimit_eff);
                //Fill hits inside of the defined peak and noise range
                if(peakrange) {
                    BeamProfile_H.rpc[T][S][P]->Fill(hit.GetStrip());
                    PeakHitList.rpc[T][S][P].push_back(hit);
                } else {
                    StripNoiseProfile_H.rpc[T][S][P]->Fill(hit.GetStrip());
                    NoiseHitList.rpc[T][S][P].push_back(hit);
                }
                //Then define time range for fake efficiency
                float highlimit_fake = BMTDCWINDOW;
                float lowlimit_fake = highlimit_fake
                    - (highlimit_eff-lowlimit_eff);
                bool fakerange = (hit.GetTime() >= lowlimit_fake
                    && hit.GetTime() < highlimit_fake);
                //Fill the hits inside of the fake window
                if(fakerange) {
                    FakeHitList.rpc[T][S][P].push_back(hit);
                }
            } else {
                //Fill the hits inside of the defined noise range
                StripNoiseProfile_H.rpc[T][S][P]->Fill(hit.GetStrip());
                NoiseHitList.rpc[T][S][P].push_back(hit);
            }
        }
    }
}

```

4110

4111

Source Code B.13: For each entry of the raw ROOT data file, the code loops over the list of channels and corresponding time stamps contained in branches `TDC_channel` and `TDC_TimeStamp` and constructs `RPCHit` objects that are filled in the peak, noise and fake hit lists and also fills the time, hit, beam and noise profiles.

4112

4- Multiplicity counter: the hit multiplicity counter of the corresponding detectors is incremented.

4113 **5-a-1 Efficiency runs - Is the hit within the peak window? :** if the hit is contained in the peak
 4114 window previously defined by Formula B.3, it is filled into the beam hit profile histogram of the
 4115 corresponding chamber, added into the list of peak hits and increments the counter of *in time* hits.
 4116 The term *in time* here refers to the hits that are likely to be muons by arriving in the expected time
 4117 window. If the hit is outside of the peak window, it is filled into the noise profile histogram of
 4118 the corresponding detector, added into the list of noise/gamma hits and increments the counter of
 4119 noise/gamma hits.

4120 **5-a-2 Efficiency runs - Is the hit within the fake window? :** if the hit is contained in the fake
 4121 window previously defined by Formula B.4, it is added into the list of fake hits. Counting the fake
 4122 hits outside the peak window allows to estimate the probability to detect in time background or noise.

4123 **5-b- Noise/gamma rate runs - Noise histograms are filled:** the hit is filled into the noise profile
 4124 histogram of the corresponding detector, added into the list of noise/gamma hits and increments the
 4125 counter of noise/gamma hits.

```
4126
  4127   for(UInt tr = 0; tr < GIFInfra->GetNTrolleys(); tr++) {
    4128     UInt T = GIFInfra->GetTrolleyID(tr);
      4129     for(UInt sl = 0; sl < GIFInfra->GetNSlots(tr); sl++) {
        4130       UInt S = GIFInfra->GetSlotID(tr,sl) - 1;
        4131       UInt nStripsPart = GIFInfra->GetNStrips(tr,sl);
        4132       string rpcID = GIFInfra->GetName(tr,sl);
        4133       for (UInt p = 0; p < GIFInfra->GetNPartitions(tr,sl); p++) {
          4134         //Clusterize noise/gamma data
          4135         sort(NoiseHitList.rpc[T][S][p].begin(),
            4136             NoiseHitList.rpc[T][S][p].end(),SortHitbyTime);
          4137         Clusterization(NoiseHitList.rpc[T][S][p],
            4138             NoiseCSize_H.rpc[T][S][p],NoiseCMult_H.rpc[T][S][p]);
          4139         //Clusterize muon data and fill efficiency histograms based on
          4140         //the content of peak and fake hit vectors if efficiency run
          4141         if(IsEfficiencyRun(RunType)){
            4142           //Peak data
            4143           sort(PeakHitList.rpc[T][S][p].begin(),
              4144               PeakHitList.rpc[T][S][p].end(),SortHitbyTime);
            4145           Clusterization(PeakHitList.rpc[T][S][p],
              4146               PeakCSize_H.rpc[T][S][p],PeakCMult_H.rpc[T][S][p]);
            4147           if(PeakHitList.rpc[T][S][p].size() > 0)
              4148             EfficiencyPeak_H.rpc[T][S][p]->Fill(DETECTED);
            4149           else EfficiencyPeak_H.rpc[T][S][p]->Fill(MISSED);

            4150           //Fake data
            4151           if(FakeHitList.rpc[T][S][p].size() > 0)
              4152             EfficiencyFake_H.rpc[T][S][p]->Fill(DETECTED);
            4153           else EfficiencyFake_H.rpc[T][S][p]->Fill(MISSED);
            4154         }
          4155         //Save and reinitialise the hit multiplicity
          4156         HitMultiplicity_H.rpc[T][S][p]->Fill(Multiplicity.rpc[T][S][p]);
          4157         Multiplicity.rpc[T][S][p] = 0;
        4158       }
      4159     }
    4160   }
```

4128 *Source Code B.14: Loops to clusterize the hit lists and fill efficiency and multiplicity histograms.*

4129 After the loop on the hit list of the entry is over, the next step is to clusterize the 3D lists filled

4130 in the previous steps, as displayed in Source Code B.14. A 3D loop is then started over the active
 4131 trolley, slot and RPC partitions to access these objects. Each `NoiseHitList` and `PeakHitList`, in
 4132 case of efficiency run, are clusterized as described in section B.5.2. There corresponding cluster size
 4133 and multiplicity histograms are filled at the end of the clustering process.

4134 Then, the peak and fake efficiency histograms are filled in case of efficiency run. The selection is
 4135 simply made by checking whether the RPC detected signals in the peak window or/and fake window
 4136 during this event. In the case a hit is recorded in either of both time windows, the histogram is
 4137 filled with 1. On the contrary, the histogram is filled with 0. Finally, it is useful to remind that
 4138 at this level, it is not possible yet to discriminate in between a muon hit and noise or gamma hit.
 4139 the histograms `PeakCSize_H`, `PeakCMult_H` and `EfficiencyPeak_H` are then subjected to noise and
 4140 background contamination. This contamination is estimated thanks to the fake efficiency histogram
 4141 `EfficiencyFake_H` and corrected at the moment the results will be written into output CSV files and
 4142 the histograms `MuonCSize_H`, `MuonCMult_H` and `Efficiency0_H` will be filled. The correction will be
 4143 explained in Section B.6.4.3.

4144 Finally, the loop ends on the filling of the general hit multiplicity histogram of each detector
 4145 partitions.

4146 **B.6.4 Results calculation**

4147 As mentioned in section B.2.1, the analysis of DAQ data provides the user with 3 CSV files and
 4148 a ROOT file associated to each and every ROOT data file. The fourth CSV file is provided by the
 4149 extraction of the CEAN main frame data monitored during data taking and will be discussed later.
 4150 After looping on the data in the previous part of the analysis macro, the output files are created and a
 4151 3D loop on each RPC readout partitions is started to extract the histograms parameters and compute
 4152 the final results.

4153

4154 **B.6.4.1 Rate normalisation**

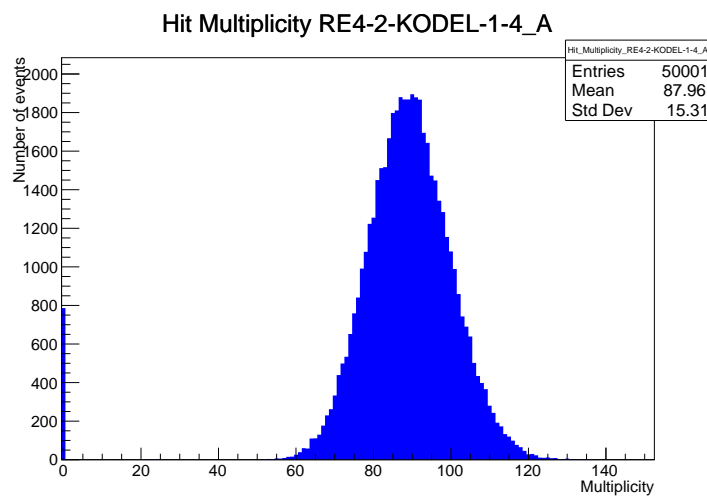


Figure B.2: The effect of the quality flag is explained by presenting the reconstructed hit multiplicity of a data file without `Quality_flag`. The artificial high content of bin 0 is the effect of corrupted data.

4155 The hit rate normalization corresponds to translating a number of hits recorded during the full duration
 4156 of data taking into a rate per unit area value. In order to achieve such result, it is first needed
 4157 to know the total integrated time and the active area of the read-out partition on which the hits are
 4158 counted. The total integrated is simply the noise window used for each event multiplied by the total
 4159 number of events stored in the data file.

```
4160
  if(!isNewFormat){
    TF1* GaussFit = new TF1("gaussfit","[0]*exp(-0.5*((x-[1])/[2])**2)",0,Xmax);
    GaussFit->SetParameter(0,100);
    GaussFit->SetParameter(1,10);
    GaussFit->SetParameter(2,1);
    HitMultiplicity_H.rpc[T][S][p]->Fit(GaussFit,"LIQR","");
    HitMultiplicity_H.rpc[T][S][p]->Fit(GaussFit,"LIQR","");
    TF1* SkewFit = new TF1("skewfit","[0]*exp(-0.5*((x-[1])/[2])**2) / (1 +
  ← exp(-[3]*(x-[4])))",0,Xmax);
    SkewFit->SetParameter(0,GaussFit->GetParameter(0));
    SkewFit->SetParameter(1,GaussFit->GetParameter(1));
    SkewFit->SetParameter(2,GaussFit->GetParameter(2));
    SkewFit->SetParameter(3,1);
    SkewFit->SetParameter(4,1);
    HitMultiplicity_H.rpc[T][S][p]->Fit(SkewFit,"LIQR","");
    HitMultiplicity_H.rpc[T][S][p]->Fit(SkewFit,"LIQR","");
    double fitValue = SkewFit->Eval(1,0,0,0);
    double dataValue = (double)HitMultiplicity_H.rpc[T][S][p]->GetBinContent(2);
    double difference = TMath::Abs(dataValue - fitValue);
    double fitTOdataVSentries_ratio = difference / (double)nEntries;
    bool isFitGOOD = fitTOdataVSentries_ratio < 0.01;
    double nSinglehit = (double)HitMultiplicity_H.rpc[T][S][p]->GetBinContent(1);
    double lowMultRatio = nSinglehit / (double)nEntries;
    bool isMultLOW = lowMultRatio > 0.4;
    if(isFitGOOD && !isMultLOW){
      nEmptyEvent = HitMultiplicity_H.rpc[T][S][p]->GetBinContent(1);
      nPhysics = (int)SkewFit->Eval(0,0,0,0);
      if(nPhysics < nEmptyEvent)
        nEmptyEvent = nEmptyEvent-nPhysics;
    }
  }
  double corrupt_ratio = 100.*(double)nEmptyEvent / (double)nEntries;
  outputCorrCSV << corrupt_ratio << '\t';
  float rate_norm = 0.;
  float stripArea = GIFIInfra->GetStripGeo(tr,sl,p);

  if(IsEfficiencyRun(RunType)){
    float noiseWindow = BMTDCWINDOW - TIMEREJECT - 2*PeakWidth.rpc[T][S][p];
    rate_norm = (nEntries-nEmptyEvent)*noiseWindow*1e-9*stripArea;
  } else
    rate_norm = (nEntries-nEmptyEvent)*RDMNOISEWDW*1e-9*stripArea;
```

4162 *Source Code B.15: Definition of the rate normalisation variable. It takes into account the number of non corrupted entries and the time window used for noise and background calculation, to estimate the total integrated time, and the strip active area to express the result as rate per unit area.*

4163 Nevertheless, to analyse old data format files, not containing any quality flag, it is needed to
 4164 estimate the amount of corrupted data via a fit as the corrupted data will always fill events with a
 4165 fake "0 multiplicity". Indeed, as no hits were stored in the DAQ ROOT files, these events artificially
 4166 contribute to fill the bin corresponding to a null multiplicity, as shown in Figure B.2. In the case the
 4167 mean of the hit multiplicity distribution is high, the contribution of the corrupted data can easily be

evaluated for later correction by comparing the level of the bin at multiplicity 0 and of a skew fit curve that should indicate a value consistent with 0. A skew fit has been chosen over a Poisson fit as it was giving better results for lower mean multiplicity values. Nevertheless, for low irradiation cases, as explained in Appendix A.4.3, the hit multiplicity distribution mean is, on the contrary, rather small and the probability to record events without hits can't be considered small anymore, leading to a difficult and non-reliable estimation of the corruption.

As can be seen in Source Code B.15, conditions have been applied to prevent bad fits and wrong corruption estimation in cases where :

- The difference in between the data for multiplicity 1 and the corresponding fit value should be lower than 1% of the total amount of data : $\frac{|n_{m=1} - sk(1)|}{N_{tot}} < 0.01$ where $n_{m=1}$ is the number of entries with multiplicity 1, $sk(1)$ the value of the skew fit, as defined by Formula 5.2, for multiplicity 1 and N_{tot} the total number of entries.
- The amount of data contained in the multiplicity 0 bin should not exceed 40% of the total data content: $\frac{n_{m=0}}{N_{tot}} \leq 0.4$ where $n_{m=0}$ is the number of entries with multiplicity 0. This number has been determined to be the maximum to be able to separate the excess of data due to corruption from the hit multiplicity distribution.

Those 2 conditions need to be fulfilled to estimate the corruption of old data format files. If the fit was successful, the level of corruption is written in `Offline-Corrupted.csv` and the number of corrupted entries, refered as the integer `nEmptyEvent`, is subtracted from the total number of entries when the rate normalisation factor is computed as explicitated in Source Code B.15. Note that for new data format files, the number of corrupted entries being set to 0, the definition of `rate_norm` stays valid.

B.6.4.2 Rate and activity

At this point, the strip rate histograms, `StripNoiseProfile_H.rpc[T][S][p]`, only contain an information about the total number of noise or background rate hits each channel received during the data taking. As described in Source Code B.16, a loop on the strip channels will be used to normalise the content of the rate distribution histogram for each detector partitions. The initial number of hits recorded for a given bin will be extracted and 2 values are computed.

- The strip hit rate, defined as the number of hits recorded in the bin normalised like described in the previous section, using the variable `rate_norm` and the corresponding bin in histogram `StripNoiseProfile_H.rpc[T][S][p]` is updated, and
- the strip activity, defined as the number of hits recorded in the bin normalised to the average number of hits per bin contained in the partition histogram, using the variable `averageNhit`. This value provides an information on the homogeneity of the detector response to the gamma background or of the detector noise. An activity of 1 corresponds to an average response. Above 1, the channel is more active than the average and bellow 1, the channel is less active. This value is filled in the histograms `StripActivity_H.rpc[T][S][p]`.

```

int nNoise = StripNoiseProfile_H.rpc[T][S][p]->GetEntries();
float averageNhit = (nNoise>0) ? (float) (nNoise/nStripsPart) : 1.;

for(UInt st = 1; st <= nStripsPart; st++){
    float stripRate =
        StripNoiseProfile_H.rpc[T][S][p]->GetBinContent(st)/rate_norm;
    float stripAct =
        StripNoiseProfile_H.rpc[T][S][p]->GetBinContent(st)/averageNhit;

    StripNoiseProfile_H.rpc[T][S][p]->SetBinContent(st,stripRate);
    StripActivity_H.rpc[T][S][p]->SetBinContent(st,stripAct);
}

```

Source Code B.16: Description of the loop that allows to set the content of each strip rate and strip activity channel for each detector partition.

On each detector partitions, which are read-out by a single FEE, all the channels are not processed by the same chip. Each chip can give a different noise response and hence, histograms using a chip binning are used to investigate chip related noise behaviours. The average values of the strip rate or activity grouped into a given chip are extracted using the using the function `GetChipBin()` and stored in dedicated histograms as described in Source Codes B.17 and B.18 respectively.

```

float GetChipBin(TH1* H, UInt chip){
    UInt start = 1 + chip*NSTRIPSCHIP;
    int nActive = NSTRIPSCHIP;
    float mean = 0.;

    for(UInt b = start; b <= (chip+1)*NSTRIPSCHIP; b++) {
        float value = H->GetBinContent(b);
        mean += value;
        if(value == 0.) nActive--;
    }

    if(nActive != 0) mean /= (float)nActive;
    else mean = 0.;

    return mean;
}

```

Source Code B.17: Function used to compute the content of a bin for an histogram using chip binning.

```

for(UInt ch = 0; ch < (nStripsPart/NSTRIPSCHIP); ch++) {
    ChipMeanNoiseProf_H.rpc[T][S][p]->
        SetBinContent(ch+1,GetChipBin(StripNoiseProfile_H.rpc[T][S][p],ch));
    ChipActivity_H.rpc[T][S][p]->
        SetBinContent(ch+1,GetChipBin(StripActivity_H.rpc[T][S][p],ch));
}

```

Source Code B.18: Description of the loop that allows to set the content of each chip rate and chip activity bins for each detector partition knowing the information contained in the corresponding strip distribution histograms.

The activity variable is then used to evaluate the homogeneity of the detector response to background or of the detector noise. The homogeneity h_p of each detector partition can be evaluated

4219 using the formula $h_p = \exp(-\sigma_p^R / \langle R \rangle_p)$, where $\langle R \rangle_p$ is the partition mean rate and σ_p^R is the
 4220 rate standard deviation calculated over the partition channels. The more homogeneously the rates
 4221 are distributed and the smaller will σ_p^R be, and the closer to 1 will h_p get. On the contrary, if the
 4222 standard deviation of the channel's rates is large, h_p will rapidly get to 0. This value is saved into
 4223 histograms as shown in Source Code B.19 and could in the future be used to monitor through time,
 4224 once extracted, the evolution of every partition homogeneity. This could be of great help to under-
 4225 stand the apparition of eventual hot spots due to ageing of the chambers subjected to high radiation
 4226 levels. The monitored homogeneity information could then be combined with a monitoring of the
 4227 activity of each individual channel in order to have a finer information. Monitoring tools have been
 4228 suggested and need to be developed for this purpose.

```
4229
float MeanPartSDev = GetTH1StdDev(StripNoiseProfile_H.rpc[T][S][p]);
float strip_homog = (MeanPartRate==0)
    ? 0.
    : exp(-MeanPartSDev/MeanPartRate);
StripHomogeneity_H.rpc[T][S][p]->Fill("exp -#left(#frac{\#sigma_{Strip}
    \rightarrow Rate}{\#mu_{Strip Rate}}\#right)",strip_homog);
StripHomogeneity_H.rpc[T][S][p]->GetYaxis()->SetRangeUser(0.,1.);

4230
float ChipStDevMean = GetTH1StdDev(ChipMeanNoiseProf_H.rpc[T][S][p]);
float chip_homog = (MeanPartRate==0)
    ? 0.
    : exp(-ChipStDevMean/MeanPartRate);
ChipHomogeneity_H.rpc[T][S][p]->Fill("exp -#left(#frac{\#sigma_{Chip}
    \rightarrow Rate}{\#mu_{Chip Rate}}\#right)",chip_homog);
ChipHomogeneity_H.rpc[T][S][p]->GetYaxis()->SetRangeUser(0.,1.);
```

4231 *Source Code B.19: Storage of the homogeneity into dedicated histograms.*

4232 **B.6.4.3 Correction of muon performance parameters**

4233 By previously filling the peak and fake efficiency histograms as well as the peak and noise cluster
 4234 size and cluster multiplicity it is possible to compute the efficiency of muon detection, the muon
 4235 cluster size, as well as the muon cluster multiplicity. This calculation is based on independent
 4236 event probabilities. The independent events that can be measured in the data are, " μ : A muon was
 4237 detected" and " γ : noise or background was detected". It is trivial to realize that the data in the peak
 4238 window corresponds to the intersection of both events, " $\mu \cup \gamma$: a muon or noise or background was
 4239 detected". This way, the efficiency measured in the peak window is actually the probability of the
 4240 event $\mu \cup \gamma$ while the efficiency in the fake window is then the probability of the event γ alone.
 4241 Assuming that μ and γ are independent, the probability of their intersection can be written as in
 4242 Formula B.5.

$$(B.5) \quad P(\mu \cup \gamma) = P(\mu) + P(\gamma) - P(\mu)P(\gamma)$$

4243 Isolating the probability of the event μ alone, actually corresponding to the muon detection
 4244 efficiency, can be then calculated with the quantities that are contained in the peak and fake histogram
 4245 as in Formula B.6.

$$(B.6) \quad P(\mu) = \frac{P(\mu \cup \gamma) - P(\gamma)}{1 - P(\gamma)} \quad \Leftrightarrow \quad \epsilon_\mu = \frac{\epsilon_{peak} - \epsilon_{fake}}{1 - \epsilon_{fake}}$$

```

if(IsEfficiencyRun(RunType)){  

    //Evaluate the probabilities for each detection case with errors  

    float P_peak = EfficiencyPeak_H.rpc[T][S][p]->GetMean();  

    float P_fake = EfficiencyFake_H.rpc[T][S][p]->GetMean();  

    float P_muon = (P_peak-P_fake)/(1-P_fake);  

    float P_both = P_muon*P_fake;  

    float P_peak_err = sqrt(P_peak*(1.-P_peak)/nEntries);  

    float P_fake_err = sqrt(P_fake*(1.-P_fake)/nEntries);  

    float P_muon_err = sqrt(P_muon*(1.-P_muon)/nEntries);  

    float P_both_err = sqrt(P_both*(1.-P_both)/nEntries);  

    Efficiency0_H.rpc[T][S][p]->Fill("muon efficiency",P_muon);  

    Efficiency0_H.rpc[T][S][p]->Fill("muon efficiency error",P_muon_err);  

    //For each case get the fraction of events it represents  

    float F_both = P_both/P_peak;  

    float F_muon = (P_muon-P_both)/P_peak;  

    float F_fake = (P_fake-P_both)/P_peak;  

    float F_both_err = F_both*(P_both_err/P_both+P_peak_err/P_peak);  

    float F_muon_err = (P_muon_err+F_both_err+F_muon*P_peak_err)/P_peak;  

    float F_fake_err = (P_fake_err+F_both_err+F_fake*P_peak_err)/P_peak;  

    //Get the measured cluster sizes correcting using the fractions  

    float CS_peak = PeakCSIZE_H.rpc[T][S][p]->GetMean();  

    float CS_fake = NoiseCSIZE_H.rpc[T][S][p]->GetMean();  

    float CS_peak_err = 2*PeakCSIZE_H.rpc[T][S][p]->GetStdDev()  

        /sqrt(PeakCSIZE_H.rpc[T][S][p]->GetEntries());  

    float CS_fake_err = 2*NoiseCSIZE_H.rpc[T][S][p]->GetStdDev()  

        /sqrt(NoiseCSIZE_H.rpc[T][S][p]->GetEntries());  

    float CS_muon = (CS_peak-CS_fake*(F_fake+F_both/2.))/(F_muon+F_both/2.);  

    float CS_muon_err = (CS_peak_err  

        +(F_fake+F_both/2.)*CS_fake_err  

        +CS_muon*F_muon_err  

        +CS_fake*(F_fake_err+F_both_err/2.))  

        /(F_muon+F_both/2.);  

    MuonCSIZE_H.rpc[T][S][p]->Fill("muon cluster size",CS_muon);  

    MuonCSIZE_H.rpc[T][S][p]->Fill("muon cluster size error",CS_muon_err);  

    //Finally get the muon cluster multiplicity as peak-fake  

    float noiseWindow = BMTDCWINDOW - TIMEREJECT - 2*PeakWidth.rpc[T][S][p];  

    float peakWindow = 2*PeakWidth.rpc[T][S][p];  

    float CM_peak = PeakCMult_H.rpc[T][S][p]->GetMean();  

    float CM_fake = NoiseCMult_H.rpc[T][S][p]->GetMean()*peakWindow/noiseWindow;  

    float CM_muon = CM_peak-CM_fake;  

    float CM_peak_err = 2*PeakCMult_H.rpc[T][S][p]->GetStdDev()  

        /sqrt(PeakCMult_H.rpc[T][S][p]->GetEntries());  

    float CM_fake_err = 2*NoiseCMult_H.rpc[T][S][p]->GetStdDev()  

        /sqrt(NoiseCMult_H.rpc[T][S][p]->GetEntries())  

        * peakWindow/noiseWindow;  

    float CM_muon_err = CM_peak_err + CM_fake_err;  

    MuonCMult_H.rpc[T][S][p]->Fill("muon cluster multiplicity",CM_muon);  

    MuonCMult_H.rpc[T][S][p]->Fill("muon cluster multiplicity  

    ↳ error",CM_muon_err);  

    //Write in the output CSV file  

    outputEffCSV << P_muon << '\t' << P_muon_err << '\t'  

        << CS_muon << '\t' << CS_muon_err << '\t'  

        << CM_peak << '\t' << CM_peak_err << '\t';
}

```

Source Code B.20: Analysis algorithm to compute muon efficiency, cluster size and multiplicity knowing the peak and fake efficiency, cluster size and multiplicity.

When it comes to the computation of the muon cluster size, a similar reasoning than for the muon detection efficiency computation can be used. Indeed, using Formula B.5, out of the total number of events where a muon or noise or background can be expressed as a sum of fractions of events μ , γ and $\mu \cap \gamma$, the later being the event corresponding to the detection of both events simultaneously, as showed in Formula B.7. The fractions can be expressed as a ratio of the probabilities already known, using this time the notation $P(\mu \cap \gamma)$ instead of $P(\mu)P(\gamma)$. This choice was made to make the code a little clearer.

$$(B.7) \quad 1 = F_\mu + F_\gamma + F_{\mu \cap \gamma} = \frac{P(\mu) - P(\mu \cap \gamma)}{P(\mu \cup \gamma)} + \frac{P(\gamma) - P(\mu \cap \gamma)}{P(\mu \cup \gamma)} + \frac{P(\mu \cap \gamma)}{P(\mu \cup \gamma)}$$

Each ones of these events have an associated cluster size. The cluster size of the noise or background already is measured thanks to the clusterization of the noise hit list. In the same way, the peak cluster size corresponds to the cluster measured for the event $\mu \cup \gamma$. Nevertheless, the cluster of the event $\mu \cap \gamma$ is not known but it can be assumed that the probability of having more than 1 noise or background cluster contained in the peak window is very low if the peak wondow duration is compared to the background rate that rarely seen to go beyond 2000 Hz/cm² [to be confirmed]. Hence, the cluster size that is likely to be measured in such kind of event where both a muon and a background or noise cluster was recorded is the average of the muon cluster size and the background cluster size. The cluster size $C_{\mu \cup \gamma}$ probed in the peak can then be written as in Formula B.8 and leads to the expression for the muon cluster size C_μ written in Formula B.9.

$$(B.8) \quad C_{\mu \cup \gamma} = C_\mu F_\mu + C_\gamma F_\gamma + \frac{C_\mu + C_\gamma}{2} \times F_{\mu \cap \gamma}$$

$$(B.9) \quad C_\mu = \frac{C_{\mu \cup \gamma} - C_\gamma \times (F_\gamma + F_{\mu \cap \gamma}/2)}{F_\mu + F_{\mu \cap \gamma}/2}$$

Finally, the computation of the muon cluster multiplicity comes quite naturally as the cluster multiplicity measured in the peak to which is subtracted the background cluster multiplpicity taken in a window of similar width. These calculations, as well as the error propagation that was not explicitated here, can be seen going through Source Code B.20.

B.6.4.4 Strip masking tool

The offline tool is automatically called at the end of each data taking to analyse the data and offer the shifter DQM histograms to control the data quality. After the histograms have been published online in the DQM page, the shifter can decide to mask noisy or dead channels that will contribute to bias the final rate calculation by editing the mask column of `ChannelsMapping.csv` as can be seen in Figure B.3.

From the code point of view, the function `GetTH1Mean()` is used to retrieve the mean rate partition by partition after the rates have been calculated strip by strip and filled into the histograms `StripNoiseProfile_H.rpc[T][S][p]`, as described through Source Code B.21.

Once the mask for each rejected channel has been updated, the shifter can manually run the offline tool again to update the DQM plots, now including the masked strips, as well the rate results written in the output CSV file `Offline-Rate.csv`. If not done during the shifts, the strip masking

4281 procedure needs to be carefully done by the person in charge of data analysis on the scans that were
 4282 selected to produce the final results.

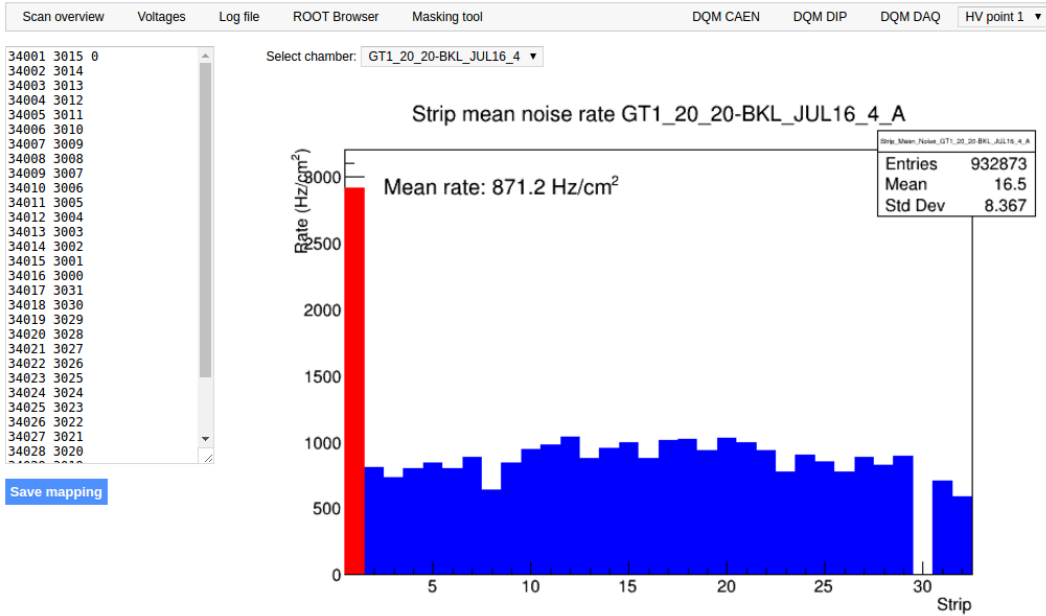


Figure B.3: Display of the masking tool page on the webDCS. The window on the left allows the shifter to edit ChannelsMapping.csv. To mask a channel, it only is needed to set the 3rd field corresponding to the strip to mask to 0. It is not necessary for older mapping file formats to add a 1 for each strip that is not masked as the code is versatile and the default behaviour is to consider missing mask fields as active strips. The effect of the mask is directly visible for noisy channels as the corresponding bin turns red. The global effect of masking strips will be an update of the rate value showed on the histogram that will take into consideration the rejected channels.

```

float GetTH1Mean (TH1* H){
    int nBins = H->GetNbinsX();
    int nActive = nBins;
    float mean = 0.;

    for(int b = 1; b <= nBins; b++){
        float value = H->GetBinContent (b);
        mean += value;
        if(value == 0.) nActive--;
    }

    if(nActive != 0) mean /= (float)nActive;
    else mean = 0.;

    return mean;
}

```

4283
Source Code B.21: The function GetTH1Mean() is used to return the mean along the y-axis of TH1 histograms containing rate information. In order to take into account masked strips whose rate is set to 0, the function looks for masked channels and decrement the number of active channels for each null value found.

4285 **B.6.4.5 Output CSV files filling**

```

for (UInt tr = 0; tr < GIFInfra->GetNTrolleys(); tr++) {
    UInt T = GIFInfra->GetTrolleyID(tr);
    for (UInt sl = 0; sl < GIFInfra->GetNSlots(tr); sl++) {
        UInt S = GIFInfra->GetSlotID(tr,sl) - 1;
        float MeanNoiseRate = 0.;
        float ClusterRate = 0.;
        float ClusterSDev = 0.;

        for (UInt p = 0; p < GIFInfra->GetNPartitions(tr,sl); p++) {
            float MeanPartRate = GetTH1Mean(StripNoiseProfile_H.rpc[T][S][p]);
            float cSizePart = NoiseCSize_H.rpc[T][S][p]->GetMean();
            float cSizePartErr = (NoiseCSize_H.rpc[T][S][p]->GetEntries()==0)
                ? 0.
                : 2*NoiseCSize_H.rpc[T][S][p]->GetStdDev() /
                    sqrt(NoiseCSize_H.rpc[T][S][p]->GetEntries());
            float cMultPart = NoiseCMult_H.rpc[T][S][p]->GetMean();
            float cMultPartErr = (NoiseCMult_H.rpc[T][S][p]->GetEntries()==0)
                ? 0.
                : 2*NoiseCMult_H.rpc[T][S][p]->GetStdDev() /
                    sqrt(NoiseCMult_H.rpc[T][S][p]->GetEntries());
            float ClustPartRate = (cSizePart==0) ? 0.
                : MeanPartRate/cSizePart;
            float ClustPartRateErr = (cSizePart==0) ? 0.
                : ClustPartRate * cSizePartErr/cSizePart;

            outputRateCSV << MeanPartRate << '\t'
                << cSizePart << '\t' << cSizePartErr << '\t'
                << cMultPart << '\t' << cMultPartErr << '\t'
                << ClustPartRate << '\t' << ClustPartRateErr << '\t';

            RPCArea += stripArea * nStripsPart;
            MeanNoiseRate += MeanPartRate * stripArea * nStripsPart;
            ClusterRate += ClustPartRate * stripArea * nStripsPart;
            ClusterSDev += (cSizePart==0)
                ? 0.
                : ClusterRate*cSizePartErr/cSizePart;
        }
        MeanNoiseRate /= RPCArea;
        ClusterRate /= RPCArea;
        ClusterSDev /= RPCArea;
        outputRateCSV << MeanNoiseRate << '\t' << ClusterRate << '\t'
            << ClusterSDev << '\t';
    }
}

```

4287 *Source Code B.22: Description of rate result calculation and writing into the CSV output Offline-Rate.csv. Are saved into the file for each detector, the mean partition rate, cluster size and cluster mutiplicity, along with their errors, for each partition and as well as a detector average.*

4288 All the histograms have been filled. Parameters will then be extracted from them to compute the
4289 final results that will later be used to produce plots. Once the results have been computed, the very
4290 last step of the offline macro is to write these values into the corresponding CSV outputs. Aside of
4291 the file Offline-Corrupted.csv, 2 CSV files are being written by the macro OfflineAnalysis(),
4292 Offline-Rates.csv and Offline-L0-EffCl.csv that respectively contain information about noise
4293 or gamma rates, cluster size and multiplicity, and about level 0 reconstruction of the detector effi-
4294 ciency, muon cluster size and multiplicity. Details on the computation and file writing are respec-

4295 tively given in Sources Codes B.22 and B.20.

4296 **Noise/gamma background variables** are computed and written in the output file for each detector
 4297 partitions. A detector average of the hit and cluster rate is also provided, as shown through Sources
 4298 Code B.22. The variables that are written for each partition are:

- 4299 • The mean partition hit rate per unit area, `MeanPartRate`, that is extracted from the histogram
`StripNoiseProfile_H` as the mean value along the y-axis, as described in section B.6.4.4. No
 4300 error is recorded for the hit rate as this is considered a single measurement. No statistical error
 4301 can be associated to it and the systematics are unknown.
- 4303 • The mean cluster size, `cSizePart`, is extracted from the histogram `NoiseCSize_H` and it's
 4304 statistical error, `cSizePartErr`, is taken to be 2σ of the total distribution.
- 4305 • The mean cluster multiplicity per trigger, `cMultPart`, is extracted from the histogram `NoiseCMult_H`
 4306 and it's statistical error, `cMultPartErr`, is taken to be 2σ of the total distribution. It is impor-
 4307 tant to point to the fact that this variable gives an information that is dependent on the buffer
 4308 window width used for each trigger for the calculation.
- 4309 • The mean cluster rate per unit area, `ClustPartRate`, is defined as the mean hit rate normalised
 4310 to the mean cluster size and it's statistical error, `ClustPartRateErr`, is then obtained using the
 4311 relative statistical error on the mean cluster size.

4312 **Muon performance variables** are computed as discussed in the Section B.6.4.3 and written in
 4313 the output file for each detector partitions as shown through Sources Code B.20. It is reminded that
 4314 this offline tool doesn't include any tracking algorithm to identify muons from the beam and only
 4315 relies on the hits arriving in the time window corresponding to the beam time and is corrected thanks
 4316 to the estimation of the contribution of the background and noise to the efficiency of the detector.
 4317 Assuming that the detection of background and muons were independent events, a probabilistic
 4318 approach was then used to correct efficiency, muon cluster size and muon cluster multiplicity. The
 4319 variables that are written for each partition are:

- 4320 • The muon efficiency, referred to as the probability to detect a muon in the peak window
`P_muon`, also filled in histogram `Efficiency0_H`. The statistical error related to the efficiency,
 4321 `P_muon_err`, is computed using a binomial distribution, as the efficiency measures the proba-
 4322 bility of "success" and "failure" to detect muons.
- 4324 • The mean muon cluster size, `CS_muon`, and its related statistical error, `CS_muon_err`, also filled
 4325 in the histogram `MuonCSize_H`.
- 4326 • The mean muon cluster multiplicity, `CM_muon`, and its related statistical error, `CM_muon_err`,
 4327 also filled in the histogram `MuonCMult_H`.

4328 In addition to these 2 CSV files, the histograms are saved in ROOT file `Scan00XXXX_HVY_Offline.root`
 4329 as explained in section B.2.1.1.

4330 B.7 Current information extraction

4331 Detectors under test at GIF++ are connected both to a CAEN HV power supply and to a CAEN
4332 ADC that reads the currents inside of the RPC gaps bypassing the supply cable. During data tak-
4333 ing, the webDCS records into a ROOT file called `Scan00XXXX_HVY_CAEN.root` histograms with the
4334 monitored parameters of both CAEN devices. Are recorded for each RPC channels (in most cases,
4335 a channel corresponds to an RPC gap):

- 4336 • the effective voltage, HV_{eff} , set by the webDCS using the PT correction on the CAEN power
4337 supply,
- 4338 • the applied voltage, HV_{app} , monitored by the CAEN power supply, and the statistical error
4339 related to the variations of this value through time to follow the variation of the environmental
4340 parameters defined as the RMS of the histogram divided by the square root of the number of
4341 recorded points,
- 4342 • the monitored current, I_{mon} , monitored by the CAEN power supply, and the statistical error
4343 related to the variations of this value through time to follow the variation of the environmental
4344 parameters defined as the RMS of the histogram divided by the square root of the number of
4345 recorded points,
- 4346 • the corresponding current density, J_{mon} , defined as the monitored current per unit area,
4347 $J_{mon} = I_{mon}/A$, where A is the active area of the corresponding gap,
- 4348 • the ADC current, I_{ADC} , recorded through the CAEN ADC module that monitors the dark
4349 current in the gap itself. First of all, the resolution of such a module is better than that of
4350 CAEN power supplies and moreover, the current is not read-out through the HV supply line
4351 but directly at the chamber level giving the real current inside of the detector. The statistical
4352 error is defined as the RMS of the histogram distribution divided by the square root of the
4353 number of recorded points.

4354 Once extracted through a loop over the element of GIF++ infrastructure via the C++ macro
4355 `GetCurrent()`, these parameters, organised in 9 columns per detector HV supply line, are written in
4356 the output CSV file `Offline-Current.csv`. The macro can be found in the file `Current.cc`.

References

- [1] K. Ruedenberg & W.H.E. Schwarz. “Three Millennia of Atoms and Molecules”. In: *Pioneers of Quantum Chemistry*. Ed. by Angela K. Wilson E. Thomas Strom. Vol. 1122. ACS Symposium Series, 2013, pp. 1–45.
- [2] A. Lavoisier. *Traité élémentaire de chimie*. Éditions la Bibliothèque Digitale, 2014 (first published 1789).
- [3] J. Dalton. *A New System of Chemical Philosophy*. William Dawson & Sons, 1808.
- [4] J. von Fraunhofer. “Bestimmung des Brechungs- und des Farben-Zerstreuungs - Vermögens verschiedener Glasarten, in Bezug auf die Vervollkommnung achromatischer Fernröhre”. In: *Denkschriften der Königlichen Akademie der Wissenschaften zu München*. Die Akademie, 1817, pp. 193–226.
- [5] J.J. Thomson. “XL. Cathode Rays”. In: *The London, Edinburgh, and Dublin Philosophical Magazine and Journal of Science* 44:269 (1897), pp. 293–316.
- [6] J.B. Perrin. “Nouvelles propriétés des rayons cathodiques”. In: *Comptes Rendus Hebdomadaires des Séances de L'Académie des Sciences*. Vol. 121. Académie des Sciences, 1895, pp. 1130–1134.
- [7] H. Becquerel. “Déviation du rayonnement du radium dans un champ électrique”. In: *Comptes Rendus Hebdomadaires des Séances de L'Académie des Sciences*. Vol. 130. Académie des Sciences, 1900, p. 809.
- [8] J.J. Thomson. “XXIV. On the structure of the atom: an investigation of the stability and periods of oscillation of a number of corpuscles arranged at equal intervals around the circumference of a circle; with application of the results to the theory of atomic structure”. In: *The London, Edinburgh, and Dublin Philosophical Magazine and Journal of Science* 7:39 (1904), pp. 237–265.
- [9] E. Rutherford & T. Royds. “XXIV. Spectrum of the radium emanation”. In: *The London, Edinburgh, and Dublin Philosophical Magazine and Journal of Science* 16:92 (1904), pp. 313–317.
- [10] H. Geiger. “On the scattering of the α -particles by matter”. In: *Proceedings of the Royal Society A* 81 (1908), pp. 174–177.
- [11] H. Geiger & E. Marsden. “On a diffuse reflection of the α -particles”. In: *Proceedings of the Royal Society A* 82 (1909), pp. 495–500.
- [12] H. Geiger. “The scattering of α -particles by matter”. In: *Proceedings of the Royal Society A* 83 (1910), pp. 492–504.
- [13] H. Geiger & E. Marsden. “LXI. The laws of deflexion of a particles through large angles”. In: *The London, Edinburgh, and Dublin Philosophical Magazine and Journal of Science* 25:148 (1913), pp. 604–623.

- 4393 [14] E. Rutherford. "LXXIX. The Scattering of α and β Particles by Matter and the Structure of
4394 the Atom". In: *The London, Edinburgh, and Dublin Philosophical Magazine and Journal of*
4395 *Science* 21:125 (1911), pp. 669–688.
- 4396 [15] E. Rutherford. "LIV. Collision of α particles with light atoms. IV. An anomalous effect in
4397 nitrogen". In: *The London, Edinburgh, and Dublin Philosophical Magazine and Journal of*
4398 *Science* 37:222 (1919), pp. 581–587.
- 4399 [16] O. Masson. "XXIV. The constitution of atoms". In: *The London, Edinburgh, and Dublin*
4400 *Philosophical Magazine and Journal of Science* 41:242 (1921), pp. 281–285.
- 4401 [17] W. Prout. "On the Relation between the Specific Gravities of Bodies in their Gaseous State
4402 and the Weights of their Atoms." In: *Annals of Philosophy* 6 (1815), pp. 321–330.
- 4403 [18] W. Prout. "Correction of a Mistake in the Essay on the Relation between the Specific Gravities
4404 of Bodies in their Gaseous State and the Weights of their Atoms". In: *Annals of Philosophy*
4405 7 (1816), pp. 111–113.
- 4406 [19] E. Rutherford. "Bakerian Lecture: Nuclear constitution of atoms". In: *Proceedings of the*
4407 *Royal Society A* 97 (1920), pp. 374–400.
- 4408 [20] W. Bothe & H. Becker. "Künstliche Erregung von Kern- γ -Strahlen". In: *Zeitschrift für Physik*
4409 66 (1930), pp. 289–306.
- 4410 [21] H. Becker & W. Bothe. "Die in Bor und Beryllium erregten γ -Strahlen". In: *Zeitschrift für*
4411 *Physik* 76 (1932), pp. 421–438.
- 4412 [22] I. Curie & F. Joliot. "Émission de protons de grande vitesse par les substances hydrogenées
4413 sous l'influence de rayons γ très pénétrants". In: *Comptes Rendus Hebdomadaires des Séances*
4414 *de L'Académie des Sciences*. Vol. 194. Académie des Sciences, 1932, pp. 273–275.
- 4415 [23] J. Chadwick. "Possible Existence of a Neutron". In: *Nature* 129 (1932), p. 312.
- 4416 [24] J. Chadwick. "Bakerian lecture. The neutron". In: *Proceedings of the Royal Society A* 142
4417 (1933), pp. 1–25.
- 4418 [25] Max Plank. "Ueber das Gesetz der Energieverteilung im Normalspectrum". In: *Annalen Der*
4419 *Physik* 309 (1901), pp. 553–563.
- 4420 [26] A. Einstein. "Über einen die Erzeugung und Verwandlung des Lichtes betreffenden heuris-
4421 tischen Gesichtspunkt". In: *Annalen Der Physik* 322 (1905), pp. 132–148.
- 4422 [27] N. Bohr. "I. On the constitution of atoms and molecules". In: *The London, Edinburgh, and*
4423 *Dublin Philosophical Magazine and Journal of Science* 26:151 (1913), pp. 1–25.
- 4424 [28] H.G.J. Moseley. "XCIII. The high-frequency spectra of the elements". In: *The London, Edin-
4425 burgh, and Dublin Philosophical Magazine and Journal of Science* 26:156 (1913), pp. 1024–
4426 1034.
- 4427 [29] A. Sommerfeld. "Zur Quantentheorie der Spektrallinien". In: *Annalen Der Physik* 356 (1916),
4428 pp. 1–94.
- 4429 [30] P. Zeeman. "XXXII. On the influence of magnetism on the nature of the light emitted by a
4430 substance". In: *The London, Edinburgh, and Dublin Philosophical Magazine and Journal of*
4431 *Science* 43:262 (1897), pp. 226–239.
- 4432 [31] P. Zeeman. "VII. Doublets and triplets in the spectrum produced by external magnetic forces".
4433 In: *The London, Edinburgh, and Dublin Philosophical Magazine and Journal of Science*
4434 44:266 (1897), pp. 55–60.
- 4435 [32] P. Zeeman. "VII. Doublets and triplets in the spectrum produced by external magnetic forces.—(II.)"
4436 In: *The London, Edinburgh, and Dublin Philosophical Magazine and Journal of Science*
4437 44:268 (1897), pp. 255–259.

BIBLIOGRAPHY

- 4438 [33] P. Zeeman. "XXI. Measurements concerning radiation-phenomena in the magnetic field.—(I.)"
4439 In: *The London, Edinburgh, and Dublin Philosophical Magazine and Journal of Science*
4440 45:273 (1898), pp. 197–201.
- 4441 [34] W. Gerlach & O. Stern. "Der experimentelle Nachweis der Richtungsquantelung im Mag-
4442 netfeld". In: *Zeitschrift für Physik* 9 (1922), pp. 349–352.
- 4443 [35] W. Pauli. "Über den Einfluß der Geschwindigkeitsabhängigkeit der Elektronenmasse auf den
4444 Zeeman-Effekt". In: *Zeitschrift für Physik* 31 (1925), 373–385.
- 4445 [36] W. Pauli. "Über den Zusammenhang des Abschlusses der Elektronengruppen im Atom mit
4446 der Komplexstruktur der Spektren". In: *Zeitschrift für Physik* 31 (1925), 765–783.
- 4447 [37] G.E. Uhlenbeck & S. Goudsmit. "Spinning Electrons and the Structure of Spectra". In: *Nature*
4448 117 (1926), pp. 264–265.
- 4449 [38] W. Pauli. "Zur Quantenmechanik des magnetischen Elektrons". In: *Zeitschrift für Physik* 43
4450 (1927), 601–623.
- 4451 [39] L. De Broglie. "Recherches sur la théorie des Quanta". PhD thesis. University of Paris, 1924.
- 4452 [40] E. Schrödinger. "An Undulatory Theory of the Mechanics of Atoms and Molecules". In:
4453 *Phys. Rev.* 28 (1927), pp. 1049–1070.
- 4454 [41] P. Dirac. "The quantum theory of the emission and absorption of radiation". In: *Proceedings
4455 of the Royal Society A* 114 (1928), pp. 243–265.
- 4456 [42] P. Dirac. "The quantum theory of the electron". In: *Proceedings of the Royal Society A* 117
4457 (1928), pp. 610–624.
- 4458 [43] J. R. Oppenheimer. "On the Theory of Electrons and Protons". In: *Phys. Rev.* 35 (1930),
4459 pp. 562–563.
- 4460 [44] P. Dirac. "Quantised singularities in the electromagnetic field". In: *Proceedings of the Royal
4461 Society A* 133 (1931), pp. 60–72.
- 4462 [45] J. R. Oppenheimer. "Note on the Theory of the Interaction of Field and Matter". In: *Phys.
4463 Rev.* 35 (1930), pp. 461–477.
- 4464 [46] H.A. Bethe. "The Electromagnetic Shift of Energy Levels". In: *Phys. Rev.* 72 (1947), pp. 339–
4465 341.
- 4466 [47] H.F.J. Dyson. "The Radiation Theories of Tomonaga, Schwinger, and Feynman". In: *Phys.
4467 Rev.* 75 (1949), pp. 486–502.
- 4468 [48] H. Yukawa. "On the Interaction of Elementary Particles. I". In: *Proc. Phys. Math. Soc. Jap.*
4469 17 (1935), pp. 48–57.
- 4470 [49] C.D. Anderson & S.H. Neddermeyer. "Cloud Chamber Observations of Cosmic Rays at 4300
4471 Meters Elevation and Near Sea-Level". In: *Phys. Rev.* 50 (1936), pp. 263–271.
- 4472 [50] S.H. Neddermeyer & C.D. Anderson. "Note on the Nature of Cosmic-Ray Particles". In:
4473 *Phys. Rev.* 51 (1937), pp. 884–886.
- 4474 [51] J.C. Street & E.C. Stevenson. "New Evidence for the Existence of a Particle of Mass Inter-
4475 mediate Between the Proton and Electron". In: *Phys. Rev.* 52 (1937), pp. 1003–1004.
- 4476 [52] C.M.G. Lattes et al. "Processes involving charged mesons". In: *Nature* 159 (1947), pp. 694–
4477 697.
- 4478 [53] C.M.G. Lattes et al. "Observations on the Tracks of Slow Mesons in Photographic Emulsions
4479 (Part 1)". In: *Nature* 160 (1947), pp. 453–456.

- 4480 [54] C.M.G. Lattes et al. “Observations on the Tracks of Slow Mesons in Photographic Emulsions
4481 (Part 2)”. In: *Nature* 160 (1947), 486–492.
- 4482 [55] R. Blokland et al. “High Energy Photons from Proton-Nucleon Collisions”. In: *Phys. Rev.*
4483 77 (1950), pp. 213–218.
- 4484 [56] G.D. Rochester & C.C. Butler. “Evidence for the Existence of New Unstable Elementary
4485 Particles”. In: *Nature* 160 (1947), 855–857.
- 4486 [57] A. Pais. “Some Remarks on the V-Particles”. In: *Phys. Rev.* 86 (1952), pp. 663–672.
- 4487 [58] M. Gell-Mann. “Symmetries of Baryons and Mesons”. In: *Phys. Rev.* 125 (1962), pp. 1067–
4488 1084.
- 4489 [59] K. Nishijima & T. Nakano. “Charge Independence for V-particles”. In: *Progress of Theoretical
4490 Physics* 10 (1953), 581–582.
- 4491 [60] K. Nishijima. “Charge Independence Theory of V-Particles”. In: *Progress of Theoretical
4492 Physics* 13 (1955), pp. 285–304.
- 4493 [61] M. Gell-Mann. “The interpretation of the new particles as displaced charge multiplets”. In:
4494 *Il Nuovo Cimento* 4 (1956), 848–866.
- 4495 [62] W. Heisenberg. “Über den Bau der Atomkerne. I”. In: *Zeitschrift für Physik* 77 (1932), 1–11.
- 4496 [63] V.E. Barnes et al. “Observation of a Hyperon with Strangeness Minus Three”. In: *Phys. Rev.
4497 Lett.* 12 (1964), pp. 204–206.
- 4498 [64] M. Gell-Mann. “A schematic model of baryons and mesons”. In: *Physics Letters* 8 (1964),
4499 pp. 214–215.
- 4500 [65] G. Zweig. *An SU(3) Model for Strong Interaction Symmetry and its Breaking*. Tech. rep.
4501 CERN-TH-401. CERN, 1964.
- 4502 [66] G. Zweig. *An SU(3) Model for Strong Interaction Symmetry and its Breaking (II)*. Tech. rep.
4503 CERN-TH-412. CERN, 1964.
- 4504 [67] E.D. Bloom et al. “High-Energy Inelastic $e - p$ Scattering at 6° and 10° ”. In: *Phys. Rev. Lett.*
4505 23 (1969), pp. 930–934.
- 4506 [68] M. Breidenbach et al. “Observed Behavior of Highly Inelastic Electron-Proton Scattering”.
4507 In: *Phys. Rev. Lett.* 23 (1969), pp. 935–939.
- 4508 [69] B.J. Bjørken & S.L. Glashow. “Elementary particles and SU(4)”. In: *Physics Letters* 11
4509 (1964), pp. 255–257.
- 4510 [70] J. Iliopoulos & L. Maiani S. Glashow. “Weak Interactions with Lepton-Hadron Symmetry”.
4511 In: *Phys. Rev. D* 2 (1970), pp. 1285–1292.
- 4512 [71] J.H. Christenson et al. “Evidence for the 2π Decay of the K_2^0 Meson”. In: *Phys. Rev. Lett.* 13
4513 (1964), pp. 138–140.
- 4514 [72] M. Kobayashi & T. Maskawa. “CP-Violation in the Renormalizable Theory of Weak Inter-
4515 action”. In: *Progress of Theoretical Physics* 49 (1973), pp. 652–657.
- 4516 [73] H. Harari. “A new quark model for hadrons”. In: *Physics Letters B* 57 (1975), pp. 265–269.
- 4517 [74] B. Richter et al. “Discovery of a Narrow Resonance in e^+e^- Annihilation”. In: *Phys. Rev.
4518 Lett.* 33 (1974), pp. 1406–1408.
- 4519 [75] S. Ting et al. “Experimental Observation of a Heavy Particle J ”. In: *Phys. Rev. Lett.* 33
4520 (1974), pp. 1404–1405.
- 4521 [76] S.W. Herb et al. “Observation of a Dimuon Resonance at 9.5 GeV in 400 GeV Proton-
4522 Nucleus Collisions”. In: *Phys. Rev. Lett.* 39 (1977), pp. 252–255.

BIBLIOGRAPHY

- 4523 [77] S. Abashi et al. “Search for High Mass Top Quark Production in $\bar{p}p$ Collisions at $\sqrt{s} =$
4524 1.8 TeV”. In: *Phys. Rev. Lett.* 74 (1995), pp. 2422–2426.
- 4525 [78] F. Abe et al. “Observation of Top Quark Production in $\bar{p}p$ Collisions with the Collider De-
4526 tector at Fermilab”. In: *Phys. Rev. Lett.* 74 (1995), pp. 2626–2631.
- 4527 [79] F. Tkachov. “A contribution to the history of quarks: Boris Struminsky’s 1965 JINR publi-
4528 cation”. In: (2009).
- 4529 [80] O.W. Greenberg. “Spin and Unitary-Spin Independence in a Paraquark Model of Baryons
4530 and Mesons”. In: *Phys. Rev. Lett.* 13 (1964), pp. 598–602.
- 4531 [81] M.Y. Han & Y. Nambu. “Three-Triplet Model with Double $SU(3)$ Symmetry”. In: *Phys.*
4532 *Rev.* 139 (1965), B1006–B1010.
- 4533 [82] R.P. Feynman. “The behavior of hadron collisions at extreme energies”. In: *Conf. Proc.*
4534 C690905 (1969), pp. 237–258.
- 4535 [83] J.D. Bjorken & E.A. Paschos. “Inelastic Electron-Proton and γ -Proton Scattering and the
4536 Structure of the Nucleon”. In: *Phys. Rev.* 185 (1969), pp. 1975–1982.
- 4537 [84] M. Gell-Mann & H. Leutwyler H. Fritzsch. “Advantages of the color octet gluon picture”.
4538 In: *Physics Letters B* 47 (1973), pp. 365–368.
- 4539 [85] D.J. Gross & F. Wilczek. “Ultraviolet Behavior of Non-Abelian Gauge Theories”. In: *Phys.*
4540 *Rev. Lett.* 30 (1973), pp. 1343–1346.
- 4541 [86] H.D. Politzer. “Reliable Perturbative Results for Strong Interactions?” In: *Phys. Rev. Lett.* 30
4542 (1973), pp. 1346–1349.
- 4543 [87] S. Bethke. “ α_s 2002”. In: *Nuclear Physics B* 121 (2003), pp. 74–81.
- 4544 [88] E. Fermi. “Versuch einer Theorie der β -Strahlen. I”. In: *Zeitschrift für Physik* 88 (1934),
4545 pp. 161–177.
- 4546 [89] W. Pauli. “Dear radioactive ladies and gentlemen”. In: *Phys. Today* 31N9 (1978), p. 27.
- 4547 [90] C.L. Cowan Jr. et al. “Detection of the Free Neutrino: a Confirmation”. In: *Science* 20 (1956),
4548 pp. 103–104.
- 4549 [91] E.J. Konopinski & H.M. Mahmoud. “The Universal Fermi Interaction”. In: *Phys. Rev.* 92
4550 (1953), pp. 1045–1049.
- 4551 [92] J. Steinberger et al. L.M. Lederman M. Schwartz. “Observation of High-Energy Neutrino Re-
4552 actions and the Existence of Two Kinds of Neutrinos”. In: *Phys. Rev. Lett.* 9 (1962), pp. 36–
4553 44.
- 4554 [93] T.D. Lee & C.N. Yang. “Question of Parity Conservation in Weak Interactions”. In: *Phys.*
4555 *Rev.* 104 (1956), pp. 254–258.
- 4556 [94] G. Gamow & E. Teller. “Selection Rules for the β -Disintegration”. In: *Phys. Rev.* 49 (1936),
4557 pp. 895–899.
- 4558 [95] C.S. Wu et al. “Experimental Test of Parity Conservation in Beta Decay”. In: *Phys. Rev.* 105
4559 (1957), pp. 1413–1415.
- 4560 [96] S. Weinberg. “A Model of Leptons”. In: *Phys. Rev. Lett.* 19 (1967), pp. 1264–1266.
- 4561 [97] Y. Nambu & G. Jona-Lasinio. “Dynamical Model of Elementary Particles Based on an Anal-
4562 ogy with Superconductivity. I”. In: *Phys. Rev.* 122 (1961), pp. 345–358.
- 4563 [98] Y. Nambu & G. Jona-Lasinio. “Dynamical Model of Elementary Particles Based on an Anal-
4564 ogy with Superconductivity. II”. In: *Phys. Rev.* 124 (1961), pp. 246–254.

- 4565 [99] & J. R. Schrieffer J. Bardeen L.N. Cooper. “Microscopic Theory of Superconductivity”. In: *Phys. Rev.* 106 (1957), pp. 162–164.
- 4566
- 4567 [100] Y. Nambu. “Quasi-Particles and Gauge Invariance in the Theory of Superconductivity”. In: *Phys. Rev.* 117 (1960), pp. 648–663.
- 4568
- 4569 [101] J. Goldstone. “Quasi-Particles and Gauge Invariance in the Theory of Superconductivity”. In: *Il Nuovo Cimento* 19 (1961), pp. 154–164.
- 4570
- 4571 [102] J. Schwinger. “Gauge Invariance and Mass”. In: *Phys. Rev.* 125 (1962), pp. 397–398.
- 4572 [103] P.W. Anderson. “Plasmons, Gauge Invariance, and Mass”. In: *Phys. Rev.* 130 (1963), pp. 439–442.
- 4573
- 4574 [104] F. Englert & R. Brout. “Broken Symmetry and the Mass of Gauge Vector Mesons”. In: *Phys. Rev. Lett.* 13 (1964), pp. 321–323.
- 4575
- 4576 [105] P.W. Higgs. “Broken Symmetries and the Masses of Gauge Bosons”. In: *Phys. Rev. Lett.* 13 (1964), pp. 508–509.
- 4577
- 4578 [106] & T.W.B. Kibble G.S. Guralnik C.R. Hagen. “Global Conservation Laws and Massless Particles”. In: *Phys. Rev. Lett.* 13 (1964), pp. 585–587.
- 4579
- 4580 [107] Wikipedia. *Standard Model*. 2018. URL: https://en.wikipedia.org/wiki/Standard_Model.
- 4581
- 4582 [108] UA1 Collaboration. “Experimental observation of isolated large transverse energy electrons with associated missing energy at $s = 540 \text{ GeV}$ ”. In: *Physics Letters B* 122 (1983), pp. 103–116.
- 4583
- 4584
- 4585 [109] UA2 Collaboration. “Observation of single isolated electrons of high transverse momentum in events with missing transverse energy at the CERN pp collider”. In: *Physics Letters B* 122 (1983), pp. 476–485.
- 4586
- 4587
- 4588 [110] UA1 Collaboration. “Experimental observation of lepton pairs of invariant mass around $95 \text{ GeV}/c^2$ at the CERN SPS collider”. In: *Physics Letters B* 126 (1983), pp. 398–410.
- 4589
- 4590 [111] UA2 Collaboration. “Evidence for $Z_0 \rightarrow e^+e^-$ at the CERN pp collider”. In: *Physics Letters B* 129 (1983), pp. 130–140.
- 4591
- 4592 [112] ATLAS Collaboration. “Observation of a new particle in the search for the Standard Model Higgs boson with the ATLAS detector at the LHC”. In: *Physics Letters B* 716 (2012), pp. 1–29.
- 4593
- 4594
- 4595 [113] CMS Collaboration. “Observation of a new boson at a mass of 125 GeV with the CMS experiment at the LHC”. In: *Physics Letters B* 716 (2012), pp. 30–61.
- 4596
- 4597 [114] CMS Collaboration ATLAS Collaboration. “Combined Measurement of the Higgs Boson Mass in pp Collisions at $\sqrt{s} = 7$ and 8 TeV with the ATLAS and CMS Experiments”. In: *Physical Review Letters* 114 (2015). 191803.
- 4598
- 4599
- 4600 [115] M. Tanabashi et al. (Particle Data Group). “Review of Particle Physics”. In: *Phys. Rev. D* 98 (2018), p. 030001.
- 4601
- 4602 [116] A.A. Arkhipov. “Proton proton total cross-sections from the window of cosmic ray experiments”. In: *Elastic and diffractive scattering. Proceedings, 9th Blois Workshop, Pruhonice, Czech Republic*. 2001, pp. 293–304.
- 4603
- 4604
- 4605 [117] D.S. Harmer & K.C. Hoffman R. Davis Jr. “Search for Neutrinos from the Sun”. In: *Physical Review Letters* 20 (1968), pp. 1205–1209.
- 4606
- 4607 [118] B. Pontecorvo. “Neutrino Experiments and the Problem of Conservation of Leptonic Charge”. In: *Sov. Phys. JETP* 26 (1968), pp. 984–988.
- 4608

BIBLIOGRAPHY

- [4609] [119] SNO Collaboration. “Direct Evidence for Neutrino Flavor Transformation from Neutral-
4610 Current Interactions in the Sudbury Neutrino Observatory”. In: *Physical Review Letters*
4611 89.011301 (2002).
- [4612] [120] M. Nakagawa & S. Sakata Z. Maki. “Remarks on the Unified Model of Elementary Particles”. In: *Progress of Theoretical Physics* 28 (1962), pp. 870–880.
- [4614] [121] V.A.Rubakov & M.E. Shaposhnikov V.A. Kuzmin. “On anomalous electroweak baryon-
4615 number non-conservation in the early universe”. In: *Physics Letters B* 155 (1985), pp. 36–
4616 42.
- [4617] [122] M. Drewes & M. Shaposhnikov L. Canetti. “Matter and antimatter in the universe”. In: *New
4618 J. Phys.* 14.095012 (2012).
- [4619] [123] The ACME Collaboration. “Order of Magnitude Smaller Limit on the Electric Dipole Mo-
4620 ment of the Electron”. In: *Science* 343 (2014), pp. 269–272.
- [4621] [124] E. Corbelli & P. Salucci. “The extended rotation curve and the dark matter halo of M33”.
4622 In: *Monthly Notices of the Royal Astronomical Society* 311 (2000), pp. 441–447.
- [4623] [125] H. Pointcaré. “The Milky Way and the Theory of Gases”. In: *Popular Astronomy* 14 (1906),
4624 pp. 475–488.
- [4625] [126] J.C. Kapteyn. “First Attempt at a Theory of the Arrangement and Motion of the Sidereal
4626 System”. In: *Astrophysical Journal* 55 (1922), p. 302.
- [4627] [127] F. Zwicky. “Republication of: The redshift of extragalactic nebulae (First published in
4628 1933)”. In: *General Relativity and Gravitation* 41 (2009), pp. 207–224.
- [4629] [128] F. Zwicky. “On the Masses of Nebulae and of Clusters of Nebulae”. In: *Astrophysical Jour-
4630 nal* 86 (1937), p. 217.
- [4631] [129] H.W. Babcock. “The rotation of the Andromeda Nebula”. In: *Lick Observatory bulletin* 498
4632 (1939), pp. 41–51.
- [4633] [130] V.C. Rubin & W.K. Ford Jr. “Rotation of the Andromeda Nebula from a Spectroscopic
4634 Survey of Emission Regions”. In: *Astrophysical Journal* 159 (1970), p. 379.
- [4635] [131] D.H. Rogstad & G.S. Shostak. “Gross Properties of Five Scd Galaxies as Determined from
4636 21-CENTIMETER Observations”. In: *Astrophysical Journal* 176 (1972), p. 315.
- [4637] [132] Planck Collaboration. “Planck 2015 results. XIII. Cosmological parameters”. In: *A&A* 594.A13
4638 (2016).
- [4639] [133] N. Jarosik et al. “Seven-year Wilkinson Microwave Anisotropy Probe (WMAP*) observa-
4640 tions: Sky maps, Systematic errors, and Basic Results”. In: *ApJS* 192.14 (2011).
- [4641] [134] E. Verlinde. “Emergent Gravity and the Dark Universe”. In: *SciPost Phys.* 2 (2017), p. 016.
- [4642] [135] A. Maeder. “An alternative to the Λ CDM model: the case of scale invariance”. In: *ApJ*
4643 834.194 (2017).
- [4644] [136] S. Dimopoulos & H. Georgi. “Softly broken supersymmetry and SU(5)”. In: *Nuclear Physics
4645 B* 193 (1981), pp. 150–162.
- [4646] [137] F. Tanedo. *The Hierarchy Problem: why the Higgs has a snowball’s chance in hell*. 2012.
4647 URL: [https://www.quantumdiaries.org/2012/07/01/the-hierarchy-
4648 problem-why-the-higgs-has-a-snowballs-chance-in-hell/](https://www.quantumdiaries.org/2012/07/01/the-hierarchy-problem-why-the-higgs-has-a-snowballs-chance-in-hell/).
- [4649] [138] M. Kamionkowski & K. Griest G. Jungman. “Supersymmetric dark matter”. In: *Physics
4650 Reports* 267 (1996), pp. 10–14.
- [4651] [139] & P. Nath A.H. Chamseddine R. Arnowitt. “Locally Supersymmetric Grand Unification”.
4652 In: *Phys. Rev. Lett.* 49 (1982), pp. 970–974.

- 4653 [140] S. Dimopoulos & G. Dvali N. Arkani–Hamed. “The hierarchy problem and new dimensions
4654 at a millimeter”. In: *Physics Letters B* 429 (1998), pp. 263–272.
- 4655 [141] S. Dimopoulos & G. Dvali N. Arkani–Hamed. “Phenomenology, astrophysics, and cosmol-
4656 ogy of theories with submillimeter dimensions and TeV scale quantum gravity”. In: *Phys.
4657 Rev. D* 59 (1999), p. 086004.
- 4658 [142] T. Kaluza. “Zum Unitätsproblem der Physik”. In: *Sitzungsber. Preuss. Akad. Wiss. Berlin
4659 (Math. Phys.)* 1921 (1921), pp. 966–972.
- 4660 [143] O. Klein. “The Atomicity of Electricity as a Quantum Theory Law”. In: *Nature* 118 (1926),
4661 p. 516.
- 4662 [144] L. Randall & R. Sundrum. “Large Mass Hierarchy from a Small Extra Dimension”. In: *Phys.
4663 Rev. Lett.* 83 (1999), pp. 3370–3373.
- 4664 [145] L. Randall & R. Sundrum. “An Alternative to Compactification”. In: *Phys. Rev. Lett.* 83
4665 (1999), pp. 4690–4693.
- 4666 [146] T. Massam et al. “Experimental observation of antideuteron production”. In: *Il Nuovo Ci-
4667 mento A* 63 (1965), pp. 10–14.
- 4668 [147] ALEPH Collaboration. “Determination of the number of light neutrino species”. In: *Physics
4669 Letters B* 231 (1989), pp. 519–529.
- 4670 [148] CERN, ed. (1985).
- 4671 [149] CERN, ed. (1986).
- 4672 [150] CERN, ed. (1994).
- 4673 [151] CERN, ed. (1998).
- 4674 [152] CERN, ed. (1999).
- 4675 [153] CERN. Geneva. LHC Experiments Committee. *Letter of Intent for A Large Ion Collider
4676 Experiment [ALICE]*. Tech. rep. CERN-LHCC-93-016. ALICE Collaboration, 1993.
- 4677 [154] CERN. Geneva. LHC Experiments Committee. *ATLAS : technical proposal for a general-
4678 purpose pp experiment at the Large Hadron Collider at CERN*. Tech. rep. CERN-LHCC-94-
4679 43. ATLAS Collaboration, 1994.
- 4680 [155] CERN. Geneva. LHC Experiments Committee. *CMS : letter of intent by the CMS Col-
4681 laboration for a general purpose detector at LHC*. Tech. rep. CERN-LHCC-92-003. CMS
4682 Collaboration, 1992.
- 4683 [156] CERN. Geneva. LHC Experiments Committee. *LHCb : letter of intent*. Tech. rep. CERN-
4684 LHCC-95-5. LHCb Collaboration, 1995.
- 4685 [157] L. Evans and P. Bryant. “LHC Machine”. In: *JINST* 3 (2008). S08001.
- 4686 [158] LHCb Collaboration. “Observation of $J/\psi p$ Resonances Consistent with Pentaquark States
4687 in $\Lambda_b^0 \rightarrow J/\psi K^- p$ Decays”. In: *Physical Review Letters* 115 (2015). 072001.
- 4688 [159] LHCb Collaboration. “Observation of $J/\psi \phi$ Structures Consistent with Exotic States from
4689 Amplitude Analysis of $B^+ \rightarrow J/\psi \phi K^+$ Decays”. In: *Physical Review Letters* 118 (2017).
4690 022003.
- 4691 [160] CERN. Geneva. *High-Luminosity Large Hadron Collider (HL-LHC) Technical Design Re-
4692 port V. 0.1*. Tech. rep. CERN-2017-007-M. 2017.
- 4693 [161] CERN. Geneva. LHC Experiments Committee. *The CMS muon project : Technical Design
4694 Report*. Tech. rep. CERN-LHCC-97-032. CMS Collaboration, 1997.

BIBLIOGRAPHY

- 4695 [162] X. Tata M. Drees. “Signals for heavy exotics at hadron colliders and supercolliders”. In: *Physics Letters B* 252 (1990), pp. 695–702.
- 4696
- 4697 [163] D.A. Milstead et al. “Stable massive particles at colliders”. In: *Physics Reports* 438 (2007), pp. 1–63.
- 4698
- 4699 [164] Z. Ligeti et al. “Supermodels for early LHC”. In: *Physics Letters B* 690 (2010), pp. 280–288.
- 4700
- 4701 [165] V. Khachatryan et al. “Search for long-lived charged particles in proton-proton collisions at $\sqrt{s} = 13 \text{ TeV}$ ”. In: *Phys. Rev. D* 94 (2017). 112004.
- 4702
- 4703 [166] M. Shaposhnikov A. Kusenko. “Supersymmetric Q-balls as dark matter”. In: *Physics Letters B* 418 (1998), pp. 46–54.
- 4704
- 4705 [167] B. Koch et al. “Black holes at LHC?” In: *J. Phys. G: Nucl. Part. Phys.* 34 (2007). S535.
- 4706 [168] J. Schwinger. “Magnetic Charge and Quantum Field Theory”. In: *Phys. Rev.* 144 (1966). 1087.
- 4707
- 4708 [169] M Yu Khlopov et al. “Dark matter with invisible light from heavy double charged leptons of almost-commutative geometry?” In: *Class. Quantum Grav.* 23 (2006). 7305.
- 4709
- 4710 [170] PoS, ed. *Search for Heavy Stable Charged Particles in CMS*. Vol. EPS-HEP2009. 2009, p. 438.
- 4711
- 4712 [171] CERN. Geneva. LHC Experiments Committee. *The Phase-2 Upgrade of the CMS Muon Detectors*. Tech. rep. CERN-LHCC-2017-012, CMS-TDR-016. CMS Collaboration, 2017.
- 4713
- 4714 [172] CERN. Geneva. LHC Experiments Committee. *CMS, the Compact Muon Solenoid : technical proposal*. Tech. rep. CERN-2015-005. 2015.
- 4715
- 4716 [173] CERN. Geneva. LHC Experiments Committee. *High-Luminosity Large Hadron Collider (HL-LHC) Preliminary Design Report*. Tech. rep. CERN-LHCC-94-38. CMS Collaboration, 1994.
- 4717
- 4718
- 4719 [174] CERN. Geneva. LHC Experiments Committee. *The Phase-2 Upgrade of the CMS Level-1 Trigger - Interim Report to the LHCC*. Tech. rep. CERN-LHCC-2017-013, CMS-TDR-017. CMS Collaboration, 2017.
- 4720
- 4721
- 4722 [175] CERN. Geneva. LHC Experiments Committee. *Technical Proposal for the Phase-II Upgrade of the CMS Detector*. Tech. rep. CERN-LHCC-2015-010, CMS-TDR-15-02. CMS Collaboration, 2015.
- 4723
- 4724
- 4725 [176] F.Sauli. “GEM: A new concept for electron amplification in gas detectors”. In: *Nucl. Instr. Meth. Phys. Res.* 386 (1997), pp. 531–534.
- 4726
- 4727 [177] CERN. Geneva. LHC Experiments Committee. *CMS Technical Design Report for the Muon Endcap GEM Upgrade*. Tech. rep. CERN-LHCC-2015-012, CMS-TDR-013. CMS Collaboration, 2015.
- 4728
- 4729
- 4730 [178] A. Gelmi. *CMS iRPC at HL-LHC: background study*. 2018. URL: https://indico.cern.ch/event/732794/contributions/3021836/attachments/1657792/2654574/iRPC_bkg_study_Upgrade29_05_18.pdf.
- 4731
- 4732
- 4733 [179] P.Bortignon. “Design and performance of the upgrade of the CMS L1 muon trigger”. In: *Nucl. Instr. Meth. Phys. Res.* 824 (2016), pp. 256–257.
- 4734
- 4735 [180] The European Parliament and the Council of the European Union. “Regulation (EU) No 517/2014 of 16 April 2014 on fluorinated greenhouse gases and repealing Regulation (EC) No 842/2006”. In: *Official Journal of the European Union* 150 (2014), pp. 195–230.
- 4736
- 4737

- [181] R. Santonico and R. Cardarelli. "Development of resistive plate counters". In: *Nucl. Instr. Meth. Phys. Res.* 187 (1981), pp. 377–380.
- [182] Yu.N. Pestov and G.V. Fedotovich. *A picosecond time-of-flight spectrometer for the VEPP-2M based on local-discharge spark counter*. Tech. rep. SLAC-TRANS-0184. SLAC, 1978.
- [183] W.W. Ash, ed. *Spark Counter With A Localized Discharge*. Vol. SLAC-R-250. 1982, pp. 127–131.
- [184] I. Crotty et al. "The non-spark mode and high rate operation of resistive parallel plate chambers". In: *NIMA* 337 (1993), pp. 370–381.
- [185] I. Crotty et al. "Further studies of avalanche mode operation of resistive parallel plate chambers". In: *NIMA* 346 (1994), pp. 107–113.
- [186] R. Cardarelli et al. "Avalanche and streamer mode operation of resistive plate chambers". In: *NIMA* 382 (1996), pp. 470–474.
- [187] R. Cardarelli et al. "Performance of a resistive plate chamber operating with pure CF_3Br ". In: *NIMA* 333 (1993), pp. 399–403.
- [188] M. Abbrescia et al. "Performance of a Resistive Plate Chamber operated in avalanche mode under ^{137}Cs irradiation". In: *NIMA* 392 (1997), pp. 155–160.
- [189] M. Abbrescia et al. "Properties of C2H2F4-based gas mixture for avalanche mode operation of resistive plate chambers". In: *NIMA* 398 (1997), pp. 173–179.
- [190] P. Camarri et al. "Streamer suppression with SF6 in RPCs operated in avalanche mode". In: *NIMA* 414 (1998), pp. 317–324.
- [191] E. Cerrón Zeballos et al. "Effect of adding SF6 to the gas mixture in a multigap resistive plate chamber". In: *NIMA* 419 (1998), pp. 475–478.
- [192] E. Cerrón Zeballos et al. "A new type of resistive plate chamber: The multigap RPC". In: *NIMA* 374 (1996), pp. 132–135.
- [193] M.C.S. Williams. "The development of the multigap resistive plate chamber". In: *Nucl. Phys. B* 61 (1998), pp. 250–257.
- [194] H. Czyrkowski et al. "New developments on resistive plate chambers for high rate operation". In: *NIMA* 419 (1998), pp. 490–496.
- [195] CERN. Geneva. LHC Experiments Committee. *ATLAS muon spectrometer: Technical design report*. Tech. rep. CERN-LHCC-97-22. ATLAS Collaboration, 1997.
- [196] CERN. Geneva. LHC Experiments Committee. *ALICE Time-Of-Flight system (TOF) : Technical Design Report*. Tech. rep. CERN-LHCC-2000-012. ALICE Collaboration, 2000.
- [197] The CALICE collaboration. "First results of the CALICE SDHCAL technological prototype". In: *JINST* 11 (2016).
- [198] PoS, ed. *Density Imaging of Volcanoes with Atmospheric Muons using GRPCs*. International Europhysics Conference on High Energy Physics - HEP 2011. 2011.
- [199] C. Lippmann. "Detector Physics of Resistive Plate Chambers". PhD thesis. Johann Wolfgang Goethe-Universität, 2003.
- [200] W. Riegler. "Induced signals in resistive plate chambers". In: *NIMA* 491 (2002), pp. 258–271.
- [201] M. Abbrescia et al. "Effect of the linseed oil surface treatment on the performance of resistive plate chambers". In: *NIMA* 394 (1997), pp. 13–20.

BIBLIOGRAPHY

- [202] G.Battistoni et al. “Sensitivity of streamer mode to single ionization electrons”. In: *NIMA* 235 (1985), pp. 91–97.
- [203] M.Abbrescia et al. “Cosmic ray tests of double-gap resistive plate chambers for the CMS experiment”. In: *NIMA* 550 (2005), pp. 116–126.
- [204] JINST, ed. *Performance of the Resistive Plate Chambers in the CMS experiment*. The 9th International Conference on Positioin Sensitive Detectors. 2012.
- [205] PoS, ed. *The CMS RPC detector performance during Run-II data taking*. The European Physical Society Conference on High Energy Physics (EPS-HEP2017). 2018.
- [206] Honeywell International Inc. *Solstice(R) ze Refrigerant (HFO-1234ze): The Environmental Alternative to Traditional Refrigerants*. Tech. rep. FPR-003/2015-01. 2015.
- [207] E. Cerron Zeballos et al. “A comparison of the wide gap and narrow gap resistive plate chamber”. In: *NIMA* 373 (1996), pp. 35–42.
- [208] ALICE Collaboration. “A study of the multigap RPC at the gamma irradiation facility at CERN”. In: *NIMA* 490 (2002), pp. 58–70.
- [209] B. Bonner et al. “A multigap resistive plate chamber prototype for time-of-flight for the STAR experiment at RHIC”. In: *NIMA* 478 (2002), pp. 176–179.
- [210] S. Yang et al. “Test of high time resolution MRPC with different readout modes for the BESIII upgrade”. In: *NIMA* 763 (2014), pp. 190–196.
- [211] A. Akindinovg et al. “RPC with low-resistive phosphate glass electrodes as a candidate for the CBM TOF”. In: *NIMA* 572 (2007), pp. 676–681.
- [212] JINST, ed. *Development of the MRPC for the TOF system of the MultiPurpose Detector*. RPC2016: XII Workshop on Resistive Plate Chambers and Related Detectors. 2016.
- [213] M.C.S. Williams. “Particle identification using time of flight”. In: *Journal of Physics G* 39 (2012).
- [214] A. Alici et al. “Aging and rate effects of the Multigap RPC studied at the Gamma Irradiation Facility at CERN”. In: *NIMA* 579 (2007), pp. 979–988.
- [215] M. Abbrescia et al. “The simulation of resistive plate chambers in avalanche mode: charge spectra and efficiency”. In: *NIMA* 431 (1999), pp. 413–427.
- [216] JINST, ed. *Description and simulation of physics of Resistive Plate Chambers*. RPC2016: XII Workshop on Resistive Plate Chambers and Related Detectors. 2016.
- [217] V. Francais. “Description and simulation of the physics of Resistive Plate Chambers”. PhD thesis. LPC - Laboratoire de Physique Corpusculaire - Clermont-Ferrand, 2017.
- [218] H. Bethe. “Zur Theorie des Durchgangs schneller Korpuskularstrahlen durch Materie”. In: *Annalen der Physik* 397 (1930), pp. 325–400.
- [219] International Commission on Radiation Units and Measurements. *Stopping Powers for Electrons and Positions*. Tech. rep. Report 37. 1984.
- [220] International Commission on Radiation Units and Measurements. *Stopping Power and Ranges for Protons and Alpha Particles*. Tech. rep. Report 49. 1994.
- [221] H. Bichsel. “A method to improve tracking and particle identification in TPCs and silicon detectors”. In: *NIMA* 562 (2006), pp. 154–197.
- [222] W. W. M. Allison and J. H. Cobb. “Relativistic charged particle identification by energy loss”. In: *Annual Review of Nuclear and Particle Science* 30 (1980), 253–298.

- 4822 [223] International Commission on Radiation Units and Measurements. *Average energy to pro-*
 4823 *duce an ion pair*. Tech. rep. Report 31. 1994.
- 4824 [224] I.B. Smirnov. “Modeling of ionization produced by fast charged particles in gases”. In: *NIMA* 554 (2005), pp. 474–493.
- 4826 [225] J. Phys.: Conf. Ser., ed. <https://doi.org/10.1088/1742-6596/587/1/012035> *Results of the CAL-*
 4827 *ICE SDHCAL technological prototype*. 16th International Conference on Calorimetry in
 4828 High Energy Physics (CALOR 2014). 2015.
- 4829 [226] W. Riegler et al. “Detector physics and simulation of resistive plate chambers”. In: *NIMA*
 4830 500 (2003), pp. 144–162.
- 4831 [227] I.B. Smirnov. *HEED++ simulation program*. 2010. URL: <http://ismirnov.web.cern.ch/ismirnov/heed>.
- 4833 [228] S.F. Biagi. “Monte Carlo simulation of electron drift and diffusion in counting gases under
 4834 the influence of electric and magnetic fields”. In: *NIMA* 421 (1999), pp. 234–240.
- 4835 [229] W. H. Furry. “On Fluctuation Phenomena in the Passage of High Energy Electrons through
 4836 Lead”. In: *Phys. Rev.* 52 (1937), pp. 569–581.
- 4837 [230] H. Genz. “Single electron detection in proportional gas counters”. In: *Nucl. Instr. and Meth.*
 4838 112 (1973), pp. 83–90.
- 4839 [231] M. Abbrescia et al. “Resistive plate chambers performances at cosmic rays fluxes”. In: *NIMA* 359 (1995), pp. 603–609.
- 4841 [232] M. Abbrescia et al. “Resistive plate chambers performances at low pressure”. In: *NIMA* 394
 4842 (1997), pp. 341–348.
- 4843 [233] M. Abbrescia. “Operation, performance and upgrade of the CMS Resistive Plate Chamber
 4844 system at LHC”. In: *NIMA* 732 (2013), pp. 195–198.
- 4845 [234] F. Thyssen. “Commissioning, Operation and Performance of the CMS Resistive Plate Cham-
 4846 ber System”. PhD thesis. Universiteit Gent, 2014.
- 4847 [235] M. Bianco. “ATLAS RPC certification and commissioning with cosmic rays”. PhD thesis.
 4848 Università del Salento, 2007.
- 4849 [236] M. Bianco. “ATLAS RPC certification with cosmic rays”. In: *NIMA* 602 (2009), pp. 700–
 4850 704.
- 4851 [237] M. Abbrescia et al. “Study of long-term performance of CMS RPC under irradiation at the
 4852 CERN GIF”. In: *NIMA* 533 (2004), pp. 102–106.
- 4853 [238] H.C. Kim et al. “Quantitative aging study with intense irradiation tests for the CMS forward
 4854 RPCs”. In: *NIMA* 602 (2009), pp. 771–774.
- 4855 [239] S. Agosteo et al. “A facility for the test of large-area muon chambers at high rates”. In: *NIMA* 452 (2000), pp. 94–104.
- 4857 [240] PoS, ed. *CERN GIF ++ : A new irradiation facility to test large-area particle detectors for*
 4858 *the high-luminosity LHC program*. Vol. TIPP2014. 2014, pp. 102–109.
- 4859 [241] D. Pfeiffer et al. “The radiation field in the Gamma Irradiation Facility GIF++ at CERN”.
 4860 In: *NIMA* 866 (2017), pp. 91–103.
- 4861 [242] CAEN. *Mod. V1190-VX1190 A/B, 128/64 Ch Multihit TDC*. 14th ed. 2016.
- 4862 [243] CAEN. *Mod. V1718 VME USB Bridge*. 9th ed. 2009.
- 4863 [244] A. Fagot. *GIF Cosmic Muon Monte Carlo Simulation*. 2017. URL: <https://github.com/a-fagot/Cosmics-Simulation>.

BIBLIOGRAPHY

- 4865 [245] G. Pugliese et al. “Long-term performance of double gap resistive plate chambers under
4866 gamma irradiation”. In: *NIMA* 477 (2002), pp. 293–298.
- 4867 [246] G. Pugliese et al. “Aging study for resistive plate chambers of the CMS muon trigger detec-
4868 tor”. In: *NIMA* 515 (2003), pp. 342–347.
- 4869 [247] M. Capeans et al. on behalf of the GIF and GIF++ User Communities. “A GIF++ Gamma
4870 Irradiation Facility at the SPS H4 Beam Line”. CERN-SPSC-2009-029 / SPSC-P-339. 2009.
- 4871 [248] R. Guida et al. “Results about HF production and bakelite analysis for the CMS Resistive
4872 Plate Chambers”. In: *NIMA* 594 (2008), pp. 140–147.
- 4873 [249] F. Bellini et al. “Study of HF production in BaBar Resistive Plate Chambers”. In: *NIMA* 594
4874 (2008), pp. 33–38.
- 4875 [250] J. Eysermans. *WebDCS GIF++*. CERN. 2016. URL: <https://www.webdcs.cern.ch>.
- 4876
- 4877 [251] S. Carrillo A. Fagot. *GIF++ Offline Analysis v6*. 2017. URL: https://github.com/afagot/GIF_OfflineAnalysis.
- 4878
- 4879 [252] H. Reithler. *Filters for GIF++*. RWTH Aachen University, CMS-CERN. 2013. URL: <https://edms.cern.ch/document/1324028/1>.
- 4880
- 4881 [253] R. Cardarelli et al. “RPC performance vs. front-end electronics”. In: *NIMA* 661 (2012),
4882 S198–S200.
- 4883 [254] IEEE, ed. *Petiroc, a new front-end ASIC for time of flight application*. Vol. 2013 IEEE
4884 Nuclear Science Symposium and Medical Imaging Conference (2013 NSS/MIC). 2014.
- 4885 [255] JINST, ed. *Petiroc and Citiroc: front-end ASICs for SiPM read-out and ToF applications*.
4886 Vol. Topical Workshop on Electronics for Particle Physics 2013 (TWEPP-13). 2014.
- 4887 [256] A. Fagot. *GIF++ Data Acquisition Software for CMS RPC*. 2016. URL: https://github.com/afagot/GIF_DAQ.
- 4888
- 4889 [257] W-Ie-Ne-R. *VME 6021-23 VXI*. 5th ed. 2016.
- 4890 [258] Wikipedia. *INI file*. 2017. URL: https://en.wikipedia.org/wiki/INI_file.